Determining the Pressure – Temperature – Composition (P-T-X) conditions of magma storage

Penny E. Wieser[1], Matthew L.M. Gleeson[1], Simon Matthews[2, 3], Charlotte DeVitre[1], Esteban Gazel[4]

1. Earth and Planetary Sciences, UC Berkeley. penny_wieser@berkeley.edu, gleesonm@berkeley.edu, cdevitre@berkeley.edu

2. Earth Science Department, University of Cambridge, sm905@cam.ac.uk

3. Institute of Earth Sciences, University of Iceland, Iceland.

4. Department of Earth and Atmospheric Sciences, Cornell University, Ithaca, NY 14850, USA, egazel@cornell.edu

Determining the Pressure – Temperature – Composition (P-T-X) conditions of magma storage

Penny E. Wieser[1], Matthew L.M. Gleeson[1], Simon Matthews[2, 3], Charlotte DeVitre[1], Esteban Gazel[4]

1. Earth and Planetary Sciences, UC Berkeley. penny_wieser@berkeley.edu, gleesonm@berkeley.edu, cdevitre@berkeley.edu

2. Earth Science Department, University of Cambridge, sm905@cam.ac.uk

3. Institute of Earth Sciences, University of Iceland, Iceland.

4. Department of Earth and Atmospheric Sciences, Cornell University, Ithaca, NY 14850, USA, egazel@cornell.edu

Key Points

- Many mineral-melt barometers have standard errors of ± 2–3 kbar (± 7–11 km), which limits their ability to provide detailed constraints on magma storage in relatively thin-crusted settings (MORB and OIB).
- Different models/equations can yield very different PT conditions; model choice must be considered as one of the largest sources of systematic error in a given study.
- The paucity of independent test datasets for many methods makes it difficult to truly assess their performance; statistics calculated using the calibration dataset where only 1 variable is treated as an unknown are overly optimistic of performance in natural systems.
- It has become increasingly clear that melt inclusion studies which did not account for the vapour bubble may have underestimated storage depths by more than a factor of 2, requiring re-evaluation of melt inclusion volatile contents and storage depths globally.

Key words

1. Mineral Thermobarometry
2. Thermodynamics
3. Melt Inclusions
4. Fluid inclusions
5. Raman Spectroscopy
6. Hygrometry
7. Chemometry
8. Experimental Petrology
9. FAIR Research Framework
10. MELTS modelling
11. Pyroxene
12. Amphibole
13. Plagioclase

Abstract (100 words)

Determining the pressures and temperatures at which melts are stored in the crust and upper mantle, and the major element composition, redox state and volatile contents of these melts, is vital to constrain the structure and dynamics of magmatic plumbing systems. In turn, constraining these parameters helps understand the geochemical and structural evolution of the Earth's lithosphere, and periods of unrest at active volcanoes. We review common thermobarometers, hygrometers and chemometers based on mineral and/or liquid compositions, before discussing recent advances in melt and fluid inclusion barometry, Raman-based elastic thermobarometry, and thermodynamic modelling methods. Where possible, we investigate the accuracy and precision of each technique, and the implications for the application of each method to different research questions.

1. Introduction.

Determining the pressures, and therefore depths, at which magmas are stored and evolve in the crust and upper mantle is vital to understand the chemical and structural evolution of volcanic plumbing systems, with implications for our understanding of the formation of mineral deposits, and the evolution of the Earth's lithosphere (Lee and Anderson, 2015). Precisely constraining magma storage depths at a specific volcano using past eruptive deposits can also provide vital context to help inform the interpretation of monitoring signals during periods of volcanic unrest (e.g., distinguishing magmatic and hydrothermal signals, Pritchard et al., 2019).

Constraining the temperatures of different magmatic processes can reveal the thermal evolution of magmatic systems and are vital inputs for many other common workflows in igneous petrology, such as calculations of timescales from elemental diffusion in erupted crystals (termed "diffusion chronometry" or "geospeedometry"). In fact, because diffusion rates are strongly sensitive to temperature (following an Arrhenius relationship), uncertainty in temperature is one of the largest sources of error when obtaining timescales using these chronometers (Chakraborty and Dohmen, 2022; Costa et al., 2020). For example, Mutch et al. (2019a) show that timescales calculated from Cr diffusion in spinel change from ~4000 years at 1190°C to ~1000 yrs at 1230°C. Thus, uncertainty in temperatures affects interpretations of timescales of crustal residence (Mutch et al., 2019a), re-awakening from quiescence to eruption (Shamloo and Till, 2019), and calculations of magma ascent rates (Mutch et al., 2019b). Of course, accurately constraining magma storage depths is also vital for magma ascent rate calculations, where the speed is calculated by dividing the depth to the inferred magma body by the time calculated from diffusion chronometry (Barth et al., 2019; Klügel, 1998).

Here, we describe a multitude of approaches to determine the pressures (P) and temperatures (T) at which magmas were stored in the lithosphere, as well as the chemistry of these stored melts (Fig. 1). We pay particular attention to differences between models (Section 1.1) and the precision and accuracy of calculations (Section 1.2). For barometers, we first evaluate variations in crustal thickness in a wide variety of tectonic settings to provide context when interpreting the precision of different barometry methods (Section 1.3). Then, we review the methods used to convert measured mineral compositions with or without an equilibrium melt into magma storage pressures and temperatures (mineral barometry and thermometry), and to calculate the chemistry and H_2O contents of the melts from which a specific mineral composition grew (chemometry and hygrometry respectively, Section 2).

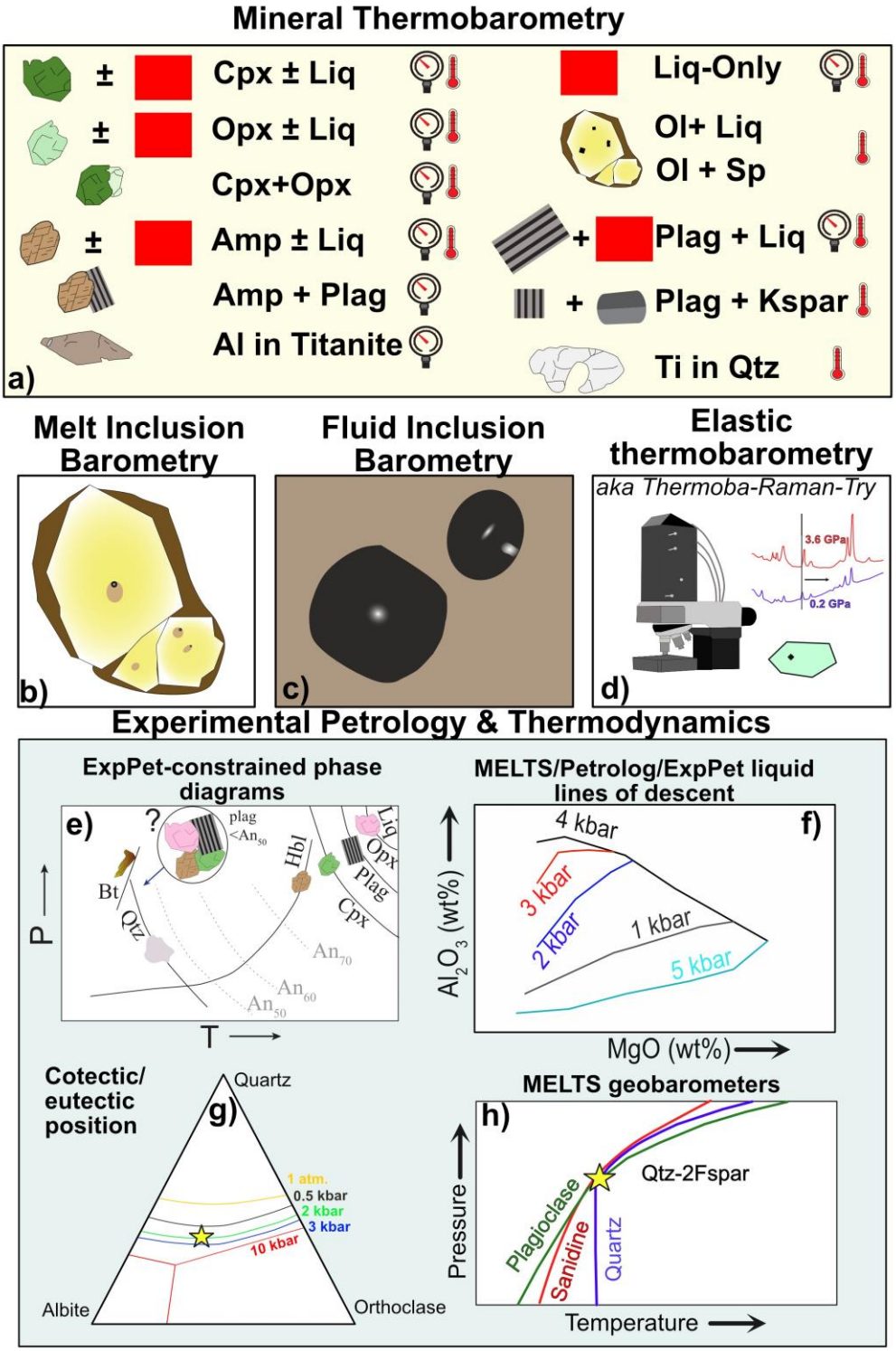

Figure 1: Summary of some of the methods used to determine pressures and temperatures of magma storage. Part e) adapted from Rutherford (2003), f) from Cashman and Edmonds (2019), g) and h) adapted from Gualda et al. (2012) and Gualda and Ghiorso (2014), respectively.

We also evaluate the methods and uncertainties involved in melt inclusion barometry, with a specific focus on the influence of CO_2 stored within melt inclusion vapour bubbles on calculated pressures (Section 3). The general proliferation of Raman spectroscopy in the Earth Sciences (Dubessy et al., 2012) has not only been important for performing direct measurements of melt inclusion vapour bubbles; it has also pushed forwards two other barometric methods. First, Raman spectroscopic measurements of fluid inclusions can provide a substantially faster method of calculating storage depths than traditional microthermometric techniques

(Section 4). Second, Raman measurements of mineral inclusions in-situ can also be used to calculate pressures and temperatures (thermoba-Raman-try, Section 6). Experimental petrology not only underpins the formulation and calibration of mineral-melt thermobarometers and volatile solubility models, it can also be used to provide direct constraints on magma storage in a specific volcanic system (Section 7). Finally, we discuss approaches using thermodynamic constraints on phase stability in igneous systems (Section 8), methods not covered in detail in this review (Section 9) and summarize the general proliferation of community data repositories and open-source tools to help inform model calibration, and aid calculations of magma storage conditions (Section 10).

1.1 Assessing and comparing models

When calculating pressure, temperature, and/or melt chemistry from the composition of erupted melts, crystals and their inclusions, the result can be highly sensitive to the choice of model/equation/parameterization, relating the measured quantity (e.g., Cpx, Amp, melt inclusion composition) to the intensive variable (e.g., P, T). Below, we discuss the origin of all these different models, and best practices for model intercomparison.

Mineral thermobarometry (Section 2) utilizes chemical reactions involving the crystallization or re-equilibration of minerals which are accompanied by a change in volume (sensitive to P) and/or a change in entropy (sensitive to T, e.g., Putirka, 2008). Chemometry (and hygrometry) relies on the fact that the composition of crystallizing/re-equilibrating phases is sensitive to the composition of the melt phase. Some thermobarometry and chemometry expressions are firmly rooted in thermodynamics, with compositional terms and the functional form of the equation determined from a specific reaction. Typically, these expressions have coefficients attached to thermodynamic terms which are calibrated empirically using the measured compositions of minerals in experiments conducted at well-constrained P-T-fO_2-H2O conditions (e.g., the Plagioclase-Liquid hygrometer of Waters and Lange, 2015).

More commonly, available equations have a general form based on thermodynamics, with the addition of empirically derived terms to improve the fit to the calibration dataset (e.g., Neave and Putirka, 2017). For example, many of the Cpx-Liq barometers of Putirka (2008) have a functional form based on Jadeite exchange between the liquid and Cpx, which is associated with a change in volume, so is P sensitive (Putirka et al., 1996):

$$P = a + \frac{bT}{10^4} + \frac{cT}{10^4}\ln(\mathrm{Jd}^{\mathrm{Cpx-Liq}}) + \cdots \text{[Equation 1]}$$

Empirical terms help to improve the fit between the calculated parameter and the known experimental conditions. The inclusion of these terms may be informed at least in part by thermodynamic reasoning (e.g., Masotta et al., 2013; Neave and Putirka, 2017; Putirka, 2008). For example, Putirka (1996) EqP1 has a term for the cation fractions of Na and Al:

$$\text{EqP1=Equation 1 terms...} + 367\ (X_{Na}^{Liq} * X_{Al}^{Liq}) \text{ [Equation 2]}$$

The fact that the best fit involved the multiplication of Na and Al cation fractions implies that these two components have identical activity coefficients (Putirka et al., 1996). However, the thermodynamic interpretation is often obscured by decisions to reduce the complexity of equations, such as wanting to avoid introducing multiple temperature-dependent terms (see Equation 12 of Putirka et al., 1996). In general, as calibration datasets have grown larger, more empirical terms have been added that have a less clear thermodynamic basis. For example, Putirka (2008, Eq31) has many additional terms relative to EqP1, including terms for the Ca, Na, K, Si, Mg and Fe_t liquid cation fractions, H_2O in the liquid, and for EnFs, DiHd, and Al cation fractions in the Cpx:

$$\text{Eq31=Equation 1 terms} \ldots + 106\,X_{Ca}^{Liq} - 166\left(X_{Na}^{Liq} + X_{K}^{Liq}\right)^2 - 50.2\,X_{Si}^{Liq} * \left(X_{Mg}^{Liq} + X_{Fe}^{Liq}\right) - 3.2\log(DiHd) - 2.2\log(EnFs) + 0.86\log(X_{Al,6\ cat}^{Cpx}) + 0.4{*}H_2O \text{ [Equation 3]}$$

New models not only arise through the addition of such empirical terms, but also through the recalibration of the coefficients of older equations. For example, Masotta et al. (2013) recalibrate the coefficients of the Putirka (2008) equations for a new calibration dataset of alkaline magmas. Other thermobarometers are purely empirical, including terms and mathematic expressions like logs, exponentials, and different powers which improve the fit to the calibration dataset without a firm tie to the thermodynamics of a specific chemical reaction. For example, the liquid-only thermometer of Helz and Thornber (1987) was calibrated based on the linear relationship between MgO and T in melting experiments on samples from the Kīlauea Iki lava lake. The amphibole-only barometer of Ridolfi and Renzulli (2012) uses multivariate least squares regression to determine

the relationship between P and amphibole composition across a number of different P ranges, with highly variable functional forms (Eq1a, Eq1b and Eq1e take the exponential of amphibole cation fractions, Eq1c and Eq1d do not). The results from these equations are selected or combined using an algorithm to give a single P. This algorithm was then tweaked by Ridolfi (2021), generating yet another model.

Most recently, machine learning approaches using regression trees have been used to parameterize the relationship between mineral and melt composition and experimental conditions (e.g., Higgins et al., 2022; Jorgenson et al., 2022; Petrelli et al., 2020). These approaches have no underlying thermodynamic basis. They are trained using measured oxide contents, rather than thermodynamically informed mineral components such as Jadeite, Diopside etc. The lack of thermodynamic basis may affect their ability to extrapolate beyond the compositions and P-T conditions for which they are calibrated. One advantage is that these models can be easily updated as new experimental data becomes available if the code for model training is released.

The diversity of empirical, thermodynamic, and machine-learning models for mineral-based thermobarometry/hygrometry/chemometry has resulted in a somewhat overwhelming choice of models to calculate magma storage conditions. Concerningly, these different models can return vastly different results. Wieser et al. (2023a) show that different Cpx-Liq and Cpx-only thermobarometers applied to the same Cpx-Liq pair passing equilibrium tests yield pressures spanning >10 kbar and temperatures spanning >100°C. Clearly, model choice is one of the largest sources of uncertainty when performing such calculations.

Melt inclusion barometry uses volatile solubility models to calculate the pressure at which a specified melt composition (major+volatile elements) is volatile saturated, for a specified temperature. The formulation of these solubility models ranges from being purely empirical (Liu et al., 2005; Shishkina et al., 2014) to purely thermodynamic (Ghiorso and Gualda, 2015; Papale et al., 2006). Some models lie between these end members, having a general form indicated by thermodynamics and some empirical coefficients accounting for silicate melt composition (semi-empirical, e.g., Dixon, 1997; Iacono-Marziano et al., 2012). Even for fully thermodynamical models, the sign and magnitude of many coefficients attached to thermodynamic terms have been criticized as being physically implausible (see Ghiorso and Gualda, 2015 and Wieser et al. 2022a for discussion of the Papale et al. 2006 model). In addition to their different functional forms, the calibration datasets of solubility models are also highly variable with respect to the range of melt compositions, fluid compositions, and P and T. For example, the model of Shishkina et al. (2014) was calibrated on variably alkaline, relatively mafic melts, and expresses volatile solubility empirically using the cation fractions of Ca, K, Na, Mg, Fe, Si and Al for CO_2, and K and Na for H_2O. In contrast, the solubility model of Dixon (1997) was calibrated on a more restricted range of relatively mafic tholeiitic to alkaline melt compositions. This model has a thermodynamic form, with an empirical correction for the effect of melt composition that is only dependent on the concentration of SiO_2 in the melt. The model MagmaSat (Ghiorso and Gualda, 2015) was calibrated on a very wide range of melt compositions (tholeiite and alkaline, from basalts to rhyolites), and is a fully thermodynamic model sensitive to all the commonly measured major oxide species. Unsurprisingly, given these differences in model formulation and calibration datasets, calculated saturation pressures can vary greatly between models, with systematic offsets of at least a factor of two not being uncommon (Wieser et al., 2022a).

In stark contrast to uncertainties associated with model choice when performing mineral thermobarometry or melt inclusion barometry, fluid inclusion barometry (Section 4) relies on the CO_2 equation of state to convert the measured density of a CO_2-rich fluid into a P for a specified entrapment temperature. Other than an ideal gas law (which does a poor job at high P), different published CO_2 equation of states predict very similar P for a given CO_2 density and T (~ 1–5% difference, Böttcher et al., 2012; Lamadrid et al., 2017; Span and Wagner, 1996; Sterner and Pitzer, 1994; Wieser and DeVitre, 2023). For example, at 1150°C for ρ_{CO_2} =0.8 g/cm^3, the relatively simple empirical expression of Sterner and Pitzer (1994) gives 5.008 kbar, while the more complex thermodynamic model of Span and Wanger (1996) gives 4.956 kbar (~3% difference). However, the conversion between measured CO_2 density to depth is substantially less simple when trapped fluids contain other species, such as H_2O or SO_2 (Hansteen and Klugel, 2008; Hurai, 2010). It is difficult to estimate the initial molar ratios of each species, and EOS for these mixed fluids are poorly constrained, if parameterized at all. Fluid inclusion barometry is also not immune to systematic error; re-equilibrium of the host crystal during magma ascent can increase the inclusion volume, reduce the CO_2 density and thus the calculated pressure/depth (Hansteen and Klugel, 2008; Wanamaker and Evans, 1989).

Thermodynamic approaches to determining the conditions of magma storage and evolution are also sensitive to the choice of model (Section 8). Thermodynamic models are typically constructed from two key components: (i) a dataset of standard state properties (e.g., enthalpy of formation, heat capacity, etc.) for all

minerals of interest, and (ii) solution models for phases with variable compositions, which describe how composition influences the thermodynamic properties of the phase. Within igneous petrology and volcanology the MELTS 'family' of thermodynamic models is the most widely used (Ghiorso et al., 2002; Ghiorso and Sack, 1995; Gualda et al., 2012). The original MELTS model was developed by Ghiorso and Sack (1995), building on the thermodynamic database of Berman (1988) to include thermodynamic models of relevant igneous solid solutions (e.g., Ghiorso, 1990; Ghiorso and Sack, 1991; Sack and Ghiorso, 1994, 1991, 1989). Since the release of this original MELTS model, various updates have been published. pMELTS includes a revised liquid thermodynamic model optimised for mantle-like bulk compositions (Ghiorso et al., 2002). Rhyolite-MELTS v.1.0.2 incorporates changes to the thermodynamic properties of quartz and the orthoclase endmember of the alkali feldspars to enable the eutectic behaviour of high-silica rhyolitic magmas to be recreated (i.e. crystallization over a narrow T range, Gualda et al., 2012). Rhyolite-MELTS v1.2.0 incorporates the mixed H_2O-CO_2 fluid model MagmaSat and is recommended for use away from the granitic ternary minimum. Rhyolite-MELTSv1.1.0 incorporates the updated CO_2 solubility model, but retains the old H_2O solubility model of rhyolite-MELTSv1.0.2 for calculations at the ternary minimum (Ghiorso and Gualda, 2015).

An alternative group of thermodynamic models developed by Tim Holland, Roger Powell and co-workers (Holland and Powell, 2004, 1998, 1990) have traditionally been utilized in metamorphic studies (Tamblyn et al., 2020), but have recently been updated for applications to mantle melting and igneous systems. For example, Jennings and Holland (2015) expand the model system, optimizing its performance for calculations of peridotite melting behaviour and the phase relationships of basaltic liquids at crustal to mantle conditions. Most recently, Holland et al. (2018) presented an updated thermodynamic database that is calibrated on a range of compositions, from peridotites through to granites. The Holland dataset is mostly accessed through a variety of software tools. THERMOCALC calculates the location of known phase boundaries and mineral reactions (Powell et al., 1998), while Perple_X (Connolly, 2009, 2005) and Theriak-Domino (de Capitani and Petrakakis, 2010) use a Gibbs Free Energy minimization approach to calculate the phase assemblage and compositions specified P-T conditions.

Comparisons between the MELTS and Holland-Powell families of models are relatively uncommon; Jennings and Holland (2015) compare the results of mantle melting calculations, and Hernández-Uribe et al. (2022) compare the equilibrium crystallization behaviour of an mid oceanic ridge basalt (MORB) magma. Importantly, Hernández-Uribe et al. (2022) do not compare fractional crystallization pathways, noting that these would be "relatively laborious" with current software tools. The recent release of MAGEMin, a Gibbs Free Energy minimisation package utilizing the Holland et al. (2018) thermodynamic models written in the programming language C (Riel et al., 2022) allows MELTS-like workflows to be performed including fractional crystallization. MAGEMin has a Julia interface and can be run in Python3 using pyMELTScalc (Gleeson et al. 2023), greatly aiding model intercomparison between the Holland and MELTS databases (see Section 8). There are also several more empirical models which have been used as alternatives to MELTS to model fractional crystallization in magmas, and therefore could place constraints on P and T (see Section 8). These include COMAGMAT (Ariskin et al., 1993) and Petrolog3 (Danyushevsky and Plechov, 2011). In Section 8, we show that the choice of thermodynamic model to use (and even the version of MELTS used) has a large influence on calculations of magma storage conditions (see also Hernández-Uribe et al., 2022).

1.2. Statistics to compare models

When trying to decide which model/equation to use to calculate magma storage conditions, and when assessing whether the chosen method has sufficient resolution to address the science question of interest, it is important to consider both accuracy and precision. Accuracy describes how close the measurement/calculation is to the true value, while precision describes how close repeated measurements/calculations are to one another. For example, if you measure a small, very homogenous region of a Cpx crystal five times using an electron probe microanalyser (EPMA), and calculate Cpx-only pressures from these measurements, you may obtain 5, 5.5, 6, 4.9, and 6.2 kbar. The precision could be quantified using 1 standard deviation of these measurements (e.g., ±0.47 kbar). However, the Cpx may have formed at 8 kbar, in which case these calculations are relatively precise, but inaccurate (mean offset of 2.5 kbar). It is also worth distinguishing between random and systematic errors. Random error describes scatter about the true value (affecting precision, not accuracy), while systematic error describes a constant offset from the true value (affecting accuracy not precision).

Most publications calibrating new mineral-melt thermobarometers or chemometers describe the fit between calculated and experimental values for a given parameter using the root mean square error (RMSE)

and the R^2 value (see Table 1, RMSE= standard error estimate, SEE, for linear regressions). When equations are applied to natural systems, these RMSE errors are often quoted as the error on the calculation. This is problematic for several reasons. The RMSE and R^2 alone do not properly distinguish between random and systematic error, so fails to capture different model performances. Many different metrics (Table 1) can be useful to assess model performance.

Metric	Good at	Bad at
R^2 value: Correlation coefficient of the linear regression between the measured (x) and predicted (y) value.	Assessing precision and random uncertainty. Low precision (lots of random uncertainty) = low R^2 value.	Assessing accuracy and systematic uncertainty.
Gradient and Intercept of the linear regression	Assessing systematic uncertainty, which will generate a gradient different from 1, and an intercept different from zero.	Assessing precision/random uncertainty (as averages all measurements).
Root mean square error (RMSE) aka. SEE $RMSE = \sqrt{\frac{1}{N}\sum_{i=1}^{N}(x_i - y_i)^2}$	Describes how concentrated the data is around the linear regression.	Struggles to distinguish between low precision and accurate vs. high precision with a systematic offset. Sensitive to outliers.
Mean Absolute Error (MAE) $MAE = \frac{1}{N}\sum_{i=1}^{N}\lvert x_i - y_i\rvert$	Similar to the RMSE but no squared term. Gives less weight to larger errors than the RMSE	Struggles to distinguish between low precision and accurate vs. high precision with a systematic offset
Mean Bias Error (MBE) $MBE = \frac{1}{N}\sum_{i=1}^{N}(x_i - y_i)$	Identifies average model bias, as no absolute or squared term.	Doesn't identify random error, as + and – errors cancel out.

Table 1: Metrics used to assess models, where x is the measured parameter (e.g., P, T) and y is the model-predicted parameter. RMSE and SEE are identical for a linear regression, for higher order regressions, they differ as only the SEE accounts for the degrees of freedom.

In Fig. 2, we demonstrate the issues associated with using *only* the root mean square error (RMSE) and R^2 to assess model performance. Instead, we suggest that the RMSE, R^2, gradient, intercept and MBE should all be presented on figures to allow assessment of both random and systematic uncertainty (e.g. Putirka et al. 2003). To demonstrate this, we compare the relative performance of three hypothetical barometers, plotting the experimental P on the x axis, and the calculated P on the y axis (Fig. 2). All barometers have the same RMSE error. However, it is visually apparent that their performance varies greatly. While Fig. 2a has a very high R^2 value, its low gradient and high intercept reveals that it substantially overpredicts P at P<12 kbar, and underpredicts P at P>12 kbar. While Fig. 2b has a lower R^2 value, it has no substantial systematic offsets, meaning it is a far more accurate barometer across a wide range of pressures than that shown in Fig. 2a (indicated by the gradient close to one, an intercept close to zero, and the low MBE). The barometer in Fig. 2c also has a gradient close to 1, but the higher intercept and MBE indicate that it systematically overpredicts at all pressures. Clearly, if you wish to distinguish the absolute depth of magma storage, perhaps to compare to geophysical inversions of magma storage depths, or signals of unrest, the barometer in Fig. 2b is the best, despite its lower R^2. However, if you only wish to distinguish differences in storage pressures between different crystal populations (without caring about the actual depth), the barometer in Fig. 2a is the best, as it is the most precise. Use of all 5 metrics in tandem is essential for identifying systematic and random uncertainty.

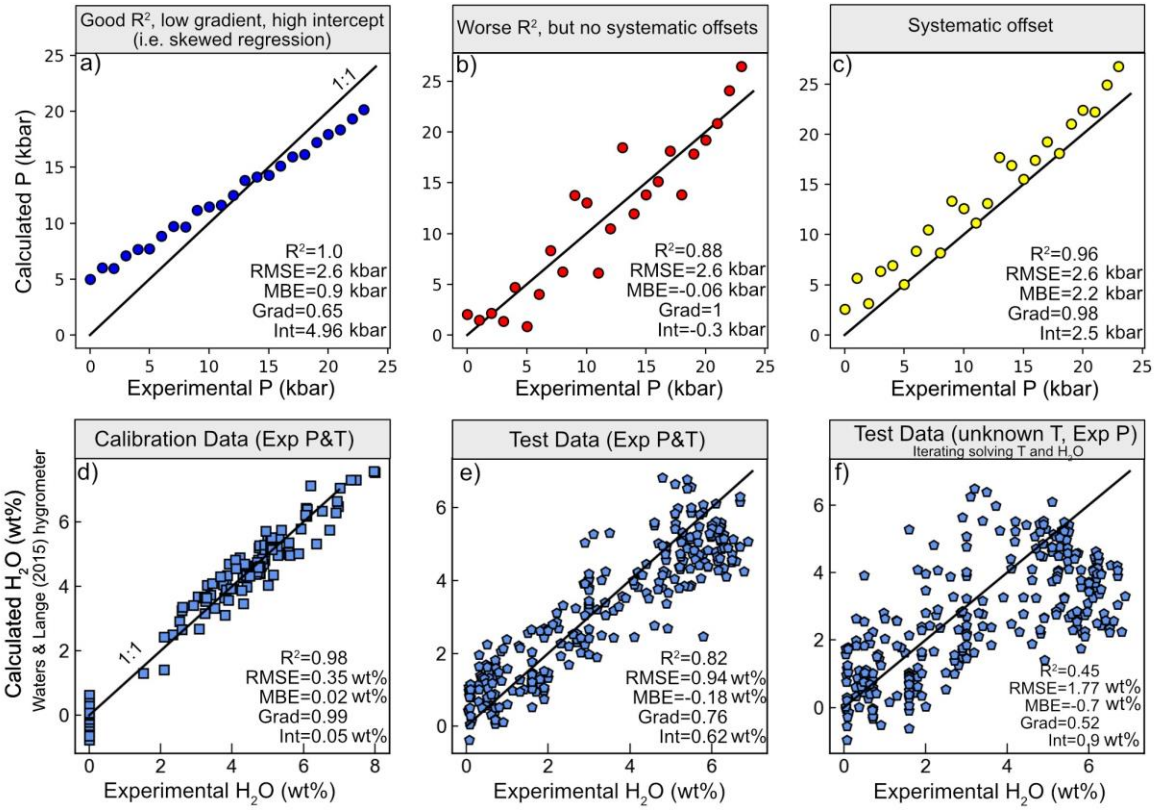

Figure 2: Schematic figure showing the limitations of using just R^2 and RMSE to assess thermobarometers. a-c) Three hypothetic barometers with the same RMSE, but vastly different performance. d-f) Comparing experimental and calculated H_2O using the Waters and Lange (2015) hygrometer for: d) the calibration dataset using experimental T and P, e) the ArcPL dataset using experimental T and P, and f) the ArcPL dataset iteratively solving H_2O and T (using Eq24a of P2008, see Section 2.8 for more detail).

It is also challenging to directly compare the quoted RMSE and R^2 values from different models, because these statistics are not calculated in an equivalent manner. Many of the statistics reported in the abstracts of papers proposing new models describe the fit to the calibration dataset (e.g., the commonly quoted ±1.7 kbar value for the Cpx-Liq barometer of Putirka et al. 2003; the ±0.35 wt% H_2O value for the Waters and Lange, 2015, Plag-Liq hygrometer). In other papers, the number reported in the abstract is the fit to a test dataset (e.g., Jorgenson et al., 2022; Petrelli et al., 2020), which inevitably makes the equation look "worse" than one assessed using calibration data. Indeed, it is apparent in the main text of many thermobarometry papers that the RMSE is much larger when applied to test data not used in the calibration dataset, or when applied to a global dataset containing a mix of new and calibration data (e.g., RMSE=4.2 kbar for the Cpx-Liq Putirka et al. 2003 barometer vs. the commonly quoted RMSE=1.7 kbar, Fig. 3a). The size of the test dataset can also vary greatly, influencing the statistics. For example, the test dataset of Petrelli et al. (2021) only contains 59 experiments conducted at <15 kbar, which come from only 4 studies. Some reported statistics are calculated using only experiments for a select subregion of compositional space (e.g., Neave and Putirka, 2017 for Cpx-Liq equilibria in tholeiites), while others report the fit for a global dataset with a much larger compositional range, again leading to larger apparent errors (e.g., Putirka 2008). For many equations, a paucity of experimental data resulted in all data being used for calibration, leaving no test dataset (e.g., Waters and Lange, 2015 for Plag-Liq hygrometry, Ghiorso and Gualda, 2015 for volatile solubility). Additionally, some proportion of the error in any quoted statistic (e.g. RMSE) will represent uncertainty in the experimental data used for testing (both analytical and experimental sources of scatter), making it difficult to differentiate failures of the calibration equation vs. the data used to assess it. This is a particular problem for models where higher quality data was saved for calibration, with less strict filters applied to test data (Putirka et al. 2003, 2008, K. Putirka, written comms).

Ideally when calibrating any new equation/model (for thermobarometry, chemometry, volatile solubility modelling etc.), data should be subdivided into a test dataset and a calibration dataset. It is then standard

practice for many machine learning workflows to further subdivide the calibration dataset into train and validation datasets (this split may be made repeatedly during model training, e.g., Petrelli et al. 2020). The train-validation split allows investigation of the effect of adding/removing terms, changing the regression algorithm, and tweaking the regression tuning parameters. Only once the model is fully tweaked should it be applied to the test dataset to assess its performance on unseen data. While it is then tempting to continue to change parameters to improve the fit to the test dataset, this strategy is generally criticized in the world of machine learning, as it means the testing dataset has "leaked" into the training of the model, so no longer provides an independent assessment of the model validity. The complete isolation of a testing dataset prior to model tuning and choice of parameters is important for machine learning and other regression workflows, because otherwise it is difficult to assess model performance on samples which are distinct in P-T-X space from those used in model calibration (Lones, 2021). To address this, in some biomedical studies, a test dataset is kept completely separate, and held under "lock and key" by a honest broker to avoid such leakage (Dobbin and Simon, 2011; Shedden, 2008). In igneous petrology, the difficult balance to strike is between having a large test dataset to robustly assess model performance, versus having too small a calibration dataset to adequately capture variation in melt or mineral composition.

It is also worth noting that the RMSE value is an average for the fit across the entire P or T range, while the actual error when applied to natural samples will vary as a function of P and T. RMSE and R^2 values are also not always calculated across the same P and T range (e.g., 0–40 kbar for Putirka, 2008, 0–20 kbar for Petrelli et al. 2020). These pressure ranges are also often far larger than the pressure ranges of interest in volcanic systems, and models tend to perform worse at lower pressures (Putirka, 2008).

Finally, mineral-melt thermobarometers and chemometers are often assessed using experimental data, where T, P (and often H_2O and fO_2) are constrained. In natural systems, it is common that several intensive parameters are poorly constrained. For example, a T and H_2O-sensitive barometer is normally assessed using the test dataset, inputting the experimental temperature and the measured H_2O content in the experimental charge. Similarly, thermometers with P-sensitive terms are normally assessed using the experimental P, and hygrometers are assessed using experimental T and P. In natural systems, the most common scenario is that *both* P and T are unknown, so must be iteratively solved using a thermometer and a barometer. Thus, to estimate a realistic error when applied to natural systems, statistics should be calculated by iteratively solving the same variables that would be unknown in natural samples. Of course, this adds additional uncertainty; when applying a T-sensitive barometer, any deviation from the true T will affect the calculated P. Additional uncertainties related to parameters which cannot be iteratively solved (e.g., uncertainty in H_2O in Cpx-Liq thermobarometers) should be propagated with Monte-Carlo techniques using a realistic uncertainty for H_2O in a specific system of interest (e.g. Wieser et al. 2022b).

Using the T-sensitive Plag-Liq hygrometer of Waters and Lange (2015) as an example, we demonstrate how the apparent performance of an equation can vary based on the number of constrained intensive parameters, and the dataset used to test it. First, we show H_2O contents for the model calibration dataset using experimental temperatures (Fig. 2d). This comparison yields the RMSE quoted in the abstract of the Waters and Lange (2015) paper that is commonly quoted in the literature as the error on the method (±0.35 wt%). Next, we evaluate this hygrometer using a newly compiled test dataset of variably hydrous experiments at 0–17 kbar spanning from basalts to dacites (ArcPL, Wieser et al., 2023a-b). We only include experiments where H_2O was measured using quantitative methods (Fourier Transform infrared spectroscopy - FTIR, secondary ion mass spectrometry - SIMS, Raman, calibrated volatiles-by-difference, solubility laws, see Section 2.8), and discard experiments which were present in the Waters and Lange (2015) calibration dataset. Using experimental T to calculate H_2O for this new test dataset yields statistics that are noticeably worse than those calculated from the calibration dataset (e.g., ±0.94 wt% vs. ±0.35 wt%, Fig. 2e). In a scenario where T is not known (i.e., when this method is applied to natural systems), the statistics decline further: iterating the hygrometer with the Plag-Liq thermometer of Putirka (2008, Eq24a) results in a RMSE of ±1.77 wt% (Fig. 2f, see Section 2.8 for detailed discussion). Thus, simply quoting the uncertainty from the original publication may underestimate the error by a factor of ~5 when applied to natural systems. We observe similarly large declines in model performance moving from calibration to test data to iterative solving for many mineral-melt equilibria (see Section 2, and Wieser et al. 2023a).

Thus, at present, it is not possible to select the best thermobarometer for a given application simply based on quoted statistics alone. Instead, to pick the most suitable model, it is worthwhile to check the natural

compositions of interest vs. the calibration range of the model of interest (calibration datasets for many models are available in Thermobar, Wieser et al. 2022b). After identifying models calibrated on suitable compositions, we encourage authors to compile a test dataset of experimental compositions most similar to their system. Ideally these experiments would not have used during calibration of the model. If the planned workflow in the natural system will involve iterative calculations, these same iterative workflows should be applied to the test dataset. These tests will provide a more realistic estimate of the uncertainty associated with the calculation than simply quoting RMSE values. If there is very little data to help pick, it may be best to perform calculations using several different equations calibrated on relevant compositional and P-T ranges. An average for all these models could be calculated, with the difference between models giving insight into the error in the calculation. At the moment, only a very small proportion of studies compare the results from multiple equations (e.g., Erdmann et al., 2016; Geiger et al., 2018; Sas et al., 2017; Sheehan and Barclay, 2016 for Cpx-Liq equilibrium, Rasmussen et al., 2022; Wieser et al., 2021 for volatile solubility).

1.3. What accuracy and precision are required?

In the 2008 RiMG short course, K. Putirka described his Cpx barometer as: *'a chisel, not a pen knife'* (K. Putirka, written comms). Once realistic estimates are made of the precision and accuracy of different thermobarometers using relevant test datasets, it is worth thinking about what scientific questions can be addressed with confidence within the associated uncertainties of each methods. Petrological barometers calculate pressure, which can be converted into depth by making assumptions about crustal and upper mantle densities. Converting pressures to depths allows comparisons to geophysical inversions of magma storage locations within the crust (e.g., Rasmussen et al., 2022), and to field observations in exposed crustal and upper mantle sections. Thus, it is useful to think of errors in the context of crustal and lithospheric thicknesses worldwide.

Oceanic crust formed away from the influence of mantle plumes ranges in thickness from ~5–8.5 km, with an average thickness of ~7±0.8 km (White et al., 1992). Assuming an average density of 2900–3000 kg/m^3 (Afonso et al., 2007), this corresponds to an average Moho pressure of ~2 kbar. To be able to conclusively pull apart different crustal storage geometries (e.g., upper vs. lower crust) and distinguish between storage regions at different levels in the crust, a RMSE error of $\pm$0.25–0.5 kbar would be needed. No mineral-based barometers applicable to MORB lavas achieve anything like this precision (Fig. 3a vs. d). In fact, even if magma is stored below the Moho (e.g., in slow spreading ridges, Bennett et al., 2019; Drignon et al., 2019), available mineral-melt models can't confidently differentiate upper mantle vs. crustal storage.

Crust in ocean island basalts (OIBs) is thicker than in MORB settings because the newer volcanic pile rests on top of older oceanic crust (total crustal thickness of 14–24 km in Hawai'i, Leahy et al., 2010; 14–15 km in La Palma, Ranero et al., 1995), and/or because the plume increases melting extents at the mid-oceanic ridge (e.g., ~11–39 km in Iceland). The elevated crustal thickness in OIBs, corresponding to pressures of 3–4 kbar or greater, means that mineral-based barometers with uncertainties of 2–3 kbar can begin to distinguish storage at the Moho vs. the shallow (e.g., Gleeson et al., 2021). Mineral-based barometers are also aided by the fact that OIB lithosphere can be extremely thick relative to MORB as a result of conductive cooling as the oceanic crust moves away from the ridge (e.g., 45–60 km thick in the Galápagos, Gibson and Geist, 2010; 50–110 km thick in the Hawaiian Islands, Li et al., 2004), and many OIB magmas are stored at sub Moho depths (e.g., Barker et al., 2021; DeVitre et al., 2023; Gleeson et al., 2021), Again, this makes uncertainties of 2-3 kbar less problematic. It is only in volcanic arcs, and particularly continental arcs with thicker crust (Profeta et al., 2016) that mineral-melt barometers can reliably distinguish between storage in the upper, middle and lower crust.

While mineral-melt thermobarometers often show a reasonably constant error regardless of the pressure, solubility models show a clear increase in error at higher volatile contents, so are best described using percentage errors (e.g., H_2O =±10% and CO_2 = ±20% for Shishkina et al., 2014, H_2O=±10% and CO_2=±17% for Iacono-Marziano et al., 2012). Systematic offsets between solubility models also tend to increase reasonably proportionally with increasing P (Wieser et al., 2022a). Even the large errors resulting from volume estimates during vapour bubble reconstructions when performing melt inclusion barometry (more detail in section 3) are percentage, not absolute errors. Many uncertainties associated with fluid inclusion barometry scale with pressure (Fig. 3, see Section 4). In general, methods with percentage errors that scale with the value of the quantity, rather than absolute errors, are better suited to distinguishing subtle variations in magma storage in relatively thin-crusted tectonic settings (Fig 3b-c). Interesting, Ridolfi (2021) and Mutch et al. (2016) express the errors on their amphibole barometers as percent errors (e.g. 12- 16%, see Fig. 3b), although, these errors only

describe the fit to the calibration data, and their magnitude is highly debated (see Erdman et al. 2016, and section 2.6).

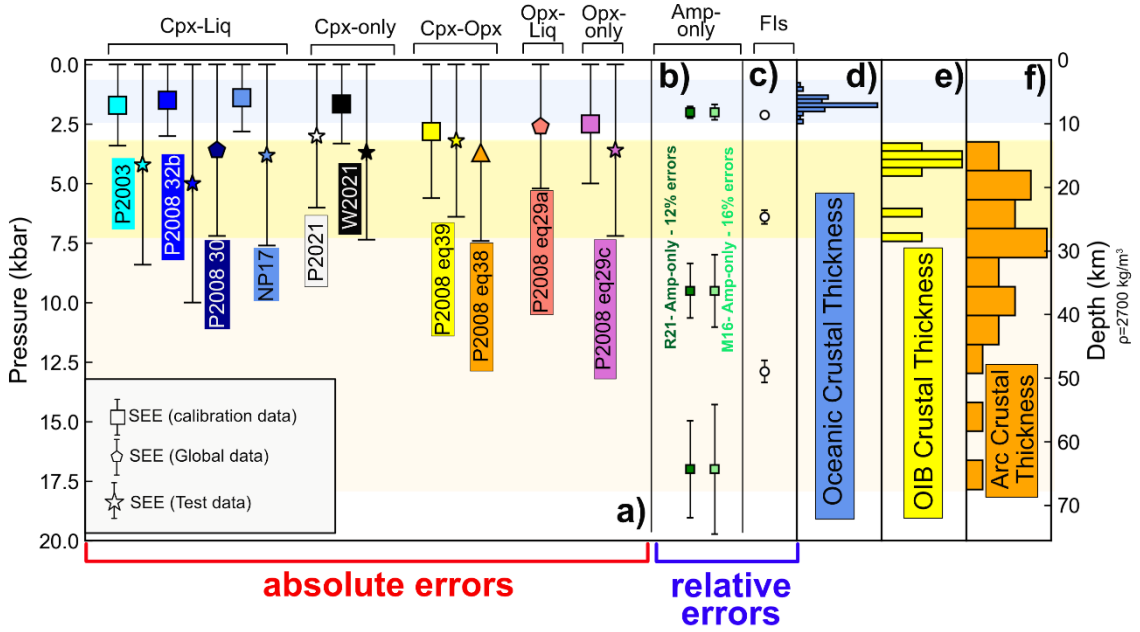

Figure 3: Comparison of quoted errors on barometers to estimates of crustal thickness (assuming ρ=2700 kg/m³). a) We anchor each method with an absolute uncertainty such that the upper part of the 1σ error bar sits at 0 kbar. This visualization shows the range of pressures/depths which cannot be statistically distinguished from storage at the surface. The symbol shape represents whether the quoted SEE/RMSE was for the calibration dataset, a test dataset, or global data. b-c). Relative (%) uncertainties are shown for different pressures. for e), we calculate FI errors assuming an uncertainty in CO_2 density of ±0.01 g/cm³ and ±50 K for entrapment T). Oceanic crustal thickness compilation from Chen (1992), OIB thicknesses compiled for this study (see supporting information), Continental arcs from Profeta et al. (2016). Errors for melt inclusions are highly sensitive to bubble volumes, so a generic example cannot be given (see Fig. 24b). Abbreviations: ***P2003****: Putirka et al. (2003),* ***P2008****: Putirka (2008),* ***NP17:*** *Neave and Putirka (2017),* ***W2021****: Wang et al. (2021),* ***R21****: Ridolfi (2021),* ***M16****: Mutch et al. (2016).*

1.4. Influence of analytical error on precision and accuracy

Measurement of any quantity in igneous systems is subject to analytical error. Mineral and melt compositions are typically measured using an electron microprobe (EPMA), which is associated with random and systematic uncertainties (see Wieser et al. 2023b for a more detailed discussion). Pressure estimates from melt inclusions rely on volatile measurements by FTIR or SIMS, EPMA measurements of the host and melt phase, Raman spectroscopy measurements of the vapour bubble, and estimates of the relative volume of the vapour bubble (see Section 3 for a detailed discussion). Pressure estimates from fluid inclusions rely on measurements of the fluid using Raman Spectroscopy/Microthermometry, and an independent estimate of T using mineral or mineral-melt thermometry (e.g. using EPMA analyses). Thermodynamic methods of inverting liquid compositions or liquid lines of descent rely on EPMA or energy-dispersive spectroscopy (EDS) measurements of glasses, or whole-rock X-ray fluorescence (XRF) measurements.

As many of the methods discussed in this review rely on EPMA analysis, we briefly discuss the uncertainties relating to this method. The fundamentally random process of x-ray generation, and subsequent detection by spectrometers is a significant source of uncertainty, termed 'counting statistics'. The magnitude of this uncertainty depends on the concentration in the sample and the beam current and voltage (affecting x-ray production), and the analysis time and spectrometer efficiency (affecting x-ray detection). Most simply, unless long count times and higher beam currents are used, low concentration elements (<1 wt%) tend to be associated with relatively large percentage errors. When analytical errors on all measured oxides are propagated through thermobarometry equations using Monte-Carlo methods, they can generate a large range in calculated P and T.

For example, Wieser et al. (2023b) show that measurement of Na_2O in crustal Cpx using popular analytical conditions (e.g., 10 s, 10 nA) yields a 1σ error of ~10–40%. Most importantly, the magnitude of this error is often underestimated by factors of 2–4X because secondary standards with higher Na_2O concentrations

than the sample are routinely used to assess precision. Secondary standards should only be used to assess accuracy, not precision, as precision of an EPMA analysis is very closely related to the concentration of the element of interest, so varies greatly depending on the individual mineral composition. The large imprecision of many Na_2O in Cpx measurements is problematic because this oxide is often used to calculate the abundance of the P-sensitive Jadeite component. Propagating typical analytical errors through popular expressions for Cpx-Liq thermobarometry can generate highly correlated PT arrays spanning 3–5 kbar, which could be incorrectly interpreted as transcrustal storage (Wieser et al., 2023b-c). Analytical errors also affect the experimental data used to calibrate thermobarometers. As many experimental studies perform <5 measurements on each phase, random analytical error does not get sufficiently averaged out, so the reported phase composition may not be the true phase composition (affecting model calibration, and calculated statistics on test data, see Wieser et al. 2023b, see also Section 2.3).

To visually demonstrate the effect of analytical precision on different mineral-melt thermobarometers, we perform Monte-Carlo simulations using Thermobar (Wieser et al., 2022b, Fig. 4). We use analytical errors estimated by the EPMA based on counting statistics for experimental phase compositions reported by Krawczynski et al. (2012). For each phase, we produce 500 synthetic compositions with each element normally distributed about a measured value in the experiment, with the standard deviation equal to that estimated by the EPMA. We also include ±5% relative error for H_2O in the liquid, which is a very conservative estimate of the error associated with FTIR and SIMS measurements. For two-phase equilibrium (e.g., Cpx-Liq), we consider all possible matches between the 500 synthetic compositions for each phase (250,000 pairs total). We then perform thermobarometry calculations on all synthetic compositions, showing the spread of calculated P and T relative to the median of the distribution (Fig. 4).

In general, the influence of analytical error on calculated T is relatively minor ($1\sigma<20$°C). The broadest distribution of calculated temperatures comes from equations that are very sensitive to melt H_2O content, such as Liq-only T from P2008 Eq14 and Eq22 (Fig. 4a), Opx-Liq T from P2008 Eq28a (Fig. 4b), and Cpx-Liq T from P2008 Eq30 (Fig. 4e). For calculated P, the spread of simulations is highly variable, with barometry methods sensitive to a component with a relatively low concentration showing a very wide spread of pressure (e.g., Na in Cpx, Fig. 4j). In contrast, barometers sensitive to high concentration elements show very narrow distributions (e.g., Al in Amphibole, Ridolfi, 2021, Medard and Pennec, 2022, Fig. 4h).

We also test the OPAM liquid barometer, where pressures are calculated from the composition of melts co-saturated in olivine, plagioclase, and augite (see Section 2.2). As the experiments of Krawczynski et al. (2012) are too H_2O-rich for OPAM, we use estimates of analytical precision for measurements of submarine basaltic glasses from the Galápagos Spreading Centre (Gleeson and Gibson, 2021). Notably, the analytical errors have a very similar magnitude to those from Krawczynski et al. (2012). This method is very sensitive to analytical uncertainty, returning a similar range of calculated pressures to Cpx-based mineral-based barometers. The model of Voigt et al. (2017) is particularly sensitive, because of the inclusion of a term for the Cr content of the liquid, which has a low concentration, so is associated with poor analytical precision.

Overall, the effect of propagated analytical error on P and T depends greatly on the selected equation (e.g., Fig. 4f and i), as well as the analytical conditions used. Thus, studies should propagate EPMA-estimates of counting statistic errors from each analysis not secondary standards using their chosen equation. Analytical errors should be propagated for all thermobarometric techniques, including melt inclusion and fluid inclusion barometry (see Section 5 for an example). If propagated analytical errors are of similar magnitude to the resolution required to investigate the geological process of interest, time must be spent optimizing analysis (See section 2.3). Counting statistics are of course, only one source of analytical uncertainty. There are also notable offsets between different EPMA laboratories (e.g., Wieser et al. 2023b), and even between different operators on the same EPMA (see Kohn and Spear, 1991). These systematic uncertainties will increase the spread in calculated P and T for a given liquid, or crystal vs. that shown on Fig. 4.

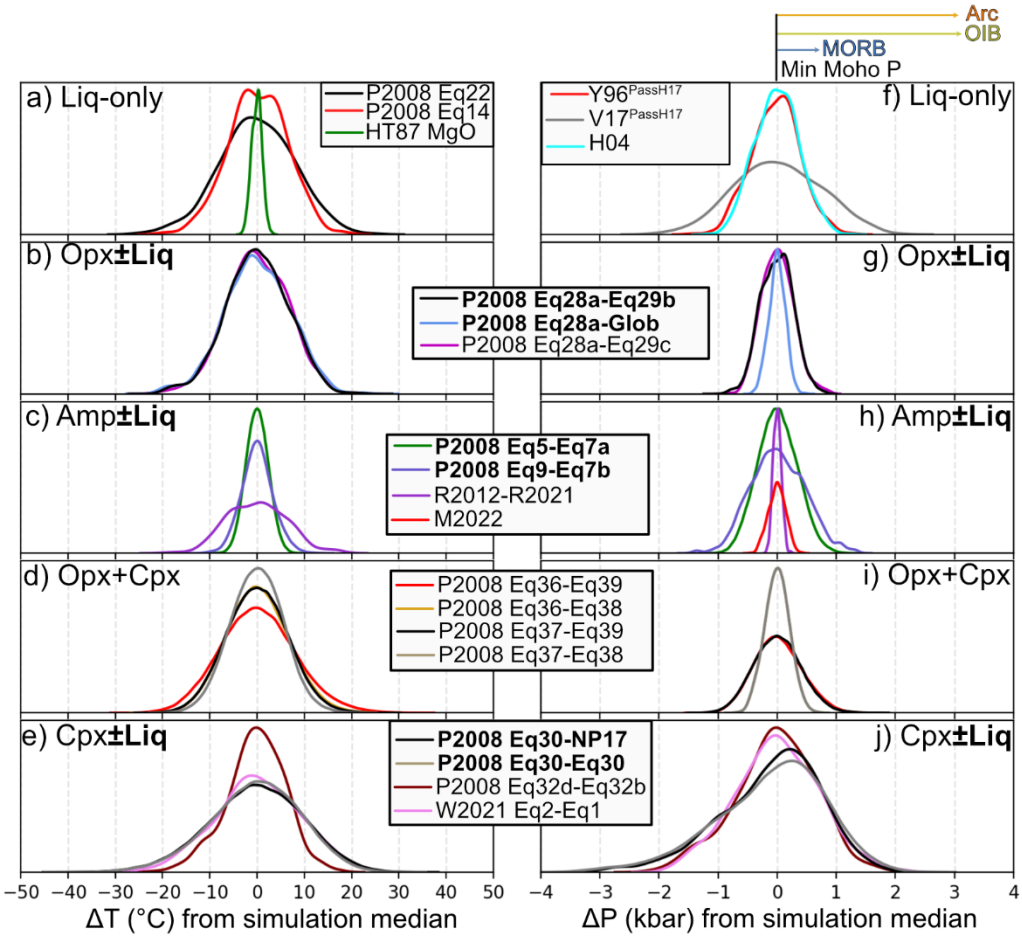

Figure 4: Monte Carlo simulations of the influence of analytical precision on thermometry (a-e) and barometry (f-j) calculations. All panels except f show analytical uncertainties from EPMA counting statistics from Krawczynski et al. (2012) with H_2O of ±5%. As OPAM (panel f) is not applied to arc magmas, we propagate EPMA errors from natural Galápagos glasses from Gleeson and Gibson (2021). The bars at the top show approximate minimum and maximum Moho pressures from each tectonic setting (see Fig. 3).

2. Mineral Thermobarometry and Chemometry

The seminal review of Putirka (2008, hereafter P2008) summarizes several decades of thermobarometric work, and proposes a large number of new empirical expressions linking the compositions of Cpx±Liq, Opx±Liq, Cpx+Opx, Plag±Liq, and Plag+Kspar to P and T. These new equations have similar forms to those published in older papers, but have recalibrated coefficients, and additional terms to improve performance when applied to the large compilation of experiments published in 2008 (LEPR; Library of Experimental Phase Relationships, Hirschmann et al., 2008). In the same issue, Anderson et al. (2008) summarized available P-T constraints on granitic rocks. To avoid repetition, we largely focus on new methods developed since 2008, as well as assessing the performance of these 2008 models using new experiments published in the last 15 years. Specifically, we assess models using a new test dataset of experiments conducted on arc magma compositions (ArcPL – Arc post LEPR, Wieser et al. 2023a-b) at variably hydrous (H_2O= 0–16.6 wt%, median=4.7 wt%) crustal conditions (0–17 kbar). Importantly, the experiments in this new dataset were not used during the calibration of most models, and any overlaps were removed when testing a specific model. Our focus on arcs is partially a result of the experimental data available not used in model calibration, but also reflects the fact there has been very little focus on this tectonic setting, despite the fact it is one of the few places where the crust is thick enough that mineral-based barometers may be able to resolve different crustal storage regions within uncertainty (Fig. 3). For methods not applicable to arc magmas (e.g. OPAM, section 2.2), we compile other available experiments. For many methods, there are not sufficient 'test' experiments available for MORB, OIB and alkali lavas to build on the comparisons presented by Masotta et al. (2013), Masotta and Mollo (2019), Neave et al. (2019) and Neave and Putirka (2017), so we refer readers to these papers.

520

521 **2.1. Liquid-only thermometry**

522 A huge variety of liquid-only thermometers exist, with varying complexity and calibration ranges. For
523 example, the thermometer of Helz and Thornber (1987) uses just the MgO content of the liquid, calibrated on
524 compositions from the Kīlauea Iki lava lake. In contrast, P2008 eq14 has terms for the MgO, FeO_t, Na_2O, K_2O,
525 H_2O and Mg# in the liquid, and was calibrated/tested on 1536 olivine-saturated liquids. There are also a number
526 of olivine-liquid thermometers with a term for the partitioning of Mg between olivine and liquid (D_{Mg}^{Ol-Liq}). In
527 their supporting spreadsheet, Putirka (2008) replace this term with the theoretical value of D_{Mg} predicted by
528 Beattie (1993) to produce a liquid-only thermometer. Here, we discuss the best-performing thermometers for
529 our new test dataset.

530 As P and H_2O may be poorly constrained in many systems, we first assess the sensitivity of various
531 thermometers to these parameters. We randomly select 40 experiments - for each liquid composition, we make
532 100 duplicates with the experimental H_2O content perturbed by ±3 wt% (Fig. 5a), and separately perturb the
533 experimental P by ±5 kbar (Fig. 5b). We take the calculated T at these perturbed values and subtract the
534 calculated T at the measured P and H_2O (ΔT, ΔP). Thermometers with a H_2O term show variable, but relatively
535 high sensitivity to H_2O, with the average calculated T dropping by ~9 to 16°C per wt% H_2O added (Fig. 5a). For
536 comparison, we show the quoted RMSE of each thermometer. Uncertainty in H_2O of 3 wt% introduces a
537 systematic error comparable in size to the stated RMSE (Fig. 5a). Thermometers are substantially less sensitive
538 to P; uncertainty in P of 5 kbar results in <30°C of variation. Even a full 10 kbar of uncertainty in P doesn't exceed
539 the quoted RMSE (Fig. 5b).

540 Given the sensitivity of calculated temperatures to H_2O, we only use experiments where H_2O was
541 determined using quantitative methods (calibrated volatile-by-difference, FTIR, SIMS, Raman spectroscopy). We
542 perform calculations using experimental P and measured H_2O, because there are no suitable liquid barometers
543 or hygrometers to iteratively solve all unknowns. For the ArcPL dataset, the best liquid-only thermometer is an
544 adapted version of the Ol-Liq thermometer of P2008 Eq22, where the olivine D_{Mg} term is replaced with the
545 calculated D_{Mg} value from Beattie (1993), converting it into a Liq-only thermometer (Fig. 5c). Surprisingly, this
546 adapted Ol-Liq thermometer does a very good job of predicting T in experiments without olivine, including melts
547 with high SiO_2 contents (square symbols). We also use the new liquid-only thermometer calibrated on
548 experiments containing olivine from Shi et al. (2021). This thermometer performs very well for experiments
549 containing olivine, with slightly better statistics than Eq22D_{Mg} (Fig. 5d). Unsurprisingly, given it was calibrated
550 with Ol-bearing liquids in mind, it drastically overpredicts T at MgO<~ 2–3 wt% for experiments without olivine
551 (Supporting Fig. 1) – although this still presents an interesting contrast with Eq22D_{Mg}.

552 We also calculate the liquidus T using rhyolite-MELTS v1.2.0, v.1.0.2 and pMELTS (Gualda et al. 2012;
553 Gualda and Ghiorso, 2015, Ghiorso et al., 2002, Fig. 5e, Supporting Fig. 2). All three versions of MELTS give similar
554 statistics; pMELTS has the higher R^2 and lowest MBE and RMSE (R^2=0.89, MBE=44°C, RMSE=58°C), but shows
555 significantly worse performance than v1.0.2 for the lowest T liquids. It is notable that the MBE for all 3 versions
556 is relatively high (44–56°C vs. -0.12°C for eq22DMg), which demonstrates that MELTS consistently overestimates
557 liquidus temperatures (Fig. 5e). The other disadvantage of MELTS calculations vs. empirical approaches is the
558 additional computational expense; 2000 liquidus calculations take 47 minutes using pyMELTScalc through
559 alphaMELTS for Python compared with 0.015 seconds using eq22DMg through Thermobar on a desktop
560 computer with 128 Gb RAM and a 10–core 10th generation Intel i-9 processor. Liquidus temperatures can also
561 be calculated using the Holland et al. (2018) thermodynamic model, implemented through the Julia-based Gibbs
562 Free Energy minimization software MAGEMin (Reil et al. 2022). The fit between the experimental and calculated
563 T is considerably worse than that achieved by rhyolite-MELTS v1.2.0, with temperatures often overestimated by
564 100–200^{o}C, particularly for experiments performed at <1100^{o}C (Fig. 5f). These calculations take similar times to
565 MELTS calculations. In summary, if melt H_2O contents are well constrained, empirical liquid-only thermometers
566 such as eq22DMg of Putirka (2008) perform surprisingly well across a surprisingly wide range of melt
567 compositions.

568

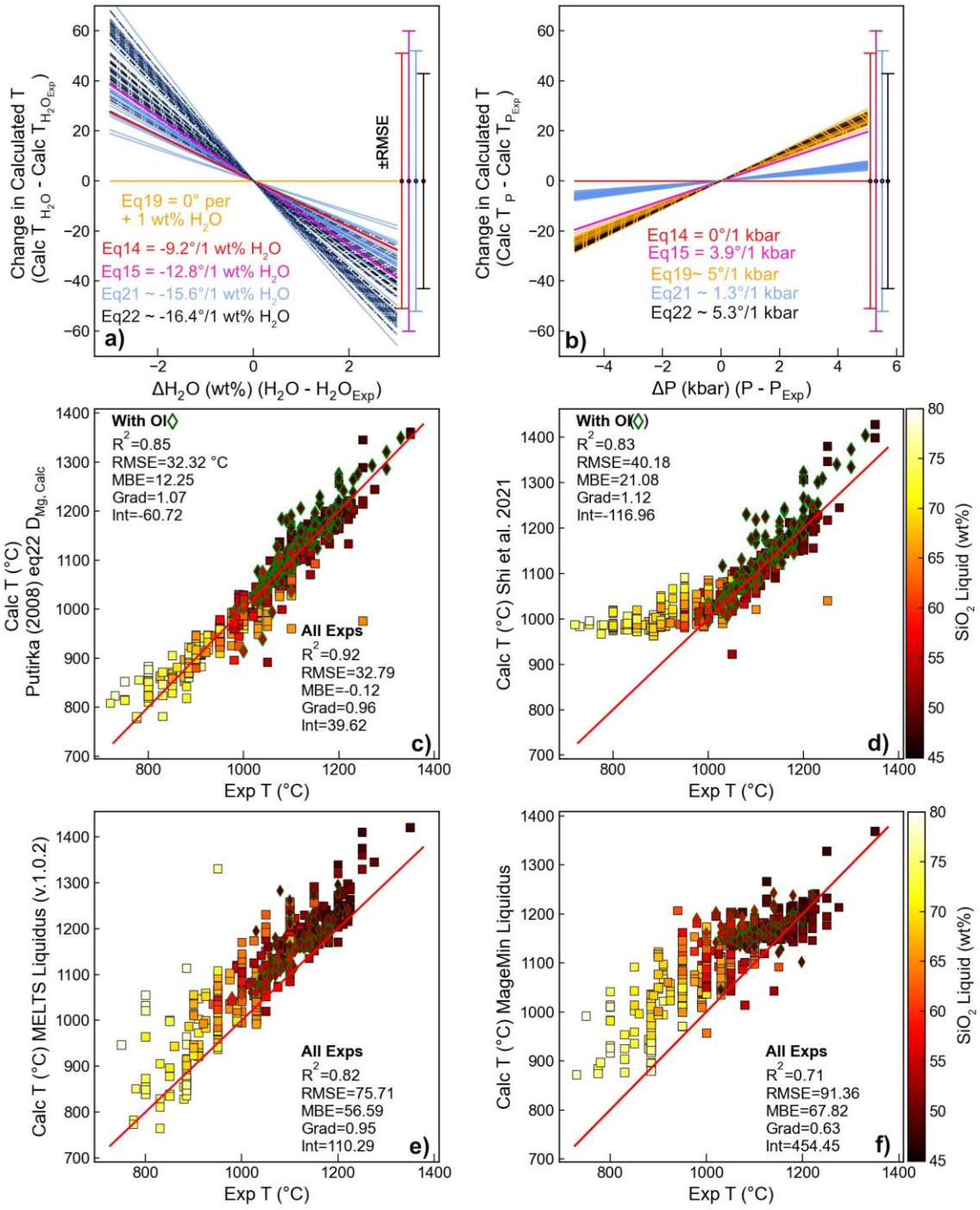

Figure 5: Assessing Liquid-only thermometers. a-b) Sensitivity of calculated T to H_2O (a) and pressure (b). For 40 randomly selected experiments (each represented by a line), we perturbate the experimental H_2O content by ±3 wt% (a), and pressure by ±5 kbar (b). These plots show that increasing H_2O causes a drop in calculated T, and an increase in P causes a smaller increase in T. c-f) Experimental T vs. calculated T for experiments where H_2O was measured by quantitative methods (FTIR, SIMS, Raman, calibrated volatiles by difference). Experiments containing olivine are shown as green-outlined diamonds, and experiments without olivine as black-outlined squares. All symbols are colored by the SiO_2 content of the melt. MELTS (part e) and MAGEMin (part f) liquidus T calculated using Fe^{3+}/Fe_T=0.15 (calculated T are not very sensitive to Fe^{3+} but having Fe^{3+}>0 is necessary for the algorithm to converge).

2.2. Liquid-only barometry

Barometric methods based on the composition of silicate melts rely on the fact that the thermodynamic variance of the system (i.e., the degrees of freedom) is lower in multi-phase saturated systems, so the melt composition contains information about the conditions of magma storage. This is typically discussed with regards to magma evolution along mineral cotectics, or at invariant points such as eutectics, where the degrees of freedom is close to zero (i.e., high-silica rhyolites, Ludden, 1978; Vogt, 1931). The positions of these cotectics and eutectics are sensitive to pressure because of differences in the volume of common igneous minerals. Thus, if the influence of P and melt composition on the location of cotectics/eutectics can be determined by thermodynamic or empirical parameterisations, measured compositions of lavas saturated in the required phases can be used to calculate P (e.g., Grove et al., 1992; Gualda et al., 2012; Wilke et al., 2017; Yang et al., 1996, Fig. 1g).

Thermodynamic approaches to liquid-only barometry have become increasing common in the last decade, with the rhyolite-MELTS thermodynamic models used to assess the storage pressure of evolved, rhyolitic magmas from several locations worldwide (Gualda and Ghiorso, 2014; Harmon et al., 2018; Pamukcu et al., 2015). The application of thermodynamic methods to liquid-only barometry is addressed in detail in Section 8. Here, we instead focus on empirical methods calibrated using experimental data.

2.2.1. OPAM Barometry

Experimental work on the location of the olivine-plagioclase-augite-melt (OPAM) cotectic has been ongoing for at least 3 decades. Early work constrained the position of the OPAM cotectic at 0.001 kbar in the simplified CaO-MgO-Al_2O_3–SiO_2 (CMAS)+FeO (Shi, 1992) and CMAS+FeO+Na_2O systems (Shi, 1993). Further experiments on natural MORB compositions demonstrated that minor components in the liquid phase (e.g., Ti, Na, and K) and the expansion of the clinopyroxene stability field at higher pressures strongly influences the cotectic position (Grove et al., 1992; Yang et al., 1996). Using these observations, Grove et al. (1992) provided a set of empirical equations to locate the position of the olivine+plagioclase+melt and OPAM cotectics as a function of melt chemistry and pressure. Yang et al. (1996, hereafter Y96) built on this work with an updated parameterisation for the location of the OPAM cotectic, expressing the Mg, Ca, and Al molar fractions (X_{Mg}, X_{Ca}, and X_{Al}) of an OPAM-saturated melt as a function of P and the remaining molar fractions (e.g., X_{Si}, X_{Ti}). For example, their expression for the molar fraction of Ca has the following form:

$$X_{Ca} = 1.133 - 0.00339 * P(kbar) - 0.569 * X_{Na} - 0.776 * X_K - 0.672 * X_{Ti} - 0.214 * X_{Fe} - 3.355 * X_{Si} + 2.830 * {X_{Si}}^2 \text{ [Equation 4]}$$

These equations were updated by Voigt et al. (2017, hereafter V17), who used new experimental data to show that Cr_2O_3 has a strong influence on clinopyroxene phase stability. Their equations have the same functional form, with an addition of a term for the molar fraction of Cr, separate terms for ferrous and ferric Fe molar fractions, and updated coefficients for the other parameters:

$$X_{Ca} = 1.07 - 0.02707 * P(GPa) - 0.634 * X_{Na} - 0.618 * X_K - 0.515 * X_{Ti} - 0.188 * X_{Fe^{2+}} - 0.597 * X_{Fe^{3+}} - 3.044 * X_{Si} + 2.477 * {X_{Si}}^2 - 9.367 * X_{Cr} \text{ [Equation 5]}$$

Herzberg (2004) (hereafter H04), develop an alternative approach, relating P to liquid components projected onto an Anorthite, Diopside, Enstatite ternary diagram from Olivine:

$$P(GPa) = -9.1168 + 0.2446 * (0.4645 * En + An)$$
$$-0.001368 * (0.4645 * En + An)^2 \text{ [Equation 6]}$$

Despite the greater simplicity of pressure calculations using the H04 OPAM parameterisation, the Y96 and V17 molar fraction equations have formed the basis of most OPAM barometry over the last decade (V17: Bell et al., 2021; Stock et al., 2018, Y96: (Baxter et al., 2023; Caracciolo et al., 2022, 2020; Halldórsson et al., 2022). The methods used to extract pressure information from these expressions vary. Early studies used the equations of Y96 to calculate the position of the OPAM cotectic at multiple pressures and plotted these positions on an olivine-clinopyroxene-quartz pseudoternary diagram (projected from plagioclase). Visual comparison of the position of the calculated OPAM cotectic to natural melt compositions projected onto the same pseudoternary diagram were used to estimate the pressure of magma storage (Geist et al., 1998; Maclennan et al., 2001). Kelley and Barton (2008) use a complex approach calculating theoretical and measured normative mineral components at different pressures, regressing these components against pressure to determine the best fit for each measured sample. More recent studies have determined the pressure of the minimum misfit

between calculated X_{Mg}, X_{Ca}, and X_{Al} using the equations of Y96 or V17, and measured X_{Mg}, X_{Ca}, and X_{Al} in their samples without requiring the conversion to normative mineral components (Hartley et al. 2018).

Regardless of the calculation method used to obtain P, OPAM barometry requires input melt compositions to be saturated in all 3 solid phases (olivine, clinopyroxene, and plagioclase). Solving for pressure using the equations of Y96 or V17 for samples that are not saturated in all 3–phases could lead to erroneous results and may explain the wide range in calculated P estimated for some systems (e.g., 1.4– 7.7 kbar at Laki in Iceland; Kelley and Barton, 2008). Therefore, it is important to determine which samples are co-saturated before interpreting OPAM calculations. One way to ensure 3–phase saturation in the target melts is via textural observations, such as petrographic observations of euhedral crystals with no disequilibrium textures. Alternatively, in systems with abundant whole-rock or matrix glass data spanning a range of MgO contents, comparing liquid lines of descent with mass balance approaches or fractional crystallization models (e.g.., MELTS, Petrolog3, Danyushevsky and Plechov, 2011; Gualda et al., 2012) can be used to confirm 3–phase saturation.

An approach that can be applied to individual liquid compositions without textural or LLD context to calculate P and check for cosaturation was developed by Hartley et al. (2018). They determined the probability of three-phase saturation using a Chi-squared distribution to calculate the misfit between the predicted (X_i^{Pred}) and measured (X_i^{Meas}) molar fractions for Mg, Ca and Al:

$$\chi^2 = \sum_{i=1}^{3} \left[\frac{X_i^{Meas} - X_i^{Pred}}{\frac{\sigma_{X_i}}{100} X_i^{Meas}} \right]^2 \quad \text{[Equation 7]}$$

Here, σ_{X_i} is an estimate of the relative analytical uncertainty for each cation under consideration (expressed as a percentage). As X_i^{Pred} is a function of the system pressure, users can determine the best-fit model pressure by locating the position of the minimum possible χ^2 value ($\chi^2{}_{Min}$). To assess whether the melt is truly three-phase saturated, Hartley et al. (2018) compare $\chi^2{}_{Min}$ to the cumulative distribution function of the Chi-squared distribution with 2 degrees of freedom. A probability is selected as a cut off value (e.g., p=0.05, p=0.2); Hartley et al. use a probability of fit, P_f, which can be thought of as 1 minus the p value. If $\chi^2{}_{Min}$ is less than the critical value of the chi squared cumulative distribution function for this chosen cut off (i.e., p-value and n=2 degrees of freedom), the liquid is assumed to be three-phase saturated. By considering the results of OPAM calculations on experimental melt compositions (including the Yang et al. 1996 calibration data), Hartley et al. (2018) determine that a 'probability of fit' filter of p~0.2 (P_f=0.8) results in a good fit between the experimental and calculated pressures, while minimising the number of 'false negatives' (i.e., melt compositions which are OPAM saturated, but would fail this test). The minimisation method and co-saturation check of Hartley et al. (2018) (hereafter H18) has been utilised by several studies investigating the storage conditions of MORBs and OIBs (Bell et al., 2021; Stock et al., 2018, Baxter et al., 2023; Caracciolo et al., 2022, 2020; Halldórsson et al., 2022).

Baxter et al. (2023) evaluated the performance of the Y96 equations using 315 OPAM saturated experimental melt compositions, ranging from 1 atm to 12.5 kbar pressure. They filter these experiments using the H18 filter and exclude those with MgO<4 wt%, leaving 95 experiments. Comparing calculated and experimental pressures for these filtered experiments yields a RMSE of ±1.51 kbar, which is similar to the 'random error' of ±1.32 kbar estimated by Hartley et al. (2018, definition uncertain). However, both studies evaluated the performance of the Y96 equations using a dataset which included some experiments used in the Y96 calibration. For example, 57% of the 95 experiments assessed by Baxter et al. (2023) are part of the Y96 calibration dataset. If we rerun their comparison using only experimental data that was not used in the Y96 calibration the RMSE increases from ±1.51 kbar to ±1.89 kbar. A particular issue is that only 7/41 of the remaining experiments were conducted at >0.001 kbar, making it very hard to assess the performance of the Y96 barometer without new test data at higher pressures.

To test the performance of all three OPAM barometers listed here (Y96, V17, and H04), and the success of the H18 filter, we compile an experimental dataset of OPAM saturated experiments not used to calibrate either Y96 or V17. N=188 overlap with the dataset of Baxter et al. (2023), with N=38 experiments not in that compilation. Fig. 6 demonstrates that there are strong correlations between the calculated and experimental pressures for all OPAM methods when the H18 saturation check is not applied (R^2 of 0.51, 0.52, and 0.42 for Y96, V17, and H04 respectively, all symbols, grey statistics on Fig. 6). Despite having the highest R^2 value of the three methods tested here, calculated pressures determined using the V17 expressions display the largest uncertainties (RMSE=3.19 kbar) and a systematic offset to high pressures (MBE = 1.22 kbar, Fig. 6b). The Y96

expression has a smaller systematic offset (gradient=0.98, MBE=0.3 kbar), as well as a lower RMSE (2.32 kbar, Fig. 6a). The parameterisation of H04 also returns a relatively low RMSE (2.37 kbar) and similar MBE to the Y96 method (0.3 kbar), but has a lower gradient of the correlation (0.82; Fig. 6c).

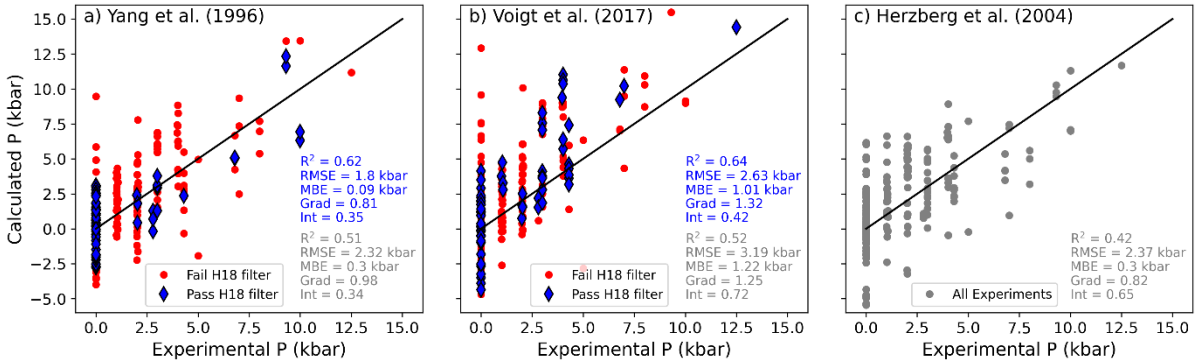

Figure 6: Experimental vs. calculated P using the OPAM expressions of Yang et al. (1996), Voigt et al. (2017) and Herzberg (2004) for OPAM-saturated experiments on MORB-like compositions. The calculated pressure was determined using the Chi-squared method of Hartley et al. (2018, H18) for the Yang et al. (1996) and Voigt et al. (2017) equations (a,b). Samples passing the co-saturation filter of Hartley et al. (2018) are shown as blue diamonds, while those that fail are shown as red circles. The filter is not applicable to the method of Herzberg et al. (2004, part c). Statistics using all experiments are shown in grey text, statistics for experiments passing the H18 filter are shown in blue text.

The larger uncertainty and systematic offset in pressures estimated using V17 likely originates from the sensitivity of these expressions to the Cr_2O_3 content of the melt phase. Only 53 of the 225 experiments used in this analysis (~24%) report melt Cr_2O_3 contents, despite most experiments using natural basalt compositions that likely contain at least trace amounts of Cr_2O_3. Adding Cr_2O_3 into the melt phase changes the stability of pyroxene (see Fig. 3, Onuma and Tohara, 1983), and thus the pressure estimated by OPAM barometry (Voigt et al., 2017). Consequently, the systematic offset to higher pressures obtained by applying the V17 expressions to our compiled experimental database might result from the absence of reported Cr_2O_3 in most experiments, and uncertainty as to whether Cr was even present in starting materials (Wieser et al. 2023b). Additionally, it is unclear how precise the analyses of Cr_2O_3 in these experiments are; typical analytical conditions can result in large errors for this low concentration oxide (propagating into a much wider spread of pressures than using Y96 or H04, Fig. 4f). Despite its poor performance on our test dataset, we cannot rule out the possibility that V17 may be the best parameterization in natural Cr containing systems, even if it behaves poorly on Cr-free experiments. Further experimental work on Cr-bearing experiments where the Cr content of the melt was characterized with high precision at a range of pressures are required to assess the performance of the V17 expressions as an OPAM barometer in natural systems.

Interestingly, although all N=225 experiments were OPAM saturated, only 27% (N=61) pass the H18 cosaturation filter when the equations of Y96 are used (blue diamonds, Fig. 6a). While the statistics for calculated vs. experimental pressures are greatly improved using only experiments which pass the filter, it is concerning how many false negatives this filter produces, particularly as only 18 of the experiments which passed the filter were performed at pressures above 0.001 kbar. To further assess the performance of the H18 saturation filter, we isolated experiments on MORB-like compositions that are saturated in only one or two (N = 172) of the three key mineral phases in OPAM barometry. Using the Y96 expression, 19% of these non-OPAM saturated experiments pass the H18 co-saturation filter (false positives). These results demonstrate that the H18 co-saturation filter should not be used in isolation to identify which samples are suitable for OPAM barometry. Therefore, petrological observations of three-phase saturation remain critical for determining pressures via OPAM barometry.

To date, OPAM barometry has mostly been used to evaluate the storage pressure of MORBs, or tholeiitic to transitional OIBs (these compositions broadly overlap with the calibration dataset of Yang et al. 1996). Unfortunately, the uncertainty associated with OPAM barometry assessed using our independent test dataset (RMSE = 1.8 – 2.32 kbar, Fig. 6) indicates that this method does not have the resolution to distinguish between upper vs lower crustal storage at most mid-ocean ridges. However, at hotspot influenced ridges (e.g., Iceland) and regions of plume derived volcanism (e.g., ocean islands), the thickened crust (Fig. 3e) means that OPAM can provide insights into the characteristics of magma storage in these locations if independent checks

for 3–phase saturation are performed prior to pressure calculation (via petrographic observations or liquid line of descent analysis). For example, melt inclusion and matrix glass data from Barðarbunga, Iceland, indicates that there is a slight difference in the entrapment pressure of melt inclusions and the final equilibration pressure of the matrix glasses (Hartley et al. 2018; Caraccioli et al. 2022).

2.2.2. Other liquid-based barometers

The effect of H_2O on phase boundaries in the OPAM system has not been investigated in detail, meaning this method cannot be applied to arc magmas with confidence. To provide a liquid-based thermobarometer with application to more hydrous systems like volcanic arcs, Blundy (2022) create parametrizations for the stability of clinopyroxene-hornblende-orthopyroxene-magnetite-plagioclase-ilmenite (CHOMPI) as a function of P, T, and the ratio of H_2O and CO_2 in the fluid, including a cosaturation check to establish whether CHOMPI phases were present based on just a liquid composition. However, Wieser et al. (2023d) show this cosaturation test classifies ~44% of ArcPL experiments lacking the CHOMPI assemblage as CHOMPI-saturated (false positives), and unsurprisingly these experiments show a poor correspondence between calculated and experimental pressure (as the system is not low variance). The logic behind the CHOMPI approach has been generalized to liquids saturated in a wider variety of phases by Weber and Blundy (2023), who apply a regression tree machine learning algorithm to a training dataset of liquids ranging from basalt to rhyolite. As this model is still being tweaked and is currently a preprint (Weber, written comms), we do not comment on it further.

2.3. Clinopyroxene±Liquid

The majority of Cpx-Liq thermobarometers rely on the exchange of diopside hedenbergite (DiHd, $CaFeSi_2O_6$) and Jadeite (Jd, $NaAlSi_2O_6$) between Cpx and liquid. Here, we briefly summarize the most recent parameterizations of Cpx equilibrium, and workflows that have been developed for calculating P and T in natural systems. A detailed discussion of pre-2008 models can be found in Putirka (2008, and refs within), and a description of the best Cpx-Liq models for our test dataset and sensitivity to P and T as well as the best equilibrium tests to use can be found in Wieser et al. (2023a-b).

Putirka (2008) propose a number of equations based on Cpx-Liq equilibria (Eq30, Eq31, Eq32c for P, Eq33 for T), expanding and recalibrating the models of Nimis (1995) and Putirka et al. (1996, 2003) to account for an increase in experimental data, particularly hydrous experiments. More recently, several new equations have been calibrated which focus on a more limited subset of compositional space than these global regressions (Fig. 7). Neave and Putirka (2017) calibrate a Cpx-Liq barometer for application to tholeiitic basalts from ocean island settings (specifically Iceland) using 6 experimental studies (N=113 experiments) with mafic-intermediate compositions, and pressures ranging from atmospheric to 20 kbar (Neave and Putirka, 2017, Fig. 7, red diamonds). Masotta et al. (2013) conduct experiments and compile available literature data on trachytic to phonolitic compositions (Fig. 7, blue pentagons), to calibrate a Cpx-Liq barometer applicable to more alkaline compositions, which are poorly represented in the calibration dataset of P2008. Their expressions have a very similar/identical form to those of Putirka (2008), with recalibrated coefficients. Brugman and Till (2019) note that in high-silica melts, there is very little Al_2O_3 in Cpx (<2 wt%), and the calculated Jd component is very low or even zero. Along with the fact that high Si compositions are very poorly represented in P2008, they showed that this results in existing Cpx-Liq thermometers overestimated temperatures in evolved melts by up to 170˚C. Thus, Brugman and Till (2019) compiled recent studies from the literature on rhyolitic compositions (e.g., Almeev et al., 2012; Bolte et al., 2015; Gardner et al., 2014) supplemented with their own experiments on the Scaup Lake Rhyolite (Fig. 7, cyan squares), to calibrate a new thermometer for highly evolved melts which is independent of Jadeite, P, and H_2O content.

Another key shift in the use of Cpx-based barometry since 2008 has accompanied the rapid rise in programming literacy amongst petrologists, allowing the development of new workflows based on existing thermobarometry equations. For example, while experimental studies have clearly paired Cpx and liquid compositions, it is significantly more challenging in natural systems to identify such pairs. Typically, a given volcanic eruption will erupt a narrow range of liquid compositions along with a much more chemically diverse crystal cargo, incorporating Cpx crystals grown from a wide variety of melt compositions. Additionally, many whole rock compositions are a mix of crystals and melts, so are not representative of true liquids (Reubi and Blundy, 2009; Ubide et al., 2022). A variety of algorithms have been developed to try to identify matched pairs, by combining erupted Cpx compositions with liquids erupted over a longer time period at a given edifice, or even compilations of whole-rock data from an entire volcanic region.

For example, Maclennan et al. (2001) assessed magma storage pressures of basalts from the Icelandic Northern Volcanic Zone by filtering possible Cpx-Liq matches using the K_D equilibrium test of Putirka (1999).

Winpenny and Maclennan (2011) devised a more complex test for Cpx-Liq equilibrium, using equation 35 of Wood and Blundy (1997) for K_D, and trace element equilibrium tests. Specifically, they use trace elements measured in Cpx, and then use the partition coefficients from Wood and Blundy (1997) to calculate the expected trace element contents of equilibrium liquid compositions. By comparing these predicted liquid compositions to available trace element data for compiled liquids (for Ce or La, Nd or Sm, and Yb, Dy and Y depending on data availability), they assess all possible matches between Cpx erupted at Borgarhraun, and ~1000 whole-rock and glass analyses from Icelandic Basalts for equilibrium. However, this method requires trace element data in both Cpx and liquids/whole-rock, which isn't widely available in the literature for different volcanic systems (and is rarely collected as part of thermobarometric studies). Furthermore, the trace element partition coefficients used in these calculations are highly sensitive to the temperature of the system, complicating calculations (Sun and Liang, 2012; Wood and Blundy, 1997).

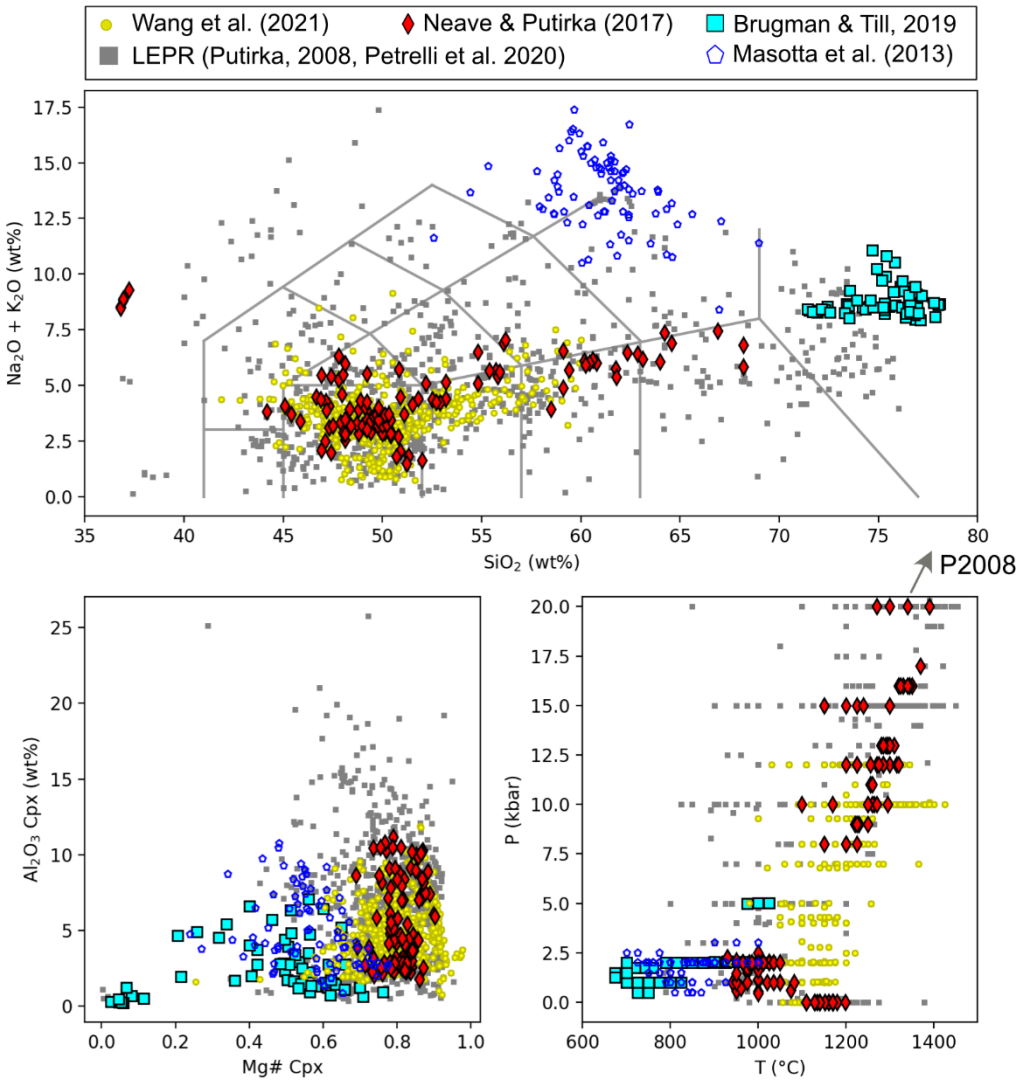

Figure 7: Calibration range of Cpx-Liq and Cpx-only thermobarometers. Since the compilation of the LEPR database in 2008 (Hirschmann et al., 2008) used to calibrate Putirka (2008) and Petrelli et al. (2020, grey squares), many new thermobarometers have focused on specific regions of compositional space: Brugman and Till (2019, cyan squares), Masotta et al. (2013, blue pentagons), Neave and Putirka (2017, red diamonds). TAS lines drawn using Stevenson (2015).

Neave and Putirka (2017) and Neave et al. (2019) develop an R code (also used by Gleeson et al., 2021 and Stock et al., 2018) to identify equilibrium Cpx-Liq pairs using components which can be calculated from elements measured routinely by electron microprobe (Diopside-Hedenbergite, DiHd; Enstatite-Ferrosilite, EnFs; Calcium Tschermak, CaTs). Specifically, they assess the difference in the measured components in the Cpx and

the equilibrium components calculated from the liquid composition using Eq35 of P2008 for K_D, equations from Mollo et al. (2013) for DiHd and EnFs, and from Putirka (1999) for CaTs. As the selected K_D equilibrium equation is sensitive to T, and the DiHd, EnFs and CaTs equations sensitive to P and T, equilibrium tests must be calculated concurrently with P and T estimates. A computationally optimized algorithm loosely based on the Neave R algorithm which was never publicly released was incorporated in the Open-Source Python3 tool Thermobar (Wieser et al. in 2022b). This tool allows comparison of 100s of Cpx and Liq within seconds, with highly customizable equilibrium filters. Even with fast matching codes, identifying Cpx-Liq pairs is associated with substantial uncertainty regarding choice of equilibrium tests, and the chosen cut-off parameter (see Wieser et al. 2023a for arc magmas). In many systems, very few to no matches are found with erupted liquids, requiring generation of synthetic liquids to match to measured Cpx (e.g., Scruggs and Putirka, 2018). Another approach is to pair Cpx rims with matrix glass or groundmass separates (Klügel et al., 2020), although because this method focuses on rims, it may only reveal the depth of the uppermost storage chambers (neglecting deeper pressure information preserved in core compositions).

Issues associated with identifying equilibrium liquids can be circumvented using Cpx-only barometers. Putirka (2008) present two Cpx-only barometers (eq32a-b) and a Cpx-only thermometer (eq32d). Wang et al. (2021) show that these (and other existing) Cpx-only thermobarometers perform poorly in mafic and intermediate melt compositions. To address this, Wang et al. (2021) select 559 experiments conducted at 0–12 kbar with liquid SiO_2 contents between 42–60 wt% to calibrate a new barometer which is independent of T and H_2O (Fig. 7, yellow circles). They use the PyTorch python library (Paszke et al., 2019) to implement a gradient descent algorithm to select Cpx cation components to include in a non-linear term for a Cpx-only barometer, rather than selecting components based on thermodynamic reasoning. They also present a thermometer, which is independent of P but requires knowledge of the H_2O content of the liquid.

Most recently, supervised machine learning methods have been applied to Cpx-based equilibrium to develop thermobarometry expressions (e.g., random forests, Higgins et al., 2022, extra trees, Jorgenson et al., 2022; Petrelli et al., 2020). Unlike more traditional empirical thermobarometers which are underlain by thermodynamic principles, measured oxide data are fed into these algorithms, rather than calculated components such as Jadeite. Wieser et al. (2023a) show that the Cpx-only barometers of Wang et al. (2021) and Jorgenson et al. (2022) show similar performance to popular Cpx-Liq barometers for the ArcPL dataset, justifying the use of Cpx-only barometers as an alternative to trying to identify equilibrium liquids. That said, just because Cpx-Liq and Cpx-only barometry show similar performance, it is worth nothing that neither approach performs particularly well, with neither method yielding R^2>0.74, or RMSE <2.1 kbar. Additionally, all expressions have low gradients, overpredicting at lower pressures, and underpredicting at higher pressures.

The relatively poor performance of Cpx-based barometry on independent test datasets (e.g., high RMSE, low gradients, inability to distinguish magma storage within ~10–15 km) is at least partially the result of low analytical precision when measuring Na_2O in experiments used to calibrate and test barometers (see Wieser et al. 2023b, and Section 1.4). Of course, analytical precision also affects measurements of natural samples and can result in an anomalously large spread of calculated P and T, which can be incorrectly attributed to transcrustal storage because of spurious trends in P-T space. For example, Wieser et al. (2023c) show that a the entire P-T range of the lunar Cpx analysed by Luo et al. (2023) can be explained by the propagation of analytical uncertainty. To further demonstrate the importance of error propagation, we calculate pressures using Cpx and melt inclusion compositions from the first two weeks of the 2018 eruption of Kīlauea Volcano (Wieser et al., 2022c). Cpx-hosted melt inclusions yield relatively shallow saturation pressures, which overlap very well with the pressure at which a highly evolved magma was drilled in this region in 2005 (Teplow et al., 2009, yellow star, Fig. 8a). We use the PEC-corrected melt inclusion compositions and analyses of the Cpx composition close to the melt inclusion to calculate Cpx-Liq and Cpx-only pressures. These barometers return a much greater spread of pressures than melt inclusion saturation pressures, with a notable offset to significantly higher values (Fig. 8). In fact, these calculated depths are similar to the 3–4 kbar estimated by Putirka (2008) for Cpx erupted during the Pu'u O'o eruption of Kīlauea. However, there are no other geological or geophysical indications that Cpx-saturated magmas are stored this deep.

To interpret the large spread of calculated pressures, we simulate 5000 Cpx compositions, with the variability of each oxide following a normal distribution centred on the mean measured Cpx composition, with a standard deviation equal to the average counting statistic precision estimated from the EPMA output. We calculate pressures using these 5000 synthetic Cpx paired with the average liquid composition, and show ±2σ of these simulations as a red error bar (Fig 8b-e). The simulated spread in calculated pressures resulting from analysis of an entirely homogenous Cpx using typical EPMA operating conditions almost exactly matches the

observed spread in calculated pressures (2σ error bars for each overlain on each histogram). This illustrates how, without sufficient averaging of individual analyses, it would be easy to incorrectly invoke storage at a range of pressures spread throughout the crust. While iteration of Putirka (2008, eq30) for T and Neave and Putirka (2017) for P produces calculated pressures that align within error of the melt inclusion saturation pressures, the other Cpx-based barometers estimate far too high pressures compared to melt inclusions and drilling depths. This demonstrates both the lack of precision and accuracy of Cpx-based methods. Even without analytical uncertainty, the RMSE on these barometers mean there is no way to reliably distinguish storage at ~0.5 kbar from storage at 4 kbar; limiting the applicability of these methods in systems where magma is stored in the upper part of a relatively thin crust.

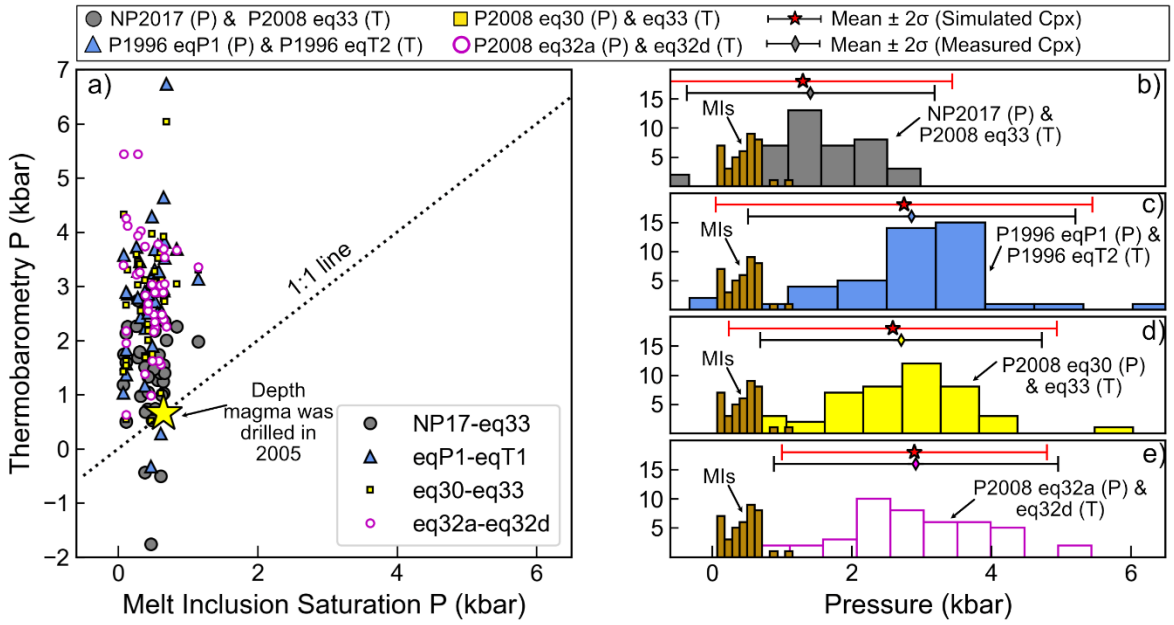

Figure 8: Comparison of melt inclusion saturation pressures (Wieser et al. 2022c), and Cpx-Liq and Cpx-only barometry for samples erupted during the first two weeks of the 2018 Kīlauea eruption. a) Melt inclusion saturation pressures calculated in MagmaSat (Ghiorso and Gualda, 2015) using VESIcal (Iacovino et al., 2021) cluster tightly at shallow pressures. These pressures are very similar to the pressure at which an evolved magma body was drilled in 2005 in the same area (yellow star, Teplow et al. 2009). Cpx-Liq and Cpx-only pressures calculating using PEC-corrected melt inclusion-host pairs show substantial scatter, extending to substantially deeper pressures. b-e) Histograms showing calculated pressures for each iterative mineral barometry calculation. Error bars with black lines show ±2σ for these calculations. Red error bars show ±2σ for Monte-Carlo simulations for the mean composition of each Cpx and Liq, with 5000 Cpx compositions simulated using estimates of analytical precision for these Cpx measurements.

The relatively poor performance of many Cpx-based barometers can also be attributed to the fact that many expressions are parameterized in terms of Cpx components (e.g. Jd, DiHd) calculated from EPMA oxide data (e.g., Neave and Putirka, 2017, Putirka, 2008). An alternative technique calculates site occupancy and cell volumes using a combination of single-crystal X-ray diffraction and measured oxide data (Dal-Negro et al., 1989). This technique was used extensively in the 80s-90s, and was recently applied by Tommasini et al. (2022) to natural Cpx crystals from Popocatépetl Volcano. They show that XRD-informed site assignments and the resulting calculated mineral components differ greatly from the routines used by Neave and Putirka (2017) and Putirka (2008) using EPMA data alone. This discrepancy between components calculated using EPMA data and the true crystal structure may reflect an additional source of uncertainty plaguing Cpx-based barometers. Single crystal XRD may also be vital to help us determine where Na is going (pairing with Al, Fe^{3+} or Cr^{3+}), which will further enhance our understanding of how Cpx composition relates to pressure. However, while single-crystal X-ray diffraction has been applied to natural crystals, the small size of experimental Cpx means that it is very difficult to obtain these parameters for experiments in order to calibrate expressions using these parameters (Dal-Negro et al., 1989, Tommasini et al. 2022). Additionally, a workflow involving XRD would be far more time

consuming from a sample preparation perspective than existing EPMA-based techniques, which may severely restrict its uptake by the community, even if it results in improved barometer performance.

A number of papers have also shown the importance of considering the petrogenetic history of a Cpx population when interpreting thermobarometry calculations. For example, Hammer et al. (2016) assessed the influence of disequilibrium crystal growth on Cpx barometry using X-ray mapping and quantitative spot analyses of clinopyroxene crystals from a post-shield ankaramite erupted from Haleakalā volcano, Hawai'i. Their work demonstrates the complexity of interpreting Cpx compositions in regions where disequilibrium growth processes occur. Specifically, texturally and compositionally distinct domains within individual crystals thought to have formed by high degrees of undercooling during crystallisation have distinct distributions of Cpx Jd contents, so return very different P estimates. They find offsets within individual crystals up to ~3.5 kbar. In contrast, Ubide et al. (2019a, 2019b) calculate P-T-H_2O for different domains in sector zoned Cpx from Stromboli, and show remarkably constant results regardless of the textural context (although without individual calculated PTs, it is not possible to directly compare the statistical differences between these different studies). Clearly, further work is required to understand how the formation of different chemical domains in magmatic systems affect the distribution of P- and T-sensitive Cpx components, and thus the results from thermobarometric calculations.

The relatively recent appreciation that most magmas are stored in predominantly crystal-rich "mushy" environments also adds additional complexity to the interpretation of clinopyroxene-based barometric estimates, because clinopyroxene chemistry can be influenced by chemical processing in these crystal-rich regions. For example, residual melt compositions can be modified by reactive porous flow, driven by disequilibrium between a percolating melt phase and the surrounding crystal framework (Boulanger et al., 2020; Gleeson et al., 2021; Lissenberg and MacLeod, 2016; Sanfilippo et al., 2020). Critically, the melts formed from this process are rarely observed at the surface, which makes it difficult to quantify their chemistry to pair with erupted Cpx compositions. Cpx-Liq and Cpx-only barometry is also affected by the fact that reactive porous flow might drive interstitial melt compositions (and thus the Cpx compositions) outside the compositional range used to calibrate existing expressions (Fig. 7). Gleeson et al. (2021) demonstrate the importance of accounting for mush processes in their study of Cpx from wehrlite xenoliths found on Isla Floreana in the southern Galápagos. These crystals have Na_2O contents up to ~1.3 wt% and returned apparent crystallisation pressures up to ~18 kbar using the clinopyroxene-only thermobarometers of Putirka (2008; eq. 32b-32d). In contrast, Cpx-Opx barometry (using the same crystals), melt inclusion and clinopyroxene-liquid thermobarometry from neighbouring scoria cones on the same island indicate that magma storage was dominantly located at around ~7 kbar (Gleeson et al., 2022, 2021). Based on rare earth element signatures in these pyroxenes (elevated LREE contents relative to MREE and HREE contents) the authors concluded that the anomalously high pressure estimates of the wehrlitic clinopyroxene crystals result from chemical modification of Na_2O (and REE) by reactive porous flow in olivine ±clinopyroxene mush zones. Comparison with other thermobarometric techniques (E.g., Opx-Cpx, melt inclusions, Gao et al., 2022, Gleeson et al. 2021), as well as identifying trace element patterns indicative of reactive flow, provide one method to interpret the spuriously high pressure estimates returned from these cumulate Cpx.

In summary, to push Cpx-based thermobarometry forward, we need to improve the experimental datasets available to calibrate and test barometers (Wieser et al. 2023a-b), develop new methods to relate chemical components to parameters we can easily measure in natural samples and experimental charges (Tommasini et al. 2022), and increase our understanding of natural processes causing variation in Cpx compositions (Gleeson et al., 2021; Hammer et al. 2017, Neave et al., 2019; Ubide et al., 2019b, 2019a),

2.4. Orthopyroxene±Liq

Beattie (1993) presented the first Opx-Liq thermometer based on the use of non-regular solution models to calculate saturation temperatures. Putirka (2008) then calibrated two different equations (Eq28a, 28b) using the LEPR dataset, both of which are sensitive to P and H_2O. Eq28a uses the composition of the Opx and Liq, while Eq28b only uses the composition of the liquid to calculate the temperature of Opx saturation. Wood (1974) published the first Opx barometer, which used the Al content of Opx in equilibrium with Garnet. Putirka (2008) calibrated a more widely applicable Opx-only barometer (Eq29c) and two Opx-Liq barometers (Eq29a, Eq29b) using the LEPR database. The main pressure-sensitive component in Eq29a is a Jadeite-like component in the Opx, while Eq29b uses the (Fe, Mg) Al_2SiO_6 Opx component. Both equations also contain terms for other liquid cation fractions, and Opx cation fractions on the basis of 6 oxygens. Eq29c (Opx-only) uses the cation fractions of Al, Ca, Cr and Al in the Opx, as well as terms for T. It is worth noting that several of the Putirka (2008) Opx thermobarometers are prone to numerical issues resulting from the presence of logarithmic terms.

For example, Eq29c (Opx-only) has a term for the logarithm of the cation fraction of Cr in Opx. If Cr was not measured or reported in Opx, this term cannot be evaluated (the case for 63% of the experiments in our test dataset). Similarly, Eq28b has a term calculated from the log of the (Fe, $Mg)_2Al_2SiO_6$ component in the Opx divided by terms involving the cation fractions of Si, Al, Fe, Mn, and Mg in the liquid. In ~9% of experiments (mostly at <3 kbar, but a few at 5 and 8 kbar), the (Fe, $Mg)_2Al_2SiO_6$ component in the Opx is 0, the log of which yields infinity. A value of zero for the (Fe, $Mg)_2Al_2SiO_6$ component can also occur in Opx where the calculated Al_{VI} component is zero, which is particularly common in low pressure Opx (Al_{VI}=0 in 7% of the Opx considered here, all at <2.5 kbar). To address the numerical issue associated with the (Fe, $Mg)_2Al_2SiO_6$ component, in later versions of the spreadsheets from Putirka (2008), two additional Opx-Liq barometers were included ("Global" and "Felsic"). These equations simply use the ratio of the measured Al_2O_3 content in Opx and Liq. The global model was calibrated on 795 Opx-Liq pairs, and the felsic model on 40 pairs.

In natural systems, it is even more difficult to assess the equilibrium relationships between erupted Opx and Liquid compositions than for Cpx-Liq, because only $K_{D,Fe-Mg}^{Opx-Liq}$ has been widely explored as an equilibrium test. Putirka (2008) find that K_D in experimental charges roughly correlates with the cation fraction of Si in the liquid (X_{Si}) (1σ=0.06). In the ArcPL dataset, there is no significant correlation between K_D and X_{Si} (R^2=0.01, Fig. 9a), although ~67% lie within the given error bound of the predicted value. In natural systems is it very plausible that liquids and orthopyroxenes that are not chemically related could yield K_D values passing these relatively broad equilibrium tests (particularly if 2σ is used as the cut off). One way to avoid this problem is to use an Opx-only barometer (e.g., Eq29c of P2008), However, this equation contains a temperature-sensitive term, and given no Opx-only thermometer exists to our knowledge, a liquid composition may still need to be used to estimate (or iteratively calculate) the temperature.

Using experimental P and H_2O (that was measured by quantitative methods), Eq28a (Opx and Liq comps) and Eq28b (only Liq comps) are remarkably good thermometers. Eq28a has a slightly higher R^2 (0.90 vs 0.85), and lower RMSE (39 vs. 48°C, Supporting Fig. 3). Using experimental T and H_2O measured by quantitative methods, Eq29b is the best Opx-Liq barometer (R^2=0.58, RMSE=3.01 kbar, Supporting Fig. 4), and has a decent gradient and intercept relative to other mineral-melt barometers we evaluate in this review (grad=0.67, int=1.2). Eq29a performs slightly worse in terms of R^2 and RMSE but has a slightly better gradient and intercept (R^2=0.50, RMSE=3.65 Gradient=0.74, Int=0.3 kbar). The global barometer is noticeably worse (R^2=0.47, RMSE=3.47 kbar, grad=0.59, int=1.4). The Opx-only barometer (Eq29c) is difficult to compare because of the presence of many experiments without reported Cr measurements in Opx that return numerical errors; for available data, R^2=0.04, RMSE=4.63 (Supporting Fig. 4d).

As discussed, it is probable in natural systems that neither T nor P is known, and melt H_2O is relatively uncertain. We investigate the sensitivity of calculated P to T, and calculated T to P (Fig. 10) by perturbing the experimental T by ±100°C and P by ±5 kbar. The Putirka (2008) Global and Felsic barometers have no T term, so show no changes in P with T. Eq29a (dark blue lines, Fig. 10a) shows a relatively small increase in calculated P with increasing T, while Eq29b shows a larger increase (light blue lines, Fig. 10a). Eq29c, the Opx-only barometer, shows variable sensitivity to T, with P increasing in some samples, and decreasing in others as T is increased (grey lines, Fig. 10a). The strong change in calculated P as a function of T for Eq29c, a drop of up to 10 kbar for +100°C for some samples, is problematic, as there is no way to determine temperature simply from Opx compositions at present. The three Opx-Liq thermometers also show variable changes with P (some increasing, some decreasing, Fig. 10b). However, the uncertainty in calculated T for changes in P of 10 kbar (equivalent to the crustal thickness in most arcs) is comparable to the stated RMSE on these thermometers.

Overall, the relatively large change in calculated P (and to a lesser extent T) with relatively small changes in the other parameter means that we can expect Opx-based thermobarometers to show far worse statistics when solved iteratively than when tested with only a single unknown.

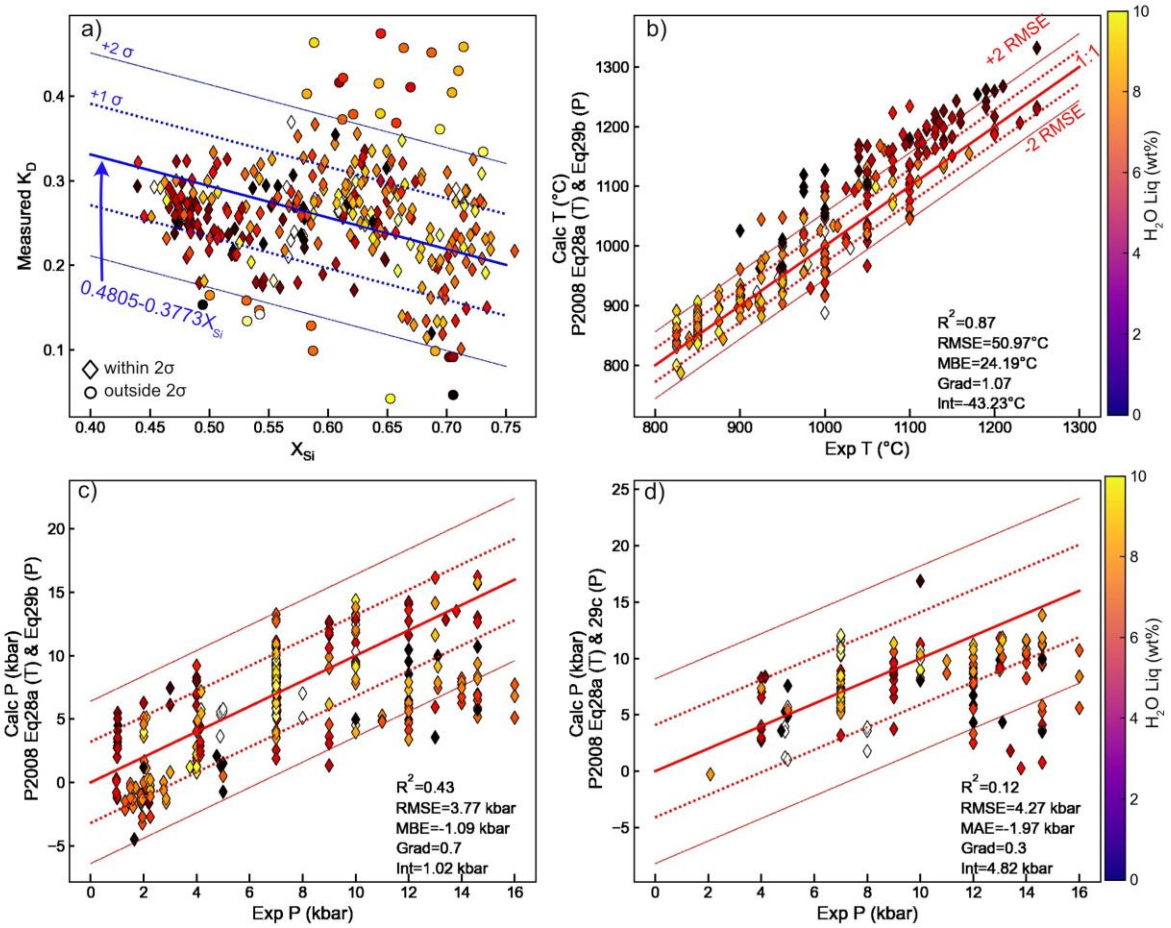

Figure 9: Opx-Liq and Opx-only thermobarometry. a) Comparison of measured K_D with that predicted from the X_{Si} content of the liquid using Putirka (2008). b-c) Comparison of calculated and experimental T and P by iterating Eq28a(T) and Eq29b(P). d) Iteration of Eq28a (for T, Opx-Liq) with Eq29c (Opx-only, P) of Putirka (2008). Dotted lines around the 1:1 line show ± the quoted 1σ, with dashed lines showing ±2 σ. All symbols colored by H_2O content, with H_2O>10 wt% white, to emphasize the scale at lower H_2O contents.

We also investigate the change in P when using iterative calculations when we perturb the experimental H_2O content by ±3 wt%. When T from Eq28a is iterated with all barometers, calculated T decreases with increasing H_2O (Fig. 10d). Iteration of Eq28a (T)-Eq29a (P) (dark blue line) and Eq28a (T)-Eq29b (P) (light blue line) show a small increase in calculated P with increasing H_2O content (Fig 10c). Both these barometers have terms multiplying H_2O by a constant, resulting in a consistent change in P for varying H_2O contents in non-iterative calculations (+0.748 kbar/1 wt% H_2O for Eq29a, and +0.784 for Eq29b, dashed blue lines, Fig. 10c). However, because increased H_2O contents cause T to drop using Eq28a (Fig. 10b), which causes a decrease in the calculated P (Fig. 10a), the influence of H_2O on calculated P in iterative calculations is slightly less than that obtained in calculations using the experimental T. This complex feedback between equations during iterative calculations results in a greater variability in the influence of H_2O on calculated P for different samples. Eq29c has no H_2O term but shows the strongest sensitivity to T (Fig. 10a), resulting in a large drop in P with increasing H_2O when iterated with Eq28a (Fig. 10c). The high sensitivity of Eq29c to H_2O is concerning because an Opx-only barometer is most likely to be applied in systems where liquid compositions (and thus, H_2O contents) are poorly constrained. As the Global and Felsic barometers have no T or H_2O term, they show no sensitivity to H_2O.

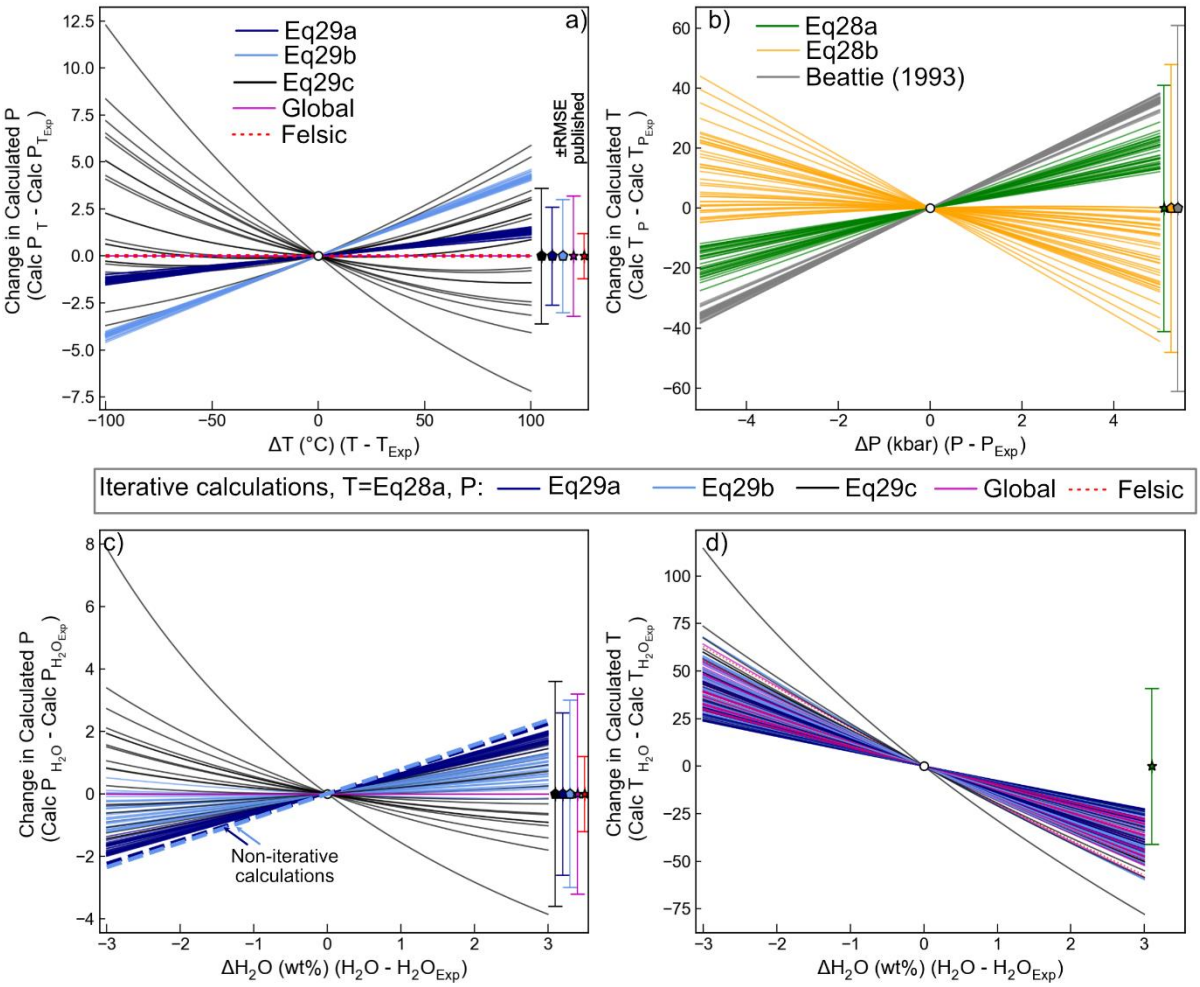

Figure 10: Assessing the sensitivity of Opx thermobarometry to variation in P, T and H_2O for N=40 randomly selected experiments. a) Change in calculated P for perturbing the experimental T by ± 100 °C. b) Change in calculated T by perturbing P by ±5 kbar. c-d) Change in calculated P and T for iterative calculations perturbing experimental H_2O content by ±3 wt%. For all plots, the calculated P or T at experimental conditions is subtracted from the calculation at experimental conditions (plotting at 0, 0). Calculations performed in Thermobar (Wieser et al., 2022b).

Ideally, given the effects of H_2O on calculated P and T (Fig. 10c-d), we would only assess experiments where H_2O is known by quantitative methods (as for Liq-only). However, only 147/324 experiments from 10/23 studies have reported Opx-Liq compositions where H_2O was measured quantitatively. Thus, all experiments are shown in Fig. 9, with the same calculations using only experiments with quantitative H_2O measurements shown in Supporting Fig. 5 (the statistics for which are actually less favourable).

Iterating the best thermometer (Eq28a) and barometer (Eq29b) yields a very good match to experimental T in ArcPL using experimental H_2O contents (Fig. 9b). The thermometer performs worse for experiments with low H_2O contents (darker symbols, < 2–3 wt%). Based on a similar observation for the LEPR dataset, Putirka (2008) suggest that Opx may re-equilibrate faster in hydrous liquids. Calculated P from iteration of Eq28a-Eq29b is reasonably accurate (Fig. 9c, grad=0.7, MBE=-1.09 kbar, int=-1 kbar), but very imprecise (RMSE=3.77 kbar), so this barometer will be of limited utility in relatively thin-crusted settings such as OIBs and MORBs (Fig. 3). Unlike for thermometers, there is no clear relationship between barometer performance and H_2O content. Although we cannot perform very many calculations for Eq29c because of the absence of Cr data, calculated Opx-only pressures (Eq29c) iterated with Eq28a shows a reasonable correspondence to the 1:1 line (Fig. 9d) at <12 kbar, although substantially more experiments with reported Cr contents are required to robustly assess this barometer.

Overall, Opx-Liq thermobarometry has been relatively neglected given its performance; no new calibrations have been proposed since 2008. In particular, the relative absence of systematic uncertainty when Opx-based barometers are tested on ArcPL contrast strongly with other mineral barometers discussed here. We suggest that future experimental and theoretical work to further develop Opx-based thermobarometry is warranted, with a particular focus on the development of more robust equilibrium tests. Ensuring starting materials contain Cr contents comparable to natural systems, and ensuring all elements are measured at high precision within experimental Opx (particularly Cr) may lead to improved thermobarometry calibrations. This may provide a particularly promising barometer in arc magmas, where Opx is relatively common, and magmas are relatively H_2O-rich.

2.5. Two Pyroxene (Cpx-Opx) Thermobarometry

Two pyroxene (Cpx-Opx) thermobarometry is widely used in the literature, likely reflecting the fact that these phases crystallize together across a wide range of P, T, and H_2O contents in a variety of tectonic settings. For example, Cpx-Opx thermobarometry has been applied to OIB basalts from the Galápagos by Gleeson et al. (2021), to mafic arc basalts from SW Japan by Zellmer et al. (2014), and to arc dacites from the Aucanquilcha Volcanic Cluster by Walker et al. (2013). Additionally, it is common that Cpx and Opx form crystal clusters, and calculations from these touching pairs are easier to justify than trying to select equilibrium liquids for each crystal (c.f. Opx-Liq and Cpx-Liq thermobarometry). Opx-Cpx thermobarometry can also be applied in systems where it is difficult to analyse the composition of the liquid (e.g., highly crystalline lavas or xenoliths, Gao et al., 2022; Gleeson et al., 2021).

As discussed above for Opx-Liq equilibrium, one of the main limitations of Cpx-Opx thermobarometry is the paucity of equilibrium tests to help filter out pairs which are not in equilibrium (in experiments and natural samples). The only established equilibrium test compares the exchange of Fe-Mg in Cpx and Opx ($K_{D,Fe-Mg}^{Cpx-Opx}$). Putirka (2008) suggest that K_D=1.09±0.14 in high temperature systems, while K_D=0.7±0.2 in subsolidus systems. However, it is difficult to know where to draw the line between these different filters; what value would be correct to use in a supra-solidus dacitic-rhyolitic melt that is a similar temperature to a subsolidus mafic cumulate? K_D values for our compiled experiments lie mostly within the high T bracket (±1σ shown in pink), although a number extend to higher values (Fig. 11a). There is no strong relationship between T and measured K_D. Another way to assess the equilibrium value would assume that the Cpx and Opx are each in equilibrium with the liquid, so the Opx-Cpx K_D value can be obtained from the Cpx-Liq and Opx-Liq K_D values from Putirka (2008):

$$K_{D,Fe-Mg}^{Cpx-Opx} = \frac{K_{D,Fe-Mg}^{Cpx-Liq}}{K_{D,Fe-Mg}^{Opx-Liq}} = \frac{e^{-0.107-\frac{1719}{T(K)}}}{0.4805 - 0.3733 * X_{Si,Liq}} \text{ [Equation 8]}$$

This approach could be advantageous, because there are far more Cpx-Liq and Opx-Liq experiments than Cpx-Opx experiments, so the individual Px-Liq equilibrium values are better constrained. Values calculated using this expression lay between the subsolidus and high T value (red dots, Fig. 11a), with very little variation with temperature. This is because higher T drives up the Cpx-Liq K_D, but higher T liquids tend to have lower Si contents, which drives up Opx-Liq K_D. Unfortunately, Equation 8 appears to underestimate the K_D value for many of the experimental samples given here, which is perhaps unsurprising as we find the Cpx-Liq K_D expression underestimates many of the Cpx-Liq K_D values (by up to ~0.5), while the Opx-Liq expression tends to overestimate many of the Opx-Liq K_D values. Dividing these two relatively uncertain quantities compounds errors. The fact so many of our experimental Cpx-Opx pairs sit outside any estimate of equilibrium could suggest that several are not in equilibrium, so should not be used to assess thermobarometers. However, we find no discrepancy between K_D and the offset between calculated and predicted P and T. This suggests instead, that more experimental and theoretical work is needed to robustly assess K_D. Thus, we proceed to assess thermobarometers using all Cpx and Opx pairs in the ArcPL compilation.

The T-independent barometer of P2008 (Eq38) performs very poorly for high Mg# Cpx (R^2=0.29, RMSE=4.09) and even worse for low Mg# Cpx (<0.68, cyan diamonds, Fig. 11b, R^2=0.01, RMSE=13.72). Iteration of P2008 Eq37–39 and Eq36–Eq39 show very similar statistics to one another for calculated P and T, with Eq36–Eq39 showing slightly better behaviour. Neither thermometer is very promising (Fig. 11c, e) producing more of a data cloud than a meaningful correlation. At lower temperatures, two pyroxene thermometers tend to overestimate temperatures (also noted by Ziberna et al., 2021). Iterated barometers are similarly disappointing; even for Cpx with Mg#>0.68, the RMSE is 3.69 kbar (Eq3 7–Eq39, Fig. 11d) and 4.12 kbar (Eq3 6–Eq39, Fig. 11c).

Overall, we suggest that substantially more experiments where Opx and Cpx are stabilized at a variety of pressures and melt compositions are required to improve Cpx-Opx thermobarometers, particularly in more evolved systems with lower Cpx Mg#s. Additional experiments would also help to better constrain controls over the equilibrium value at a variety of temperatures and melt compositions.

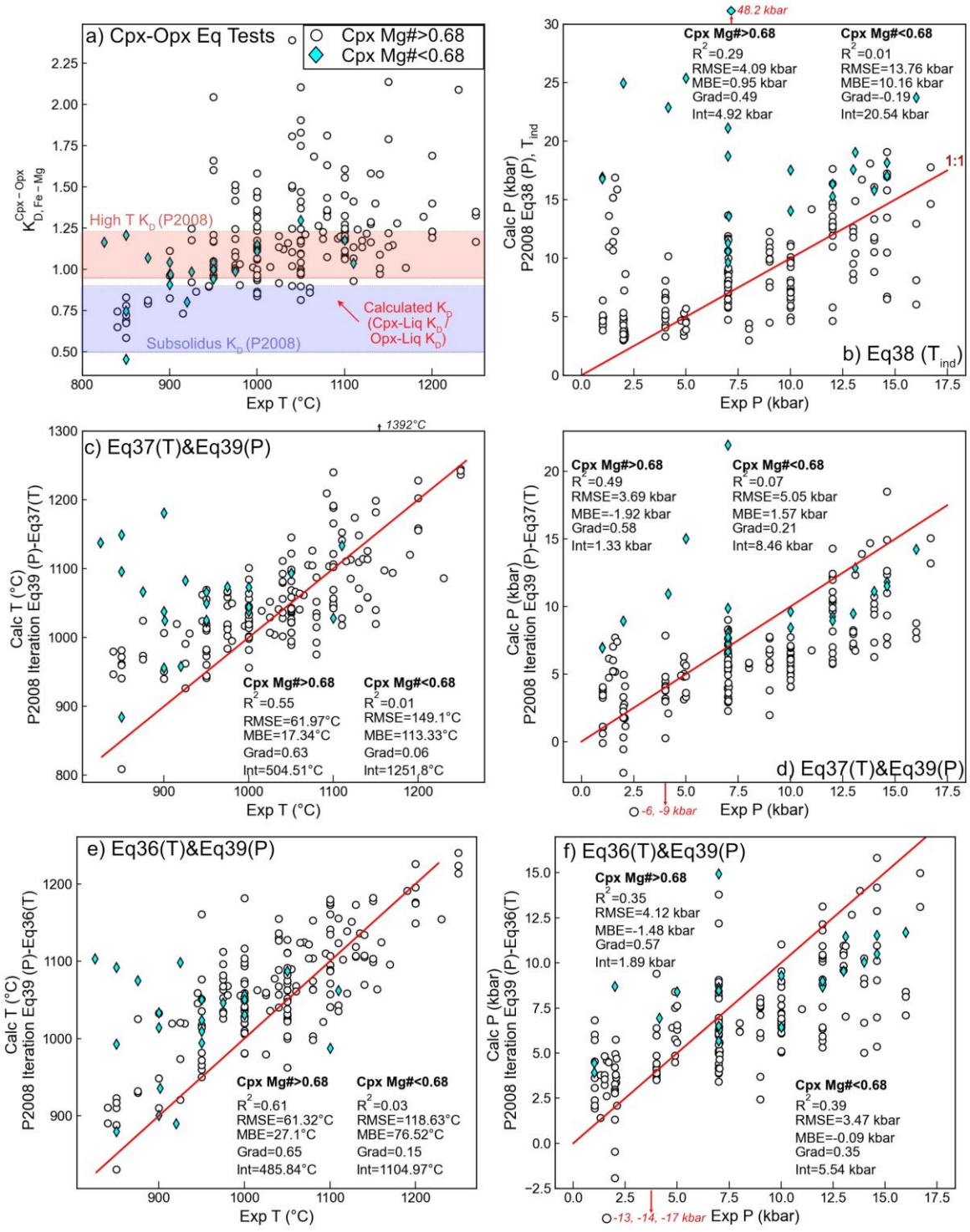

Figure 11: Assessing two-pyroxene thermobarometers. a) Measured $K_{D,Fe-Mg}^{Cpx-Opx}$ values for the ArcPL dataset against experimental T. The range of equilibrium values from Putirka (2008) for "HighT" and "Subsolidus" systems are shown as colored bars. K_D values calculated from the Cpx-Liq (T-dependent) and Opx-Liq (Si-dependent) K_D values (Equation 8) are shown as small red dots. b-f) Comparison of predicted and experimental P and T for different combinations of equations from P2008. 1:1 line shown in red. In all plots, Cpx-Opx pairs with

Cpx Mg#<0.68 are colored cyan, and Mg#>0.68 colored white. To maintain scale, a few experiments returning extreme values are excluded from plots. Their y coordinate is labelled with a red arrow.

2.6. Amphibole thermobarometry and Chemometry

Amphibole (Amp)-only and Amp-Liq thermobarometry have been used extensively to calculate P and T in volcanic and plutonic igneous systems (e.g., Higgins et al., 2022; Scruggs and Putirka, 2018). Amphibole chemometers are also becoming widely used to probe the compositions of melts present at depth within plumbing systems which are not always well represented at the surface (e.g., Humphreys et al., 2019; Zhang et al., 2017).

2.6.1 Amphibole thermobarometry

Amphibole barometry stems from the seminal work of Hammestrom and Zen (1986), who showed that the Al^{VI} and Al^{Tot} contents of hornblendes from calc-alkaline plutons emplaced at different depths correlate with estimates of pressure, and that the same compositional-pressure relationships were seen in experimental products. Hollister et al. (1987) analysed rim compositions from plutons where the pressure of emplacement could be estimated from phase assemblages in the surrounding country rock. They confirmed the Al-pressure relationship of Hammestrom and Zen (1986) and proposed an updated calibration. Additional calibrations have also been developed for Amp-Plag, Amp-Garnet, and Amp-Plag-Qtz (see Molina et al., 2021 and refs. within).

More recently, Mutch et al. (2016) present an Amp-only barometer parameterized in terms of Al^{tot} calibrated using a dataset comprising: i) their new experiments on 3 different bulk compositions, ii) the experiments of Johnson and Rutherford (1989), Schmidt (1992), Thomas and Ernst', 1990), iii) published analyses from plutons with independent depth constraints (Ague, 1997; Hammestrom and Zen, 1986), and iv) their new analyses on amphiboles from the Yerrington Batholith in Nevada. Mutch et al. (2016) exclude experiments where garnet or phengite was stabilized, as this alters the Al^{T}-pressure relationship. Importantly, their compiled dataset shows a curvature in Al^{T} vs. pressure space relationship at 0.5–3 kbar not seen by previous workers. They parameterize this empirically relating pressure to a second order polynomial of Al^{T}.

While Al^{T} in amphibole is controlled by both T and P, so can only be used as a barometer on an isotherm or near a solidus (Médard and Le Pennec, 2022), correlations between P and Al^{VI} have been noted by Krawczynski et al. (2012), Helz (1982), Larocque and Canil (2010) and Schmidt (1992) in a wide variety of systems. Médard and Le Pennec (2022) present a T-independent barometer using a simple linear regression of P and Al^{VI}, calibrated on 47 published experimental compositions with Si-rich silicate melts in equilibrium with Biotite, Plagioclase, and Magnetite. They state that this barometer has a RMSE of 0.86 kbar (or 0.72 kbar for <4 kbar). They also test their expression on 22 biotite-bearing experiments not used in calibration, which lie within the stated RMSE window. However, all their tests are at <4 kbar, which makes it difficult to evaluate the precision of the barometer at higher pressures.

Importantly, all the Al-based amphibole-only barometers discussed so far are only applicable in the presence of certain phases. For example, Hammestrom and Zen (1986) warned about the applicability of their regressions in rocks without quartz, where Al^{T} can be significantly higher at a given P. Mutch et al. (2016) emphasize that their barometer should only be applied to amphibole rims in equilibrium with melts saturated in plagioclase ($An_{15–80}$), biotite, quartz, alkali feldspar, Fe-Ti oxides, and apatite (e.g., near solidus, low variance volcanic systems). In higher T melts with fewer co-crystalizing phases and higher thermodynamic variance, the equilibria controlling amphibole composition are still poorly understood (Putirka, 2016). Médard and Le Pennec (2022) test their barometer using 7 Bt-free experiments, resulting in a RMSE of 1.4 kbar, which is a large % error given these experiments were conducted at ~ 1–2 kbar. Thus, they suggest that this barometer should not be used in biotite-free rocks. While limited in their applicability to silicic systems saturated in a large number of phases, the amphibole-only barometers discussed thus far are extremely useful for determining pluton emplacement depths and crustal exhumation rates in orogenic belts, or when investigating the formation and evolution of Porphyry copper deposits (Anderson, 1996; Hollister et al., 1987; Mutch et al., 2016).

In contrast to these studies focused on low variance silicic systems, Ridolfi et al. (2010) compile calcic amphibole analyses from experiments conducted on a wide range of melt compositions and phase assemblages to generate an empirical amphibole-only thermometer (Eq1), oxybarometer (Eq2) and hygrometer (Eq3). Ridolfi et al. (2010) justify the application of Amp-based methods in less evolved systems with fewer phases (and therefore higher variance) by pointing out that most volcanic amphiboles exist close to their stability limits (shown by abundant breakdown textures). They suggest that close to the amphibole stability curve, the variance of the system is lower so amphibole composition is more closely related to P, T and fO_2. Ridolfi et al. (2010) also

present an Al^T barometer calibrated on 9 amphiboles (Eq4) but find that attempts to perform a similar calibration on their larger experimental dataset performs poorly, particularly for magnesiohastingsite amphiboles which are common in nature, but sparse in available experiments.

Ridolfi and Renzulli (2012) compile additional experiments and apply more stringent filters to produce an amphibole-only barometer (e.g., removing amphiboles with 1σ for SiO_2>0.9 wt%, Piston cylinder experiments conducted at <6 kbar etc.). Of the 61 experimental amphiboles remaining, 19 (31%) are magnesiohastingsite, which is close to the proportion of magnesiohastingsites (42%) in their natural compilation. This is in stark contrast to the dataset of Ridolfi et al. (2010), which contained no magnesiohastingsites (or pargasites or kaersutites). Ridolfi and Renzulli (2012) create several different regressions to calculate P using amphibole cation fractions calculated on the basis of 13 oxygens. For example, Eq. 1a was calibrated on N=61 experiments, and expresses P in terms of the exponential of compositional terms (Si, Ti, Al, Fe, Mg, Ca, Na, K). However, using comparisons to seismic depths from Ridolfi et al. (2010) for a variety of natural systems, they show that this equation overestimates at low P, and underestimates at high P. They calibrate 4 additional expressions using a smaller subset of analyses (N=20–41) in different pressure ranges (Eq1b and 1e use exponentials, 1c and 1d use multilinear regressions). They present an algorithm where the user calculates P for each equation, and these different values are averaged/combined in a variety of different ways to construct a final P.

To test the expressions of Ridolfi and Renzulli (2012), Erdmann et al. (2014) compile a series of experiments not used in their calibration dataset. While T, melt SiO_2 content and fO_2 are reasonably well predicted in their new dataset, they demonstrate a very poor correspondence between calculated and experimental P, and calculated and experimental H_2O contents. Erdmann et al. (2014) suggest the P discrepancy results from the fact that the Si-Al content of an amphibole is more strongly related to the liquid composition and T than P. In particular, they note that the calibration dataset of Ridolfi and Renzulli (2012) is skewed, with amphiboles from felsic and intermediate melts clustered at lower P, and mafic to intermediate melts at higher Molina et al. (2021a) also publish a short note stating that they test Ridolfi and Renzulli (2012) using a dataset of experiments compiled by Molina et al. (2021b), and obtain "*unsustainable pressure estimates*".

Putirka (2016) further examine Amp-only and Amp-Liq equilibrium, presenting two P-independent Amp-only thermometers (Eq5 and SiHbl), two P-dependent Amp-only thermometers (Eq6 and Eq8), two P-independent Amp-Liq thermometer (Eq4b and Eq9), and a P-independent Liq-only amphibole saturation thermometer (Eq4a). He also presents three T-independent Amp-Liq barometers (Eq7a, b, c). Using an extensive test dataset, Putirka (2016) show that Amp-only and Amp-Liq equilibrium do a reasonably good job of predicting pressure when averaged, but conclude that P estimates from individual amphibole grains are '*nearly useless for understanding crustal processes'*. They hypothesize that the main limitation of Amp-based barometry is the fact that none of the common amphibole components have particularly large changes in volume when they precipitate from the liquid (ΔV fusion), or large molar volume contrasts between different components in the amphibole itself. For example, even though Jadeite in pyroxene is not a particularly sensitive barometer at crustal conditions, relative to Diopside it has a significantly more negative ΔV fusion (Fig. 12a), and a smaller molar volume (8% smaller, Fig. 12b, Putirka, 2016). As Jadeite has both a smaller molar volume and a more negative ΔV fusion (Fig. 12c), the amount of Jadeite vs. Diopside in Cpx are sensitive to P. In contrast, there is a pretty weak relationship between the ΔV fusion and the molar volume for different amphibole components (Fig. 12b-c, Putirka, 2016). While the exchange of different amphibole components is not particularly P-sensitive, Putirka (2016) do show that the partition coefficient of Al between amphibole and liquid is correlated to P, explaining why amphibole barometers are normally parameterized in terms of Al and other oxides, rather than explicitly calculated mineral components (e.g. Jadeite in Cpx).

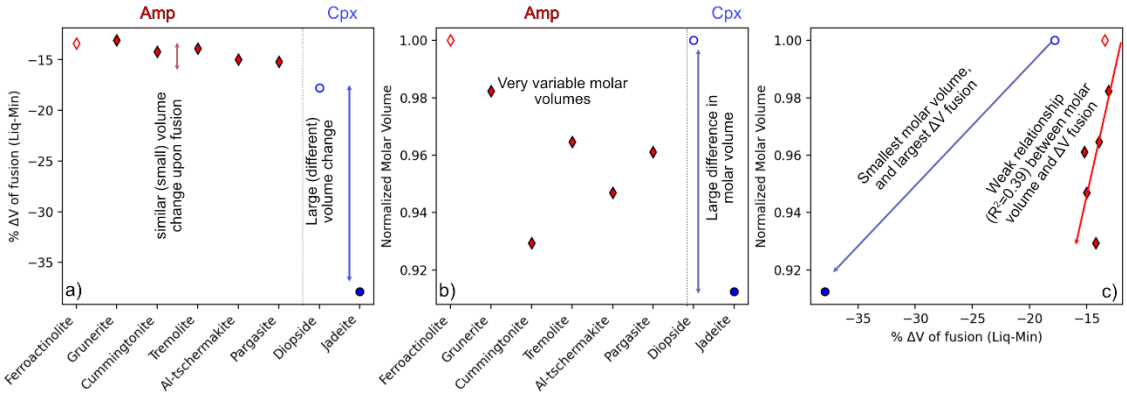

Figure 12. Comparison of molar volumes and volumes of fusion for Amp vs. Cpx components. a) Changes in volume following precipitation of different mineral components from the liquid (ΔV fusion). Amphibole components show significantly smaller changes than jadeite, and the different Amp components show very similar ΔV fusion. b) Molar volume normalized to the component of each phase with the highest molar volume (ferroactinolite for Amp, diopside for Cpx). c) Correlation between normalized molar volume and ΔV fusion. Thermodynamic data from table 1 of Putirka (2016).

We use ArcPL data not used for calibration of the Putirka (2016) equations to test their performance and sensitivity to other terms present in the regression (see Supporting Figs. 6–8). The best performing Amp-only thermometer for this dataset is Eq5 (R^2=0.7, RMSE=41.5°C, Fig. 13a, Supporting Fig. 6), which has the advantage of being independent of P and H_2O in the liquid. The best Amp-Liq thermometer is Eq9 (R^2=0.76, RMSE=34°C, Fig. 13b, Supporting Fig. 8), which is P independent and not very sensitive to H_2O in the liquid (Supporting Fig. 7, ~1°C change in T per 1 wt% H_2O). Like Putirka (2016), we find that all three Amp-Liq barometers show disappointing statistics (RMSE= 3–4 kbar, Grad=0. 3–0.5, Supporting Fig. 8, e.g., Fig. 13c). In particular, the pressures for the higher P experiments of Blatter et al. (2023), and Müntener et al. (2001) are greatly underestimated, although the barometer does a reasonable job of the lower P data, which clusters around the 1:1 line at ~ 2–5 kbar. The skew at high P means that even after the averaging suggested by Putirka (2016), Amp-Liq barometry can give misleading results.

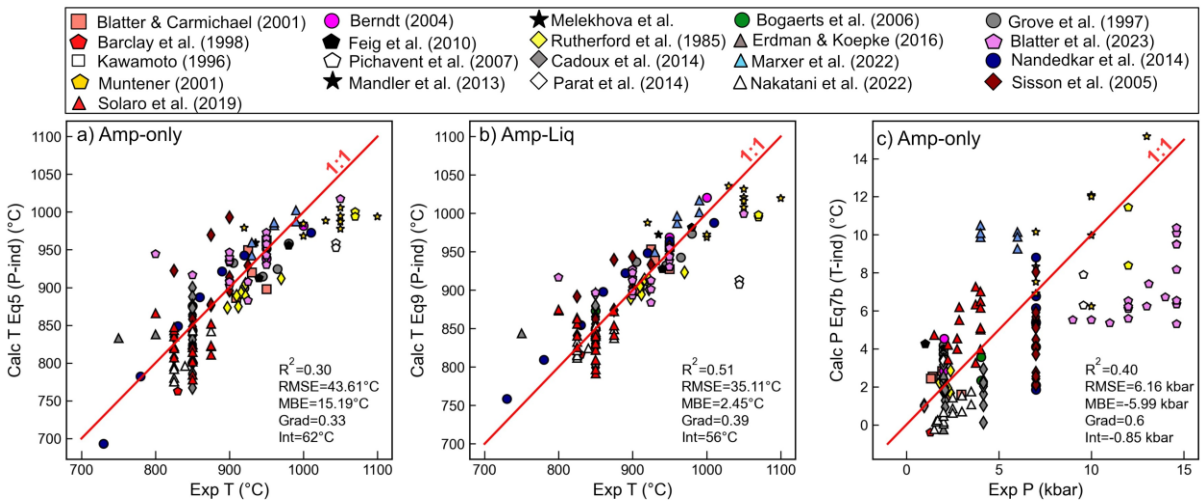

Figure 13 – Assessing Amp-Liq and Amp-only thermobarometers from Putirka (2016) using experiments not used during model calibration. Only experiments passing the K_D filter of Putirka (2016) are shown.

Ridolfi (2021) updated the Ridolfi and Renzulli (2012) amphibole-only barometer, perhaps partially in response to the criticism of Erdmann et al. (2014), Molina et al. (2021) and Putirka (2016), and partially because of an increase in the number of amphibole-bearing experiments. Using an expanded experimental dataset, they tweak the algorithms used to select between different P equations and add more stringent filters to give users warning of when the equations are being applied to amphiboles failing quality tests or outside the model calibration range (based on totals, unbalanced charge, low B cations, etc, low and high Ca cations, low Mg cations). We tested this new algorithm and quality filter on experiments from ArcPL not used during calibration

(Alonso-Perez et al., 2009; Berndt, 2004; Blatter and Carmichael, 2001; Bogaerts et al., 2006; Cadoux et al., 2014; Erdmann and Koepke, 2016; Grove et al., 1997; Kawamoto, 1996; Marxer et al., 2022; Nakatani et al., 2022; Parat et al., 2014; Rutherford et al., 1985; Sisson et al., 2005; Sisson and Grove, 1993; Solaro et al., 2019, Blatter et al. 2023). Of our compiled experiments (N=193), 112 pass the quality check filters of Ridolfi (2021, Fig. 14a). For those passing the quality filters, calculated P show a moderate correspondence to experimental P, although calculations clearly lie well outside the stated ±12% error in the abstract of Ridolfi (2021, red dashed lines, Fig. 14b). The overall fit to these experiments yields R^2=0.36 and RMSE=3.6 kbar. The experiments conducted at 2 kbar by Sisson and Grove (1993) show particularly poor results, returning pressures which are up to 15 kbar too high. Excluding these experiments yields R^2=0.67 and RMSE=2.7 kbar. Compared to the Putirka (2016) Amp-Liq barometers, this Amp-only barometer does a much better job of recreating the high pressures of Blatter et al. (2023), although it does still underestimate to a degree. Despite the criticism of this method in the literature, it is noteworthy that Amp-only barometry doesn't perform any worse than Opx-Liq and Opx-Cpx based on our dataset, but it should be noted that none of these methods are precise enough to be useful for many volcanological questions. As amphibole-only T from Ridolfi and Renzulli (2012) require a P to be entered, we also test how effective this thermometer is using pressures obtained from the 2021 barometer. The correlation between calculated and experimental T is reasonably good (Fig. 14a, R^2=0.53, RMSE=53˚C), although the RMSE is twice that stated in the abstract of Ridolfi (2021, 22°C, shown with dashed red lines, Fig. 14a).

We examined the Sisson and Grove (1993) experiments in the context of the calibration dataset of Ridolfi (2021) to try to understand the poor performance of the barometer. These experiments plot to substantially higher amphibole Na_2O contents at lower pressures than any of the calibration experiments (Fig. 14d). To investigate whether this offset to higher Na_2O contents could explain the anomalously high calculated P, for each Sisson and Grove (1993) amphibole, we perturb the Na_2O content by ±2 wt%. Pressures for measured amphibole compositions are shown as squares (Fig. 14e), with a line stretching from each square showing the change in pressure as Na_2O is changed. The colors indicate the root equation from Ridolfi (2021) algorithm used to determine P, with the rapid jumps in pressure reflect a flip to a different equation selected by the algorithm. For the samples with high calculated P (>7.5 kbar), it is very clear that Eq1e (and to a lesser extent 1d and 1a) is highly sensitive to the Na_2O content, rapidly shooting up to extremely high pressures for very small changes in Na_2O. It may well be that these natural samples lie outside the Na_2O range used to calibrate Eq1e (the calibration data for each specific equation is not available). The Alonso-Perez et al. (2009) experiments (red squares) where pressure is underestimated are also clearly offset from the calibration dataset in T – Na_2O space (Fig. 14c). This comparison emphasises the importance of ensuring that sample compositions are well represented in the calibration dataset of the chosen model, not just in terms of P-T space, but also compositional space. It also shows that having the correct functional form for a barometer routed in thermodynamics is essential to minimize extrapolation issues commonly seen with empirical fits.

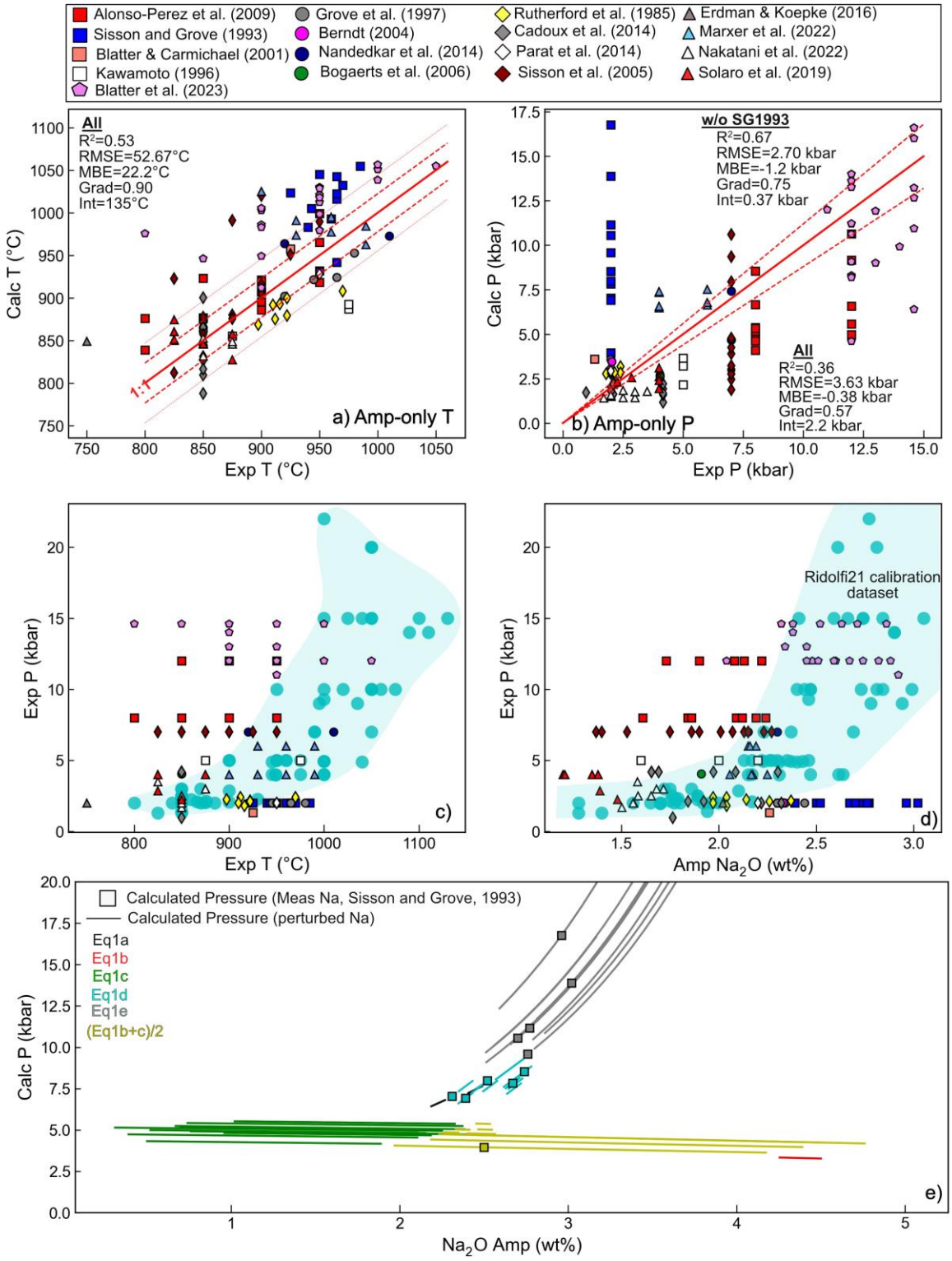

Figure 14: Assessing Amp-only thermometers and barometers. a) Comparing experimental and calculated T using the thermometer of Ridolfi and Renzulli (2012) iterated with Ridolfi (2021). b) Comparing experimental and calculated P using the new barometer of Ridolfi (2021, T-independent). c-d) Visualizing experimental compositions relative to the calibration dataset (cyan dots and field) of Ridolfi (2021). Many of the experiments showing the largest discrepancies in calculated pressure (e.g., red and blue squares, magenta diamonds) lie outside the calibration range of Ridolfi (2021) in Pressure-Na_2O space. e) To visualize the effect of Na_2O on calculated pressure, we perturb the Na_2O content of the experiments of Sisson and Grove (1993) by ±2 wt%. The lines are not continuous, with jumps to a different pressure as the algorithm flips between different 'root'

equations (indicated by the color of the line). Experimental Na_2O (and calculated pressures) are indicated with squares, with the calculations following the perturbation shown as lines.

2.6.2 Amphibole Chemometry

Ridolfi and Renzulli (2012) also present equations to calculate the contents of SiO_2, TiO_2, Al_2O_3, FeO_t, MgO, CaO, and K_2O in the melt from which amphiboles crystallized. These equations are parameterized in terms of amphibole composition and pressure. However, given the uncertainties discussed above calculating pressures from amphibole compositions, these P-sensitive parameterizations can be problematic to implement in natural systems. Erdmann et al. (2014) show that the predicted SiO_2 content is a reasonable match above 65 wt% SiO_2, but tends to overpredict SiO_2 for more mafic melts. Putirka (2016) use their newly compiled dataset to produce an updated expression (Eq10) for melt SiO_2 from the amphibole using the temperature of the melt and the cation fraction of Al in the amphibole.

Zhang et al. (2017) compile a reasonably similar calibration dataset to Putirka (2016), and produce multiple regressions to calculate melt oxide components from a variety of amphibole site positions (e.g., Si-Ti-Mg-Fe-Ca in amphibole for predicting SiO_2 in the melt). These expressions are P-independent, and only Eq3 (for SiO_2) and Eq5 (for TiO_2) are T-sensitive. Zhang et al. (2017) calibrate multiple equations for some melt oxide contents (e.g., 4 equations for SiO_2, 2 equations for FeO_t). We test the 133 ArcLEPR amphiboles which pass the Zhang et al. (2017) equilibrium filter ($K_{D,\ Fe\text{-}Mg}$=0.28±0.11) and do not appear in their calibration dataset. The calculated statistics are similar if a K_D filter isn't used. Overall, unlike many of the barometers discussed in this review, these chemometers perform well for experiments they were not calibrated on (Fig. 15). Eq2 of Zhang et al. (2017) does a good job of predicting melt SiO_2 content across a wide range, showing much better performance than Eq10 of Putirka, 2016 (Fig. 15a vs. b). The statistics of the fit are similarly good for melt Al_2O_3 (Eq14). There is more scatter for other oxides, and reasonably large differences between the different provided equations, but it is not always clear which equation is better (e.g., Fig. 15c). It is notable that the worst performance is seen for experiments with oxide contents towards the tail end of the calibration dataset (grey histograms, Fig. 15). For example, Eq12 and Eq13 do a good job of predicting K_2O until ~3.5 wt% K_2O; very few experiments in the calibration dataset had such high K_2O contents (Fig. 15g). Similarly, the fit is better at lower MgO contents, where the calibration dataset is concentrated (Fig. 15e). In general, our tests demonstrate that amphibole compositions can be used to estimate the melt compositions from which they grew, as long as the results are carefully evaluated relative to the calibration range of the model.

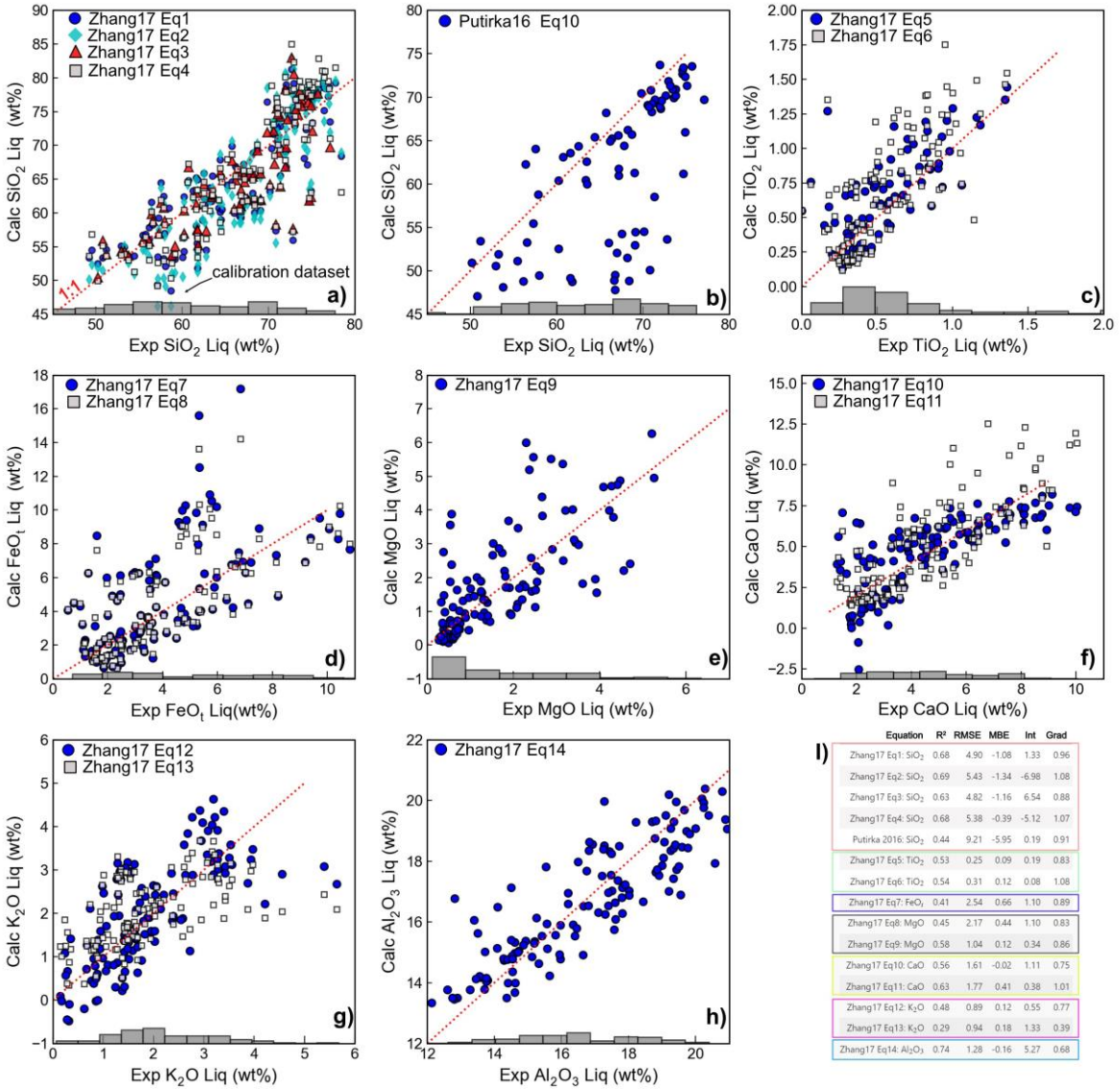

Figure 15 – Assessment of amphibole chemometers of Zhang et al. (2017, panel a, c-h) and Putirka (2016, panel b). For equation 3 and 5 of Zhang et al. (2017) and Putirka (2016) eq10, we use temperatures calculated from co-solving T from Ridolfi and Renzulli (2012) and P from Ridolfi (2021). Putirka (2016) eq10 also requires P from Ridolfi (2021) to be input. These equations have fewer datapoints on the plot, as we exclude P and Ts where Ridolfi (2021) returns an input warning. i) shows the statistics for each equation. The filtered test dataset comprises 133 experimental charges not used by Zhang et al. (2017) during calibration, and 10 experimental charges from Barclay (2004), Blatter and Carmichael (2001), and Grove et al. (1997), which were used by Zhang et al. (2017) in their test, but not calibration dataset.

We do not test predictions of H_2O and fO_2 using amphibole-only chemometers, as there are limited reliable experimental data with well constrained values for these parameters that were not used during model calibration.

2.7. Olivine-Spinel Aluminium-exchange thermometry

The aluminium content of olivine has been used as a thermometer in the mantle (De Hoog et al., 2010), and Al partitioning between olivine and spinel has been used in igneous rocks (Wan et al., 2008; Coogan et al., 2014). Here we focus on the olivine-spinel Al-exchange thermometer, which offers an advantage over Mg-Fe olivine-liquid thermometry because Al in spinel and olivine and Cr in spinel are more resistant to diffusional modification during crystal storage and transport than Fe-Mg in olivine (Spandler & O'Neill, 2009). Additionally, while olivine crystals are frequently out of equilibrium with erupted liquids (Sides et al., 2014b; Wieser et al., 2019), the fact spinels are trapped inside olivine crystals makes it more straightforward to identify mineral-mineral pairs which grew together.

The mechanism by which aluminium substitutes into olivine remains somewhat uncertain, despite the fact that constraining this reaction is vital to identify which chemical parameters should appear in a thermodynamically-constrained thermometry model. Of the possible substitutions, two mechanisms have been the focus of the most attention:

$MgAl_2O_4^{spinel} \rightarrow (Mg, Al)AlO_4^{olivine}$ (mechanism 1)

$MgAl_2O_4^{spinel} + 2\ SiO_2 \rightarrow (MgAl_2V)Si_2O_8^{olivine}$ (mechanism 2)

In the first mechanism there is a coupled substitution of Al into both the octahedral and tetrahedral sites in olivine, while the second has substitution only onto the octahedral site, with charge balance maintained by vacancies (V). It is also possible coupled substitutions could take place with Cr and Na in the octahedral site (and Al in the tetrahedral site), or Al in the octahedral site with Fe^{+3} in the tetrahedral site (Taura et al., 1998). Critically, if the mechanism 1 is dominant, the thermometer should depend only on the Al contents of the co-existing olivine and spinel (in addition to any chemical parameters controlling the activity coefficient for Al in either phase), but if mechanism 2 dominates, the thermometer will depend also on the activity of SiO_2 (a_{SiO_2}).

A thermometer based on Al-exchange was first calibrated by Wan et al. (2008) using a series of experiments at 1 bar with the bulk composition varied such that olivine and spinel co-crystallised at a range of temperatures and Cr contents. They found that the experimental data could be adequately modelled with a formula depending on the ratio of Al in olivine to Al in spinel, as well as the spinel Cr# (Cr/[Cr + Al], molar). The dependency on Cr# comes from its effect on the activity coefficient of Al in spinel. Wan et al. (2008) justified the extrapolation of the thermometer to higher P and T than the calibration dataset by comparing temperatures derived from the Al-exchange thermometer with temperatures calculated from the two-pyroxene thermometer for a suite of olivine and spinel bearing mantle xenoliths. Although there was considerable scatter around the 1:1 line (1σ = 64˚C) they found no systematic offset between the two thermometers. The behaviour of the thermometer at 1 bar was tested with an additional set of experiments, for which experimental temperatures were reproduced with 1σ=22˚C.

The thermometer was further tested and recalibrated with new experimental data by Coogan et al. (2014), extending the calibration range to higher fO_2 values (ΔQFM=-0.5 to ΔQFM = +1.3). They also tested the thermometer's dependence on a_{SiO_2}. They found fO_2 had no systematic effect on the performance of the thermometer and the effect of a_{SiO_2} was within the uncertainty of the thermometer, indicating that Al incorporation into olivine by vacancy formation (mechanism 2) is unlikely to be important in most systems. This was corroborated by an experimental diffusion study by Zhukova et al. (2017) which found that Al incorporation by vacancy formation was favoured only at higher a_{SiO_2} values than is found in most igneous systems where the thermometer is applied. Further improvements have been made to both the calibration and the mathematical formulation of the thermometer by Zhang and Namur (2022).

Despite the increased calibration range of the Coogan et al. (2014) model, many natural samples possess olivine and spinel pairs with compositions which still lie outside the calibration range. This includes the study reporting the highest equilibration temperatures from this method (~1570°C, Trela et al., 2017), which have spinels with Cr_2O_3 contents higher than any of the spinel crystals used to calibrate the thermometer. Trela et al. justified such an extrapolation based on the global correlation between the Al_2O_3 K_D and spinel Cr#, and the fact that these melts also recorded extreme mantle potential temperatures and olivine liquidus Ts. However, it has also been suggested in other locations that application of this method to spinel crystals with much higher TiO_2 contents than the calibration dataset may be invalid, because these higher TiO_2 may affect the activity coefficient of Al in spinel (e.g., Jennings et al., 2019; Wong et al., 2022). Jennings et al. (2019) suggest that in the absence of a wider calibration range, it is best to apply the thermometer only to spinel crystals that are close to the calibration range.

To robustly assess how effectively the olivine-spinel method can be extrapolated, we need a suite of experiments with compositions lying outside the current calibration range. However, because application of the thermometer relies on precise measurements of the low concentrations of Al_2O_3 in olivine, generally only experiments performed for the purpose of calibrating this thermometer can be used, and all such experiments have been used during model regression (by Wan et al. 2009, or Coogan et al. 2014). Experiments conducted for other purposes cannot be used to formulate a test dataset, because Al_2O_3 concentrations in olivine were generally not measured at all, or were measured with low precision.

The lack of an independent test dataset also makes it difficult to robustly constrain the uncertainty of this method even when applied within the calibration range. Most studies cite the quoted standard error on the fit for the calibration data as being a minimum estimate of the uncertainty (Matthews et al., 2021, 2016; Wong et al., 2022), but as discussed above, statistics calculated on calibration datasets tend not to reflect the true error when applied to data not used for calibration. A final problem with this method is that there is no independent equilibrium test to assess whether the spinel and olivine are in equilibrium. The ubiquity of Mg-Fe diffusive resetting means these elements are an unreliable test of equilibrium (c.f. Prissel et al., 2016). The slow diffusion of Al in olivine (Spandler & O'Neill, 2009) means that parts of a host olivine crystal could be out of equilibrium with their spinel inclusions if olivine crystallisation occurred over a protracted time with changing temperature (or melt composition). Maps of the aluminium content of olivine crystals have revealed near-ubiquitous zoning in crystals from Iceland (Matthews et al., 2021), adding complexity to identifying equilibrium pairs. Matthews et al. (2021) and Trela et al. (2017) therefore recommended the aluminium content of olivine crystals should be mapped with a high current electron beam before identifying locations for quantitative analysis.

2.8. Plagioclase-Liquid thermometry and hygrometry

Plagioclase (Plag) is a very common mineral in a wide variety of tectonic settings (e.g., MORBs, OIBs, Arcs), motivating the development of a number of thermometers, barometers and hygrometers parameterizing and liquid equilibrium (Putirka, 2008, 2005; Sugawara, 2001; Waters and Lange, 2015). However, the exchange of the anorthite (An)-albite (Ab) component between liquid and Plag is sensitive to T, P, and H_2O. If none of these variables are constrained by independent methods, there is a substantial solution space to explore. There also isn't much consensus as to what equilibrium tests should be used to filter Plag-Liq pairs. Putirka (2008) note that Ab-An exchange values for experiments (K_D^{An-Ab}) are normally distributed, with experiments with T<1050°C having values of 0.1±0.05, and experiments with T>1050°C having values of 0.27±0.1. However, plotting our experimental data (along with the calibration dataset of Waters and Lange, 2015) shows a more continuous variation of K_D with temperature (Supporting Fig. 9) although there is a relatively abrupt step up to higher values between 1000–1100°C. We tentatively suggest this step up may result from the C1–I1 structural phase transition which occurs near this temperature, and has been shown to affect plagioclase Mg partitioning behaviour (Mutch et al., 2022). Using the criteria of Putirka (2008) would exclude a number of experiments close to the cut off (Supporting Fig. 9)– We instead apply an exponential fit through the experimental data, excluding experiments outside ±0.11 (Supporting Fig. 9a-b). Not applying this filter affects calculated statistics very little for the following discussion.

First, we assess sensitivity of thermometers to H_2O (Fig. 16a), thermometers to P (Fig. 16b), hygrometers to T (Fig. 16c), and hygrometers to P (Fig. 16d), by independently perturbing experimental P, T and H_2O. It is apparent from Fig. 16a that Plag-Liq temperatures are strongly sensitive to H_2O; an increase of just 1 wt% H_2O causes an average drop in T of ~31°C for eq24a and 36°C for eq23. This change in calculated T is comparable to the RMSE of these thermometers. Thermometers are less sensitive to P; with the calculated change in T only reaching the same magnitude as the RMSE for a change of ~10 kbar (Fig. 16b). Notably, the Plag-Liq hygrometers of Masotta and Mollo (2019), Putirka (2008) and Waters and Lange (2015) are extremely sensitive to T; calculated H_2O contents drop more than the RMSE of the hygrometer for a change in T of just 10–20°C (Fig. 16c). These hygrometers are less sensitive to P, with P changes of 10 kbar causing variations well within the quoted RMSE (Fig. 16d).

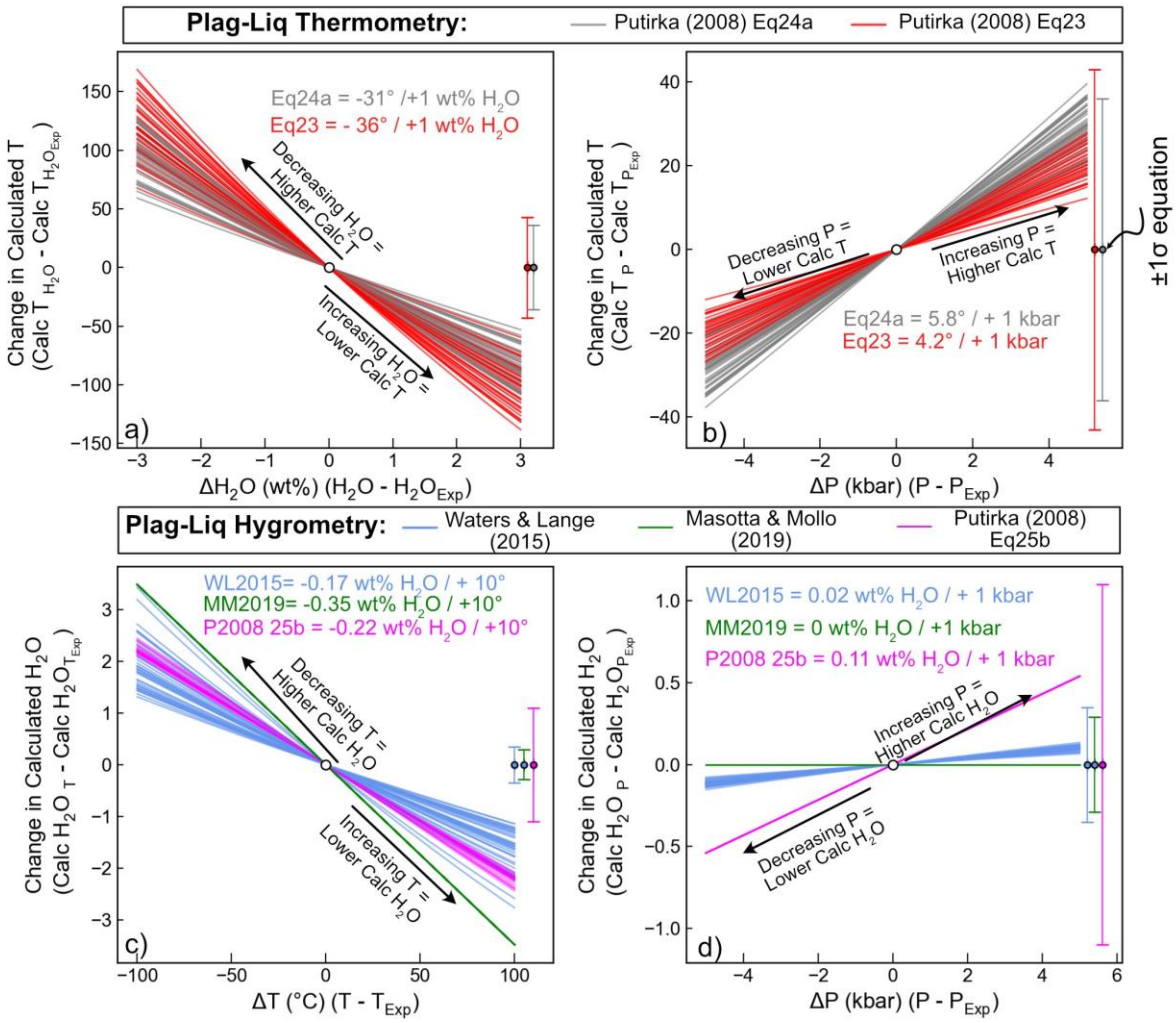

Figure 16: Testing the sensitivity of Plag-Liq thermometers to H_2O (a) and pressure (b), and Plag-Liq hygrometers to T (c) and P (d). 40 experiments from our new compilation were randomly selected (each represented by a colored line). We perform calculations at the experimental P, T and H_2O content (0,0) on all plots, and then vary H2O by ± 3 wt% (a), P by ± 5kbar (b, d), and T by ± 100 °C (c). We subtract the quantity calculated at experimental conditions from the quantity at these new conditions. Error bars show the quoted RMSE on each expression. We label the average perturbation for these 40 samples on the figure.

Before assessing hygrometers using our new dataset, it is worth considering how well we really know the "true" value of H_2O in each experiment. In the compiled Plag-Liq dataset, only 33% of experiments measure H_2O by FTIR, 5% by SIMS and 4.8% by Raman spectroscopy. A further 16% report H_2O using the EPMA-based water-by-difference method, with some mention of a calibration method. 17% have calculated H_2O using a solubility model for a pure H_2O fluid or using a measured X_{H2O} value in the fluid (Andújar et al., 2015; Costa, 2004; Mandler et al., 2014), or provide enough information for us to perform these calculations using MagmaSat in VESIcal (Ghiorso and Gualda, 2015, Iacovino et al. 2019). Interestingly, Waters and Lange (2015) calibrate their hygrometer by calculating H_2O in each experiment in their calibration dataset using the solubility model of Zhang et al. (2007), rather than using measured H_2O contents. If they had they used MagmaSat instead, calculated H_2O contents for these experiments would differ by an average of 0.3 wt% (the max discrepancy is 0.78 wt%), which would likely result in slightly different model parameters. Additionally, if the starting materials contained even small amounts of CO_2 (e.g., from contamination, Blatter et al., 2013), the amount of H_2O in the melt would not equal that calculated using a pure H_2O solubility model.

Ideally, we would restrict our comparison to experiments which performed FTIR, SIMS or Raman measurements of H_2O. However, this results in a much smaller dataset, with N=163 vs. N=358 if calibrated VBD

and solubility water contents are included. This smaller dataset also has a very restricted T range (Supporting Fig. 10). It also seems unjustified to exclude experiments using solubility models, given that is how the H_2O contents were determined to calibrate the Waters and Lange (2015) model. Thus, we choose to proceed with the larger experimental dataset.

Using experimental T and P, the Waters and Lange hygrometer performs reasonably well on the ArcPL dataset, with a RMSE of ±1.21 wt% (Fig. 16a). There is a marked deviation to anomalously low calculated H_2O contents for experiments with H_2O>7 wt% (cyan squares); if these are excluded, the RMSE is 0.94 wt%, although this is still far higher than the quoted RMSE of 0.35 wt%. The poor performance at high H_2O may reflect the fact that these super-hydrous compositions are poorly represented in the calibration dataset of this hygrometer (white histogram, Fig. 16a-b). When using experimental H_2O contents and pressures, the statistics reported for the thermometer of P2008 Eq24a on a global dataset are very similar to those estimated from our new dataset (we calculate RMSE=33°C vs. the stated RMSE=36°C shown as red dotted lines, Fig. 16c).

As discussed in section 1.2, the extreme sensitivity of Plag-Liq thermometers to H_2O content, and hygrometers to T, means that the comparisons shown in Fig. 16a and c do not accurately represent the true error when these equations are applied to natural systems, where in the vast majority of instances, neither H_2O nor T is known. To address this issue with many under constrained intensive variables, we investigate whether H_2O and T can be solved iteratively using a plagioclase hygrometer and thermometer, as an adaptation of the popular workflow of iterating barometers and thermometers. Arguably, as we perform these calculations using experimental P, we are still overestimating their performance on natural systems where H_2O, T and P are all unknown. The absence of a reliable plagioclase-liquid barometer (see Section 2.9) means that three-way iteration will not work. However, given these equations are far less sensitive to pressure (Fig. 16), uncertainty in pressure shouldn't hinder the model performance substantially.

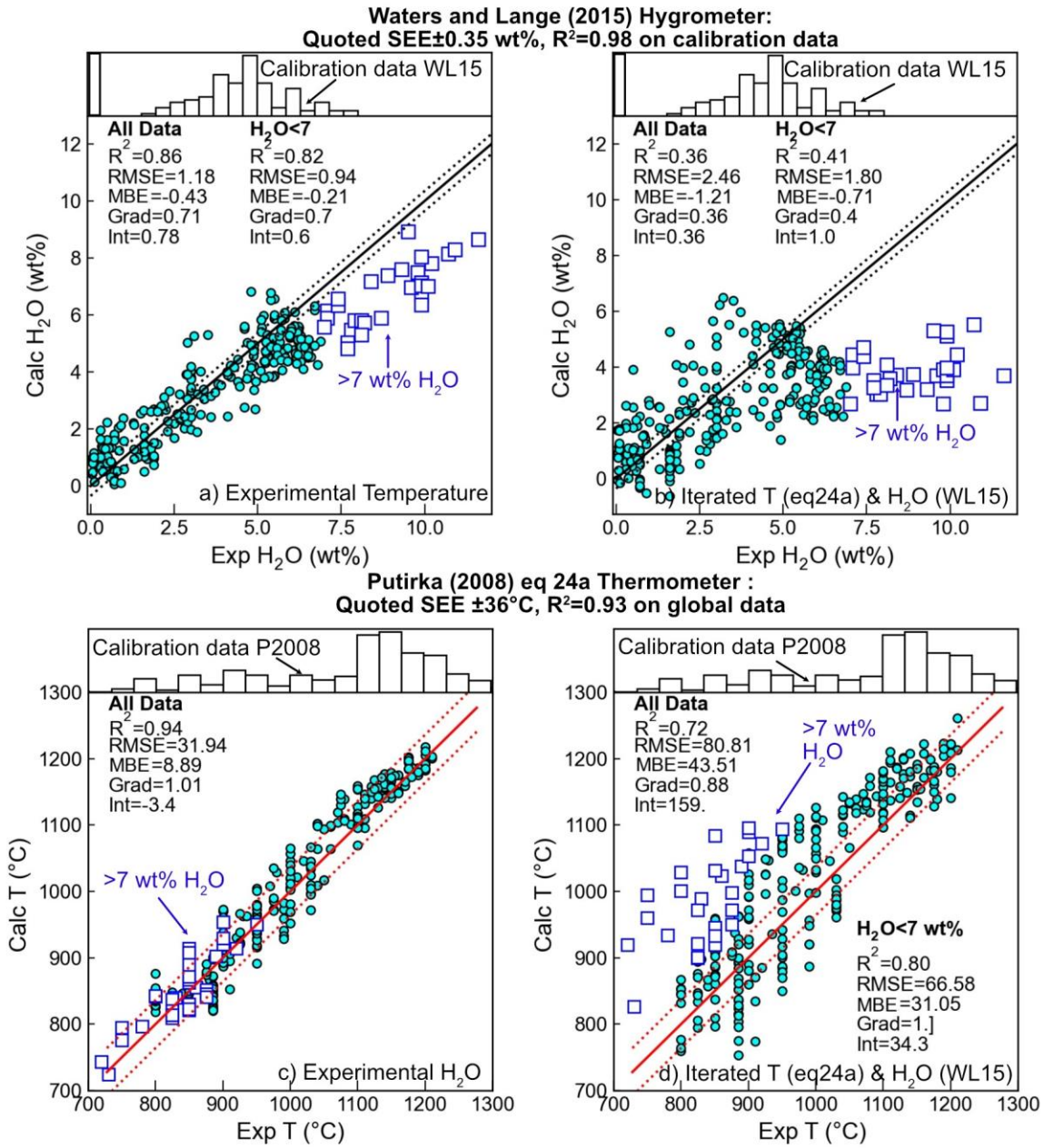

Figure 16. Evaluating Plag-Liquid hygrometers (a-b) and thermometers (c-d). Only experiments with H_2O measured by quantitative methods are shown. a) Calculations of H_2O using Waters and Lange (2015) with calculations performed using experimental T. The hygrometers performance drops substantially for H_2O>7; the white histogram on top indicates that relatively few experiments used to calibrate this model had such high H_2O contents. b) Iterative calculations using Waters and Lange (2015) and Putirka (2008) eq24a. c) Calculations using Putirka (2008) eq24a and experimental H_2O contents, and d) Iterative calculations using Putirka (2008) eq24a and Waters and Lange (2015). 1:1 line shown with ±stated RMSE for each expression

Unsurprisingly, iteration of Plag-Liq hygrometers and thermometers yields worse statistics than hygrometry calculations performed using experimental T. For example, excluding experiments with H_2O>7 wt%, the iterated RMSE is 1.77 wt% (vs. 0.94 wt% using experimental T; Fig 16a vs. b). Calculated T using the iterative method are also substantially worse than those obtained using known H_2O contents (RMSE=66 vs. 33°C for all data, RMSE=58°C for H_2O<7 wt%, Fig. 17c-d). The statistics for these iterative calculations are more indicative of the sort of precision these methods can achieve in natural system. We also suggest that such an iterative approach may be more accurate than calculating H_2O using temperatures derived from other phases which may not have formed at the same temperature as Plag (e.g., Fe-Ti thermometry, Black and Andrews, 2020; Crabtree and Lange, 2011; Pineda et al., 2021).

The iterated thermometer has reasonable performance compared to other mineral-melt thermometers discussed, and the hygrometer has sufficient precision to distinguish dry (0–2 wt%), moderately wet (2–4 wt%) and wet (>4 wt%) lavas. However, when applied outside of the experimental products used for calibration, Plag-Liq hygrometry cannot achieve anything like the <<0.5 wt% error often quoted for this method. Future improvements would be possible with a larger dataset of experiments where H_2O contents are known, as combining different methods for estimating H_2O contents in experiments undoubtedly adds uncertainty, particularly when using volatile contents calculated using volatile solubility models (see Wieser et al., 2022a). Additionally, given the relative success of iterating two different expressions with different underlying datasets, we suggest that recalibrating Plag-Liq hygrometers without a T term, but with compositional terms like those in Plag-Liq thermometers to incorporate the effect of temperature, may be more successful than having to iterate two independently calibrated expressions.

2.9. Plagioclase-Liquid barometry

Putirka (2005) proposed a Plag-Liq barometer calibrated on 187 Plag-Liq pairs, which yields a RMSE of 1.8 kbar for the calibration dataset and RMSE of 2.2 kbar on N=292 test data. However, Putirka (2008) re-evaluated this barometer using new experimental data, and found that it performed very badly, with a RMSE of 3.8 kbar excluding 1 atm data, and even worse statistics when this 1atm data was included. They tried to find a global model to adequately predict pressures in their new dataset and found that while some regression worked on some subsets of the database, no regression could fit all data. They suggested that new experiments with the specific purpose of developing a Plag-Liq barometer are required to move forward. Despite their warning that *"the status of plagioclase-liquid as a barometer is firmly in doubt"*, a concerningly large number of studies have performed Plag-Liq barometry after 2008 (e.g., Budd et al., 2016; Cheng et al., 2014; Dahren et al., 2012; Geiger et al., 2018, 2016a, 2016b; Guo et al., 2018; Jamshidi et al., 2015; Siegburg et al., 2018). The majority of these studies quote a 2.47 kbar RMSE to justify this approach. However, this value from Putirka (2008) was only the fit to under half the data; the full dataset gave RMSE= 3.6–3.8 kbar.

As Plag-Liq barometers are still being widely used in the community, we briefly assess their sensitivity to T and H_2O, and then evaluate their performance on our new dataset. The T term in P2008 Eq25b means that the barometer is reasonably sensitive to T, with an average increase in +0.25 kbar per +10°C increase in T (Fig. 18a). The barometer alone isn't sensitive to H_2O. However, this barometer is normally used in natural systems through iteration with the Eq24a thermometer, which is H_2O-sensitive (Fig. 18b). When iterated, the barometer is very H_2O-sensitive; an increase in H_2O by 1 wt% causes the P to drop by an average of ~1 kbar (Fig. 18c).

We assess barometry performance on our test dataset, filtering out pairs which fail the anorthite-albite (An-Ab) equilibrium test provided in the supporting spreadsheet of Putirka (2008). Using experimental T, the barometer performs extremely poorly (RMSE=3.8 kbar, R^2 of 0, Fig. 18d). When P and T are iterated, the performance is even worse (RMSE=4.0 kbar, Fig. 18e). It is notable that in Fig. 18d-e that experiments performed at 2 kbar yield P>10 kbar, while experiments performed at 10 kbar yield P<0 kbar. To put the performance of these barometers into perspective, we compare each experimental P to a random experimental pressure drawn without replacement from the experimental dataset (Fig. 18f). The RMSE for this randomly selected number is almost identical to that of the iterated barometer. Thus, until new experiments are done to specifically investigate the Plag-Liq barometer, this method is only as reliable as researchers using a random number generator spanning the crustal thickness in their location of interest than Plag-Liq barometry to estimate magma storage pressures!

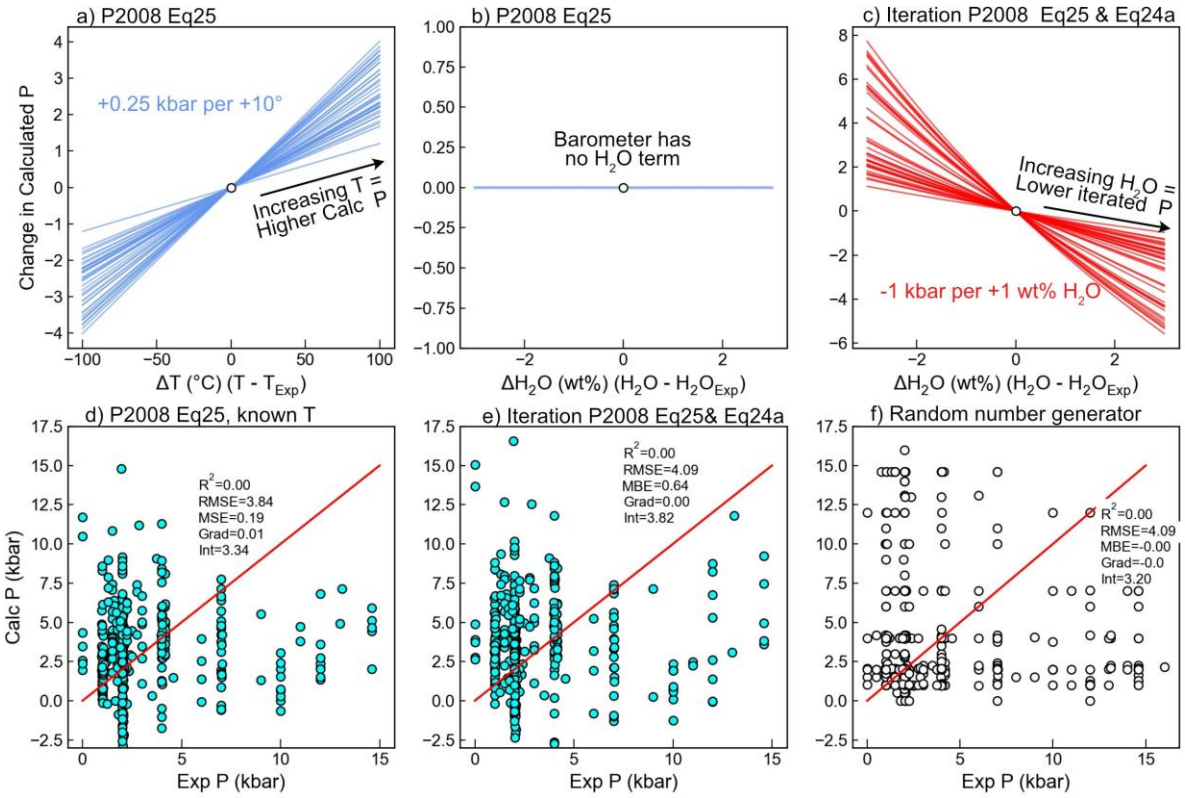

Figure 18. Assessment of the Plag-Liq barometer of Putirka (2008) Eq25. a-b) Assessing sensitivity of the barometer to T and H_2O for a subset of experiments. c) Testing the sensitivity of the iterative combination of Eq25 (P) and Eq24a (T) to melt H_2O content. d) Testing the barometer using experimental T and H_2O contents, after applying the An-Ab equilibrium test of Putirka (2008). e) As for panel d, but solving P and T iteratively (still using experimental H_2O). f) Assessing the performance of a randomly selecting a P value from the experimental dataset.

2.10. Fe-Ti oxides

The partitioning of Fe and Ti between cubic and rhombohedral oxides has been employed in estimating magmatic T and fO_2. The Fe-Ti geothermobarometer is advantageous owing to the rapid cation exchange between the oxides, allowing equilibrium to be restored quickly following a change in magmatic conditions (days to weeks; Venezky and Rutherford, 1999). The exchange is described by the following reaction:

$$\underset{\text{Ilmenite (rhombohed.)}}{FeTiO_3} + \underset{\text{Magnetite (cubic)}}{Fe_3O_4} = \underset{\text{Ulvöspinel (cubic)}}{Fe_2TiO_4} + \underset{\text{Hematite (rhombohed.)'}}{Fe_2O_3}$$

where there is solid solution between ilmenite and hematite (the rhombohedral oxides), and magnetite and ulvöspinel (spinel series, or cubic oxides). The dependence on oxygen fugacity is described by the redox reaction:

$$\underset{\text{Magnetite (cubic)}}{4Fe_3O_4} + O_2 = \underset{\text{Hematite (rhombohed.)}}{6Fe_2O_3}.$$

The main challenge in calibrating a Fe-Ti geothermobarometer comes from the extremely complex solid solution of the rhombohedral oxides. Naturally occurring rhombohedral oxides incorporate significant quantities of MgO, MnO, and Al_2O_3 in addition to FeO, Fe_2O_3, and TiO_2, and have complex cation ordering transitions at lower temperatures, in addition to magnetic ordering. This means that complex expressions are required to accurately represent endmember activities, and multiple miscibility gaps exist. This complexity prevents simple empirical calibration of a geothermobarometer expression, and instead requires numerical solutions of expressions derived from a complex thermodynamic formulation.

The first implementation of the Fe-Ti geothermobarometer was made by Buddington and Lindsley (1964), and improved by a number of subsequent studies as further experimental data became available (e.g., Andersen and Lindsley, 1988; Spencer and Lindsley, 1981). The most recent update of the geothermobarometer was provided by Ghiorso and Evans (2008), building on the older thermodynamic model of Ghiorso and Sack (1991) using a calibration dataset with 5X more experiments (N=267 vs. N=57) and much better experimental

constraints on cation ordering. In particular, the calibration range was extended to significantly higher T and fO_2, where previous versions of the model extrapolated poorly. Each update to the thermometer represents increasing sophistication of the underlying thermodynamic model, and therefore more complex numerical techniques to apply them as a geothermobarometer. An open-source implementation of the geothermobarometer was provided by Ghiorso and Prissel (2020) through the ENKI portal.

Blundy and Cashman (2008) use an independent set of experiments to estimate the uncertainty on several versions of the Fe-Ti geothermobarometer, finding one sigma uncertainties of 44˚C and 0.2 5–0.34 log units fO_2 for the Ghiorso and Evans (2008) model, but no systematic deviation at high or low temperatures. However, it is likely that the uncertainty will vary across composition space, as the sensitivity of the thermometer depends on the composition of the Fe-Ti oxides, with the best sensitivity below the NNO buffer and away from the miscibility gap (Ghiorso and Evans, 2008).

2.11. Ti in Quartz (TitaniQ) thermometer

In silicic rocks where quartz is a dominant phenocryst (e.g., granites and rhyolites), there are far fewer available thermometers relative to more mafic systems. To address this, Wark and Watson (2006) perform experiments containing quartz and rutile at 600–1000˚C at 10 kbar to produce an empirical relationship relating the Ti content of quartz to the temperature. They state that this thermometer has an uncertainty of ±2˚C at >500 ˚C using SIMS measurements of Ti, and that this thermometer can also be applied to systems without rutile if an independent estimate of Ti activity is obtained (e.g., from Fe-Ti equilibrium). This thermometer was recalibrated by Kawasaki and Osanai (2008) using natural metamorphic rocks in ultrahigh temperature granulites and Thomas et al. (2010), who perform additional experiments between 5–20 kbar, generating an expression incorporating a term for pressure.

Importantly, Thomas et al. (2010) implied that if temperature was known independently, the equation could be inverted to solve for pressure. Wilson et al. (2012) test this inversion method on samples from the Oruanui eruption, which has been well studied, so has independent estimates of pressure from melt inclusions, and temperature and Ti activity from Fe-Ti oxides. They show that using Fe-Ti oxides to constrain temperature and Ti activity, calculated pressures from Ti in quartz are 3–10X higher than those inferred from melt inclusion saturation pressures. Similarly, if melt inclusion and Fe-Ti oxide temperatures and pressures are used, inferred Ti activity is far too low. If pressures are used from melt inclusions and Ti activity from Fe-Ti oxide, temperatures are well below the H_2O-saturated solidus for granite. Similar discrepancies with previously published pressures, temperatures and Ti activities are present for calculations on the Bishop tuff. Wilson et al. (2012) suggest that Ti activities may be highly variable in igneous systems, so activities from Fe-Ti oxides cannot be reliably used with TitaniQ. Additionally, they suggest Ti in Qtz records complex histories that cannot be simply related to changes in pressure and temperature over other variables, such as quartz growth conditions or melt composition. For example, Huang and Audétat (2012) show that Ti concentrations in Qtz depend on the crystal growth rate, so this thermobarometer should not be applied to hydrothermal fluids where growth rates are fast and highly variable.

Thomas and Watson (2012) partially rebut Wilson et al. (2012), in particular critiquing the validity of their calculations of Ti activity (e.g., Ghiorso and Gualda, 2013) and temperature estimates from Fe-Ti oxides (Ghiorso and Evans, 2008) in the Oruanui rhyolites that underly a lot of the arguments of Wilson et al. (2012). Instead, Thomas and Watson (2012) use MELTS to estimate temperature and Ti activity based on the affinity for rutile saturation from inputted melt compositions, yielding pressures similar to melt inclusions. They admit that the approach of Wark and Watson (2006) was oversimplified in its suggestion of using a fixed value of Ti activity. An excellent discussion of this Bishop Tuff controversy can be found in Putirka (2017), along with adjustment of published coefficients for different equations.

Acosta et al. (2020) identified that Ti in Qtz temperatures are offset ~100–150˚C to lower temperatures than other thermometers in silicic systems, particularly at <4 kbar. To address the source of these offsets, they perform hydrothermal quartz growth experiments at 800 ˚C and 1 kbar with different fluid compositions. They find that Ti in Qtz is sensitive to the Ti/Si ratio of the fluid, rather than the concentration or activity of Ti. Clearly, significantly more experimental work is needed to determine magma storage conditions precisely and accurately in silicic systems from Ti in Qtz.

3. Melt inclusion barometry

Melt inclusions (MIs) are small pockets of melt trapped during crystal growth, which become isolated from the external melt as the surrounding crystalline host fully encloses them. MI which were trapped from a volatile-saturated magma can be used to deduce magma storage depths because the solubility of CO_2 and H_2O

in silicate melts is a strong function of pressure (Dixon, 1997; Goranson, 1931). If MI were trapped from a volatile-undersaturated magma, calculated pressures are minimum estimates (Hauri et al., 2018; Matthews et al., 2016).

Numerous recent reviews have detailed the theory, methods and advances relating to melt inclusion analysis and interpretation, as well as several specific problems associated with determination of magma storage depths from these archives. For example, Wallace et al. (2021) present a comprehensive review of olivine-hosted melt inclusions, describing melt inclusion formation, post-entrapment crystallization, and the wealth of information recorded by melt inclusions (e.g., trace element contents for tracking magma batches, processes controlling magmatic H_2O contents, calculating ascent rates, and storage pressures). Rose-Koga et al. (2021) provide a number of guidelines involving sample preparation, analysis and data reporting associated with melt inclusion analysis and interpretation. Barth and Plank (2021) discuss the processes which can alter H_2O contents in melt inclusions after their entrapment, producing regime diagrams describing how melt inclusions can act as hygrometers and barometers (revealing pre-eruptive H_2O contents), or speedometers (revealing ascent rates using H^+ diffusion). Wieser et al. (2022a) provide a detailed history of different solubility models used to calculate melt inclusion saturation pressures and highlight the large discrepancies between different models. In particular, they emphasize the importance of carefully examining the calibration range of each solubility model compared to the P-T-X range of melt inclusions from a given volcano. To avoid repetition, we refer readers to these papers, and focus our discussion on issues involving magma storage depth determinations from melt inclusions which have not yet been reviewed in detail. We specifically focus on the growing realization that the CO_2 contents of melt inclusions have been significantly underestimated, because of the presence of a substantial CO_2 within vapour bubbles that were not measured in most published studies.

3.1 Vapour bubble growth systematics

The vast majority of studies have used olivine-hosted melt inclusions to determine magma storage depths (e.g., Aster et al., 2016; Moore et al., 2015; Ruscitto et al., 2010; Sides et al., 2014; Wallace et al., 2021). This focus on olivine may reflect the fact that it is one of the first crystallizing phases (important for studies focusing on the most primitive melt compositions), it is relatively abundant, and tends to have melt inclusions which are larger than those in other phases from the same sample suite (Bennett et al., 2019, Wieser et al. 2022c). It has also been suggested that the absence of cleavage in olivine makes leakage less likely than in say pyroxene, which has a strong cleavage (Kress and Ghiorso, 2004). Finally, the simple chemistry of olivine, well-constrained $K_{D,Fe\text{-}Mg,}$ and low partition coefficients for REE and other trace elements of geological interest means that correcting melt inclusions for post-entrapment crystallization (PEC) is more straightforward than in plagioclase and pyroxene (Danyushevsky and Plechov, 2011; Kress and Ghiorso, 2004; Neave et al., 2017; Wieser et al., 2022c).

However, as a consequence of the fact that olivine is often the first phase to crystallize in a magma, there is significant potential for melt inclusions to experience substantial amounts of cooling prior to eruption (e.g., ~150–170˚C in high forsterite olivines from the 2018 eruption of Kīlauea, Lerner et al., 2021; Wieser et al., 2021). This results in a large amount of PEC. Crystallization of denser olivine from less dense silicate melt, combined with differential contraction of the melt and host during cooling, causes the pressure in the inclusion to drop, driving the growth of a vapour bubble (often termed a shrinkage bubble, Kress and Ghiorso, 2004; Steele-Macinnis et al., 2011; Wallace et al., 2015). Because the solubility of CO_2 is strongly dependent on pressure, if there is sufficient time between bubble growth and syn-eruptive quenching, a significant proportion of the total CO_2 content of the melt inclusion will diffuse into the vapour bubble (Fig. 19, Maclennan, 2017, Wieser et al. 2021). Rapid diffusive re-equilibration of H_2O between the melt inclusion and a more H_2O-poor carrier melt as a result of fast H+ diffusion rates in olivine can also drive the growth of a vapour bubble (Aster et al., 2016; Gaetani et al., 2012).

3.2 Raman measurements of vapour bubbles

In situ Raman spectroscopic measurements of vapour bubbles over the last decade have demonstrated that a large and often dominant proportion of the total CO_2 content of melt inclusions is held within the bubble (Fig. 19, Allison et al., 2021; Aster et al., 2016; DeVitre et al., 2023a; Hanyu et al., 2020; Hernandez et al., 2018; Lerner et al., 2021; Moore et al., 2015, 2018, 2021; Wieser et al., 2021). To our knowledge, the first Raman analyses of a melt inclusion vapour bubble were made by Steele-Macinnis et al. (2011) in samples from Solchiaro Volcano, Italy. They found a distinctive signal consisting of two strong peaks which is indicative of the presence of a CO_2 fluid (Fig. 20b). This contradicted the dominant hypothesis at the time that these bubbles were vacuums or voids. In two almost concurrent papers, Hartley et al. (2014) and Moore et al. (2015) present Raman measurements in melt inclusion vapour bubbles from Laki, Kīlauea, Fuego and Seguam, demonstrating that 40

to >90% of the total CO_2 is held within the bubble. More recent work has found similar proportions spanning a range of tectonic settings (Fig. 19).

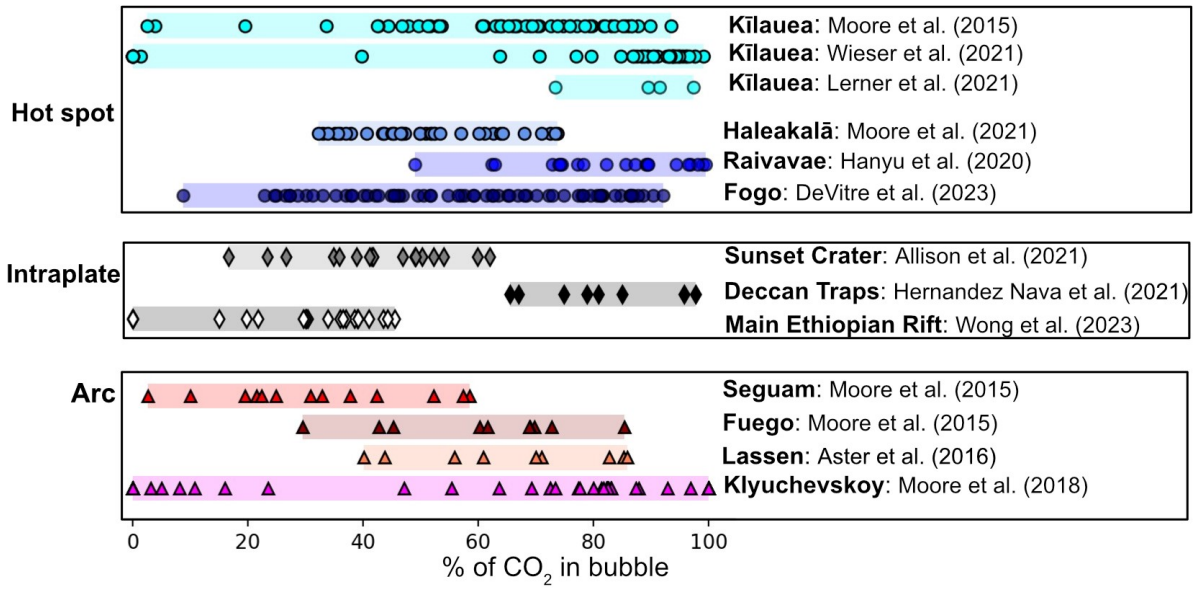

Figure 19 – Percent of the total melt inclusion CO_2 content held in the vapour bubbles from studies which have used an instrument-specific Raman calibration. Refs: Allison et al., 2021; Aster et al., 2016; DeVitre et al., 2023a; Hanyu et al., 2020; Hernandez Nava et al., 2021; A. H. Lerner et al., 2021; Moore et al., 2021, 2018, 2015; Wong et al., 2023.

Raman spectroscopic analyses of CO_2 in vapour bubbles rely on the strong correlation between the density of CO_2 and the distance between the two strong CO_2 spectral peaks collectively termed the Fermi diad. This distance is commonly called the splitting, diad splitting, or diad separation (Δ, Fig. 20b). However, the relationship between density and diad splitting has been shown to vary as a function of instrument hardware and acquisition parameters (Lamadrid et al., 2017, Fig. 20c). This means that the relationship between the diad splitting and CO_2 density must be determined for the acquisition parameters and specific data processing strategy used by each Raman laboratory. The absolute differences in CO_2 densities for a measured diad splitting on different Raman instruments are very large (Fig. 20c). For example, the vapour bubble shown in Fig. 20a yields a splitting of 103.10 cm^{-1} on the Cornell WITEC Alpha300R (Fig. 20b). Following the protocol of Lamadrid et al. (2017), this splitting is corrected based on the measured distance between two peaks from the atomic spectra of Ne to give a splitting of 103.197 cm^{-1}. Using the densimeter calibrated for this exact instrument, acquisition parameters and Ne correction regime (DeVitre et al. 2021), the density of this bubble is ρ=0.17 g/cm^3 (Fig. 20c). However, if the densimeter of Kawakami et al. (2003) was instead used, the calculated density would be nearly twice as high (ρ=0.29 g/cm^3, Fig. 20c).

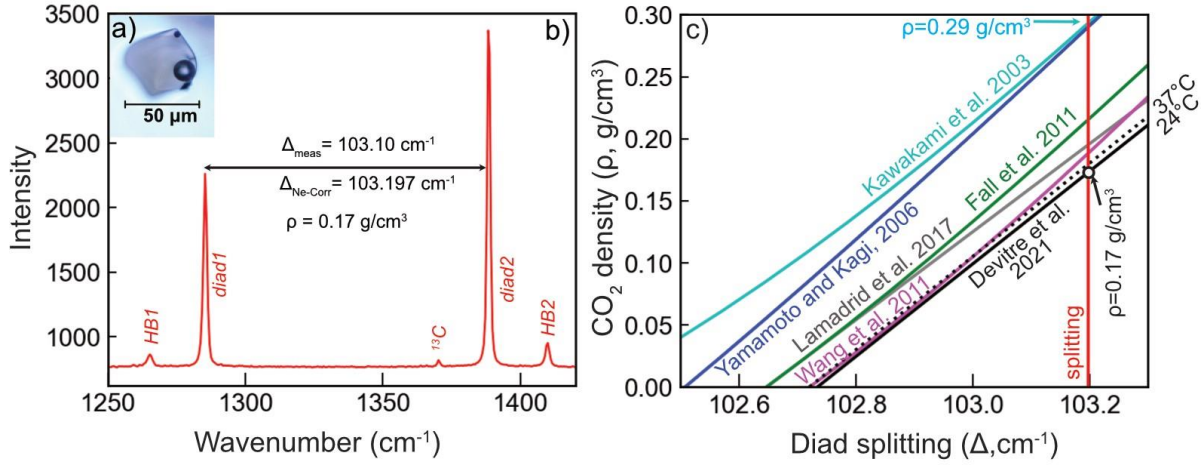

Figure 20 – Determining CO_2 density using Raman Spectroscopy. a) Image of an olivine-hosted melt inclusion from the Twin Lakes Crater, OR. b) Raman spectra showing the strong Fermi diad (peaks at ~1285 and 1388 cm^{-1}) with hot bands on either side. The distance between the peaks is the diad splitting (Δ=103.10 cm^{-1}). After

correction for the measured splitting of the Ne emission spectra (Lamadrid et al. 2017), this corresponds to a CO_2 density of 0.17 g/cm^3 using the splitting-density relationship developed on this specific instrument (DeVitre et al. 2021). c) The relationship between density and splitting is different on each Raman instrument (e.g., DeVitre et al., 2021; Fall et al., 2011; Kawakami et al., 2003; Lamadrid et al., 2017; Rosso and Bodnar, 1995; Wang et al., 2019; Yamamoto and Kagi, 2006). If the Kawakami et al. (2003) densimeter was used for this vapour bubble, it would give a density of 0.29 g/cm^3.

The most robust way to calibrate a specific Raman spectrometer for a given analytical protocol is to measure the diad splitting for ultra-pure CO_2 gas held at a variety of pressures (and thus densities). This is often achieved using a high-pressure optical cell (HPOC) or a fluid density calibration apparatus (FDCA). These apparatus feed pure CO_2 gas into a chamber where the pressure is tightly controlled, and ideally the temperature too. The measured P and T in the cell can be converted into a CO_2 density using the CO_2 equation of state (EOS, e.g., Span and Wagner, 1996). Raman measurements are made on this trapped fluid with known density, and the splitting is determined for each Raman acquisition. The relationship between the measured diad splitting and CO_2 density is often parameterized over a number of discrete density windows, as the shape of the curves vary (DeVitre et al., 2021).

Despite the importance of measuring CO_2 in melt inclusion vapour bubbles being recognised in ~2014–2015 (Hartley et al., 2014; Moore et al., 2015) and the calibration issue being highlighted in 2017 (Lamadrid et al., 2017), only published melt inclusion vapour bubble measurements made at Virginia Tech and Cornell have calibrated their Raman using a gas cell apparatus.

Only the Cornell calibration closely controls and measures the T of the CO_2 gas, which is required to convert pressure into density with high accuracy and precision (DeVitre et al., 2021). A few more laboratories have used lower cost methods, where samples with known CO_2 densities are measured in a manner analogous to primary standards for EPMA calibration. For example, Allison et al. (2021) developed a calibration line by measuring the splitting-density relationships for fused silica capillary capsules (FSCC). The CO_2 density in these capsules was calculated from the mass of loaded CO_2 and the volume of the capillary, which allowed the calibration line to be determined at low densities (FSCCs ranged from 0.008–0.133 g/cm^3). Wieser et al. (2021) calibrated their Raman at low densities using 19 synthetic fluid inclusions (SFI) in quartz standards (0.04–0.14 g/cm^3) which were measured on the calibrated Virginia Tech Raman, with the same calibration being used by Wong et al. (2023). Mironov et al. (2020) use a similar approach, developing a calibration line using 8 melt inclusion vapour bubbles measured at Virginia Tech with densities between 0.013–0.22 g/cm^3.

Other studies measuring vapour bubbles have converted measured diad splitting into densities using a published calibration line developed in a different laboratory (e.g., Bali et al., 2018; Hartley et al., 2014; Taracsák et al., 2019; Venugopal et al., 2020). The choice of densimeter in these studies varies widely, and the choice of one densimeter instead of another is not justified. For example, Hartley et al. (2014) using Kawakami et al. (2003, cyan line on Fig. 19c), Taracsák et al. (2019) and Venugopal et al. (2020) using Wang et al. (2011, salmon line), and Bali et al. (2018) and Robidoux et al. (2018) using Fall et al. (2011, green line). The offset of their densities from the true value is not known, although a correction could be applied retrospectively if samples with known CO_2 densities were analysed on the same instrument with the same analytical conditions.

Thermodynamic limits on the density of CO_2 at ambient conditions reveal a possible issue with the selection of a densimeter from the literature developed for a different instrument. The CO_2 phase diagram shows that at room T (20–26°C), the maximum possible density of CO_2 gas is ~0.2–0.26 g/cm^3 (Fig. 21a). A vapour bubble with a higher bulk density will consist of an inner sphere of CO_2 gas of ρ=0.2–0.26 g/cm^3, and a coexisting outer shell of CO_2 liquid with ρ>0.7 g/cm^3 (see inclusion at Temp b on Fig. 21a). It is not thermodynamically possible for densities between these values to be measured by Raman spectroscopy unless the sample is heated above the critical point of CO_2 at 31°C (supercritical CO_2 can have any density, Span and Wagner et al. 1996). While laser heating may occur during Raman analysis, which can account for the small number of measurements above 0.26 g/cm^3 on calibrated instruments (Fig. 21b, DeVitre et al., 2023b; Dubessy et al., 2012; Hagiwara et al., 2021), the presence of a significantly larger number of measurements with ρ>0.26 g/cm^3 in studies which did not perform an instrument specific calibration may indicate that these densities have been overestimated through selection of an inappropriate literature calibration. For example, had the Kawakami et al. (2003) densimeter been used for the melt Inclusion in Fig. 20a, an impossible density of 0.29 g/cm^3 would have been obtained.

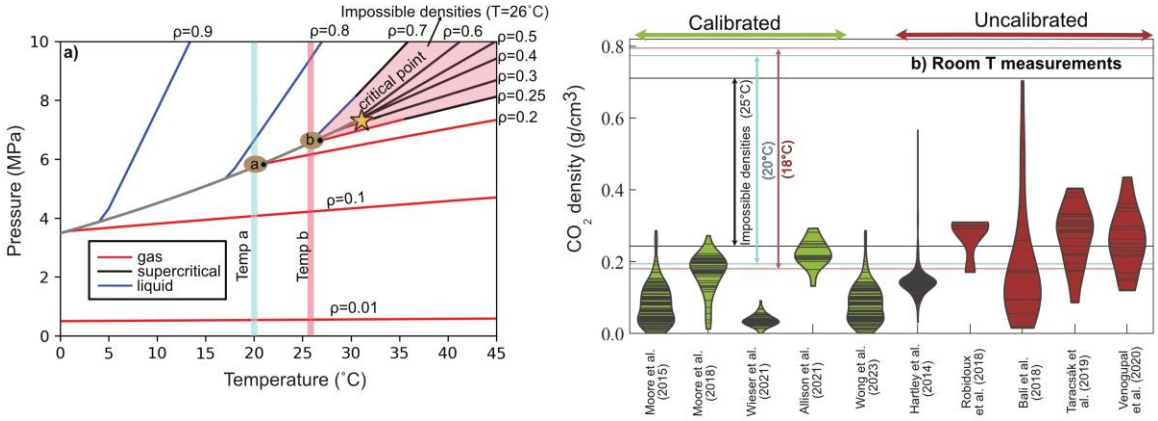

Figure 21 – a) Phase diagram of CO_2, drawn using the NIST webbook with the Span and Wagner (1996) EOS. At Temp a (20°C), a CO_2 fluid with ρ>0.2 g/cm^3 will comprise of a vapour with ρ=0.194 g/cm^3, and a liquid with ρ=0.773 g/cm^3. At Temp B (26°C), the liquid will have a density of ~ρ=0.7 g/cm^3 and the vapour will have a density of ~ρ=0.25 g/cm^3. Impossible densities at 26°C are shown in pink. b) Compilation of the densities of room T melt inclusion vapour bubble measurements by Raman spectroscopy, shown as a Violin plot where each horizontal line represents 1 measurement. Studies which used an instrument-specific calibration are colored green, those which did not are colored dark red. The maximum density of a vapour and minimum density of a liquid phase at three temperatures are shown with horizontal lines. Even with a room T of 25°C, many of the densities reported by uncalibrated studies are thermodynamically impossible. Refs: (Allison et al., 2021; Bali et al., 2018; Hartley et al., 2014; Moore et al., 2018, 2015; Robidoux et al., 2018; Taracsák et al., 2019; Venugopal et al., 2020; Wieser et al., 2021; Wong et al., 2023).

Once the relationship between measured splitting and CO_2 density for a specific Raman instrument and data reduction strategy is determined, the amount of the CO_2 held in the vapour bubble (in ppm equivalent in the glass) is calculated using mass balance:

$$CO_2(ppm\ equivalent) = 10^4 \frac{Vol\%_{VB} \times \rho_{CO_2}}{\rho_{melt}} \text{ [Equation 9]}$$

Where $Vol\%_{VB}$ is the vol% of the vapour bubble, ρ_{CO_2} is the density of the CO_2 fluid (determined by Raman spectroscopy), and ρ_{melt} is the density of the silicate melt (e.g., using DensityX, Iacovino and Till, 2019). Equation 9 can be used to demonstrate the large effect of the choice of densimeter on calculated CO_2 contents. For example, using a typical melt density (e.g., 2.7 g/cm^3) and a bubble volume percent of ~3.9% (as in the melt inclusion shown in Fig. 20a), the true vapour bubble CO_2 density of 0.17 g/cm^3 means the bubble contributes 2455 ppm CO_2 to the melt inclusion. However, if a literature densimeter was randomly chosen from those in Fig. 20b, the amount of CO_2 contributed by the bubble could be as high as 4188 ppm. These discrepancies in Raman calibration propagate to large uncertainties in magma storage depths. Wieser et al. (2021) show that for a typical Kīlauea melt inclusion with a vapour bubble occupying 5% of the inclusion volume, different densimeters could yield storage depths ranging from 4 to 18 km. Thus, constraining the splitting to CO_2 density relationship for each individual instrument is vital to avoid the introduction of very large systematic errors on calculated storage pressures (and therefore depths). Arbitrary choice of a Raman calibration is likely the largest source of systematic error in many published melt inclusion studies, only overshadowed by studies which didn't measure the bubble at all. Raman analyses without an instrument-specific calibration must be considered as qualitative. They are useful to determine whether CO_2 is present in vapour bubbles in any given system, but systematic errors spanning a factor of 3 are unacceptable when it comes to determining magma storage depths.

3.3 Other uncertainties reconstructing vapour bubbles

Once a Raman instrument is calibrated, there are four additional major sources of uncertainty affecting estimates of the amount of CO_2 held in vapour bubbles, discussed below.

3.3.1. Volume proportions of vapour bubbles

The first source of uncertainty is associated with determining the relative volume of the vapour bubble and melt inclusion (i.e. the $Vol\%_{VB}$ term in Equation 9). The vast majority of melt inclusion studies estimate volumes using transmitted light images, where a best fit ellipse is fitted to the 2D outline of the melt inclusion and vapour bubble, and the third (z) dimension is estimated either as an average of the two visible axes, or the

minimum of the two measured axes. Tucker et al. (2019) simulate the uncertainty associated with 2D sectioning of 3D ellipsoids, concluding that the best estimate is obtained when the third (z) dimension is calculated from the average of the 2 visible dimensions. They quantify the 1σ uncertainty of this method (-48% to +37%), which translates into a significant error in calculated storage depths where vapour bubbles contain a large proportion of the total inclusion CO_2.

However, in many cases, melt inclusions have faceted faces (e.g., Fig. 20a) or more complex shapes that can deviate significantly from a perfect ellipsoid. A best fit ellipse fitted to a more cubic shape may result in the melt volume being overestimated, and by extension, the bubble volume and CO_2 content underestimated (Hanyu et al., 2020). Mironov et al. (2020) compared methods of calculating the z dimension using the measured x-y dimensions to direct measurements of the 3rd dimension using a vertically calibrated microscope, or by polishing two orthogonal faces so the x-y and z direction can be measured. They find that volume measurements using z from a vertically calibrated microscope or by polishing an orthogonal plane were in good agreement ($\pm$10 %) with each other, but differed from the z-axis assumption methods by up to 45%. Thus, they suggest that researchers should measure the 3rd axis using these relatively low-cost methods, rather than inferring it from 2D measurements.

The most accurate and precise approach to determine the volume of each phase is to use x-ray tomography (i.e. nanoCT, µCT; Richard et al., 2019; Hanyu et al., 2020; Jorgenson et al., 2021). Hanyu et al. (2020) showed that optical methods fitting ellipses tend to overestimate MI volumes by ~20%, even in fairly ellipsoidal shaped MI (they did not assess the effect of strong asymmetry or faceting). Attempts have been made to constrain volumes using 3D confocal Raman imaging (Aradi et al., 2021; Schiavi et al., 2020). There are additional compilations associated with the fact that the different refractive indices of the host crystal, melt and vapour can caused vertical distortion (Everall, 2010). This can make vapour bubbles appear oblate (Schiavi et al., 2020). Raman mapping is also significantly slower than µCT, and data segmentation is even more time consuming.

Most recently, DeVitre et al. (2023a) perform nano-CT scans for MI of various shapes and sizes, including those with extreme asymmetry or faceting. They compare these CT volumes to those calculated using 2D methods (measuring x-y, calculating z), and 3D methods where z is measured using a vertically calibrated microscope, or by polishing an orthogonal surface. For relatively ellipsoidal shapes, the median offset between 2D and CT methods is ~±15–20% (similar to Hanyu et al. 2020), although for certain melt inclusion morphologies, the offsets can be ~±50%, similar to the uncertainty estimated from slicing simulations of Tucker et al. (2019) of 1σ=-48% to +37%. For the most faceted or complex shaped MI, the systematic mis-prediction of volume inflicted using averaging or minimum axis 2D methods results in an uncertainty of up to ~3 kbar in the saturation pressures (meaning MI could have been trapped at crustal levels at 7–8 km, or in the mantle, 17–18km). For regular, relatively ellipsoidal-shaped melt inclusions, DeVitre et al. (2023a) find that measuring the 3rd dimension (via microscope, motorized-z stage Raman, or on an orthogonal plane) returns values within ±10% of CT measurements, although the offsets are larger for more irregularly shaped inclusions. Overall, DeVitre et al. (2023a) suggest that the orthogonal plane method is the most time-and cost-effective way to reduce uncertainty associated with bubble volumes. While CT is clearly superior, these measurements cost ~100$/hr, with high quality scans needing several hours. Data reduction is also time consuming and computationally expensive. At the moment, the CT method has not been scaled up to datasets typical of melt inclusion studies (e.g., N>100) in a time or cost-effective manner. We suggest that it makes more sense to constrain the volumes of all melt inclusion to within ±20% of the true value for all melt inclusions (and published studies), compared with a smaller number of super precise CT scans, and a larger number of imprecise 2D optical methods. Developing fast, inexpensive, and precise ways to estimate vapour bubble volumes is an important frontier to address to optimize melt inclusion barometry.

3.3.2. Secondary phases in vapour bubbles

Another major source of uncertainty when reconstructing bubble CO_2 comes from the presence of carbon-bearing phases on the wall of the bubble, which may sequester 100s-1000s of ppm of CO_2 (Aster et al., 2016; Moore et al., 2015; Schiavi et al., 2020; Tucker et al., 2019; Venugopal et al., 2020). These phases can be identified optically in larger bubbles (Tucker et al., 2019), and produce distinctive peaks in Raman spectra, particularly if the laser is focused near the bubble wall or line scans and 3D maps are used (Fig. 22d, Moore et al., 2015; Robidoux et al., 2018; Schiavi et al., 2020). Secondary phases can also be identified using BSE, SE and/or EDS imaging on an SEM of an exposed bubble walls (Robidoux et al., 2018; Schiavi et al., 2020; Tucker et al., 2019; Wieser et al., 2020).

The occurrence of secondary phases on bubble walls is highly variable, and their genesis is poorly understood. It appears that carbonate species (e.g., Mg, Fe, Na, and Ca carbonates) are more common in more H_2O-rich melt inclusions (e.g., arcs and wet OIBS like Fogo vs. dry OIBs such as Kīlauea). Even at a given volcano, some eruptions may have a reasonable proportion of melt inclusions containing carbonate (e.g., 1960 Kīlauea, Moore et al., 2015; Tucker et al., 2019), while other eruptions have no carbonate (e.g., 2018 Kīlauea, Lerner et al., 2021; Wieser et al., 2021). Most intriguingly, even within a single crystal, some melt inclusions contain carbonate while others do not, and within a single melt inclusion with multiple bubbles, some have all their CO_2 as carbonate, some have a mix of carbonate and CO_2 fluid, and some consist only of CO_2 fluid (Fig. 23). It has been suggested that solid phases form on bubble walls as a paragenetic sequence during cooling of the vapour bubble, with sulfide precipitation at 500–700˚C, magnesite ($MgCO_3$) precipitation at <350 ˚C, and carbonate and sulfide precipitation from liquid H_2O at <150 ˚C (Robidoux et al., 2018).

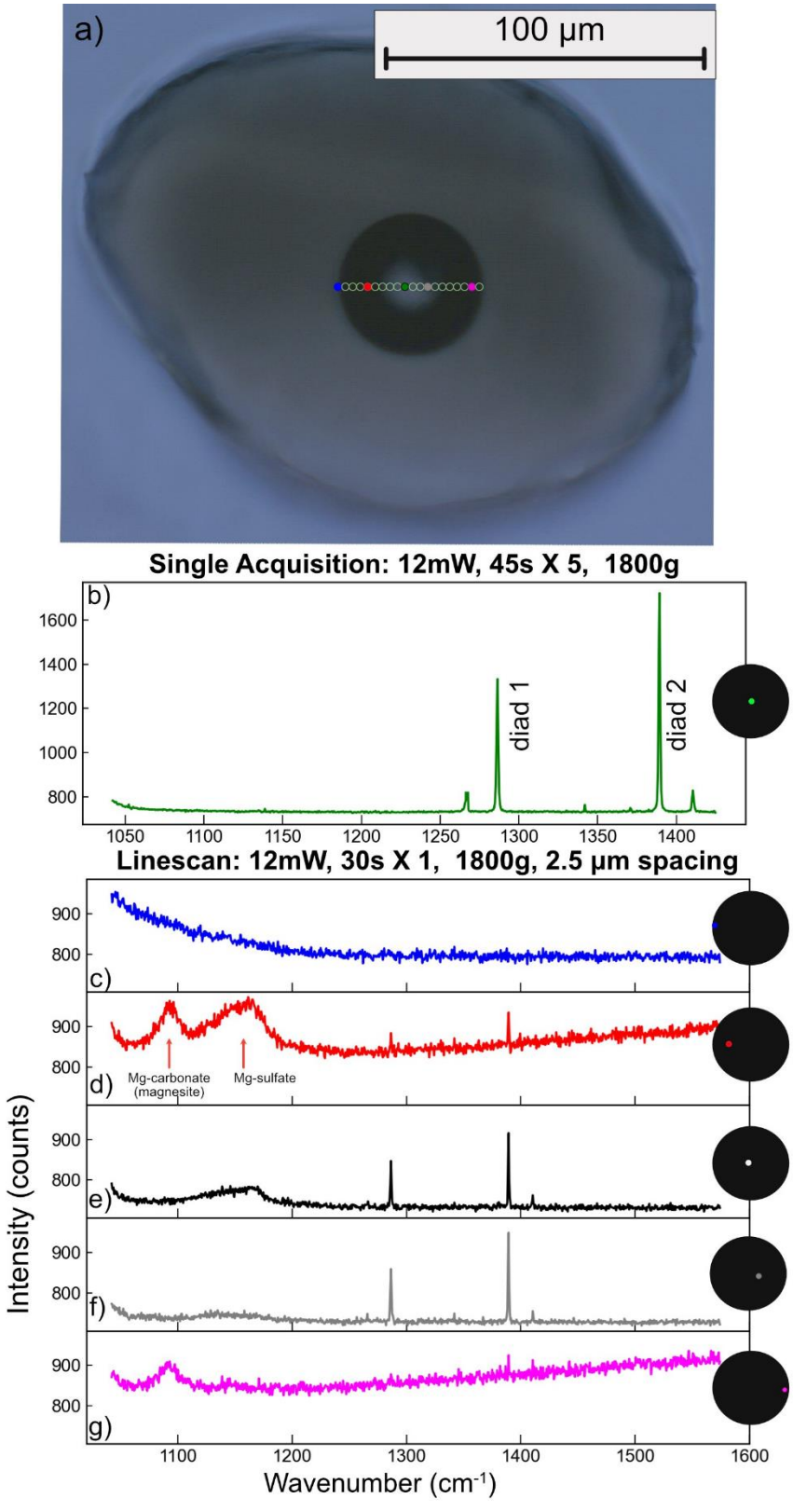

Figure 22 – Comparing a Raman acquisition in the centre of a melt inclusion vapour bubble (scan b) with individual acquisitions taken as part of a line scan across the bubble (c-g). A carbonate and sulfate peak is only apparent at specific locations near the bubble edge, and does not appear in the central acquisition.

Clearly, the carbonate forming reactions are subject to very local variations in condition (on the scale of the diameter of a single melt inclusion), and significant further work is required to understand them further. Quantifying the amount of CO_2 present within carbonate is non-trivial. Tucker et al. (2019) do preliminary mass balance calculations based on optical observations, considering different thicknesses of carbon on the wall of bubbles. Schiavi et al. (2020) determine the volume of carbonate and S-bearing species using 3D Raman mapping, showing that solid phases can account for 21–50% and 16–60% of the C and S budget respectively. Several experimental approaches have been developed for bubble-bearing melt inclusions as an alternative to mass balance reconstructions using Raman Spectroscopy (see below), some of which can help to resolve the carbonate problem.

3.3.2.1 Experimental homogenization approaches

Two broad homogenization strategies have been used to account for carbonate in vapour bubbles. The 'in situ' strategy involves reheating of individual crystals in a Linkam or Vernadsky heating stage in an fO_2 controlled Ar or He atmosphere, making observations of the melt inclusion of interest under an optical microscope. The crystal is heated until the vapour bubble and other secondary phases redissolve, and then the sample is rapidly quenched to obtain a single-phase melt inclusion. This method allows the operator to view the melt inclusion and quench the crystal just after the inclusion homogenizes, meaning a different reheating path can be used for each crystal. The 'bulk' strategy heats crystals in batches in various experimental apparatus. This had the advantage of being far less time consuming

and allowing reheating at different pressures (see below), but has the disadvantage of meaning crystals trapped at a range of temperatures may be overheated or underheated (e.g., Esposito et al., 2012).

Regardless of whether a single crystal or a batch of crystals is heated, performing reheating experiments at atmospheric pressure often results in vapour bubbles not fully redissolving, or dissolving at spuriously high temperatures. For example, Le Voyer et al. (2017) individually heat melt inclusions from Mt. Shasta in the Cascade Arc using a Vernadsky-type heating stage, noting that many inclusions retain their vapour bubble, even if they are heated up to 1500˚C. The failure to homogenize the bubble has been attributed to the fact that at atmospheric pressure, the host exerts less pressure on the melt inclusion than was present during natural cooling at depth in the magmatic system (Danyushevsky et al., 2002; Esposito et al., 2012). Additionally, if sufficient time passes between post-entrapment crystallization and syn-eruptive quenching, chemical changes such as FeO or H^+-loss through the host crystal may occur, which cannot be reversed by reheating (Aster et al., 2016; Bucholz et al., 2013). To account for the excess bubble growth resulting from these irreversible changes, the inclusion must be overheated, often by many hundreds of degrees to get the bubble to disappear. This is concerning because overheating results in extensive re-equilibration between the melt inclusion and host, erasing important chemical information (e.g., major element zoning preserving quench rate, Newcombe et al., 2014; information on the amount of PEC; Wieser et al., 2021). An additional problem with heating at 1 atmosphere is that melt inclusions may rupture/decrepitate (Tuohy et al., 2016). This is a particular problem for melt inclusions closer to the polished surface or the crystal, inclusions trapped at high pressures in the plumbing system, and more H_2O-rich inclusions.

Crystals can also be heated at elevated pressures (e.g., Piston cylinder apparatus, Rasmussen et al., 2020, internally heated gas pressure vessel, Skirius, 1990). The confining pressure exerted around the crystal can help prevent decrepitation, and aid bubble dissolution. To get around the issue that reheating can cause H^+ loss, and to try to resorb bubbles which have experienced extensive H^+ loss, Mironov et al. (2015) homogenize melt inclusions in an internally heated pressure vessel (IHPV) under high H_2O pressure achieved through a hydrated silicate melt matrix. Specifically, they heat melt inclusions from lavas which are thought to have diffusively lost 3 wt% H_2O (such extensive H_2O-loss favours near-ubiquitous bubble growth). They find that bubbles remain after heating under dry and damp conditions, but a large proportion disappear at higher H_2O pressures where the melt inclusion is rehydrated. This indicates that, at least in wet arc magmas, diffusive H_2O loss can account for the observation that bubbles often persists after heating (rather than resulting from a lack of confining pressure during heating in 1 atm apparatus). This reheating method was adapted by Rasmussen et al. (2020), who use a piston cylinder apparatus with KBr and $Mg(OH)_2$ as the hydrated matrix to achieve a higher experimental success rate.

One limitation of these hydrated experimental reheating methods is that the initial H_2O content of the system must be estimated when preparing the hydrated matrix, and melt inclusion water contents will be reset to this value (Buso et al., 2022). While Rasmussen et al. (2020) use unheated melt inclusion volatile contents as a guide, there is still the risk of adding too much or too little H_2O to any specific inclusion. Additionally, while an approximate estimate of initial H_2O contents can be placed based on the point of homogenization, there is a non-unique play off between the confining P, T and H_2O content required to obtain complete homogenization of the bubble (e.g. Mironov et al., 2015 show that instead of increasing H_2O by 1 wt%, P could be increased by 6.5 kbar, or T increased by 100°C). Thus, as with the techniques mentioned above, a limitation of these bulk homogenization experiments is that the same experimental conditions must be applied to all melt inclusions in a given capsule, even if they formed on different P-T-H_2O paths in nature (Rasmussen et al., 2020).

All the methods discussed so far attempt to redissolve the bubble entirely, so measurements only need to be performed on a single homogenous glass phase. In contrast, DeVitre et al. (2023a) developed a reheating method where the aim is to redissolve the carbonate phase back into the vapour bubble where it can be measured using Raman spectroscopy, rather than redissolve the bubble into the melt. They heat individual crystals using a Linkam TS1400XY stage which heats from room T to 1400˚C at up to 200 ˚C/min, and quenches using Ar or He flow combined with a water-cooled plate at 240 ˚C/min. Heating is conducted in an fO_2 controlled Ar atmosphere to prevent oxidation of the melt and olivine. As the melt inclusion is progressively heated under a microscope, it passes through the glass transition temperature, and goes dark. The liquidus temperature is estimated from the major element composition of the system and a reasonable range of volatile contents (using MELTS, or a liq thermometer). As the liquidus temperature is reached, the melt inclusion clears to a brown glass, and the inclusion is held at this temperature for ~8–10 minutes to redissolve any carbonate on the walls of the bubble back into the fluid phase, before being rapidly quenched on a water-cooled plate. The advantage of this method is that it only heats the inclusion to the liquidus, rather than to higher temperatures needed to resorb the bubble. Heating to the lowest possible T is advantageous, because it limits olivine dissolution, and preserves the major element information held in the melt and olivine. Raman acquisitions collected before and after

heating indicate that the carbonate is effectively redissolved back into the bubble (Fig. 23e), and that inclusions experience minimal H_2O-loss. After heating, bubbles without carbonate return CO_2 contents within uncertainty of pre-heating estimates (CO_2 contents change by ~±10% accounting for slight changes in bubble volume, or errors associated with measuring the same bubble proportion using 2D images). The main disadvantage of this method over complete homogenization methods is the fact that Raman is used to measure the bubble after heating, which requires accurate estimates of the relative volume of the vapour and melt phase.

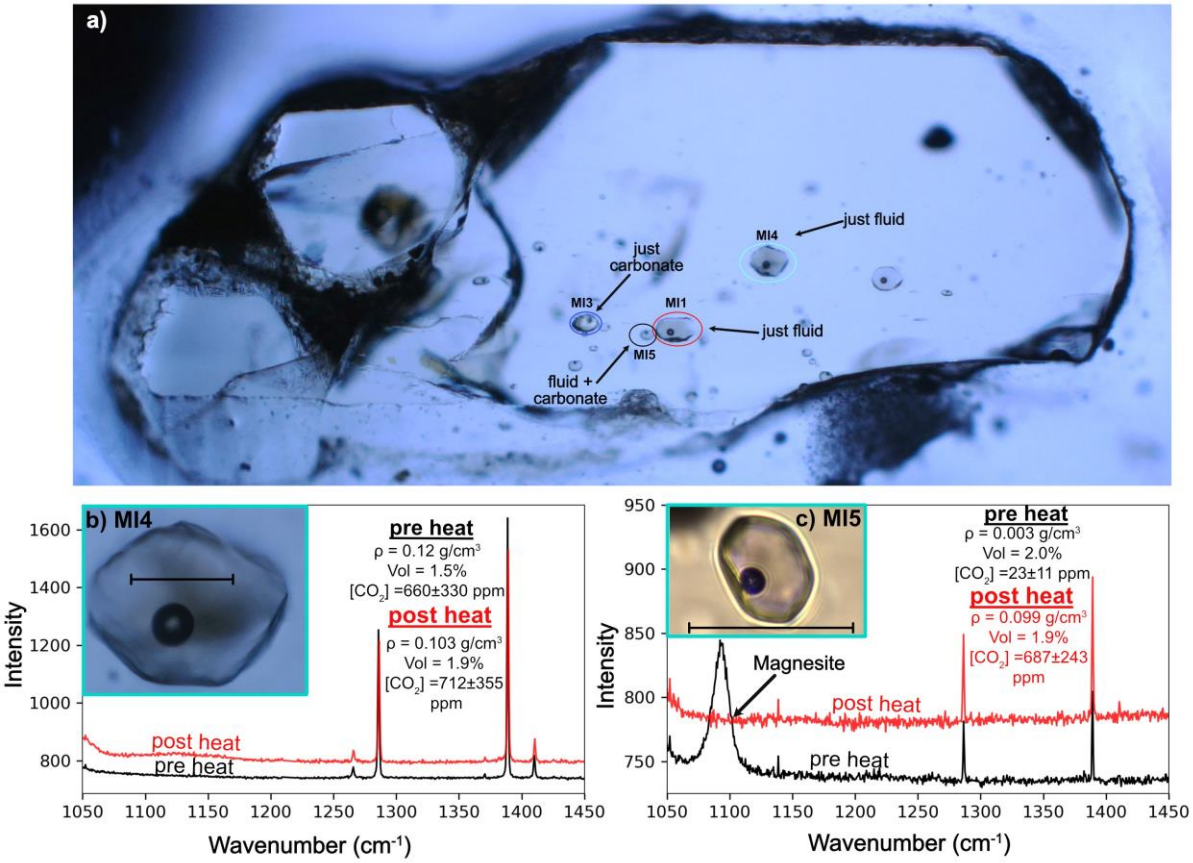

Figure 23: Olivine crystal with numerous melt inclusions with variable carbon partitioning between fluid and solid phases. A) Two melt inclusions (MI1, MI4) have a strong fermi diad but no carbonate phases (see spectra b), while MI5 has a fermi diad and a carbonate peak (see spectra c), and MI3 has just a carbonate peak b) pre and post-heating, MI4 has very similar densities and volumes, with CO_2 contents within error. c) pre-heating, MI5 has a prominent magnesite peak, and weak Fermi diads. After reheating using the method of DeVitre et al., 2023a, the amount of CO_2 increases substantially, and the magnesite peak completely disappears. Scalebar on b-c shows 50 µm

3.3.3. Theoretical vapour bubble reconstruction methods

A variety of methods have also been developed to reconstruct the CO_2 content of a vapour bubble theoretically, although there have been relatively few comparisons with Raman approaches on a single inclusion basis (e.g. Aster et al., 2016, Wieser et al. 2021). Anderson and Brown (1993) investigated bubble CO_2 in a suite of melt inclusions from Kīlauea Iki, calculating an internal pressure for each melt inclusion using the measured CO_2 content in the melt phase of the inclusion. This internal pressure was then used to calculate the density of CO_2 in the coexisting vapour phase using an equation of state. To convert these densities into CO_2 amounts, they assumed all bubbles occupied 0.5 vol% prior to syn-eruptive quenching, which is the point at which CO_2 diffusion and bubble growth become decoupled. Riker (2005) adapt this method for Mauna Loa, calculating the pre-quench bubble volume as a factor of the T drop experienced by each melt inclusion, accounting for the fact different melt inclusions experience different amounts of cooling, and therefore PEC. Aster et al. (2016) further adapt this method for melt inclusions from Lassen Volcanic Centre, tracking the volume of a growing vapour bubble using phase volume and density information from Rhyolite-MELTS, and vapour compositions to partition

elements into the bubble using the volatile solubility model of Iacono-Marziano et al. (2012). This method was also used in the Cascade Arc by Johnson and Cashman (2020) and Walowski et al. (2016).

In contrast to these methods reconstructing the vapour bubble volume *pri*or to bubble expansion accompanying syn-eruptive quenching, Tucker et al. (2019) use the equation of state method outlined by Anderson and Brown (1993) to calculate CO_2 density in the bubble, and then calculate the amount of CO_2 in the bubble using the measured bubble volume. This measured-volume method generates extremely high CO_2 estimates (and therefore storage pressures) for Hawaiian melt inclusions (4000–10,000 ppm). Using the measured bubble volume assumes that the vapour bubble and melt continue to exchange CO_2 until the glass transition T (~725˚C), such that the bubble is always in equilibrium with the measured melt composition. However, vapour bubbles experience two distinct phases of growth. The first phase of bubble growth at high T accompanies PEC or diffusive H_2O loss. High temperatures mean that CO_2 can easily diffuse from the melt into the growing vapour bubble. The second phase of bubble growth occurs during syn-eruptive quenching, where CO_2 becomes diffusion-limited as the temperature drops, but the bubble volume continues to grow until the temperature cools below the glass transition temperature (Maclennan, 2017). Wieser et al. (2021) compare the Tucker EOS method to Raman measurements at Kīlauea and show that the Tucker method overestimates bubble CO_2 by a factor of 10–20X compared to the Raman method for melt inclusions which grew most their bubble during syn-eruptive quenching (where CO_2 migration was diffusion limited). The measured-volume EOS method results in calculated magma storage depth of 5–20 km for melt inclusions while the Raman method and geophysics indicate magmas were stored at 1–5 km. For melt inclusions contained in high-Fo olivines, where most of the bubble grew during PEC at high temperatures, EOS methods are still 1.5–2X too high, as the method still neglects a non-negligible increase in bubble volume upon quench which is not accompanied by CO_2 diffusion.

To unravel the relative importance of these two stages of vapour bubble growth, good estimates are required of the amount of PEC, the amount of H_2O-loss, the quench rate, and the glass transition T (Maclennan, 2017; Rasmussen et al., 2020). Rasmussen et al. (2020) produce a Python3 tool, MIMiC (Melt Inclusion Modification Corrections), which calculates bubble CO_2 using empirical parametrizations of volume and density changes, with uncertainties quantified by Monte-Carlo techniques. However, while constraining the amount of PEC is relatively straightforward in systems with a well-defined liquid line of descent where the initial FeO content can be easily estimated (e.g., Kīlauea Volcano, Wieser et al., 2021), it can be very challenging in systems with a large amount of scatter in FeO at a given MgO number (e.g., Rasmussen et al., 2017; Walowski et al., 2019), perhaps because of variability in primary FeO contents and/or mixing of diverse melt compositions (e.g., Maclennan, 2008). Reconstructing initial H_2O contents can also be very challenging, and the arc magmas at the point of melt inclusion entrapment may be substantially more hydrous than the amount of H_2O measured in the melt inclusion (Gavrilenko et al., 2019; Goltz et al., 2020).

3.3.4. Co-entrapped vapour bubbles

All the methods discussed thus far rely on the assumption that vapour bubbles formed after melt inclusion entrapment, through some combination of PEC, cooling, and H^+ loss. However, it has been long recognised that bubbles may also become trapped at the point of melt inclusion formation. These are termed co-entrapped bubbles. In fact, determining magma storage depths from melt inclusion saturation pressures *requires* that the melt was volatile saturated at the point of melt inclusion formation. This assumption necessitates that there is an excess volatile phase available to co-entrap. If co-entrapped bubbles are added back in by mass balance techniques, the amount of CO_2 could be drastically overestimated.

Many studies simply select a threshold volume above which bubbles are assumed to be co-entrapped (e.g., 5%, Lowenstern, 2003; Robidoux et al., 2018, or 10%, Buso et al., 2022; Moore et al., 2015). However, the maximum vapour bubble volume that can form without requiring co-entrapment is a function of the amount of cooling, and the amount of diffusion H^+ loss, and varies greatly between different eruptions (Tucker et al., 2019). Tucker et al. (2019) examine distributions of bubble volumes from Hawai'i, discarding outliers which clearly lie outside the main distribution of bubble volumes (8 vol%+). In suites where there are abundant fluid inclusions in crystals addition to bubble-bearing melt inclusions, co-entrapped bubbles can often be identified based on the fact that they have larger relative volumes than other vapour bubbles, and CO_2 densities more similar to fluid inclusions (Lerner et al., 2021, Hanyu et al., 2020).

Alternatively, co-entrapped bubbles can be identified by comparing bubble volumes to variables such as H_2O content, CO_2 density, and PEC amount. For example, Wieser et al. (2021) show that there is a correlation between the amount of PEC (0–33%) and the volume of the vapour bubble (1–6 vol%) at Kīlauea. The 5% cut off from Lowenstern (2003) would clearly be inappropriate in this instance. Instead, samples lying significantly off the observed PEC-volume trend were classified as co-entrapped. While bubble growth in H_2O-poor, CO_2-rich

systems can be relatively well predicted based on the amount of PEC and the cooling path alone (Maclennan, 2017; Riker, 2005; Wieser et al., 2021), it is more complicated in H_2O-rich magmas which have the potential to experience large amounts of bubble growth following H_2O loss. In these situations it is more robust to use bubble growth models, and any bubbles which exceed even the most extreme model scenarios were likely co-entrapped (e.g., Allison et al. 2021, DeVitre et al. 2023a). For example, Ruscitto et al. (2011) report the presence of bubbles with volumes spanning 6–16 vol % in high Mg olivines from Mt. Shasta, and conclude that these bubble volumes can grow through a combination of PEC and H_2O loss, so were not necessarily co-entrapped. In contrast, Allison et al. (2021) found that melt inclusions at Sunset Crater, Arizona, with bubbles >3.5 vol% were likely to be co-entrapped. These two contrasting scenarios highlight the issue with selecting a single universal volume % as a cut off.

Even using bubble growth models, the details of specific inclusion must be considered, else co-entrapped bubbles with volumes within the range predicted by the growth model could be overlooked, even if they were co-entrapped. Allison et al. (2021) subdivide bubble-bearing melt inclusions from Sunset Crater, AZ, into 2 groups based on bubble volumes, densities, offset trends in Olivine forsterite-total CO_2 space, and bubble growth models. They conclude that group 2 inclusions (>3.5 vol%) co-entrapped a bubble. To more robustly identify co-entrapped vapour bubbles, we are in desperate need of a forward-model of bubble growth, accounting for both H_2O and CO_2. The model of Maclennan (2017) only considered CO_2 (not H_2O) and is not publicly available. While the Monte-Carlo methods incorporated in the model of Rasmussen et al. (2020) have huge potential for this problem, currently this code only works to correct melt inclusions, and cannot be run forward for a hypothetical P-T-X path post-entrapment. In summary, it is becoming very clear that the CO_2 contents of bubbles must be accounted for to obtain reliable storage depths, and that as a community, substantially more work is required to a) develop reliable bubble growth models to ensure co-entrapped bubbles don't result in spurious CO_2 contents b) calibrate individual Raman instruments and perform measurements at >33°C and appropriate laser powers c) improve methods to determine relative volumes d) further investigate experimental homogenization methods.

3.4. Decrepitation

Another issue affecting melt inclusion saturation pressures is the process of decrepitation, where the internal pressure of the inclusion exceeds the strength of the host mineral, and cracks open. Decrepitation commonly occurs during magma ascent, as the confining pressure exerted by the surrounding liquid drops. Maclennan (2017) compile a global dataset of melt inclusions from MORBs, OIBS, and continental settings, noting that 95% yield saturation pressures <2 kbar, which is close to the experimental decrepitation threshold of Wanamaker et al. (1990). Using their model of P-T-V-X evolution of melt inclusions, they conclude that pressure difference between olivine and melt causes decrepitation in most tectonic settings, so preserved CO_2 contents are minimum estimates. They note that decrepitation can be partially mitigated if the melt inclusion is trapped from a significantly undersaturated melt, so the melt inclusion experiences significant cooling and PEC at depth before it ascends, which reduces the internal pressure of their inclusion. Similarly, sequestration of CO_2 in a vapour bubble can also help to reduce the pressure of the liquid below the decrepitation threshold. The modelling of Maclennan (2017) suggested that entrapment pressures up to twice the decrepitation threshold (i.e., ~4 kbar) could be preserved if ascent conditions allow for bubble formation while remaining below the decrepitation threshold.

However, a number of studies have been published since 2017 yielding significantly higher saturation pressures than those in compilation of Maclennan (2017), and their inferred decrepitation thresholds. In the glass phase alone, DeVitre et al. (2023a) measure CO_2 contents of up to 1.3 wt%, corresponding to glass-only saturation pressures of ~1-7 kbar. Once CO_2 in the vapour bubble is included, pressures rise to ~2-11 kbar. Similarly high glass CO_2 contents (1.2 wt%) are reported by Buso et al. (2022) in melt inclusions from the French Massive Central, corresponding to entrapment depths of >10 kbar. Once bubbles are dissolved using homogenization methods, saturation pressures in these samples extend to 15–25 kbar. Glass-only measurements from Haleakala, HI, cluster at 1–3 kbar, and extend to 2–6 kbar after accounting for the bubble (Moore et al., 2021). Melt inclusions from Isla Floreana in the Galápagos record glass-only saturation pressures of 1.1–7.2 kbar (median=5 kbar, bubbles not measured). Critically, one bubble-free inclusion records a glass-only saturation pressure of ~7 kbar, where the lack of decrepitation cannot be attributed to the presence of a bubble keeping the inclusion below the decrepitation threshold. This high pressure overlaps with the pressure calculated from Cpx-based barometry, indicating it is not an outlier (Gleeson et al., 2022, 2021). There are numerous other examples of saturation pressures calculated from the glass phase only yield saturation pressures >2 kbar from many alkali ocean island settings (e.g., French Polynesia, Hanyu et al., 2020; El Hierro,

Taracsák et al., 2019), and studies accounting for the glass and bubble exceeding 2-4 kbar (e.g., Sunset Crater, AZ, at 3-5 kbar, Allison et al., 2021, Deccan Traps between ~ 2–7 kbar, Hernandez Nava et al., 2021, Pico Volcano, Azores, 2.2-6.6 kbar, Van Gevre et al. 2023).

The existence of melt inclusions with glass-only saturation pressures of >>2-4 kbar and glass + bubble saturation pressures of >4 kbar suggests decrepitation may not be as important a process as Maclennan (2017) suggests. While Maclennan (2017) conclude that "*decrepitation of melt inclusions, where the inclusion ruptures and loses CO_2 to the external melt, is the dominant process that controls the observed distribution of CO_2 in the compiled data set*". We suggest that the paucity of alkaline, CO_2-rich settings in the compilation of Maclennan (2017), combined with the fact most studies did not measure the vapour bubble, led to a dataset that was skewed to anomalously low pressures.

3.5. Melt inclusions hosted in other mineral species

While storage depths calculated from olivine-hosted melt inclusions have dominated the literature in the past few decades, there are a growing number of studies measuring melt inclusions in plagioclase (Bennett et al., 2019; Blundy et al., 2010; Drignon et al., 2019; Koleszar et al., 2012; Neave et al., 2017; Wieser et al., 2022c), ortho- and clinopyroxene (Araya et al., 2019; Koleszar et al., 2012; Wieser et al., 2022c), and amphibole (Koleszar et al., 2012). In more silicic systems, quartz-hosted inclusions are also commonly examined (Bégué et al., 2015; Quinn, 2014; Wallace et al., 1999), along with plagioclase (Bacon et al., 1992, Wright et al., 2012) and ortho- and clinopyroxene (Wright et al., 2012). Saturation pressures from inclusions in other phases often overlap with those determined from olivine (Wieser et al., 2022c), and may even yield deeper saturation pressures (Bennett et al. 2019) indicating that the "rupture resistance" of these other mineral phases may have been underestimated. Also, to gain an unbiased understanding of storage condition in a wide range of melt compositions, it is certainly advantageous to consider more than one mineral phase, particularly as in many systems olivine is restricted to a relatively narrow range of melt compositions (if present at all). However, significantly more work is needed to understand bubble growth and post-entrapment processes in these other phases, as well as rates of diffusive H_2O-loss.

4. Fluid inclusion Barometry

Crystals growing in a fluid-saturated magma trap pockets of melt and exsolved fluid in varying proportions, varying from pure melt (melt inclusions), melt and varying proportions of fluids (melt inclusions with co-entrapped vapour bubbles), and pockets of pure fluid with little or no attached melts (fluid inclusions – FIs, Steele-Macinnis et al., 2011). In CO_2–rich, H_2O-poor volcanic systems such as mid-oceanic ridge basalts and ocean island basalts (OIBs), the exsolved vapour phase (and thus the fluid being trapped) is almost pure CO_2 at pressures >200 bars (Gerlach and Graeber, 1985). In these relatively anhydrous systems, the density of FIs can act as an excellent barometer, because the density of a CO_2–rich fluid, along with an estimate of its entrapment temperature, can be converted into a pressure using the pure CO_2 equation of state (e.g., Span and Wagner, 1996).

Despite clear potential, a Web of Science search demonstrates that FI barometry has been underutilized by igneous petrologists in the last 10 years relative to other petrological barometers (Fig. 24c-d). Conventionally, the densities of FIs have been determined by observing phase changes during heating and cooling in a temperature-controlled microscope stage (microthermometry, Sorby, 1858). The relatively small number of existing studies in volcanic settings that use microthermometric techniques to obtain FI densities show the enormous potential of this method (Fig. 24c, see Hansteen and Klugel, 2008 and refs within). For example, FI in quartz-rich xenoliths from volcanoes in the Aeolian arc yield densities corresponding to both deep (~16–20 km) and shallow (4–6 km) pressures within the crust (Frezzotti et al., 2003). The deeper regions likely represent the primary magma storage zones, with shallower depths recording re-equilibration of FI during temporary residence at shallower levels during ascent towards the surface. The ability of FI to identify multi-stage ascent has also been demonstrated at Mt Etna (Frezzotti et al., 1991) at Mt. Etna, Cabo Verde (Klügel et al., 2020), Azores (Zanon and Frezzotti, 2013) and the Canary Islands (Hansteen et al., 1998).

It has long been established that Raman spectroscopy can be used as an alternative to Microthermometry to determine the density of CO_2-rich fluid inclusions (e.g., Rosso and Bodnar, 1995). This has been aided by recent improvements in the spatial and spectral resolution of confocal Raman spectroscopy, along with the development of precise ways to calibrate the relationship between peak parameters and CO_2 density for different Raman instruments (e.g., DeVitre et al., 2021; Kawakami et al., 2003; Lamadrid et al., 2017, see section 3.2). Raman analyses have many advantages over Microthermometry:

1. Confocal Raman spectrometers are becoming increasingly common in universities, where they are widely used in other subdisciplines within the Earth Sciences (e.g., paleontology, mineral physics). In contrast, the use of heating-cooling stages and the associated expertise to conduct microthermometry is more restricted.

2. Raman analyses are faster (2–4 mins) compared with the 10s of minutes required to conduct a single heating and cooling experiment. This is particularly true if there is only one fluid inclusion within the field of view at high magnification. Microthermometry can be faster on fluid inclusion trails as phase changes in multiple inclusions can be observed in one experiment.

3. Raman analyses only require only one surface to be ground down to within ~50–100 µm of the fluid inclusion, with a good enough polish to be able to visualize the FI on the Raman microscope. Normally, all that is required to achieve this is relatively fine wet-and-dry paper (2000–7000 grade) and a quick 30 s polish on 1 µm Aluminium polishing paper, while microthermometry requires a crystal to be prepared into a double polished wafer, with a good enough polish to see phase changes in detail.

4. Raman spectroscopy can be used on CO_2 fluid inclusions with a very wide range of densities (e.g. 0.01–1.24 g/cm^3) densities. In contrast, it is very hard to observe the homogenization temperature of a fluid inclusion with a density less than the critical density of CO_2 (<~0.47 g/cm^3) or a density higher than the triple point (>1.18 g/cm^3) using microthermometry (Kobayashi et al., 2012).

5. Raman spectroscopy can be applied on FIs with diameters down to ~1 µm (Frezzotti et al., 2012, Dayton et al., 2023), while it is very difficult to observe phase changes during microthermometry for inclusions < 3–10 µm (Kobayashi et al., 2012). This is of particular importance in volcanic systems, where many fluid inclusions are very small (and smaller inclusions are more resistant to decrepitation during ascent, Bodnar et al., 1989; Campione et al., 2015; Wanamaker et al., 1990).

Relative to melt inclusion analyses and mineral barometry, estimates of magma storage depths from FIs are significantly more precise than both melt inclusions and mineral barometry, and have fewer sources of systematic uncertainty relating to the conversion of the measured quantity (density) to pressure (Dayton et al., 2023). Unlike the complex relationships relating pressure to mineral components (e.g., Jd in Cpx) or dissolved H_2O and CO_2 concentrations in silicate melts, the CO_2 equation of state is extremely well constrained, with very little offset between different parameterizations (~3% at 7 kbar, Span and Wagner, 1996; Sterner and Pitzer, 1994; Wieser and DeVitre, 2023). Additionally, unlike many mineral-melt barometers which are very temperature sensitive, the P calculated from the EOS is not all that sensitive to T (Fig. 24a). To demonstrate the high precision of this method, we propagate a ±30 K uncertainty in trapping temperature and a Raman analytical error of ±0.02 g/cm^3 using Monte-Carlo methods (Wieser and DeVitre, 2023), which yields a 12% 1σ error at 0.6 kbar, a 7% error at 2.2 kbar, and a 5% error at 5.2 kbar. These errors are significantly smaller than other petrological barometers (Fig. 24b). A final advantage over melt inclusion barometry is that far fewer analytical steps are required to obtain FI pressures (no µCT, FTIR/SIMS, EPMA measurements of glass), increasing the speed at which depths can be determined, at a far lower cost (Dayton et al., 2023). This speed is aided by open-source Python3 packages which help to automate data processing and CO_2 equation of state calculations, which were previously one of the slower aspects of the Raman fluid inclusion method (Wieser and DeVitre, 2023).

Several sources of systematic error must still be considered when interpreting fluid inclusion pressures. First, like melt inclusions, fluid inclusions may experience decrepitation upon ascent, which can yield anomalously low pressures, sometimes without clear textural evidence for CO_2-loss because of rehealing during ascent. Second, the pressure the inclusion exerts on the host can also cause deformation of the host through the movement of dislocations, increasing the inclusion volume. These two processes are captured by two of the three 'Roedders' rules of fluid inclusions: '2) *the inclusion represents a constant volume, 3) nothing has been added or lost from the inclusion'* (Bodnar, 2017; Roedder, 1984). Namely, fluid inclusion barometry assumes that a fixed mass of CO_2 was trapped in the crystal, with a fixed volume, meaning the inclusion has a fixed density, so the density measured in the laboratory is the same as the density at which the inclusion was trapped. Decrepitation violates rule 3 (and possibly 2 as well), while re-equilibration violates rule 2. While numerous work has been conducted to determine re-equilibration processes for quartz-hosted fluid inclusions (Bakker, 2017; Boullier et al., 1989; Pecher, 1981; Qin et al., 1992), to our knowledge, the only experimental constraint on olivine re-equilibration was performed by Wanamaker and Evans (1989). They re-equilibrate fluid inclusions within San Carlos olivine by holding crystals at 1400°C and atmospheric pressure for several days. We suggest that further experimental work is required to confidently predict how fluid inclusions in common mafic phases (olivine, pyroxenes etc) re-equilibrate when subject to a specific P-T-t path, with the aim of having models which can be run for a given set of samples similar to those used to model H^+ loss from melt inclusions (E.g,, Barth and Plank, 2021). However, it is clear from analyses of fluid inclusions in mantle xenoliths that return crustal pressures that re-equilibration should be taken as the norm rather than the exception, and fluid inclusions will

normally be reset to the pressures corresponding to the final region of prolonged magma stalling prior to eruption (Hansteen and Klugel, 2008).

The presence of fluid species other than CO_2 can also influence the accuracy of calculated pressures by both Raman spectroscopy and microthermometry. In igneous systems, the most common species present in the exsolved fluid phase are H_2O, SO_2, Cl, F, H_2S, N_2, CH_4, CO, and He. While some species are strongly Raman active with peaks that are close enough to the CO_2 diad to be visible in most high resolution acquisitions (e.g. SO_2 produces a sharp peak at 1151 cm^{-1}, Frezzotti et al., 2012), others will require a separate acquisition centered at higher wavenumbers (e.g. the N_2 peak is at 2331 cm^{-1}, CH4 at 2917, Frezzotti et al., 2012). Monoatomic gases (e.g. He) are Raman inactive, meaning they don't produce any peaks. Molar proportions can be estimated from peak area ratios and knowledge of scattering cross sections for different Raman-active gases (Burke, 2001). Some fluid species can also be identified (and sometimes quantified) from changes in the freezing and melting temperatures by microthermometry (Hansteen and Klugel, 2008; Van Den Kerkhof, 1990), although in many cases, the relevant phase diagram has not be constrained (e.g. C O_2-He).

Mixed H_2O-CO_2 fluids present a particularly challenging problem to fluid inclusion barometry, because H_2O is so ubiquitous in the exsolved vapour phase in igneous systems. In arc magmas H_2O will be present in non negligible molar proportions at all crustal levels (>>10 mol%, Wieser et al. 2023d). Even in CO_2 dominated systems (e.g. Hawai'i), exsolved fluids will have substantial proportions of H_2O in the vapour phase as magmas ascend towards the surface. H_2O can be identified by microthermometry through the appearance of clathrate phases, and by Raman spectroscopy through identification of the O-H stretching band at ~3600 cm^{-1} (Azbej et al., 2007). However, at room temperatures, H_2O will be present as a thin film of liquid along the edge of the inclusion. This can make it very hard to identify by Raman spectroscopy, unless the inclusion is heated to the point at which H_2O dissolves into CO_2 (e.g., to ~150°C, Esposito et al., 2016). It has also been demonstrated that this H_2O film can react with the host crystal or a thin film of melt around the fluid inclusion (Andersen et al., 1984; Esposito et al., 2016; Frezzotti et al., 2002), and/or be lost through diffusive re-equilibration with a degassed carrier melt (Mackwell and Kohlstedt, 1990). This means it can be hard to identify which FIs had non negligible quantities of H_2O at the time of entrapment.

The presence of other fluid species complicates calculations of pressure in two ways. First, CO_2 densities obtained by Raman spectroscopy or microthermometry are normally converted into an entrapment pressure using a pure CO_2 EOS, which will deviate from the true relationship defined by a mix of the species of interest. Secondly, the reaction of secondary phases to form precipitates on walls, solid crystals, or liquid films means that the measured density represents only that of the residual CO_2 fluid phase, not the initial trapped fluid. Hansteen and Klugel (2008) discuss possible corrections for mixed fluids in their review (e.g. estimating H_2O/CO_2 ratios, then using a mixed H_2O-CO_2 EOS). Looking forward, we suggest that further work into mixed fluid equation of states and phase diagrams, as well as experiments of fluid inclusion re-equilibration, is required to

continue pushing fluid inclusion barometry forward.

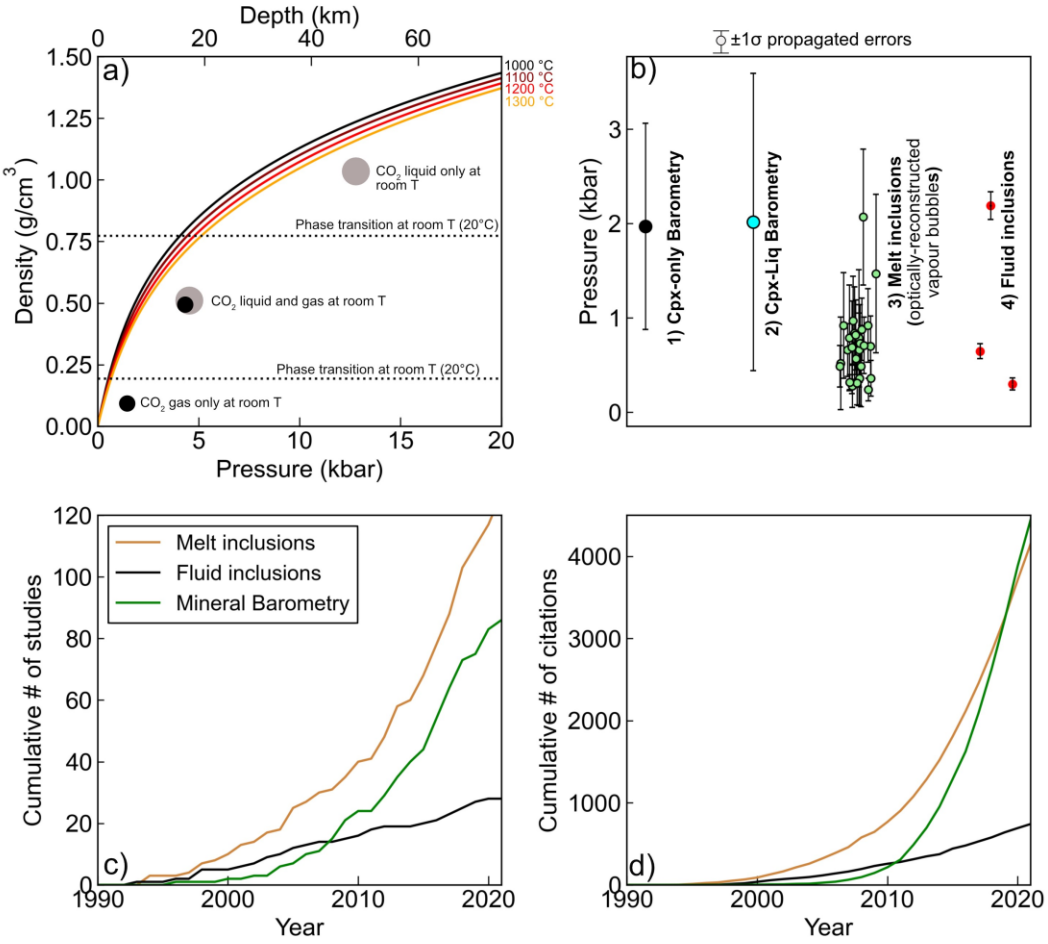

Figure 24: a) Relationship between pressure and the density of a pure CO_2 fluid (calculated using the Span and Wagner, 1996 EOS implemented in CoolProp, Bell et al., 2014). Storage depths shown for crustal densities of ρ=2700 kg/m^3. b) Monte Carlo simulations of 1σ errors for different barometry methods resulting from analytical uncertainty. Uncertainties calculated using Putirka (2008) eq32d-32b for Cpx-only and eq3 3–30 for Cpx-Liq arising from the EPMA analytical uncertainties of Neave et al. (2019, see Wieser et al. 2023b). Melt inclusion uncertainties show propagated errors in melt inclusions with vapour bubbles from the 2018 eruption of Kīlauea (Wieser et al. 2021). The large relative errors (±50%, ~1–1.5 kbar) arise from reconstructions of the volume of the vapour bubble using optical microscopy (with z=(x+y)/2, after Tucker et al. 2019). 1σ errors on calculated pressures for 3 FIs trapped at different crustal pressures, assuming an analytical error of 0.02 g/cm^3 from Raman spectroscopy, and uncertainty in T of 1σ=30 K. c) Web of Science search for number of articles using each method for barometry (full search criteria given in supporting information), and d) number of citations to these articles.

5. Can hygrometers be used as barometers?

At the opposite end of the spectra to determining pressures from fluid inclusions in CO_2-rich systems, many studies have used melt H_2O contents to estimate pressures using a pure H_2O solubility model, either through direct measurements in melt inclusions (e.g., Blundy and Cashman, 2005, Rutherford et al., 1985) or calculated H_2O contents from mineral and mineral-melt hygrometers (e.g., Amphibole Mg#s – Goltz et al., 2020, Krawczynski et al., 2012, Plag-Liq hygrometry – Ruth and Costa, 2021). For example, Ruth and Costa (2021) conduct thermobarometry on a variety of phases from Mayon Volcano (Fig. 25a). Cpx-Liq, Opx-Liq and Cpx-Opx pressures show a prominent peak at ~4 kbar (16 km). In contrast, they invoke a shallower magma reservoir at ~ 5 km based on H_2O-only saturation pressures calculated from plagioclase-liquid hygrometry (and H^+ in pyroxene). However, it is well established that primary arc magmas have non-negligible quantities of CO_2 (Shinohara, 2013; Wallace, 2005). While such H_2O-only calculations are often quoted as minimum estimates, it is worth questioning whether such minimum estimates are even useful, given that uncertainty in the amount of

CO_2 can change the calculated pressure by up to an order of magnitude (Black and Andrews, 2020; Wieser et al., 2022a).

Using a global compilation of CO_2 in the glass phase of melt inclusions (Rasmussen et al., 2020, white histogram, Fig. 25b) and a compilation from the Cascade arc (red histogram, Fig. 25b, Wieser et al., 2023d), it is apparent that arc magmas have, at the very minimum, several hundred to a thousand ppm of CO_2. These quantities of CO_2 have a very significant effect on the calculated saturation pressures. For example, the H_2O-only saturation pressure of a typical arc basalt with 4 wt% H_2O (Plank et al., 2013) is ~ 1.3 kbar (white star on grey line), while the saturation pressure accounting for 1000 ppm CO_2 is 2.8 kbar (red star on grey line, Fig. 25b). In reality, it is becoming apparent that glass-only melt inclusion measurements have substantially underestimated the CO_2 content of arc magmas. A compilation of CO_2 contents in arc magmas for studies accounting the vapour bubble extends up to ~5000 ppm (Fig. 25c). For a magma with 4 wt% H_2O, a H_2O-only saturation pressure underestimates the true storage depth of a magma with 5000 ppm CO_2 by a factor of 5.7X (Fig. 25c, white star vs. green star). While H_2O depths are indeed minimum estimates, this example shows just how misleading they can be. Even for a magma with 10 wt% H_2O, H_2O-only pressures underestimate by factors of ~1.8X if there is 5000 ppm CO_2. Thus, we speculate in many cases that accounting for CO_2 will push hygrometry estimated magma storage pressure substantially deeper, perhaps more in line with other barometry estimates (Fig. 25a).

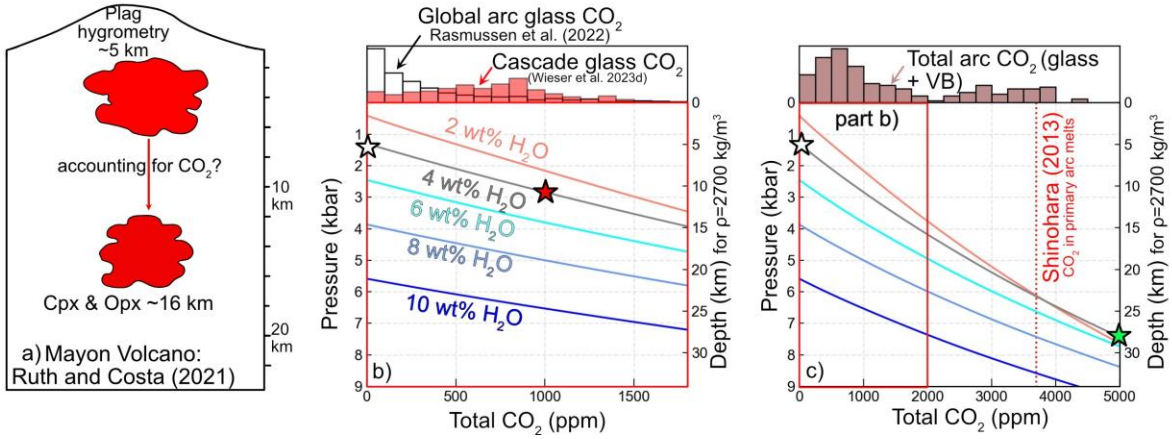

Figure 25: Sensitivity of saturation pressures to CO_2 contents. a) Schematic model of plumbing system at Mahon Volcano, adapted from Ruth and Costa (2021), where the depth of the shallower reservoir was calculated using a H_2O-only solubility model. b-c) Increase in saturation pressure with CO_2 for 5 different H_2O contents (for a typical mafic Cascade melt composition, SiO_2=54.3 wt%), calculated using the solubility MagmaSat (Ghiorso and Gualda, 2015) in VESIcal (Iacovino et al., 2021). The histograms in b) show a global compilation of arc CO_2 contents just measuring the glass phase (Rasmussen et al., 2022), and a compilation from the Cascade Arc. c) Expanded x scale (region shown in b indicated in the red box) up to 5000 ppm CO_2. Histogram shows a compilation of total arc CO_2 accounting for the vapour bubble through Raman spectroscopy or homogenization (from Mironov et al., 2015; Moore et al., 2018, Rasmussen et al., 2020). We overlay the estimate of primitive arc magma CO_2 contents from Shinohara (2013).

Therefore, we suggest that H_2O-only saturation pressures should only be used in systems where it has been demonstrated that very little CO_2 is present, in the same way that fluid inclusion barometry using the pure CO_2 EOS can only be used in systems where there is very little H_2O in the fluid phase. In more CO_2-rich systems, saturation pressure calculations should be performed for a wide range of possible CO_2 contents to determine the uncertainty associated with H_2O-only saturation pressures.

6. Elastic Thermobarometry/Thermoba-Raman-try

While the thermobarometric methods discussed thus far rely on changes in the chemistry of minerals, melts and fluids as a function of P and T, elastic thermobarometry relies on relative changes in the physical properties of inclusions and their hosts with changing P and T (Kohn et al. 2023, Cisneros and Befus, 2021). At the time of mineral growth and entrapment, a host-inclusion pair have the same pressure. However, after entrapment, the different thermal expansivity (change in volume with T) and compressibility (change in volume with P) of the two mineral species means that a residual pressure develops as the pair cool and/or ascend to the surface. This pressure can be deduced from the band/peak positions of minerals measured by Raman Spectroscopy, leading Kohn (2014) to term this method Thermoba-*Raman*-try! The magnitude of the residual

pressure depends on the P-T path taken (see Fig. 1 from Kohn, 2014). The final stress measured in the inclusion is a function of the initial P-T conditions of trapping, and the influence of differential contraction of the host-mineral pair, which can be modelled using knowledge of expansivity and incompressibility of different mineral species (Kohn, 2014). The most effective barometers are those where there is a large difference between the isothermal compressibility of the inclusion and host (i.e., changes in volume during pressure changes), while the most effective thermometers are those with the largest variations in isobaric expansivity (i.e., changes in volume during temperature changes, Kohn, 2014, Kohn et al. 2023).

Useful host-inclusion pairs are those with large differences in physical properties. There are a number of barometers using quartz inclusions, because these have a very different compressibility to host minerals such as zircon, lawsonite, and garnet (Kohn et al. 2023). Diamond is another popular host (e.g. Smith et al. 2022), along with garnet and zircon (e.g. olivine inclusions in diamond, coesite-in-diamond, and coesite-in-zircon, Kohn, 2014, Cisneros and Befus, 2020). Thermoba-Raman-try techniques can be remarkably precise; the estimated error in calculated pressure for Qtz-in-Gt inclusions is 0.3–0.5 kbar, resulting from uncertainty in the Raman band position of 0.5 cm^{-1} (Kohn, 2014). However, in general this technique has been applied to higher pressure systems where these phases are common (e.g. mantle rocks, metamorphic systems, xenoliths). Less attention has been paid to typical phases present in samples used to address volcanological research questions.

Befus et al. (2018) state that they provide the first elastic thermobarometer in igneous systems, by performing diamond anvil experiments on feldspar from atmospheric pressure to 3.6 GPa, and characterising the Raman bands. They find a clear shift of peak positions to higher pressure from 0 to ~30 kbar, with Raman shifts of the band at ~485 cm^{-1} of ~0.42 cm^{-1} per kbar for Albite, 0.45 cm^{-1} per kbar for andesine, and 0.31 cm^{-1} per kbar for anorthite. Their calibrations relating peak position with pressure could be applied to natural feldspars inclusions (e.g. Fspar in Cpx, Fspar in Ol, etc.) with known compositions, using models of host-inclusion relaxation along a PT path. They suggest that the main limitation of applying this technique to shallower crustal systems where peak shifts are rather small is the limited spectral resolution of many Raman spectrometers (~1 cm^{-1}). However, the most recent generation of Raman spectrometers have improved spectral resolution (0.1–0.4 cm^{-1}). Additionally, Befus et al. (2018) fit a cubic spline to the Raman data. If the peak shape can be determined (i.e. a Lorentzian or Gaussian), peak fitting can achieve significantly higher precision than the spectra resolution (Yuan and Mayanovic, 2017). This increase in spectral resolution accompanying peak fitting is vital for precise quantification of CO_2 densities using Raman spectroscopy. For example, a WITEC alpha300R Raman has a spectra resolution of 0.57 cm^{-1} using the 1800 grating. However, the peak fitting error on the CO_2 peaks using a pseudovoigt ranges from 0.002-0.05 cm^{-1} (error quantified in lmfit implemented in DiadFit, Newville et al., 2016; Wieser and DeVitre, 2023).

To further broader the scope of the elastic thermobarometry method, Kohn (2014) evaluate 48 inclusion-host pairs and Cisneros and Befus (2020) consider >5000 pairs, highlighting a number of inclusion-host pairs that may provide useful P-T constraints in volcanic systems (e.g., magnetite in olivine, feldspar in pyroxene, feldspar in olivine). Despite the potential of this method, in the 5 years that have passed since Befus et al. (2018) and 3 years since Cisneros and Befus (2020), none of the citing studies are focused on volcanic rocks. Kohn et al. (2023) and Cisneros and Befus (2020) identify numerous roads for improvement of the elastic thermobarometry method, including the need for measurements of elastic properties at the P-T conditions of interest, calibrations of Raman shift as a function of pressure, models for inelastic processes, nonideal geometries, and a better understanding of the effects of anisotropy on ideal P. Hopefully, the recent proliferation of interest and expertise in Raman spectroscopy by igneous petrologists measuring vapour bubbles should aid such efforts.

7. Experimental Petrology

Experimental petrology fundamentally underpins the melt inclusion, mineral-melt thermobarometry, and elastic thermobarometry methods discussed so far, because the composition of experimental products are used to calibrate models. However, experimental petrology can also be used directly to investigate magma storage conditions in a specific system. Generally, such experiments use a starting composition characteristic of a specific volcanic system or eruption, and perform experiments at a range of P, T, H_2O and fO_2 conditions. Then, experimental phase compositions are compared to natural samples to determine the most probable storage conditions (e.g., comparing glass compositions, mineral core and rim conditions, occurrence of breakdown reactions; First et al., 2021; Rutherford et al., 1985; Weber and Castro, 2017).

For example, Voigt et al. (2022) perform experiments at 0.25–5 kbar and 850–1100°C on natural starting materials from the 1257 Samalas eruption. They observe plagioclase and amphibole in their samples, so the PT space between amphibole breakdown and plagioclase instability places constraints on pre-eruptive PT conditions. Generally, once a stability region is identified, additional constraints are required to narrow down

the magma storage conditions (Bohrson and Clague, 1988). For example, Cadoux et al. (2014) overlay Fe-Ti oxide temperatures on their phase diagrams, concluding that the observed phase assemblage at Santorini is recreated experimentally at 2 and 4 kbar.

When performing experiments to deduce magma storage conditions at a given volcano, there can be a very large solution space to explore, in terms of pressure, temperature, and fO_2. If a natural Cpx has compositional similarities to one grown experimentally at a specific set of conditions, it is difficult to quantify the true uncertainty on storage conditions without exploring a very large number of experimental conditions to determine whether a very similar composition may appear at a different set of P-T-fo_2 conditions, particularly from a slightly different bulk composition). It is also vital to consider the composition of the fluid phase, which is often described in terms of the partial pressure of H_2O (P_{H2O}) or the mole fraction of H_2O in the starting composition or exsolved fluid phase (X_{H2O}). In order to reduce the size of one variable of the solution space, many experiments are performed at water-saturated conditions (i.e., X_{H2O} =1, Blatter and Carmichael, 2001; First et al., 2021; Grove et al., 1997; Nakatani et al., 2022; Sisson and Grove, 1993; Voigt et al., 2022). However, many natural systems do not contain enough H_2O to be volatile saturated at high pressures, or contain relatively large amounts of CO_2, meaning the system is volatile saturated in a fluid with X_{H2O}<1. Experiments with H_2O below the quantity required for H_2O saturation have been performed (e.g., Kawamoto, 1996), as have experiments in equilibrium with mixed CO_2–H_2O fluids (e.g., Alonso-Perez et al., 2009; Cadoux et al., 2014), although these are less common than pure H_2O-satured experiments.

Interestingly, there are many reports in the literature of phase stability being affected by X_{H2O}. For example, Keppler (1989) investigate solidus temperatures in the haplogranite system, and find that the solidus position varies as a function of the fluid phase composition for a mix of H_2O and CO_2. However, if X_{H2O} is reduced by the addition of N_2 instead, this relationship is not seen. These experiments indicate that at X_{H2O} close to 1, CO_2 is not just acting as an inert component to reduce the activity of H_2O, but is modifying the structure of the melt. Rutherford et al. (1985) also note that experiments where X_{H2O} is reduced by the presence of H_2 are not directly comparable to those where it is reduced by CO_2 (e.g., the addition of CO_2 is not simple Henry's law behaviour).

It has been shown numerous times that CO_2 affects the stability of amphibole. Given the increasing amounts of CO_2 being measured in melt inclusions in mafic arc magmas (Fig. 19), it is highly likely that the majority of high Mg# amphiboles examined at the surface formed in a system with X_{H2O} <<1. For example, Ridolfi et al. (2010) suggested that large amounts of CO_2 in a relatively high T igneous system with relatively low amounts of H_2O stabilizes OH- bearing phases such as amphibole. They suggest this may occur because of increasing solubility of OH- in the melt with increasing CO_2 dissolution (King and Holloway, 2002 suggest a reaction where molecular CO_2 and H_2O react to form carbonate and OH^-). Ridolfi et al. (2010) note that the paucity of magnesiohastingsite amphiboles in predominantly H_2O-saturated experiments may indicate that these compositions only form at high T and high CO_2 contents. Krawczynski et al. (2012) also find amphibole is stabilized at a higher temperature, with a lower Mg# in experiments with more CO_2.

In their experiments on the Mt. St. Helens dacite, Rutherford et al. (1985) find radical changes in the crystallization temperature of different phases as CO_2 is added, reducing P_{H2O} at a constant P_{total}; Plag, Px and Fe-Ti oxides crystallization temperatures increase, while the amphibole liquidus temperatures decrease. Additional experiments by Rutherford and Devine (1988) confirm that the observed phase stability is produced experimentally at 920°C, P=220Mpa, and X_{H2O}=0.67. Rader and Larsen (2013) perform experiments on low MgO basaltic-andesites to constrain the impact of small amounts of CO_2, running experiments at a range of T (900–1200°C) and P (0.001–1.8 kbar) at both X_{H2O}=1 and X_{H2O}=~0.7. They found that the plagioclase stability curve was the most sensitive to X_{H2O}, shifting 25°C for X_{H2O}=~0.7. They also observe shifts in amphibole stability. Finally, Cadoux et al. (2014) found that at 850°C and 4 kbar, there was more amphibole present when X_{H2O} was 0.9 than 1. They also find changes in the stability of both pyroxenes, ilmenite and plagioclase, as well as the liquidus phase with changes in X_{H2O}. In particular, they find that orthopyroxene is generally not stable where X_{H2O}=1 at 2–4 kbar.

In summary, these experiments show that X_{H2O} is clearly a very important variable to investigate in further experiments, and comparison of natural samples to experimental products should factor in possible differences in X_{H2O}. We believe this avenue of investigation is particularly important given the last decade of Raman work has clearly demonstrated that mafic arc magmas, have substantially more CO_2 (and thus a lower X_{H2O} ratio) than previously thought.

8. Thermobarometers based on thermodynamic modelling

Thermodynamic modelling is a powerful tool in igneous systems for exploring various hypotheses, such as whether the chemical variations in a suite of lavas can be produced by equilibrium or fractional crystallization alone, or whether processes such as crustal melting/assimilation are required (Heywood et al., 2020). However, in addition to general hypothesis testing, thermodynamical models have also been used to place quantitative constraints on magma storage conditions. Two main methods are discussed below, matching liquid lines of descent to erupted lava compositions, and multiphase saturation methods.

8.1 Liquid lines of descent

One method to determine magma storage conditions compares fractional crystallization models conducted at different conditions (e.g., P, fO_2, melt H_2O content) to observed liquid lines of descent (LLD, e.g., whole-rock XRF, glass EPMA data). Magma storage conditions in the system of interest are inferred from the model conditions providing the best fit to natural data. Comparison of observed and modelled LLDs have been used to deduce storage conditions in explosive silicic eruptions (e.g., the Campanian Ignimbrite, Campi Flegrei, Fowler et al., 2007, Bishop Tuff, Long Valley Caldera, Fowler and Spera, 2010), in trachytes and pantellerites of the East African Rift (Gleeson et al., 2017; Hutchison et al., 2018; Peccerillo, 2003; Ronga et al., 2010), in peralkaline rhyolites from Atlantic Ocean hotspots (Jeffery et al., 2017, 2016), and in basalts from Mauna Loa (Gaffney, 2002).

LLD methods are typically performed in MELTS, but other tools for modelling fractional crystallization such as COMAGMAT or Petrolog3 could also be used (Ariskin et al., 1993; Danyushevsky and Plechov, 2011). The best fit model is often determined by visual comparison between model outputs and natural samples (e.g., Fowler et al. 2007), although statistical methods have also been used. For example, Gleeson et al. (2017) develop an algorithm to calculate the smallest misfit between each datapoint and the modelled LLD path for each MELTS model. They combine the residuals of all individual samples into a weighted RMSE offset for each model.

In certain situations, storage conditions determined by LLD methods are supported by independent lines of evidence. For example, there is a close agreement between the depths of magma storage estimated by MELTS modelling and geophysical estimates of magma storage depths in the East African Rift (Hutchison et al. 2016; Gleeson et al. 2017), and between MELTS-estimated fO_2 and experiment constraints (Scaillet and Macdonald, 2001). However, as pointed out by Gleeson et al. (2017), even the best-fit models display systematic offsets between the MELTS predictions and the natural data for certain oxides (e.g., CaO, P_2O_5). These offsets indicate that there are several inaccuracies or omissions in the MELTS thermodynamic models (e.g. absence of amphibole or biotite in calc-alkaline magmas) that present severe limitations for the use of MELTS-based crystallisation models as a thermobarometric technique.

In most cases, MELTS correctly identifies the directionality caused by changing P, H_2O, or fO_2 on the LLD (e.g. enhancing or supressing the stability of a given mineral). However, it is unclear whether the predicted mineral stability for a given value of P, H_2O, or fO_2 is correct, or whether it is just relative differences that are trustworthy. While MELTS modelling may be able to distinguish a dry vs. wet LLD, it may not be able to determine whether a magma has 0.1 or 0.6 wt% H_2O. It has been shown that MELTS models at Kīlauea Volcano must be run with melt H_2O contents below those measured in melt inclusions to recreate the MgO content at which plagioclase and Fe-Ti oxide crystallize (Garcia, 2003; Wieser et al., 2022c). If H_2O contents were not independently constrained, such models could lead to incorrect inferences about the hydration state of magmas at this volcano.

To assess LLD methods further, we compare the measured composition of experimental liquids produced during fractional crystallisation experiments on a H_2O-poor tholeiitic basalts to MELTS crystallisation models (Villiger et al., 2007). We run a fractional crystallization model at the specified experimental pressure (7 kbar), fO_2 and H_2O content. We also run models at pressures of 1, 4 and 10 kbar (Fig. 26a, Supporting Figs. 11–13). We use three different MELTS versions (pMELTS, rhyolite-MELTS v1.0.2 and v1.2.0), Petrolog3 (Danyushevsky and Plechov, 2011), and MAGEMin (Riel et al., 2022) using the Holland et al. (2018) thermodynamic database. Both versions of rhyolite-MELTS show a very poor fit at the experimental pressure, predicting extensive Al_2O_3 enrichment and SiO_2 depletion relative to the experimental products (dark blue and green lines, Fig. 26e-f). The fit is far better at 1 kbar, which could lead to anomalous inferences of magma storage pressures using LLD methods. pMELTS (which has a different liquid model to rhyolite-MELTS) doesn't show such extreme Al_2O_3 enrichment at the experimental pressure, but the fit for Al_2O_3 is still better at 4 kbar than 7 kbar, and the fit for SiO_2 is best at 1–4 kbar (cyan lines). Petrolog3 shows anomalous SiO_2 depletion at all pressures (magenta lines, Fig. 26), and none of the 4 pressures used here provide a satisfactory fit to most elements

(Supporting Fig. 11). The Holland et al. (2018) database, implemented through MAGEMin, certainly does the best job of recreating Al_2O_3 systematics at experimental pressures (Fig. 26e), although the fit to SiO_2 is far better at 4 kbar than 7 kbar (black lines, Fig. 26, Supporting Fig. 11).

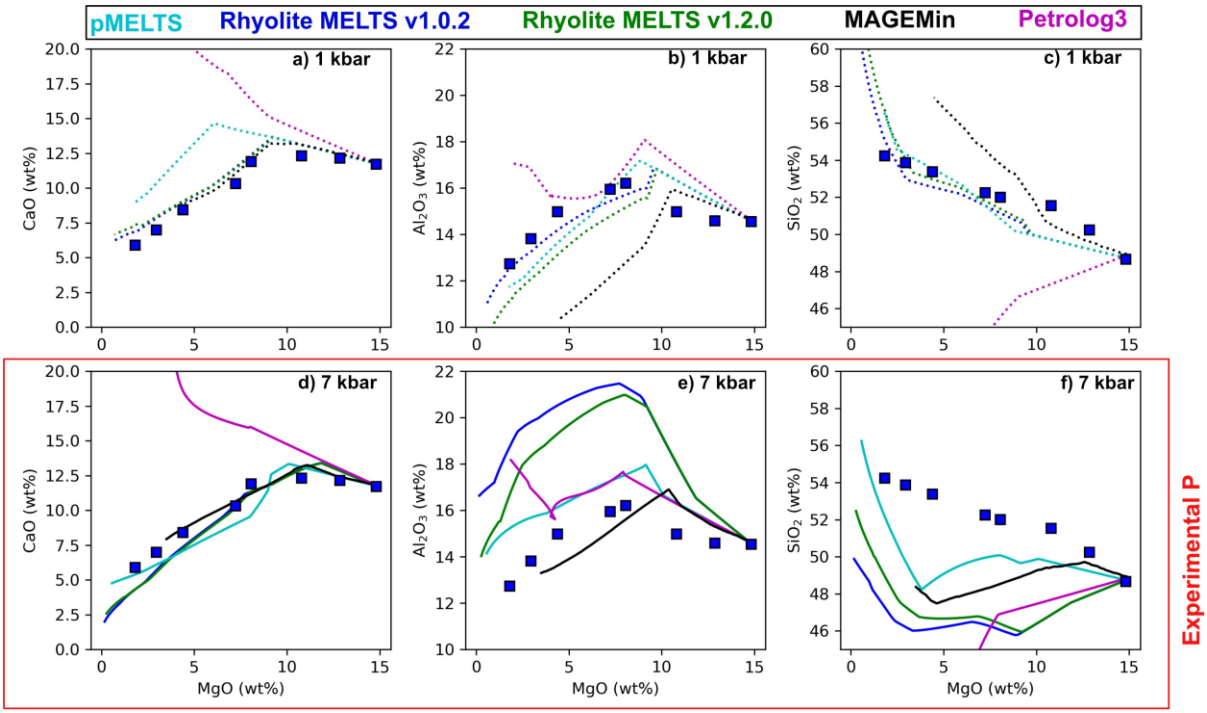

Figure 26 – Comparison of fractional crystallisation models run in rhyolite-MELTS, pMELTS, Petrolog3 and MageMin (using the Holland et al. 2018 database) *to fractional crystallization experiments from a nominally anhydrous, tholeiitic basalt from Villiger et al. (2007). MELTS calculations are performed at the experiment fO_2 (NNO), with H_2O=0.2 wt% (i.e. nominally anhydrous). While experiments were conducted at 7 kbar (solid lines), models run at 1–4 kbar provide a much better fit (particularly regarding the onset of plagioclase). Other pressures shown in Supporting Fig. 11.*

To further assess LLD methods, we use all three MELTS versions to model the fractional crystallization experiments of Nandedkar et al. (2014) conducted on a hydrous arc basalt (Fig. 27). The hydrous nature of these experiments means that the differences between rhyolite-MELTS v1.2.0 and v1.0.2 are far more noticeable compared to the H_2O-poor experiments of Villiger et al. (2007). Using v1.2.0, models run at 4 to 10 kbar provide a reasonable match to observed oxide contents. In contrast, using v1.0.2, models run at 1 kbar provide the best fit to both SiO_2 and Al_2O_3. It is concerning that these models give such different results, given they are used somewhat interchangeably in the literature, and obviously, any studies conducted prior to the release of v1.2.0 in 2015 must have used v1.0.2. pMELTS shows behaviour between the two rhyolite-MELTS models, with trends best recreated at 1–4 kbar.

These comparisons to two experimental studies demonstrate that the pressure you would deduce from LLD methods is very sensitive to both the choice of model and the oxides used for assessment of the 'best model'. In neither comparison does the experimental pressure stand out as the best model fit. It is also worth noting that for both these examples, we are using known fO_2 and H_2O contents. In reality, it is likely that P, fO_2, and H_2O are all uncertain, which leaves a very large solution space to explore (and can result in even greater ambiguity regarding the best fit model). Overall, we conclude that in their current state, LLD methods are not a reliable way to deduce storage pressure, particularly given the result can differ so much simply based on the choice of fractional crystallization model. It may be that an update of the MELTS liquid model, and/or tweaks to the thermodynamic data controlling the mineral stability fields (as performed for the qtz-2 fspar ternary) can revive this method. These comparisons also demonstrate that it is absolutely vital for papers to state the version of MELTS that they used.

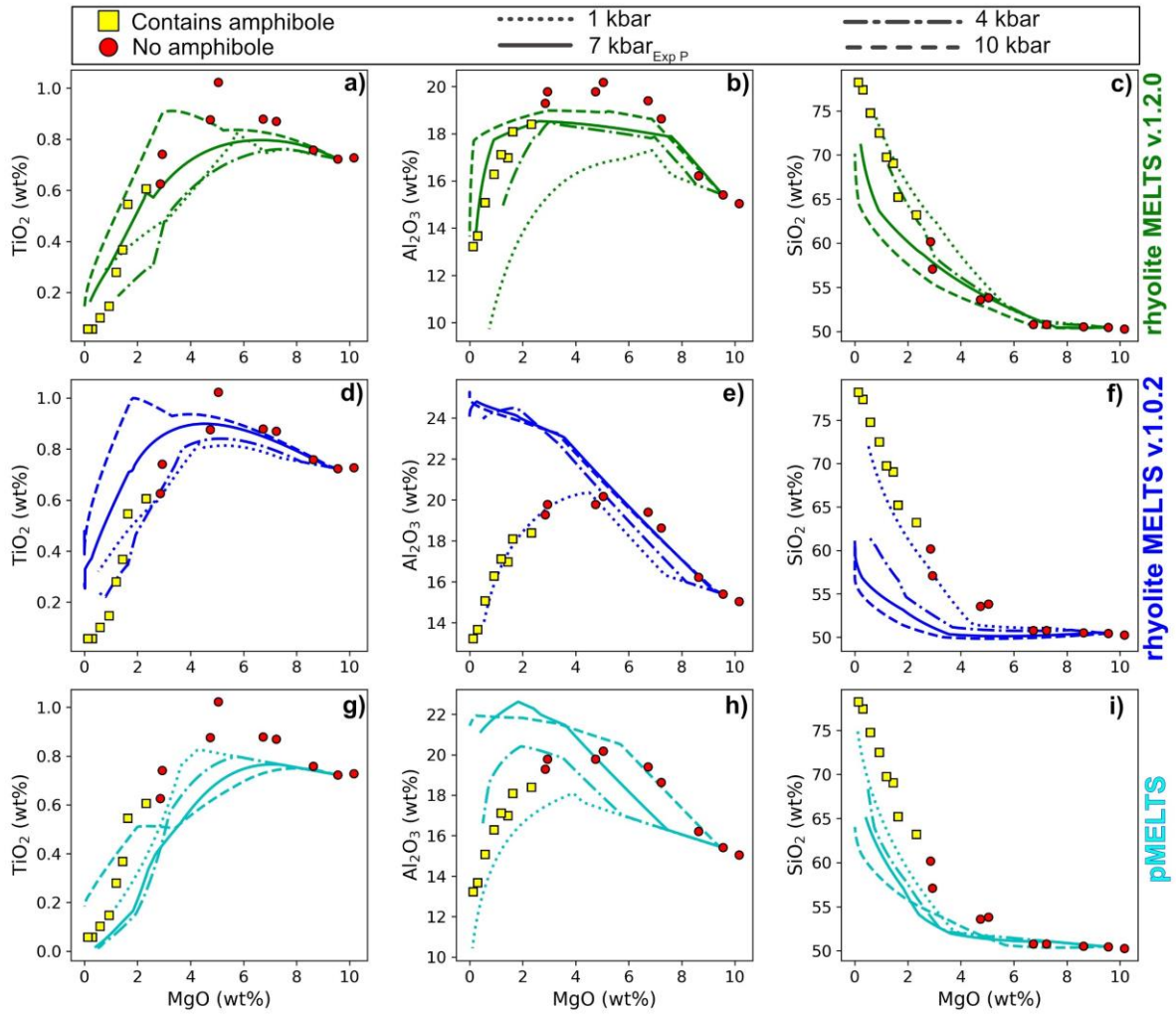

Figure 27 – Comparison of fractional crystallization experiments from Nandedkar et al. (2014) at 7 kbar to MELTS fractional crystallization models run using three different versions. Experiments containing amphibole are shown in yellow, those without amphibole in red. Models were run at the experimental fO_2 and H_2O contents, at 1, 4, 7 (Exp P) and 10 kbar. MELTS models run in pyMELTScalc using alphaMELTS for Python (Gleeson et al., 2023, Antoshechkina and Ghiorso, 2018).

8.2 Multi-phase saturation

As discussed in Section 2.2, pressure influences the location of mineral cotectics and eutectics. Under the assumption that the measured composition of a multi-phase saturated melt might contain information about the pressure of the system, rhyolite-MELTS has been used to address the crystallisation pressure of silicic and intermediate magmas that are co-saturated in quartz+feldspar (Bégué et al., 2014; Gualda et al., 2019; Gualda and Ghiorso, 2014; Pamukcu et al., 2015), feldspar+orthopyroxene±quartz (Pamukçu et al., 2021) or plagioclase+clinopyroxene+orthopyroxene (Harmon et al., 2018).

Specifically, these methods work by performing crystallisation calculations at several discrete pressures (and a specified H_2O and fO_2 value). T is progressively dropped from the liquidus, and the appearance of different phases is tracked. Mineral saturation curves (see Fig. 28a-b) are determined from these individual isobaric crystallization calculations. A residual is defined as the maximum temperature difference between the saturation curves of the phases of interest (ΔT, Fig. 28c). In many cases, the mineral saturation curves never intersect exactly at a single point, so the best fit pressure is calculated from the minimum point on the residual curve. A solution is only considered valid if the residual T gets within a pre-specified threshold value of a perfect intersection (e.g., 5°C for quartz – plagioclase – alkali-feldspar equilibrium; Gualda and Ghiorso, 2014). This threshold varies - in their application of this method to Plag-Opx-Cpx equilibrium, Harmon et al. (2018) compare experimental pressures to calculated pressures with minimum residuals from 16–121°C.

One complication of these methods is that the position of saturation curves is not just influenced by pressure, but also fO_2 and melt H_2O content. This means for natural samples; calculations must be repeated at different melt fO_2 and H_2O contents to identify the location of the minimum T offset in multivariate P-fO_2-H_2O space. In an ideal world, this would mean that MELTS could be used simultaneously as a barometer, oxybarometer, and hygrometer. However, in reality, this very large solution space can result in substantial errors which do not reproduce the true conditions for P, fO_2, or H_2O.

8.2.1 Quartz – 2 Feldspar MELTS barometry

Interest in using the co-saturation of quartz, plagioclase and alkali feldspar to help constrain pressure (Gualda and Ghiorso, 2014) led to a substantial update to the MELTS algorithm in 2012. To recreate the near invariant behaviour of pumice and melt inclusion compositions from the early erupted Bishop Tuff which have major and trace element systematics indicating a low degree of freedom, Gualda et al. (2012) tweaked the enthalpy of formation of quartz and the potassic endmember in the alkali-feldspar solid-solution (Gualda et al. 2012, rhyolite-MELTS v1.0.2). Using this new model, and the residual T method described above, Gualda and Ghiorso (2014) estimated storage pressures for a variety of quartz-saturated rhyolites. They compared these MELTS pressures to H_2O-CO_2 saturation pressures from the Bishop Tuff (Anderson et al., 2000), the Younger Toba Tuff (Chesner and Luhr, 2010) and the Mamaku Ignimbrite (Bégué et al., 2014), and found a close agreement. Based on the results in Fig. 10 of Gualda and Ghiorso (2014), we calculate an R^2 of 0.75 and RMSE of 0.38 kbar for N=30 melt inclusions when performing a linear regression between the two pressure methods. However, it is worth noting N=17 of these inclusions are from the Bishop Tuff, which was used as a reference point for the tweaking of the rhyolite-MELTS model calibration (Gualda et al. 2012).

The rhyolite-MELTS quartz-feldspar barometers have since been applied to several other systems worldwide. This includes the application of quartz-plagioclase barometry to rhyolitic eruptions of the Taupo Volcano Zone, New Zealand (Bégué et al., 2014), and quartz - 2 feldspar barometry on the matrix glass of the Peach Spring Tuff, USA (Pamukcu et al., 2015). Results indicate spatial and/or temporal variations in the magma storage conditions beneath the Taupo Volcanic Zone, as well as correlations between rhyolite SiO_2 contents and pressure (Bégué et al., 2014; Pamukçu et al., 2020). However, these papers have been the subject to a number of comment-reply articles (e.g., Wilson et al., 2021, Pamukçu et al., 2021). Most notably, Wilke et al. (2017) question the accuracy of the rhyolite-MELTS barometer following comparison of the results of the rhyolite-MELTS geobarometer with their new empirical expression for the pressure of quartz+feldspar saturated liquids. The Wilke et al. (2017) method, termed DERP (Determining Rhyolitic Pressures), is based on experiments on haplogranitic compositions which examine the influence of melt H_2O content (or activity) and the normative melt An content (largely determined by the CaO content of the liquid) on the quartz+feldspar saturation surface. Comparison of rhyolite-MELTS and DERP barometric results for melt-inclusions and matrix glasses from the Taupo Volcanic Zone and Peach Spring Tuff revealed a large offset between the two methods, with DERP typically returning pressures around twice as large as those from rhyolite-MELTS. The pressure discrepancy between the two methods correlates with the normative melt An content (a key part of the new DERP parameterisation). Thus, Wilke et al. (2017) suggest that rhyolite-MELTS may underestimate magma storage pressures in Ca-bearing rhyolites.

The relative performance of DERP and rhyolite-MELTS was revisited by Gualda et al. (2019b), who argued that the use of multi-linear fits in DERP to determine the influence of P, An content and H_2O on the quartz – 2 feldspar thermal minimum results in a functional form that is thermodynamically impossible. As a result, extrapolation of the DERP barometer outside the range of the calibration data could lead to systematic errors. Gualda et al. (2019b) also question the use of TitaniQ as an independent barometer to compare to the results from DERP in Wilke et al. (2017), as the Ti content in quartz is influenced by a wide number of parameters, including the mineral growth rate and melt Ti activity, which may limit its use as a geobarometer (see section 2.11). To assess the performance of the 2 barometers in natural systems, Gualda et al. (2019b) compare the results derived from the DERP and rhyolite-MELTS barometers to independent pressure estimates from H_2O-CO_2 saturation in melt inclusions and amphibole thermobarometry. In general, the barometric estimates provided by rhyolite-MELTS are in good agreement with the independent pressure estimates. DERP-derived pressures are typically more scattered and often higher than those derived from melt inclusion or amphibole thermobarometry. However, given the issues with amphibole barometry discussed in section 2.6, such comparisons should perhaps be interpreted with caution.

Wilke et al. (2019) responded by stating that the large range of pressured estimated by the DERP barometer in Gualda et al. (2019b) result from its sensitivity to glass Na_2O and K_2O contents, which are used to calculate the normative Qz, Or, and Ab values. Wilke et al. (2019) suggest that in hydrous rhyolitic glasses where

alkali migration during analysis is a serious issue, DERP should only be used to estimate storage pressures when data quality is assured. Furthermore, Wilke et al. (2019) note that the experimental compositions used to calibrate the DERP barometer all contain normative corundum, meaning that all CaO in the glass is used to calculate the normative An content. In many natural samples, such as the Peach Spring Tuff used by Pamukcu et al. (2015), lower Al_2O_3 contents lead to the presence of Wollastonite in the normative mineral assemblage, complicating the determination of the normative melt An content. As normative Wollastonite is not accounted for in the DERP calibration, this could explain the offset between the two barometers and indicates that DERP should only be used in systems where Corundum appears in the normative mineral assemblage.

Therefore, for most natural samples where Wollastonite is present in the normative mineral assemblage, the rhyolite-MELTS geobarometer might be more reliable than empirically calibrated alternatives like DERP. Nevertheless, questions regarding the application of the rhyolite-MELTS barometer to natural systems still remain, especially as the test datasets used to evaluate this barometer have largely relied on data from the Bishop Tuff (part of the 2012 recalibration). In addition, inclusion of the updated H_2O-CO_2 model of Ghiorso and Gualda (2015) in the rhyolite-MELTS calculations (i.e., rhyolite-MELTS v1.2.0) shifts the quartz and sanidine stability field to such an extent that 3–phase saturation cannot be simulated at any pressure for the compositions of Gualda and Ghiorso (2014) and Pamukcu et al. (2015). This indicates a further update to the quartz + sanidine ± plagioclase thermodynamic properties is necessary to align with the most recent volatile solubility model, so that users do not need to perform calculations for magmas that are typically saturated in a mixed H_2O-CO_2 fluid phase using an outdated H_2O solubility model (Ghiorso et al. 1995). We are not of aware of any new experiments that can be used as an independent test dataset for resolving the rhyolite-MELTS vs. DERP debate, and to gain a better understanding of the errors involved. Further experiments in this compositional range will be vital to move this approach forward in a rigorous manner.

8.2.2 Plagioclase – 2 pyroxene MELTS barometry

Since the inception of the rhyolite-MELTS geobarometer in 2014, the general method developed by Gualda and Ghiorso (2014) has been expanded to examine the cosaturation of other phases. Harmon et al. (2018) suggest that the rhyolite-MELTS thermodynamic models could be used to provide pressure estimates for intermediate magmas saturated in plagioclase, clinopyroxene and orthopyroxene.

To test the plagioclase – 2 pyroxene geobarometer, Harmon et al. (2018) apply their method to N = 8 experiments from the LEPR database that are saturated in 2 or more of the phases of interest. As the plagioclase - 2 pyroxene geobarometer is significantly more sensitive to fO_2 and H_2O content than the quartz -2 feldspar barometer, they use experimental fO_2 and melt H_2O contents for these comparisons to eliminate the multi-dimensional aspects of mineral stability, allowing the best fit pressure to be found. Of the 8 experiments they use, only one returned a ΔT between the 3 mineral saturation curves of <20°C, with the minimum T offset for other experiments stretching up to 121°C (i.e., the saturation curves never intercept close to one another).

The single experiment with a minimum T offset <20°C (1140mf #27 from Grove et al. 1997) returns a predicted P only 0.2 kbar offset from the true experimental P. If the threshold for the minimum T offset is relaxed, experiments with minimum T offsets between 20 and 40°C also return P estimates within ~0.25 kbar of their experimental P. However, convergence of only 4 experiments conducted at 0.00 1–1 kbar where fO_2 and melt H_2O contents are known makes it difficult to robustly assess the accuracy of the geobarometer in natural systems when applied up to the 5 kbar limit suggested by Harmon et al. (2018).

We investigate this method further using experiments from variably hydrous magmas cosaturated in plagioclase, orthopyroxene and clinopyroxene present in the ArcPL dataset conducted within the pressure range suggested by Harmon et al. (2018, 0–5 kbar, N=39). As for LLD methods, we find that the version of MELTS used for these calculations drastically affects calculations of storage conditions. Based on the flowchart provided on the MELTS-OFM website (https://melts.ofm-research.org/MELTS-decision-tree.html), rhyolite-MELTS v1.2.0 should be used for these calculations, as these experiments contain dissolved H_2O (±CO_2). However, Harmon et al. (2018) use rhyolite-MELTS v.1.0.2. For experiment PEM12–19 from Moore and Carmichael (1998), rhyolite-MELTS v.1.0.2 shows very good convergence at pressures very close to the experimental pressure (Fig. 28e). However, if rhyolite-MELTS v1.2.0 is used, the clinopyroxene stability curve intersects plagioclase and orthopyroxene at significantly higher pressures (Fig. 28a-b), leading to an estimated pressure of ~ 6 kbar (~5 kbar higher than the experimental pressure, Fig. 28c).

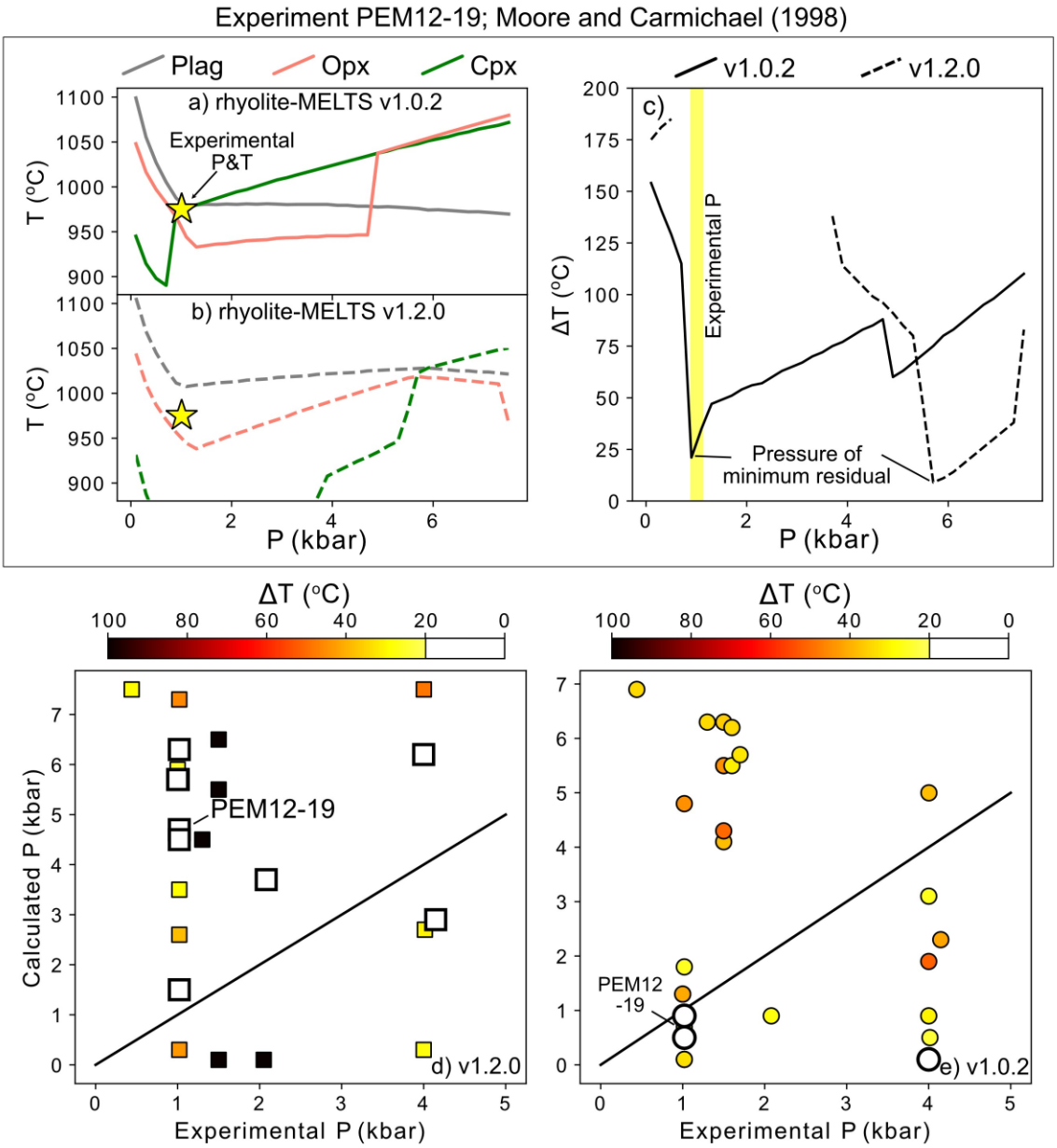

Figure 28: Assessing the Rhyolite-MELTS Plagioclase 2–pyroxene barometer of Harmon et al. (2018). a-b) Constructing mineral stability curves for Exp. PEM1 2–19 from Moore and Carmichael (1998) at the experimental fO_2 (ΔNNO=+1.1) and H_2O contents (3.6 wt%) using two different versions of MELTS. c) Calculating the maximum T offset at each pressure between the three mineral stability curves. The MELTS barometer takes the minimum residual as the best-fit T (~1 and ~6 kbar depending on the MELTS version). d-e) Testing the barometer using experiments saturated in Plag-2 pyroxene from ArcPL. Calculated pressure using the residual method plotted against the experimental pressure (calculations performed at experiment fO_2 and H_2O contents). Experiments with residuals <20°C are colored white, and larger residuals are colored based on this value. Calculations performed in pyMELTSCalc (Gleeson et al., 2022) using alphaMELTS for Python (Antoshechkina and Ghiorso, 2018).

Using rhyolite-MELTS v.1.0.2 for all N=39 experiments, N=10 do not stabilize all 3 phases at any pressure within 200°C of the liquidus, which is well below the experimental temperature in all cases. Of the remaining N=29, models converging with a residual <20 °C are shown in white on Fig. 28d-e. These produce a very poor fit to experimental pressures. If we take solutions produced at larger temperature residuals (following Harmon et al. 2018), there is no improvement. Using rhyolite-MELTS v1.2.0, N=23 experiments converge, and the fit is similarly bad, regardless of the temperature residual used. The poor performance of this barometer supports

previous criticism of the ability of MELTS to correctly predict the stability of these phases, pointing to the need for better solution models (e.g., Klein et al., 2023; Nandedkar et al., 2014; Villiger, 2004).

9. Other methods

There are of course, numerous methods to determine magma storage conditions which we do not address in detail, both in the interest of relative(!) brevity, and because there is insufficient experimental data that wasn't used during calibration to independently test models.

Additional thermometers have been developed based on:

- REE exchange between Opx-Cpx (Liang et al., 2013) and Plag-Cpx (Sun and Liang, 2012).
- Mg-Fe exchange between Ol and Cpx (Loucks, 1996).
- Ni partitioning between Ol-Liq (resulting in a H_2O-indepenent thermometer, Pu et al., 2021, 2017).
- NaSi-CaAl exchange between Amp-Plag (e.g., Holland and Blundy, 1994; Molina et al., 2021).
- Mg exchange between Plag-Cpx (Sun and Lissenberg, 2018).

Hygrometers based on:

- Cpx-Liq major element equilibrium (e.g., Armienti et al., 2013; Perinelli et al., 2016).
- Ca exchange between Ol-Liq (Gavrilenko et al., 2016).
- The highest amphibole Mg# found in a given volcanic system (Krawczynski et al., 2012).
- The H_2O contents of nominally-anhydrous minerals (NAMs) combined with models of mineral-melt partition coefficients (Demoucy et al., 2006; Towbin et al., 2023; Wade et al., 2008).
- Projections of the Ol, Cpx and Plag cotectics (Klein et al. 2023).

Barometers based on:

- Sr/Y contents of erupted lavas (Profeta et al., 2016).
- 'Multi-reaction' thermodynamic models relying on underlying thermodynamic models (e.g., Holland and Powell, 2011), where predicted and observed mineral compositions and phase fractions are compared to constrain storage conditions (E.g., Ziberna et al. 2017, Nicoli and Matthews, 2019).
- Al-Si partitioning between Plag and Amp (Molina et al., 2015).
- CaO-Mg# systematics of mid-oceanic ridge magmas (Villiger et al., 2007).

Of course, these lists are by no means exhaustive.

10. Future developments should be guided by FAIR principles

It is becoming increasingly recognised that science needs to shift to a framework where research products are findable, accessible, interoperable, and reusable (FAIR; Wilkinson et al., 2016). In the context of this review, this applies not only to research data such as analyses of experimental products and natural samples, but also the tools and workflows used to perform calculations. There have already been a few advances in this regard, but there is still lots of work to do.

From a data availability perspective, a major advance came in 2008 when Hirschmann et al. (2008) created a web-hosted database of 6,600 experiments (The Library of Experimental Phase Relationships – LEPR), which has been widely used to calibrate thermobarometers and chemometers (e.g., Jorgenson et al., 2022; Petrelli et al., 2020). This compilation represented a massive team effort, requiring most phase compositions and experimental contents to be hand typed from data tables in journal pdfs. However, the dataset is still incomplete in many aspects, stemming from missing data in the underlying publications, compounded with missing information during digitization. For example, in the LEPR download of Cpx-Liq pairs used by Petrelli et al. (2020) and Putirka (2008), 66% of experiments do not have a glass H_2O content. In some cases, this represents the fact that the experiment was anhydrous, in others the fact that authors didn't report water, and sometimes because H_2O is often presented in a different table from other chemical information, so may have been missed during digitization. Similarly, with few exceptions, the number of analyses used to produce the reported average for each phase (e.g., N=5 Cpx analyses, N=8 amphibole analyses) is not present in LEPR. This makes filtering out experiments with compositions defined by small numbers of analyses challenging, despite the importance of this given the influence of analytical error on minor, pressure-sensitive components (e.g., Cpx, Wieser et al. 2023b).

A bigger challenge is that there is no framework by which LEPR is regularly updated as new experimental studies are published. This has led to individual authors digitizing data from new experimental papers to use in their studies (Jorgenson et al., 2022, Wieser et al. 2023a-b). However, individual researchers who compile data

may not have time to format the data for inclusion in the database, because under the current academic publishing model, they would gain no credit for this activity (citations for use of the database would go to the original author team from 2008). One option moving forwards may be for LEPR to frequently publish new short articles or Zenodo dois with an author team consisting of anyone who has contributed to the curation of the database (as for open-source tools such as Numpy; e.g., Dubois et al., 1996; Harris et al., 2020). Alternatively, the responsibility could be placed on people generating experimental data, where journal editors do not allow a paper to be accepted before the experimental data is included in these databases. However, in many cases, journals do not mandate authors submitting data to a specific repository. Community guidelines for exactly how such data should be presented and archived are clearly needed, as well as ways for data curation to be valued when hiring and promoting researchers (e.g., Klöcking et al., 2023).

From a modelling perspective, there has been a rapid increase in the number of open-source, easy to use tools to perform calculations, making workflows more user-friendly, faster, more reproducible, and less susceptible to user-error and version control issues. In general, calculation tools have evolved from GUIs, macro-enabled spreadsheets and web apps, many of which require users to type every single composition by hand, to python or R packages where calculations can be run on any number of rows in a user-supplied spreadsheet using Jupyter Notebooks or web apps built on top of underlying code (e.g., Iacovino and Till, 2019; Weber and Blundy, 2023). One major contribution towards more automated workflows for thermodynamic calculations has been the development of the ENKI ThermoEngine (Thermoengine Code Contributors, 2022), allowing the MELTS thermodynamic models and algorithms to be accessed through Python. This allows creation of modelling workflows or complete packages based on the underlying MELTS models. For example, the Fe-Ti oxybarometer and thermometer of Ghiorso and Evans (2008) was originally released as a web-app where users had to hand-type major element values for each Fe-Ti oxide pair. Ghiorso and Prissel (2020) produced a Jupyter Notebook using Thermoengine which allows users to upload an excel file of matching Fe-Ti oxide pairs, and all calculations are performed automatically. The open-source Python3 package VESIcal (Iacovino et al., 2021) relies on Thermoengine to perform calculations using the solubility model Magmasat (which requires MELTS, Ghiorso and Gualda, 2015), as well as 6 other popular solubility models. Prior to VESIcal, saturation pressure calculations were performed using different tools for each solubility model in a myriad of different environments (Excel macros, web apps, web servers). The MELTS thermodynamic models can also be accessed using the alphaMELTS for MATLAB/Python packages (Antoshechkina and Ghiorso, 2018). As the alphaMELTS for MATLAB/Python packages (and Thermoengine) requires some familiarity with the underlying language, easy-to-use, wrapped functions for common workflows have been released through the pyMELTSCalc package (used for calculations in Section 8, Gleeson et al., 2023).

Calculations using the thermodynamic models/databases developed by Holland and Powell (e.g., Holland and Powell, 1998; Holland et al. 2018), which represent the main thermodynamic alternative to MELTS in igneous petrology, have traditionally performed using a variety of different software packages, including THERMOCALC, Perple_X (Connolly, 2009, 2005) and Theriak-Domino (de Capitani and Petrakakis, 2010). The learning curve for these tools is typically quite steep, and it remains challenging to integrate the thermodynamic calculations with common coding languages such as MATLAB, Python3 or Julia. Development of MAGEMin, a C-based Gibbs Free Energy minimization software with a Julia interface (Reil et al. 2022), improves the ease with which thermodynamic calculations can be performed using the Holland et al. (2018) thermodynamic database. This is because the Julia MAGEMin functions can also be used outside of the main GUI and integrated with Python3 functions. This allows the pyMELTScalc package to perform the same calculations (e.g. LLD, phase stability, phase diagrams) using MELTS or the Holland et al. (2018) thermodynamic models. Such advances are vital for model intercomparison (e.g., Fig. 26).

For mineral-melt thermobarometry and chemometry, calculations using 100s of different popular equations can be performed in Thermobar (Wieser et al., 2022b). This tool replaces a very large number of separate Excel spreadsheets, R and Matlab code released by individual thermobarometry papers, and allows more complex functions such as assessing all possible pairs for equilibrium, error propagation etc. For thermobarometers applicable to determining the conditions of mantle melting, Python package meltPT (McNab and Ball, 2023) can perform calculations using twelve published expressions.

These open-source python tools allow investigation of science questions that were almost impossible to address using existing tools requiring extensive manual data input. For example, Wieser et al. (2022a) use VESIcal to perform detailed comparisons of solubility models, including their sensitivities to different parameters. Wieser et al. (2023a-b) use Thermobar to propagate thermobarometry uncertainties using Monte Carlo methods. Open-source packages also have the advantage that the source code is version-controlled, and hosted in a public

repository (e.g., on GitHub) for anyone to inspect and adapt. This means even if the authors stop supporting the packages (perhaps moving from academia into industry), packages could be updated by a third party, although as a community we need to develop clear guidelines as to how academic credit can be allocated for such an activity. This is in stark constant with numerous tools which have simply become unusable with age. For example, the volatile solubility model of Duan (2014) is no longer available at the website listed in the paper, requiring authors to rely on archived downloads (e.g., Allison et al., 2022 rely on a version archived in 2017).

11. Conclusions

A wide diversity of methods have been used to determine the pressures, temperatures, H_2O contents and fO_2 conditions at which magmas are stored and staged as they transit from the mantle to the surface. Many thermometry methods work very well, indicating that silicate melt (±mineral) compositions are sensitive to temperature. However, it becomes more challenging to determine temperatures in subsolidus or highly evolved systems. In contrast, many mineral-based and thermodynamical barometers perform extremely poorly, struggling to reliably distinguish between different storage regions in the crust within ~10–20 km. This partially results from thermodynamic limitations; mineral compositions are not overly sensitive to the relatively narrow range of crustal pressures in the vast majority of tectonic settings on Earth. This fundamental limitation is not helped by sources of analytical and experimental uncertainty (e.g., poor analytical precision for minor components, missing elements such as Cr, Wieser et al. 2023b). Melt inclusion barometers have the potential to be more precise, because the dissolution of CO_2 and H_2O is highly sensitive to pressure. However, extensive work is required to resolve discrepancies between solubility models, as well as evaluate the influence of the vapour bubble CO_2 in many published datasets. Raman-based fluid inclusion has great potential in specific systems, although further work is needed to investigate the influence of decrepitation, elastic relaxation, and the influence of other fluid species (e.g. SO_2, H_2O etc). Thermoba-Raman-try also shows great promise, but further work is required. We propose a number of key frontiers to address in the pursuit of better thermobarometers, hygrometers and oxybarometers:

1) The development of higher quality experimental and thermodynamic datasets with precisely constrained mineral compositions, fluid compositions, dissolved volatile contents, and experimental fO_2 for recalibration of thermodynamic models (e.g., MELTS), mineral-melt thermobarometers, and volatile solubility models. Sufficient experiments need to be performed to allow full isolation of a test dataset during model calibration. More experiments using mixed H_2O-CO_2 fluids are needed to understand phase stability in relatively CO_2-rich arc magmas.
2) Development of more robust infrastructure for compiling experimental and thermodynamic data, alongside sufficient metadata to assess data quality. This will ensure that application of new and exciting machine learning techniques will not suffer from the old computer science adage: 'garbage-in, garbage-out'.
3) Further development of open-source methods to perform calculations, allowing easy intercomparison between models, error propagation, and model updates as new data becomes available.

12. Author Contributions

PW coordinated the review and was responsible for writing and coding for all sections except those listed below. MG was responsible for the OPAM, MELTS and MAGEMin sections with edits from PW, and SM for Ol-Sp and Fe-Ti oxide sections. CD contributed text to the MI and FI section, and provided edits throughout. CD and EG contributed to analytical work. All authors reviewed and edited the text.

13. Acknowledgements

PW thanks Iris Buisman for extracting the Cpx counting statistics shown in Fig. 8, and Keith Putirka for many useful conversations on thermobarometry and the formulation and calibration of his equations. PW acknowledges support from NSF EAR 2217371, the Rose Hills Innovator Program, and start up funds to UC Berkeley for computing resources. EG acknowledges support from NSF EAR 2216738.

13. Useful websites and open-source tools

Tools for petrologists – Contains Excel workbooks and python scripts for a number of petrographic workflows.	http://www.kaylaiacovino.com/tools-for-petrologists/
VESIcal GitHub, Read The Docs and YouTube pages: Code, documentation and worked examples for calculations using VESIcal	https://github.com/kaylai/VESIcal, https://vesical.readthedocs.io/en/latest/
Thermobar read the docs page: Code, documentation and worked examples for thermobarometry and hygrometry calculations using Thermobar	https://github.com/PennyWieser/Thermobar,

	https://thermobar.readthedocs.io/en/latest/,
Putirka spreadsheet compilation: Contains Excel spreadsheets for different thermobarometry calculations	https://sites.google.com/mail.fresnostate.edu/keithputirka/home
MELTS resources: Links to download different MELTS calculation tools (Matlab, python, GUI, excel).	https://magmasource.caltech.edu/gitlist
MAGEMin: Gibbs free energy minimisation solver package	https://github.com/ComputationalThermodynamics/MAGEMin
PyMageMinCalc: Python package for common petrological workflows using MAGEMin.	https://github.com/gleesonm1/pyMAGEMINcalc
PyMELTScalc: Python package for easier calculations using Melts for Python	https://github.com/gleesonm1/pyMELTScalc
ENKI server: Allows calculations to be performed using ThermoEngine infrastructure without the need for local installation.	http://enki-portal.org/
NIST Web Book: Phase data for CO_2 and calculations using the CO_2 equation of state.	https://webbook.nist.gov/cgi/cbook.cgi?ID=C124389&Mask=1
DiadFit: Code, documentation and worked examples using DiadFit for fitting Raman data and performing EOS calculations for CO_2.	https://github.com/PennyWieser/DiadFit, https://diadfit.readthedocs.io/en/latest/
CoolProp: A python package for calculating thermodynamic properties of gases using different equation of states.	http://www.coolprop.org/

14. Data Availability

Jupyter Notebooks and Excel workbooks used to make each figure are available on GitHub (https://github.com/PennyWieser/Thermobarometry_Review_2023).

References.

Acosta, M.D., Watkins, J.M., Reed, M.H., Donovan, J.J., DePaolo, D.J., 2020. Ti-in-quartz: Evaluating the role of kinetics in high temperature crystal growth experiments. Geochimica et Cosmochimica Acta 281, 149–167. https://doi.org/10.1016/j.gca.2020.04.030

Afonso, J.C., Ranalli, G., Fernàndez, M., 2007. Density structure and buoyancy of the oceanic lithosphere revisited. Geophys. Res. Lett. 34, L10302. https://doi.org/10.1029/2007GL029515

Ague, J.J., 1997. Thermodynamic calculation of emplacement pressures for batholithic rocks, California: Implications for the aluminum-in-hornblende barometer. Geol 25, 563. https://doi.org/10.1130/0091-7613(1997)025<0563:TCOEPF>2.3.CO;2

Allison, C.M., Roggensack, K., Clarke, A.B., 2022. MafiCH: a general model for H2O–CO2 solubility in mafic magmas. Contrib Mineral Petrol 177, 40. https://doi.org/10.1007/s00410-022-01903-y

Allison, C.M., Roggensack, K., Clarke, A.B., 2021. Highly explosive basaltic eruptions driven by CO2 exsolution. Nat Commun 12, 217. https://doi.org/10.1038/s41467-020-20354-2

Almeev, R.R., Bolte, T., Nash, B.P., Holtz, F., Erdmann, M., Cathey, H.E., 2012. High-temperature, low-H2O Silicic Magmas of the Yellowstone Hotspot: an Experimental Study of Rhyolite from the Bruneau–Jarbidge Eruptive Center, Central Snake River Plain, USA. Journal of Petrology 53, 1837–1866. https://doi.org/10.1093/petrology/egs035

Alonso-Perez, R., Müntener, O., Ulmer, P., 2009. Igneous garnet and amphibole fractionation in the roots of island arcs: experimental constraints on andesitic liquids. Contrib Mineral Petrol 157, 541–558. https://doi.org/10.1007/s00410-008-0351-8

Andersen, D.J., Lindsley, D.H., 1988. Internally consistent solution models for Fe-Mg-Mn-Ti oxides; Fe-Ti oxides. American Mineralogist 73, 714–726.

Andersen, T., O'Reilly, S.Y., Griffin, W.L., 1984. The trapped fluid phase in upper mantle xenoliths from Victoria, Australia: implications for mantle metasomatism. Contr. Mineral. and Petrol. 88, 72–85. https://doi.org/10.1007/BF00371413

Anderson, A.T., Brown, 1993. CO, contents and formation pressures of some Kilauean melt inclusions. American Mineralogist 78, 794–803.

Anderson, A.T., Davis, A.M., Lu, F., 2000. Evolution of Bishop Tuff rhyolitic magma based on melt and magnetite inclusions and zoned phenocrysts. Journal of Petrology 41, 449–473.

Anderson, J.L., 1996. Status of thermobarometry in granitic batholiths, in: The Third Hutton Symposium on the Origin of Granites and Related Rocks. Geological Society of America. https://doi.org/10.1130/0-8137-2315-9.125

Anderson, J.L., Barth, A.P., Wooden, J.L., Mazdab, F., 2008. Thermometers and Thermobarometers in Granitic Systems. Reviews in Mineralogy and Geochemistry 69, 121–142. https://doi.org/10.2138/rmg.2008.69.4

Andújar, J., Scaillet, B., Pichavant, M., Druitt, T.H., 2015. Differentiation Conditions of a Basaltic Magma from Santorini, and its Bearing on the Production of Andesite in Arc Settings. Journal of Petrology 56, 765–794. https://doi.org/10.1093/petrology/egv016

Antoshechkina, P., Ghiorso, M.S., 2018. MELTS for MATLAB: A new educational and research tool for computational thermodynamics. AGU Fall Meeting, abstract #ED44B-23.

Aradi, L., Spránitz, T., Guzmics, T., Szabó, C., Berkesi, M., 2021. 3D Raman imaging of multiphase fluid and melt inclusions: challenges and perspectives, in: Goldschmidt2021 Abstracts. Presented at the Goldschmidt2021, European Association of Geochemistry, Virtual. https://doi.org/10.7185/gold2021.8071

Araya, N., Nakamura, M., Yasuda, A., Okumura, S., Sato, T., Iguchi, M., Miki, D., Geshi, N., 2019. Shallow magma pre-charge during repeated Plinian eruptions at Sakurajima volcano. Sci Rep 9, 1979. https://doi.org/10.1038/s41598-019-38494-x

Ariskin, A.A., Frenkel, M.Ya., Barmina, G.S., Nielsen, R.L., 1993. Comagmat: a Fortran program to model magma differentiation processes. Computers & Geosciences 19, 1155–1170. https://doi.org/10.1016/0098-3004(93)90020-6

Armienti, P., Perinelli, C., Putirka, K.D., 2013. A New Model to Estimate Deep-level Magma Ascent Rates, with Applications to Mt. Etna (Sicily, Italy). Journal of Petrology 54, 795–813. https://doi.org/10.1093/petrology/egs085

Aster, E.M., Wallace, P.J., Moore, L.R., Watkins, J., Gazel, E., Bodnar, R.J., 2016. Reconstructing CO2 concentrations in basaltic melt inclusions using Raman analysis of vapor bubbles. Journal of Volcanology and Geothermal Research 323, 148–162. https://doi.org/10.1016/j.jvolgeores.2016.04.028

Azbej, T., Severs, M.J., Rusk, B.G., Bodnar, R.J., 2007. In situ quantitative analysis of individual H2O–CO2 fluid inclusions by laser Raman spectroscopy. Chemical Geology 237, 255–263. https://doi.org/10.1016/j.chemgeo.2006.06.025

Bacon, C.R., Newman, S., Stolper, E., 1992. Water, CO2, Cl, and F in melt inclusions in phenocrysts from three Holocene explosive eruptions, Crater Lake, Oregon. American Mineralogist 77, 1021–1030.

Bakker, R., 2017. Re-Equilibration Processes in Fluid Inclusion Assemblages. Minerals 7, 117. https://doi.org/10.3390/min7070117

Bali, E., Hartley, M.E., Halldórsson, S.A., Gudfinnsson, G.H., Jakobsson, S., 2018. Melt inclusion constraints on volatile systematics and degassing history of the 2014–2015 Holuhraun eruption, Iceland. Contrib Mineral Petrol 173, 9. https://doi.org/10.1007/s00410-017-1434-1

Barclay, J., 2004. A Hornblende Basalt from Western Mexico: Water-saturated Phase Relations Constrain a Pressure-Temperature Window of Eruptibility. Journal of Petrology 45, 485–506. https://doi.org/10.1093/petrology/egg091

Barker, A.K., Rydeblad, E.M., Silva, S.M., 2021. Magma storage at Ocean Islands: insights from Cape Verde. Crustal Magmatic System Evolution: Anatomy, Architecture, and Physico-Chemical Processes 45–78. https://doi.org/10.1002/9781119564485.ch3

Barth, A., Newcombe, M., Plank, T., Gonnermann, H., Hajimirza, S., Soto, G.J., Saballos, A., Hauri, E., 2019. Magma decompression rate correlates with explosivity at basaltic volcanoes — Constraints from water diffusion in olivine. Journal of Volcanology and Geothermal Research 387, 106664. https://doi.org/10.1016/j.jvolgeores.2019.106664

Barth, A., Plank, T., 2021. The Ins and Outs of Water in Olivine-Hosted Melt Inclusions: Hygrometer vs. Speedometer. Front. Earth Sci. 9, 614004. https://doi.org/10.3389/feart.2021.614004

Baxter, R.J.M., Maclennan, J., Neave, D.A., Thordarson, T., 2023. Depth of Magma Storage Under Iceland Controlled by Magma Fluxes. Geochem Geophys Geosyst 24, e2022GC010811. https://doi.org/10.1029/2022GC010811

Beattie, P., 1993. Olivine-melt and orthopyroxene-melt equilibria. Contr. Mineral. and Petrol. 115, 103–111. https://doi.org/10.1007/BF00712982

Befus, K.S., Lin, J.-F., Cisneros, M., Fu, S., 2018. Feldspar Raman shift and application as a magmatic thermobarometer. American Mineralogist 103, 600–609. https://doi.org/10.2138/am-2018-6157

Bégué, F., Deering, C.D., Gravley, D.M., Kennedy, B.M., Chambefort, I., Gualda, G.A.R., Bachmann, O., 2014. Extraction, Storage and Eruption of Multiple Isolated Magma Batches in the Paired Mamaku and Ohakuri Eruption, Taupo Volcanic Zone, New Zealand. Journal of Petrology 55, 1653–1684. https://doi.org/10.1093/petrology/egu038

Bégué, F., Gravley, D.M., Chambefort, I., Deering, C.D., Kennedy, B.M., 2015. Magmatic volatile distribution as recorded by rhyolitic melt inclusions in the Taupo Volcanic Zone, New Zealand. Geological Society, London, Special Publications 410, 71–94. https://doi.org/10.1144/SP410.4

Bégué, Florence, Gualda, G.A.R., Ghiorso, M.S., Pamukcu, A.S., Kennedy, B.M., Gravley, D.M., Deering, C.D., Chambefort, I., 2014. Phase-equilibrium geobarometers for silicic rocks based on rhyolite-MELTS. Part 2: application to Taupo Volcanic Zone rhyolites. Contrib Mineral Petrol 168, 1082. https://doi.org/10.1007/s00410-014-1082-7

Bell, A.F., La Femina, P.C., Ruiz, M., Amelung, F., Bagnardi, M., Bean, C.J., Bernard, B., Ebinger, C., Gleeson, M., Grannell, J., Hernandez, S., Higgins, M., Liorzou, C., Lundgren, P., Meier, N.J., Möllhoff, M., Oliva, S.-J., Ruiz, A.G., Stock, M.J., 2021. Caldera resurgence during the 2018 eruption of Sierra Negra volcano, Galápagos Islands. Nat Commun 12, 1397. https://doi.org/10.1038/s41467-021-21596-4

Bell, I.H., Wronski, J., Quoilin, S., Lemort, V., 2014. Pure and Pseudo-pure Fluid Thermophysical Property Evaluation and the Open-Source Thermophysical Property Library CoolProp. Ind. Eng. Chem. Res. 53, 2498–2508. https://doi.org/10.1021/ie4033999

Bennett, E.N., Jenner, F.E., Millet, M.-A., Cashman, K.V., Lissenberg, C.J., 2019. Deep roots for mid-ocean-ridge volcanoes revealed by plagioclase-hosted melt inclusions. Nature 572, 235–239. https://doi.org/10.1038/s41586-019-1448-0

Berman, R.G., 1988. Internally-Consistent Thermodynamic Data for Minerals in the System Na2O-K2O-CaO-MgO-FeO-Fe2O3-Al2O3-SiO2-TiO2-H2O-CO2. Journal of Petrology 29, 445–522. https://doi.org/10.1093/petrology/29.2.445

Berndt, J., 2004. An Experimental Investigation of the Influence of Water and Oxygen Fugacity on Differentiation of MORB at 200 MPa. Journal of Petrology 46, 135–167. https://doi.org/10.1093/petrology/egh066

Black, B.A., Andrews, B.J., 2020. Petrologic imaging of the architecture of magma reservoirs feeding caldera-forming eruptions. Earth and Planetary Science Letters 552, 116572. https://doi.org/10.1016/j.epsl.2020.116572

Blatter, D.L., Carmichael, I.S.E., 2001. Hydrous phase equilibria of a Mexican high-silica andesite:A candidate for a mantle origin? Geochimica et Cosmochimica Acta 65, 4043–4065. https://doi.org/10.1016/S0016-7037(01)00708-6

Blatter, D.L., Sisson, T.W., Hankins, W.B., 2013. Crystallization of oxidized, moderately hydrous arc basalt at mid- to lower-crustal pressures: implications for andesite genesis. Contrib Mineral Petrol 166, 861–886. https://doi.org/10.1007/s00410-013-0920-3

Blundy, J., 2022. Chemical Differentiation by Mineralogical Buffering in Crustal Hot Zones. Journal of Petrology 63, egac054. https://doi.org/10.1093/petrology/egac054

Blundy, J., Cashman, K., 2008. Petrologic Reconstruction of Magmatic System Variables and Processes. Reviews in Mineralogy and Geochemistry 69, 179–239. https://doi.org/10.2138/rmg.2008.69.6

Blundy, J., Cashman, K.V., Rust, A., Witham, F., 2010. A case for CO2-rich arc magmas. Earth and Planetary Science Letters 290, 289–301. https://doi.org/10.1016/j.epsl.2009.12.013

Bodnar, R.J., Binns, P.R., Hall, D.L., 1989. Synthetic fluid inclusions - VI. Quantitative evaluation of the decrepitation behaviour of fluid inclusions in quartz at one atmosphere confining pressure. J Metamorph Geol 7, 229–242. https://doi.org/10.1111/j.1525-1314.1989.tb00586.x

Bogaerts, M., Scaillet, B., Auwera, J.V., 2006. Phase Equilibria of the Lyngdal Granodiorite (Norway): Implications for the Origin of Metaluminous Ferroan Granitoids. Journal of Petrology 47, 2405–2431. https://doi.org/10.1093/petrology/egl049

Bohrson, W.A., Clague, D.A., 1988. Origin of ultramafic xenoliths containing exsolved pyroxenes from Hualalai Volcano, Hawaii. Contrib Mineral Petrol 100, 139–155. https://doi.org/10.1007/BF00373581

Bolte, T., Holtz, F., Almeev, R., Nash, B., 2015. The Blacktail Creek Tuff: an analytical and experimental study of rhyolites from the Heise volcanic field, Yellowstone hotspot system. Contrib Mineral Petrol 169, 15. https://doi.org/10.1007/s00410-015-1112-0

Böttcher, N., Taron, J., Kolditz, O., Liedl, R., Park, C.-H., 2012. Comparison of equations of state for carbon dioxide for numerical simulations. Proceedings ModelCARE2011, Leipzig, Germany. IAHS Publ. 355) 9.

Boulanger, M., France, L., Deans, J.R.L., Ferrando, C., Lissenberg, C.J., von der Handt, A., 2020. Magma Reservoir Formation and Evolution at a Slow-Spreading Center (Atlantis Bank, Southwest Indian Ridge). Front. Earth Sci. 8, 554598. https://doi.org/10.3389/feart.2020.554598

Boullier, A.-M., Michot, G., Pecher, A., Barres, O., 1989. Diffusion and/or Plastic Deformation around Fluid Inclusions in Synthetic Quartz: New Investigations, in: Bridgwater, D. (Ed.), Fluid Movements — Element Transport and the Composition of the Deep Crust. Springer Netherlands, Dordrecht, pp. 345–360. https://doi.org/10.1007/978-94-009-0991-5_28

Brugman, K.K., Till, C.B., 2019. A low-aluminum clinopyroxene-liquid geothermometer for high-silica magmatic systems. American Mineralogist 104, 996–1004. https://doi.org/10.2138/am-2019-6842

Bucholz, C.E., Gaetani, G.A., Behn, M.D., Shimizu, N., 2013. Post-entrapment modification of volatiles and oxygen fugacity in olivine-hosted melt inclusions. Earth and Planetary Science Letters 374, 145–155. https://doi.org/10.1016/j.epsl.2013.05.033

Budd, D.A., Troll, V.R., Dahren, B., Burchardt, S., 2016. Persistent multitiered magma plumbing beneath Katla volcano, Iceland. Geochem. Geophys. Geosyst. 17, 966–980. https://doi.org/10.1002/2015GC006118

Buddington, A.F., Lindsley, D.H., 1964. Iron-Titanium Oxide Minerals and Synthetic Equivalents. Journal of Petrology 5, 310–357. https://doi.org/10.1093/petrology/5.2.310

Burke, E.A.J., 2001. Raman microspectrometry of fluid inclusions. Lithos 55, 139–158. https://doi.org/10.1016/S0024-4937(00)00043-8

Buso, R., Laporte, D., Schiavi, F., Cluzel, N., Fonquernie, C., 2022. High-pressure homogenization of olivine-hosted CO₂-rich melt inclusions in a piston cylinder: insight into the volatile content of primary mantle melts. Eur. J. Mineral. 34, 325–349. https://doi.org/10.5194/ejm-34-325-2022

Cadoux, A., Scaillet, B., Druitt, T.H., Deloule, E., 2014. Magma Storage Conditions of Large Plinian Eruptions of Santorini Volcano (Greece). Journal of Petrology 55, 1129–1171. https://doi.org/10.1093/petrology/egu021

Campione, M., Malaspina, N., Frezzotti, M.L., 2015. Threshold size for fluid inclusion decrepitation: Size for Fluid Inclusion Decrepitation. Journal of Geophysical Research: Solid Earth 120, 7396–7402. https://doi.org/10.1002/2015JB012086

Caracciolo, A., Bali, E., Guðfinnsson, G.H., Kahl, M., Halldórsson, S.A., Hartley, M.E., Gunnarsson, H., 2020. Temporal evolution of magma and crystal mush storage conditions in the Bárðarbunga-Veiðivötn volcanic system, Iceland. Lithos 352–353, 105234. https://doi.org/10.1016/j.lithos.2019.105234

Caracciolo, A., Halldórsson, S.A., Bali, E., Marshall, E.W., Jeon, H., Whitehouse, M.J., Barnes, J.D., Guðfinnsson, G.H., Kahl, M., Hartley, M.E., 2022. Oxygen isotope evidence for progressively assimilating trans-crustal magma plumbing systems in Iceland. Geology 50, 796–800. https://doi.org/10.1130/G49874.1

Cashman, K.V., Edmonds, M., 2019. Mafic glass compositions: a record of magma storage conditions, mixing and ascent. Phil. Trans. R. Soc. A. 377, 20180004. https://doi.org/10.1098/rsta.2018.0004

Chakraborty, S., Dohmen, R., 2022. Diffusion chronometry of volcanic rocks: looking backward and forward. Bull Volcanol 84, 57. https://doi.org/10.1007/s00445-022-01565-5

Cheng, L.-L., Yang, Z.-F., Zeng, L., Wang, Y., Luo, Z.-H., 2014. Giant plagioclase growth during storage of basaltic magma in Emeishan Large Igneous Province, SW China. Contrib Mineral Petrol 167, 971. https://doi.org/10.1007/s00410-014-0971-0

Chesner, C.A., Luhr, J.F., 2010. A melt inclusion study of the Toba Tuffs, Sumatra, Indonesia. Journal of Volcanology and Geothermal Research 197, 259–278. https://doi.org/10.1016/j.jvolgeores.2010.06.001

Cisneros, M., Befus, K.S., 2020. Applications and Limitations of Elastic Thermobarometry: Insights From Elastic Modeling of Inclusion-Host Pairs and Example Case Studies. Geochem. Geophys. Geosyst. 21. https://doi.org/10.1029/2020GC009231

Connolly, J.A.D., 2009. The geodynamic equation of state: What and how: GEODYNAMIC EQUATION OF STATE-WHAT AND HOW. Geochem. Geophys. Geosyst. 10. https://doi.org/10.1029/2009GC002540

Connolly, J.A.D., 2005. Computation of phase equilibria by linear programming: A tool for geodynamic modeling and its application to subduction zone decarbonation. Earth and Planetary Science Letters 236, 524–541. https://doi.org/10.1016/j.epsl.2005.04.033

Coogan, L.A., Saunders, A.D., Wilson, R.N., 2014. Aluminum-in-olivine thermometry of primitive basalts: Evidence of an anomalously hot mantle source for large igneous provinces. Chemical Geology 368, 1–10. https://doi.org/10.1016/j.chemgeo.2014.01.004

Costa, F., 2004. Petrological and Experimental Constraints on the Pre-eruption Conditions of Holocene Dacite from Volcan San Pedro (36 S, Chilean Andes) and the Importance of Sulphur in Silicic Subduction-related Magmas. Journal of Petrology 45, 855–881. https://doi.org/10.1093/petrology/egg114

Costa, F., Shea, T., Ubide, T., 2020. Diffusion chronometry and the timescales of magmatic processes. Nat Rev Earth Environ 1, 201–214. https://doi.org/10.1038/s43017-020-0038-x

Crabtree, S.M., Lange, R.A., 2011. Complex Phenocryst Textures and Zoning Patterns in Andesites and Dacites: Evidence of Degassing-Induced Rapid Crystallization? Journal of Petrology 52, 3–38. https://doi.org/10.1093/petrology/egq067

Dahren, B., Troll, V.R., Andersson, U.B., Chadwick, J.P., Gardner, M.F., Jaxybulatov, K., Koulakov, I., 2012. Magma plumbing beneath Anak Krakatau volcano, Indonesia: evidence for multiple magma storage regions. Contrib Mineral Petrol 163, 631–651. https://doi.org/10.1007/s00410-011-0690-8

Dal-Negro, A., Manoli, S., Secca, L., Piccirillo, E.M., 1989. Megacrystic clinopyroxenes from Victoria (Australia); crystal chemical comparisons of pyroxenes from high and low pressure regimes. European Journal of Mineralogy 1 (1): 105–121.

Danyushevsky, L.V., McNeill, A.W., Sobolev, A.V., 2002. Experimental and petrological studies of melt inclusions in phenocrysts from mantle-derived magmas: an overview of techniques, advantages and complications. Chemical Geology 183, 5–24. https://doi.org/10.1016/S0009-2541(01)00369-2

Danyushevsky, L.V., Plechov, P., 2011. Petrolog3: Integrated software for modeling crystallization processes. Geochemistry, Geophysics, Geosystems 12, n/a-n/a. https://doi.org/10.1029/2011GC003516

Dayton, K., Gazel, E., Wieser, P., Troll, V.R., Carracedo, J.C., La Madrid, H., Roman, D.C., Ward, J., Aulinas, M., Geiger, H., Deegan, F.M., Gisbert, G., Perez-Torrado, F.J., 2023. Deep magma storage during the 2021 La Palma eruption. Sci. Adv. 9, eade7641. https://doi.org/10.1126/sciadv.ade7641

de Capitani, C., Petrakakis, K., 2010. The computation of equilibrium assemblage diagrams with Theriak/Domino software. American Mineralogist 95, 1006–1016. https://doi.org/10.2138/am.2010.3354

Demouchy, S., Jacobsen, S.D., Gaillard, F., Stern, C.R., 2006. Rapid magma ascent recorded by water diffusion profiles in mantle olivine. Geol 34, 429. https://doi.org/10.1130/G22386.1

DeVitre, C.L., Allison, C.M., Gazel, E., 2021. A high-precision CO2 densimeter for Raman spectroscopy using a Fluid Density Calibration Apparatus. Chemical Geology 584, 120522. https://doi.org/10.1016/j.chemgeo.2021.120522

DeVitre, C.L., Dayton, K., Gazel, E., Pamukçu, A., Gaetani, G., Wieser, P.E., 2023b. Laser heating effect on Raman analysis of CO2 co-existing as liquid and vapor in olivine-hosted melt inclusion bubbles. Volcanica 6, 201–219. https://doi.org/10.30909/vol.06.02.201219

DeVitre, C.L., Gazel, E., Ramalho, R.S., Venugopal, S., Steele-MacInnis, M., Hua, J., Allison, C.M., Moore, L.R., Carracedo, J.C., Monteleone, B., 2023a. Oceanic intraplate explosive eruptions fed directly from the mantle. Proc. Natl. Acad. Sci. U.S.A. 120, e2302093120. https://doi.org/10.1073/pnas.2302093120

Dixon, J.E., 1997. Degassing of alkalic basalts. American Mineralogist 82, 368–378. https://doi.org/10.2138/am-1997-3-415

Dobbin, K.K., Simon, R.M., 2011. Optimally splitting cases for training and testing high dimensional classifiers. BMC Med Genomics 4, 31. https://doi.org/10.1186/1755-8794-4-31

Drignon, M.J., Nielsen, R.L., Tepley, F.J., Bodnar, R.J., 2019. Upper mantle origin of plagioclase megacrysts from plagioclase-ultraphyric mid-oceanic ridge basalt. Geology 47, 43–46. https://doi.org/10.1130/G45542.1

Duan, X., 2014. A general model for predicting the solubility behavior of H2O–CO2 fluids in silicate melts over a wide range of pressure, temperature and compositions. Geochimica et Cosmochimica Acta 125, 582–609. https://doi.org/10.1016/j.gca.2013.10.018

Dubessy, J., Caumon, M.-C., Rull, F., Sharma, S., 2012. Instrumentation in Raman spectroscopy: elementary theory and practice, in: Ferraris, G., Dubessy, J., Caumon, M.-C., Rull, F. (Eds.), Raman Spectroscopy Applied to Earth Sciences and Cultural Heritage. European Mineralogical Union, pp. 83–172. https://doi.org/10.1180/EMU-notes.12.3

Dubois, P.F., Hinsen, K., Hugunin, J., 1996. Numerical Python. Comput. Phys. 10, 262. https://doi.org/10.1063/1.4822400

Erdmann, M., Koepke, J., 2016. Silica-rich lavas in the oceanic crust: experimental evidence for fractional crystallization under low water activity. Contrib Mineral Petrol 171, 83. https://doi.org/10.1007/s00410-016-1294-0

Erdmann, S., Martel, C., Pichavant, M., Bourdier, J.-L., Champallier, R., Komorowski, J.-C., Cholik, N., 2016. Constraints from Phase Equilibrium Experiments on Pre-eruptive Storage Conditions in Mixed Magma Systems: a Case Study on Crystal-rich Basaltic Andesites from Mount Merapi, Indonesia. J. Petrology 57, 535–560. https://doi.org/10.1093/petrology/egw019

Erdmann, S., Martel, C., Pichavant, M., Kushnir, A., 2014. Amphibole as an archivist of magmatic crystallization conditions: problems, potential, and implications for inferring magma storage prior to the paroxysmal 2010 eruption of Mount Merapi, Indonesia. Contrib Mineral Petrol 167, 1016. https://doi.org/10.1007/s00410-014-1016-4

Esposito, R., Klebesz, R., Bartoli, O., Klyukin, Y., Moncada, D., Doherty, A., Bodnar, R., 2012. Application of the Linkam TS1400XY heating stage to melt inclusion studies. Open Geosciences 4. https://doi.org/10.2478/s13533-011-0054-y

Esposito, R., Lamadrid, H.M., Redi, D., Steele-MacInnis, M., Bodnar, R.J., Manning, C.E., De Vivo, B., Cannatelli, C., Lima, A., 2016. Detection of liquid H_2O in vapor bubbles in reheated melt inclusions: Implications for magmatic fluid composition and volatile budgets of magmas? American Mineralogist 101, 1691–1695. https://doi.org/10.2138/am-2016-5689

Everall, N.J., 2010. Confocal Raman microscopy: common errors and artefacts. Analyst 135, 2512. https://doi.org/10.1039/c0an00371a

Fall, A., Tattitch, B., Bodnar, R.J., 2011. Combined microthermometric and Raman spectroscopic technique to determine the salinity of H2O–CO2–NaCl fluid inclusions based on clathrate melting. Geochimica et Cosmochimica Acta 75, 951–964. https://doi.org/10.1016/j.gca.2010.11.021

First, E.C., Hammer, J.E., Ruprecht, P., Rutherford, M., 2021. Experimental Constraints on Dacite Magma Storage beneath Volcán Quizapu, Chile. Journal of Petrology 62, egab027. https://doi.org/10.1093/petrology/egab027

Fowler, S.J., Spera, F.J., 2010. A Metamodel for Crustal Magmatism: Phase Equilibria of Giant Ignimbrites. Journal of Petrology 51, 1783–1830. https://doi.org/10.1093/petrology/egq039

Fowler, S.J., Spera, F.J., Bohrson, W.A., Belkin, H.E., De Vivo, B., 2007. Phase Equilibria Constraints on the Chemical and Physical Evolution of the Campanian Ignimbrite. Journal of Petrology 48, 459–493. https://doi.org/10.1093/petrology/egl068

Frezzotti, M.L., Andersen, T., Neumann, E.-R., Simonsen, S.L., 2002. Carbonatite melt–CO2 fluid inclusions in mantle xenoliths from Tenerife, Canary Islands: a story of trapping, immiscibility and fluid–rock interaction in the upper mantle. Lithos 64, 77–96. https://doi.org/10.1016/S0024-4937(02)00178-0

Frezzotti, M.L., De Vivo, B., Clocchiatti, R., 1991. Melt-mineral-fluid interactions in ultramafic nodules from alkaline lavas of Mount Etna (Sicily, Italy): Melt and fluid inclusion evidence. Journal of Volcanology and Geothermal Research 47, 209–219. https://doi.org/10.1016/0377-0273(91)90001-G

Frezzotti, M.L., Peccerillo, A., Bonelli, R., 2003. Magma ascent rates and depths of crustal magma reservoirs beneath the Aeolian volcanic Arc (Italy): Inferences from fluid and melt inclusions in xenoliths, in: Developments in Volcanology. Elsevier, pp. 185–205. https://doi.org/10.1016/S1871-644X(03)80030-X

Frezzotti, M.L., Tecce, F., Casagli, A., 2012. Raman spectroscopy for fluid inclusion analysis. Journal of Geochemical Exploration 112, 1–20. https://doi.org/10.1016/j.gexplo.2011.09.009

Gaetani, G.A., O'Leary, J.A., Shimizu, N., Bucholz, C.E., Newville, M., 2012. Rapid reequilibration of H2O and oxygen fugacity in olivine-hosted melt inclusions. Geology 40, 915–918. https://doi.org/10.1130/G32992.1

Gaffney, A.M., 2002. Environments of Crystallization and Compositional Diversity of Mauna Loa Xenoliths. Journal of Petrology 43, 963–981. https://doi.org/10.1093/petrology/43.6.963

Gao, R., Lassiter, J.C., Clague, D.A., Bohrson, W.A., 2022. Evolution of Hawaiian Volcano Magmatic Plumbing System and Implications for Melt/Edifice and Melt/Lithosphere Interaction: Constraints from Hualālai Xenoliths. Journal of Petrology 63, egac091. https://doi.org/10.1093/petrology/egac091

Garcia, M.O., 2003. A Petrologic Perspective of Kilauea Volcano's Summit Magma Reservoir. Journal of Petrology 44, 2313–2339. https://doi.org/10.1093/petrology/egg079

Gardner, J.E., Befus, K.S., Gualda, G.A.R., Ghiorso, M.S., 2014. Experimental constraints on rhyolite-MELTS and the Late Bishop Tuff magma body. Contrib Mineral Petrol 168, 1051. https://doi.org/10.1007/s00410-014-1051-1

Gavrilenko, M., Herzberg, C., Vidito, C., Carr, M.J., Tenner, T., Ozerov, A., 2016. A Calcium-in-Olivine Geohygrometer and its Application to Subduction Zone Magmatism. Journal of Petrology 57, 1811–1832. https://doi.org/10.1093/petrology/egw062

Gavrilenko, M., Krawczynski, M., Ruprecht, P., Li, W., Catalano, J.G., 2019. The quench control of water estimates in convergent margin magmas. American Mineralogist 104, 936–948. https://doi.org/10.2138/am-2019-6735

Geiger, H., Barker, A.K., Troll, V.R., 2016a. Locating the depth of magma supply for volcanic eruptions, insights from Mt. Cameroon. Sci Rep 6, 33629. https://doi.org/10.1038/srep33629

Geiger, H., Mattsson, T., Deegan, F.M., Troll, V.R., Burchardt, S., Gudmundsson, Ó., Tryggvason, A., Krumbholz, M., Harris, C., 2016b. Magma plumbing for the 2014-2015 Holuhraun eruption, Iceland. Geochem. Geophys. Geosyst. 17, 2953–2968. https://doi.org/10.1002/2016GC006317

Geiger, H., Troll, V.R., Jolis, E.M., Deegan, F.M., Harris, C., Hilton, D.R., Freda, C., 2018. Multi-level magma plumbing at Agung and Batur volcanoes increases risk of hazardous eruptions. Sci Rep 8, 10547. https://doi.org/10.1038/s41598-018-28125-2

Geist, D., Naumann, T., Larson, P., 1998. Evolution of Galapagos Magmas: Mantle and Crustal Fractionation without Assimilation. Journal of Petrology 39, 953–971. https://doi.org/10.1093/petroj/39.5.953

Gerlach, T.M., Graeber, E.J., 1985. Volatile budget of Kilauea volcano. Nature 313, 273–277. https://doi.org/10.1038/313273a0

Ghiorso, M., Prissel, K., 2020. ENKI Cloud App: Implementation of the Fe-Ti Oxide Geothermooxybarometer of Ghiorso and Evans, 2008. https://doi.org/10.5281/ZENODO.3866660

Ghiorso, M.S., 1990. Thermodynamic properties of hematite - ilmenite - geikielite solid solutions. Contr. Mineral. and Petrol. 104, 645–667. https://doi.org/10.1007/BF01167285

Ghiorso, M.S., Evans, B.W., 2008. Thermodynamics of Rhombohedral Oxide Solid Solutions and a Revision of the FE-TI Two-Oxide Geothermometer and Oxygen-Barometer. American Journal of Science 308, 957–1039. https://doi.org/10.2475/09.2008.01

Ghiorso, M.S., Gualda, G.A.R., 2015. An H2O–CO2 mixed fluid saturation model compatible with rhyolite-MELTS. Contrib Mineral Petrol 169, 53. https://doi.org/10.1007/s00410-015-1141-8

Ghiorso, M.S., Gualda, G.A.R., 2013. A method for estimating the activity of titania in magmatic liquids from the compositions of coexisting rhombohedral and cubic iron–titanium oxides. Contrib Mineral Petrol 165, 73–81. https://doi.org/10.1007/s00410-012-0792-y

Ghiorso, M.S., Hirschmann, M.M., Reiners, P.W., Kress, V.C., 2002. The pMELTS: A revision of MELTS for improved calculation of phase relations and major element partitioning related to partial melting of the mantle to 3 GPa. Geochem.-Geophys.-Geosyst. 3, 1–35. https://doi.org/10.1029/2001GC000217

Ghiorso, M.S., Sack, O., 1991. Fe-Ti oxide geothermometry: thermodynamic formulation and the estimation of intensive variables in silicic magmas. Contr. Mineral. and Petrol. 108, 485–510. https://doi.org/10.1007/BF00303452

Ghiorso, M.S., Sack, R.O., 1995. Chemical mass transfer in magmatic processes IV. A revised and internally consistent thermodynamic model for the interpolation and extrapolation of liquid-solid equilibria in magmatic systems at elevated temperatures and pressures. Contr. Mineral. and Petrol. 119, 197–212. https://doi.org/10.1007/BF00307281

Gibson, S.A., Geist, D., 2010. Geochemical and geophysical estimates of lithospheric thickness variation beneath Galápagos. Earth and Planetary Science Letters 300, 275–286. https://doi.org/10.1016/j.epsl.2010.10.002

Gleeson, M.L.M., Gibson, S.A., 2021. Insights Into the Nature of Plume-Ridge Interaction and Outflux of H_2O From the Galápagos Spreading Center. Geochem Geophys Geosyst 22. https://doi.org/10.1029/2020GC009560

Gleeson, M.L.M., Gibson, S.A., Stock, M.J., 2022. Constraints on the behaviour and content of volatiles in Galápagos magmas from melt inclusions and nominally anhydrous minerals. Geochimica et Cosmochimica Acta 319, 168–190. https://doi.org/10.1016/j.gca.2021.11.005

Gleeson, M.L.M., Gibson, S.A., Stock, M.J., 2021. Upper Mantle Mush Zones beneath Low Melt Flux Ocean Island Volcanoes: Insights from Isla Floreana, Galápagos. Journal of Petrology 61, egaa094. https://doi.org/10.1093/petrology/egaa094

Gleeson, M.L.M., Stock, M.J., Pyle, D.M., Mather, T.A., Hutchison, W., Yirgu, G., Wade, J., 2017. Constraining magma storage conditions at a restless volcano in the Main Ethiopian Rift using phase equilibria models. Journal of Volcanology and Geothermal Research 337, 44–61. https://doi.org/10.1016/j.jvolgeores.2017.02.026

Goltz, A.E., Krawczynski, M.J., Gavrilenko, M., Gorbach, N.V., Ruprecht, P., 2020. Evidence for superhydrous primitive arc magmas from mafic enclaves at Shiveluch volcano, Kamchatka. Contrib Mineral Petrol 175, 115. https://doi.org/10.1007/s00410-020-01746-5

Goranson, R.W., 1931. The solubility of water in granite magmas. American Journal of Science s5-22, 481–502. https://doi.org/10.2475/ajs.s5-22.132.481
Grove, T.L., Donnelly-Nolan, J.M., Housh, T., 1997. Magmatic processes that generated the rhyolite of Glass Mountain, Medicine Lake volcano, N. California. Contributions to Mineralogy and Petrology 127, 205–223. https://doi.org/10.1007/s004100050276
Grove, T.L., Kinzler, R.J., Bryan, W.B., 1992. Fractionation of Mid-Ocean Ridge Basalt (MORB), in: Mantle Flow and Melt Generation at Mid-Ocean Ridges. American Geophysical Union, pp. 281–311.
Gualda, Guilherme A R, Bégué, F., Pamukcu, A.S., Ghiorso, M.S., 2019. Rhyolite-MELTS vs DERP—Newer Does not Make it Better: a Comment on 'The Effect of Anorthite Content and Water on Quartz–Feldspar Cotectic Compositions in the Rhyolitic System and Implications for Geobarometry' by Wilke et al. (2017; Journal of Petrology, 58, 789–818). Journal of Petrology 60, 855–864. https://doi.org/10.1093/petrology/egz003
Gualda, G.A.R., Ghiorso, M.S., 2014. Phase-equilibrium geobarometers for silicic rocks based on rhyolite-MELTS. Part 1: Principles, procedures, and evaluation of the method. Contrib Mineral Petrol 168, 1033. https://doi.org/10.1007/s00410-014-1033-3
Gualda, G.A.R., Ghiorso, M.S., Lemons, R.V., Carley, T.L., 2012. Rhyolite-MELTS: a Modified Calibration of MELTS Optimized for Silica-rich, Fluid-bearing Magmatic Systems. Journal of Petrology 53, 875–890. https://doi.org/10.1093/petrology/egr080
Gualda, Guilherme A.R., Gravley, D.M., Deering, C.D., Ghiorso, M.S., 2019. Magma extraction pressures and the architecture of volcanic plumbing systems. Earth and Planetary Science Letters 522, 118–124. https://doi.org/10.1016/j.epsl.2019.06.020
Guo, K., Zhai, S.-K., Wang, X.-Y., Yu, Z.-H., Lai, Z.-Q., Chen, S., Song, Z.-J., Ma, Y., Chen, Z.-X., Li, X.-H., Zeng, Z.-G., 2018. The dynamics of the southern Okinawa Trough magmatic system: New insights from the microanalysis of the An contents, trace element concentrations and Sr isotopic compositions of plagioclase hosted in basalts and silicic rocks. Chemical Geology 497, 146–161. https://doi.org/10.1016/j.chemgeo.2018.09.002
Hagiwara, Y., Kawano, T., Takahata, K., Torimoto, J., Yamamoto, J., 2021. Temperature dependence of a Raman CO_2 densimeter from 23°C to 200°C and 7.2 to 248.7 MPa: Evaluation of density underestimation by laser heating. J Raman Spectrosc 52, 1744–1757. https://doi.org/10.1002/jrs.6188
Halldórsson, S.A., Marshall, E.W., Caracciolo, A., Matthews, S., Bali, E., Rasmussen, M.B., Ranta, E., Robin, J.G., Guðfinnsson, G.H., Sigmarsson, O., Maclennan, J., Jackson, M.G., Whitehouse, M.J., Jeon, H., van der Meer, Q.H.A., Mibei, G.K., Kalliokoski, M.H., Repczynska, M.M., Rúnarsdóttir, R.H., Sigurðsson, G., Pfeffer, M.A., Scott, S.W., Kjartansdóttir, R., Kleine, B.I., Oppenheimer, C., Aiuppa, A., Ilyinskaya, E., Bitetto, M., Giudice, G., Stefánsson, A., 2022. Rapid shifting of a deep magmatic source at Fagradalsfjall volcano, Iceland. Nature 609, 529–534. https://doi.org/10.1038/s41586-022-04981-x
Hammer, J., Jacob, S., Welsch, B., Hellebrand, E., Sinton, J., 2016. Clinopyroxene in postshield Haleakala ankaramite: 1. Efficacy of thermobarometry. Contrib Mineral Petrol 171, 7. https://doi.org/10.1007/s00410-015-1212-x
Hammestrom, J.E., Zen, E.-A., 1986. Aluminum in hornblende: An empirical igneous geobarometer. American Mineralogist.
Hansteen, T.H., Klugel, A., 2008. Fluid Inclusion Thermobarometry as a Tracer for Magmatic Processes. Reviews in Mineralogy and Geochemistry 69, 143–177. https://doi.org/10.2138/rmg.2008.69.5
Hansteen, T.H., Klügel, A., Schmincke, H.-U., 1998. Multi-stage magma ascent beneath the Canary Islands: evidence from fluid inclusions. Contributions to Mineralogy and Petrology 132, 48–64. https://doi.org/10.1007/s004100050404
Hanyu, T., Yamamoto, J., Kimoto, K., Shimizu, K., Ushikubo, T., 2020. Determination of total CO2 in melt inclusions with shrinkage bubbles. Chemical Geology 557, 119855. https://doi.org/10.1016/j.chemgeo.2020.119855
Harmon, L.J., Cowlyn, J., Gualda, G.A.R., Ghiorso, M.S., 2018. Phase-equilibrium geobarometers for silicic rocks based on rhyolite-MELTS. Part 4: Plagioclase, orthopyroxene, clinopyroxene, glass geobarometer, and application to Mt. Ruapehu, New Zealand. Contrib Mineral Petrol 173, 7. https://doi.org/10.1007/s00410-017-1428-z
Harris, C.R., Millman, K.J., van der Walt, S.J., Gommers, R., Virtanen, P., Cournapeau, D., Wieser, E., Taylor, J., Berg, S., Smith, N.J., Kern, R., Picus, M., Hoyer, S., van Kerkwijk, M.H., Brett, M., Haldane, A., del Río, J.F., Wiebe, M., Peterson, P., Gérard-Marchant, P., Sheppard, K., Reddy, T., Weckesser, W., Abbasi, H., Gohlke, C., Oliphant, T.E., 2020. Array programming with NumPy. Nature 585, 357–362. https://doi.org/10.1038/s41586-020-2649-2

Hartley, M.E., Maclennan, J., Edmonds, M., Thordarson, T., 2014. Reconstructing the deep CO2 degassing behaviour of large basaltic fissure eruptions. Earth and Planetary Science Letters 393, 120–131. https://doi.org/10.1016/j.epsl.2014.02.031

Hauri, E.H., Maclennan, J., McKenzie, D., Gronvold, K., Oskarsson, N., Shimizu, N., 2018. CO2 content beneath northern Iceland and the variability of mantle carbon. Geology 46, 55–58. https://doi.org/10.1130/G39413.1

Helz, R.T., Thornber, C.R., 1987. Geothermometry of Kilauea Iki lava lake, Hawaii. Bulletin of Volcanology 49, 651–668. https://doi.org/10.1007/BF01080357

Hernandez Nava, A., Black, B.A., Gibson, S.A., Bodnar, R.J., Renne, P.R., Vanderkluysen, L., 2021. Reconciling early Deccan Traps CO_2 outgassing and pre-KPB global climate. Proc Natl Acad Sci USA 118, e2007797118. https://doi.org/10.1073/pnas.2007797118

Hernandez, P.R., Woodcock, A., Estrada, M., Schultz, P.W., 2018. Undergraduate Research Experiences Broaden Diversity in the Scientific Workforce. BioScience 68, 204–211. https://doi.org/10.1093/biosci/bix163

Herzberg, C., 2004. Partial Crystallization of Mid-Ocean Ridge Basalts in the Crust and Mantle. Journal of Petrology 45, 2389–2405. https://doi.org/10.1093/petrology/egh040

Heywood, L.J., DeBari, S.M., Gill, J.B., Straub, S.M., Schindlbeck-Belo, J.C., Escobar-Burciaga, R.D., Woodhead, J., 2020. Across-Arc Diversity in Rhyolites From an Intra-oceanic Arc: Evidence From IODP Site U1437, Izu-Bonin Rear Arc, and Surrounding Area. Geochem. Geophys. Geosyst. 21. https://doi.org/10.1029/2019GC008353

Higgins, O., Sheldrake, T., Caricchi, L., 2022. Machine learning thermobarometry and chemometry using amphibole and clinopyroxene: a window into the roots of an arc volcano (Mount Liamuiga, Saint Kitts). Contrib Mineral Petrol 177, 10. https://doi.org/10.1007/s00410-021-01874-6

Hirschmann, M.M., Ghiorso, M.S., Davis, F.A., Gordon, S.M., Mukherjee, S., Grove, T.L., Krawczynski, M., Medard, E., Till, C.B., 2008. Library of Experimental Phase Relations (LEPR): A database and Web portal for experimental magmatic phase equilibria data: LIBRARY OF EXPERIMENTAL PHASE RELATIONS. Geochem. Geophys. Geosyst. 9, n/a-n/a. https://doi.org/10.1029/2007GC001894

Holland, T., Blundy, J., 1994. Non-ideal interactions in calcic amphiboles and their bearing on amphibole-plagioclase thermometry. Contr. Mineral. and Petrol. 116, 433–447. https://doi.org/10.1007/BF00310910

Holland, T.J.B., Green, E.C.R., Powell, R., 2018. Melting of Peridotites through to Granites: A Simple Thermodynamic Model in the System KNCFMASHTOCr. Journal of Petrology 59, 881–900. https://doi.org/10.1093/petrology/egy048

Holland, T.J.B., Powell, R., 2011. An improved and extended internally consistent thermodynamic dataset for phases of petrological interest, involving a new equation of state for solids: THERMODYNAMIC DATASET FOR PHASES OF PETROLOGICAL INTEREST. Journal of Metamorphic Geology 29, 333–383. https://doi.org/10.1111/j.1525-1314.2010.00923.x

Holland, T.J.B., Powell, R., 2004. An internally consistent thermodynamic data set for phases of petrological interest. Journal of Metamorphic Geology 16, 309–343. https://doi.org/10.1111/j.1525-1314.1998.00140.x

Holland, T.J.B., Powell, R., 1998. An internally consistent thermodynamic data set for phases of petrological interest. Journal of Metamorphic Geology 16, 309–343. https://doi.org/10.1111/j.1525-1314.1998.00140.x

Holland, T.J.B., Powell, R., 1990. An enlarged and updated internally consistent thermodynamic dataset with uncertainties and correlations: the system K2O–Na2O–CaO–MgO–MnO–FeO–Fe2O3–Al2O3–TiO2–SiO2–C–H2–O2. J Metamorph Geol 8, 89–124. https://doi.org/10.1111/j.1525-1314.1990.tb00458.x

Hollister, L., Grissom, G., Peters, E.K., Stowell, H.H., SIsson, V., 1987. Confirmation of the empirical correlation of Al in hornblende with pressure of solidification of calc-alkaline plutons 72 (3–4): 231–239.

Huang, R., Audétat, A., 2012. The titanium-in-quartz (TitaniQ) thermobarometer: A critical examination and re-calibration. Geochimica et Cosmochimica Acta 84, 75–89. https://doi.org/10.1016/j.gca.2012.01.009

Humphreys, M.C.S., Cooper, G.F., Zhang, J., Loewen, M., Kent, A.J.R., Macpherson, C.G., Davidson, J.P., 2019. Unravelling the complexity of magma plumbing at Mount St. Helens: a new trace element partitioning scheme for amphibole. Contrib Mineral Petrol 174, 9. https://doi.org/10.1007/s00410-018-1543-5

Hurai, V., 2010. Fluid inclusion geobarometry: Pressure corrections for immiscible H2O–CH4 and H2O–CO2 fluids. Chemical Geology 278, 201–211. https://doi.org/10.1016/j.chemgeo.2010.09.014

Hutchison, W., Mather, T.A., Pyle, D.M., Boyce, A.J., Gleeson, M.L.M., Yirgu, G., Blundy, J.D., Ferguson, D.J., Vye-Brown, C., Millar, I.L., Sims, K.W.W., Finch, A.A., 2018. The evolution of magma during continental

rifting: New constraints from the isotopic and trace element signatures of silicic magmas from Ethiopian volcanoes. Earth and Planetary Science Letters 489, 203–218. https://doi.org/10.1016/j.epsl.2018.02.027
Iacono-Marziano, G., Morizet, Y., Le Trong, E., Gaillard, F., 2012. New experimental data and semi-empirical parameterization of H2O–CO2 solubility in mafic melts. Geochimica et Cosmochimica Acta 97, 1–23. https://doi.org/10.1016/j.gca.2012.08.035
Iacovino, K., Matthews, S., Wieser, P.E., Moore, G., Begue, F., 2021. VESIcal Part I: An open-source thermodynamic model engine for mixed volatile (H2O-CO2) solubility in silicate melt. Earth and Space Science. https://doi.org/10.1029/2020EA001584
Iacovino, K., Till, C., 2019. DensityX: A program for calculating the densities of hydrous magmatic liquids from 427-1,627 °C and up to 30 kbar. Volcanica 2, 1–10. https://doi.org/10.30909/vol.02.01.0110
J. Bodnar, R., 2017. Fluid Inclusions, in: Bobrowsky, P., Marker, B. (Eds.), Encyclopedia of Engineering Geology, Encyclopedia of Earth Sciences Series. Springer International Publishing, Cham, pp. 1–5. https://doi.org/10.1007/978-3-319-39193-9_225-1
Jamshidi, K., Ghasemi, H., Troll, V.R., Sadeghian, M., Dahren, B., 2015. Magma storage and plumbing of adakite-type post-ophiolite intrusions in the Sabzevar ophiolitic zone, northeast Iran. Solid Earth 6, 49–72. https://doi.org/10.5194/se-6-49-2015
Jeffery, A.J., Gertisser, R., O'Driscoll, B., Pacheco, J.M., Whitley, S., Pimentel, A., Self, S., 2016. Temporal evolution of a post-caldera, mildly peralkaline magmatic system: Furnas volcano, São Miguel, Azores. Contrib Mineral Petrol 171, 42. https://doi.org/10.1007/s00410-016-1235-y
Jeffery, A.J., Gertisser, R., Self, S., Pimentel, A., O'Driscoll, B., Pacheco, J.M., 2017. Petrogenesis of the Peralkaline Ignimbrites of Terceira, Azores. Journal of Petrology 58, 2365–2402. https://doi.org/10.1093/petrology/egy012
Jennings, E.S., Gibson, S.A., Maclennan, J., 2019. Hot primary melts and mantle source for the Paraná-Etendeka flood basalt province: New constraints from Al-in-olivine thermometry. Chemical Geology 529, 119287. https://doi.org/10.1016/j.chemgeo.2019.119287
Jennings, E.S., Holland, T.J.B., 2015. A Simple Thermodynamic Model for Melting of Peridotite in the System NCFMASOCr. Journal of Petrology 56, 869–892. https://doi.org/10.1093/petrology/egv020
Johnson, E.R., Cashman, K.V., 2020. Understanding the storage conditions and fluctuating eruption style of a young monogenetic volcano: Blue Lake crater (<3 ka), High Cascades, Oregon. Journal of Volcanology and Geothermal Research 408, 107103. https://doi.org/10.1016/j.jvolgeores.2020.107103
Johnson, M.C., Rutherford, M.J., 1989. Experimental calibration of the aluminum-in-hornblende geobarometer with application to Long Valley caldera (California) volcanic rocks. Geol 17, 837. https://doi.org/10.1130/0091-7613(1989)017<0837:ECOTAI>2.3.CO;2
Jorgenson, C., Caricchi, L., Stueckelberger, M., Fevola, G., Weber, G., 2021. A myriad of melt inclusions: a synchrotron microtomography study of melt inclusions and vapour bubbles from Colli Albani (Italy) (other). pico. https://doi.org/10.5194/egusphere-egu21-13287
Jorgenson, C., Higgins, O., Petrelli, M., Bégué, F., Caricchi, L., 2022. A Machine Learning-Based Approach to Clinopyroxene Thermobarometry: Model Optimization and Distribution for Use in Earth Sciences. JGR Solid Earth 127. https://doi.org/10.1029/2021JB022904
Kawakami, Y., Yamamoto, J., Kagi, H., 2003. Micro-Raman Densimeter for CO_2 Inclusions in Mantle-Derived Minerals. Appl Spectrosc 57, 1333–1339. https://doi.org/10.1366/000370203322554473
Kawamoto, T., 1996. Experimental constraints on differentiation and H2O abundance of calc-alkaline magmas. Earth and Planetary Science Letters 144, 577–589. https://doi.org/10.1016/S0012-821X(96)00182-3
Kawasaki, T., Osanai, Y., 2008. Empirical thermometer of TiO_2 in quartz for ultrahigh-temperature granulites of East Antarctica. Geological Society, London, Special Publications 308, 419–430. https://doi.org/10.1144/SP308.21
Keppler, H., 1989. The influence of the fluid phase composition on the solidus temperatures in the haplogranite system NaAlSi3O8-KAlSi3O8-SiO2-H2O-CO2. Contrib Mineral Petrol 102, 321–327. https://doi.org/10.1007/BF00373725
King, P.L., Holloway, J.R., 2002. CO2 solubility and speciation in intermediate (andesitic) melts: the role of H2O and composition. Geochimica et Cosmochimica Acta 66, 1627–1640. https://doi.org/10.1016/S0016-7037(01)00872-9
Klein, B.Z., Jagoutz, O., Schmidt, M.W., Kueter, N., 2023. A Global Assessment of the Controls on the Fractionation of Arc Magmas. Geochem Geophys Geosyst 24, e2023GC010888. https://doi.org/10.1029/2023GC010888

Klöcking, M., Wyborn, L., Lehnert, K.A., Ware, B., Prent, A.M., Profeta, L., Kohlmann, F., Noble, W., Bruno, I., Lambart, S., Ananuer, H., Barber, N.D., Becker, H., Brodbeck, M., Deng, H., Deng, K., Elger, K., De Souza Franco, G., Gao, Y., Ghasera, K.M., Hezel, D.C., Huang, J., Kerswell, B., Koch, H., Lanati, A.W., Ter Maat, G., Martínez-Villegas, N., Nana Yobo, L., Redaa, A., Schäfer, W., Swing, M.R., Taylor, R.J.M., Traun, M.K., Whelan, J., Zhou, T., 2023. Community recommendations for geochemical data, services and analytical capabilities in the 21st century. Geochimica et Cosmochimica Acta 351, 192–205. https://doi.org/10.1016/j.gca.2023.04.024

Klügel, A., 1998. Reactions between mantle xenoliths and host magma beneath La Palma (Canary Islands): constraints on magma ascent rates and crustal reservoirs. Contributions to Mineralogy and Petrology 131, 237–257.

Klügel, A., Day, S., Schmid, M., Faria, B., 2020. Magma Plumbing During the 2014–2015 Eruption of Fogo (Cape Verde Islands). Front. Earth Sci. 8, 157. https://doi.org/10.3389/feart.2020.00157

Kobayashi, T., Yamamoto, J., Hirajima, T., Ishibashi, H., Hirano, N., Lai, Y., Prikhod'ko, V.S., Arai, S., 2012. Conformity and precision of CO_2 densimetry in CO_2 inclusions: microthermometry *versus* Raman microspectroscopic densimetry: Conformity and precision of CO_2 densimetry in CO_2 inclusions. J. Raman Spectrosc. 43, 1126–1133. https://doi.org/10.1002/jrs.3134

Kohn, M.J., 2014. "Thermoba-Raman-try": Calibration of spectroscopic barometers and thermometers for mineral inclusions. Earth and Planetary Science Letters 388, 187–196. https://doi.org/10.1016/j.epsl.2013.11.054

Kohn, M.J. and Spear, F.S., 1991. Error propagation for barometers: 2. Application to rocks. *American Mineralogist*, *76*(1-2), pp.138-147.

Kohn, M.J., Mazzucchelli, M.L. and Alvaro, M., 2023. Elastic thermobarometry. *Annual Review of Earth and Planetary Sciences*, *51*, pp.331-366.

Koleszar, A.M., Kent, A.J.R., Wallace, P.J., Scott, W.E., 2012. Controls on long-term low explosivity at andesitic arc volcanoes: Insights from Mount Hood, Oregon. Journal of Volcanology and Geothermal Research 219–220, 1–14. https://doi.org/10.1016/j.jvolgeores.2012.01.003

Krawczynski, M.J., Grove, T.L., Behrens, H., 2012. Amphibole stability in primitive arc magmas: effects of temperature, H2O content, and oxygen fugacity. Contrib Mineral Petrol 164, 317–339. https://doi.org/10.1007/s00410-012-0740-x

Kress, V.C., Ghiorso, M.S., 2004. Thermodynamic modeling of post-entrapment crystallization in igneous phases. Journal of Volcanology and Geothermal Research 137, 247–260. https://doi.org/10.1016/j.jvolgeores.2004.05.012

Lamadrid, H.M., Moore, L.R., Moncada, D., Rimstidt, J.D., Burruss, R.C., Bodnar, R.J., 2017. Reassessment of the Raman CO 2 densimeter. Chemical Geology 450, 210–222. https://doi.org/10.1016/j.chemgeo.2016.12.034

Larocque, J., Canil, D., 2010. The role of amphibole in the evolution of arc magmas and crust: the case from the Jurassic Bonanza arc section, Vancouver Island, Canada. Contrib Mineral Petrol 159, 475–492. https://doi.org/10.1007/s00410-009-0436-z

Le Voyer, M., Kelley, K.A., Cottrell, E., Hauri, E.H., 2017. Heterogeneity in mantle carbon content from CO2-undersaturated basalts. Nat Commun 8, 14062. https://doi.org/10.1038/ncomms14062

Leahy, G.M., Collins, J.A., Wolfe, C.J., Laske, G., Solomon, S.C., 2010. Underplating of the Hawaiian Swell: evidence from teleseismic receiver functions: Underplating of the Hawaiian Swell. Geophysical Journal International 183, 313–329. https://doi.org/10.1111/j.1365-246X.2010.04720.x

Lee, C.-T.A., Anderson, D.L., 2015. Continental crust formation at arcs, the arclogite "delamination" cycle, and one origin for fertile melting anomalies in the mantle. Science Bulletin 60, 1141–1156. https://doi.org/10.1007/s11434-015-0828-6

Lerner, Allan H., Sublett, D.M., Cauley, C., Wallace, P., Bodnar, R.J., 2021. Magma storage depths and excess CO2 fluids from the explosive Keanakakoi tephra (Kilauea Volcano, Hawaii) based on measurements of melt and fluid inclusions.

Lerner, A. H., Wallace, P., Shea, T., 2021. The petrologic and degassing behavior of sulfur and other magmatic volatiles from the 2018 eruption of Kīlauea, Hawai'i: melt concentrations, magma storage depths, and magma recycling. Bulletin Volcanology 83:43, 1–32.

Li, X., Kind, R., Yuan, X., Wölbern, I., Hanka, W., 2004. Rejuvenation of the lithosphere by the Hawaiian plume. Nature 427, 827–829. https://doi.org/10.1038/nature02349

Liang, Y., Sun, C., Yao, L., 2013. A REE-in-two-pyroxene thermometer for mafic and ultramafic rocks. Geochimica et Cosmochimica Acta 102, 246–260. https://doi.org/10.1016/j.gca.2012.10.035

Lissenberg, C.J., MacLeod, C.J., 2016. A Reactive Porous Flow Control on Mid-ocean Ridge Magmatic Evolution. Journal of Petrology 57, 2195–2220. https://doi.org/10.1093/petrology/egw074
Liu, Y., Zhang, Y., Behrens, H., 2005. Solubility of H2O in rhyolitic melts at low pressures and a new empirical model for mixed H2O–CO2 solubility in rhyolitic melts. Journal of Volcanology and Geothermal Research 143, 219–235. https://doi.org/10.1016/j.jvolgeores.2004.09.019
Lones, M.A., 2021. How to avoid machine learning pitfalls: a guide for academic researchers. arXiv:2108.02497 [cs].
Loucks, R.R., 1996. A precise olivine-augite Mg-Fe-exchange geothermometer. Contributions to Mineralogy and Petrology 125, 140–150. https://doi.org/10.1007/s004100050211
Lowenstern, J.B., 2003. Melt inclusions come of age: Volatiles, volcanoes, and sorby's legacy, in: Developments in Volcanology. Elsevier, pp. 1–21. https://doi.org/10.1016/S1871-644X(03)80021-9
Ludden, J.N., 1978. Magmatic evolution of the basaltic shield volcanoes of Reunion Island. Journal of Volcanology and Geothermal Research 4, 171–198. https://doi.org/10.1016/0377-0273(78)90035-5
Luo, B., Wang, Z., Song, J., Qian, Y., He, Q., Li, Y., Head, J.W., Moynier, F., Xiao, L., Becker, H., 2023. The magmatic architecture and evolution of the Chang'e-5 lunar basalts. Nature Geoscience 1–8.
Mackwell, S.J., Kohlstedt, D.L., 1990. Diffusion of hydrogen in olivine: Implications for water in the mantle. J. Geophys. Res. 95, 5079. https://doi.org/10.1029/JB095iB04p05079
Maclennan, J., 2017. Bubble formation and decrepitation control the CO2 content of olivine-hosted melt inclusions. Geochemistry, Geophysics, Geosystems 18, 597–616. https://doi.org/10.1002/2016GC006633
Maclennan, J., 2008. Concurrent Mixing and Cooling of Melts under Iceland. Journal of Petrology 49, 1931–1953. https://doi.org/10.1093/petrology/egn052
Maclennan, J., McKenzie, D., Gronvöld, K., Slater, L., 2001. Crustal accretion under northern Iceland. Earth and Planetary Science Letters 191, 295–310. https://doi.org/10.1016/S0012-821X(01)00420-4
Mandler, B.E., Donnelly-Nolan, J.M., Grove, T.L., 2014. Straddling the tholeiitic/calc-alkaline transition: the effects of modest amounts of water on magmatic differentiation at Newberry Volcano, Oregon. Contrib Mineral Petrol 168, 1066. https://doi.org/10.1007/s00410-014-1066-7
Marxer, F., Ulmer, P., Müntener, O., 2022. Polybaric fractional crystallisation of arc magmas: an experimental study simulating trans-crustal magmatic systems. Contrib Mineral Petrol 177, 3. https://doi.org/10.1007/s00410-021-01856-8
Masotta, M., Mollo, S., 2019. A New Plagioclase-Liquid Hygrometer Specific to Trachytic Systems. Minerals 9, 375. https://doi.org/10.3390/min9060375
Masotta, M., Mollo, S., Freda, C., Gaeta, M., Moore, G., 2013. Clinopyroxene–liquid thermometers and barometers specific to alkaline differentiated magmas. Contrib Mineral Petrol 166, 1545–1561. https://doi.org/10.1007/s00410-013-0927-9
Matthews, S., Shorttle, O., Maclennan, J., 2016. The temperature of the Icelandic mantle from olivine-spinel aluminum exchange thermometry. Geochemistry, Geophysics, Geosystems 17, 4725–4752. https://doi.org/10.1002/2016GC006497
Matthews, S., Wong, K., Shorttle, O., Edmonds, M., Maclennan, J., 2021. Do Olivine Crystallization Temperatures Faithfully Record Mantle Temperature Variability? Geochem Geophys Geosyst 22. https://doi.org/10.1029/2020GC009157
McNab, F., Ball, P., 2023. meltPT: A Python package for basaltic whole-rock thermobarometric analysis with application to Hawai'i. Volcanica 6, 63–76. https://doi.org/10.30909/vol.06.01.6376
Médard, E., Le Pennec, J.-L., 2022. Petrologic imaging of the magma reservoirs that feed large silicic eruptions. Lithos 428–429, 106812. https://doi.org/10.1016/j.lithos.2022.106812
Mironov, N., Portnyagin, M., Botcharnikov, R., Gurenko, A., Hoernle, K., Holtz, F., 2015. Quantification of the CO 2 budget and H 2 O–CO 2 systematics in subduction-zone magmas through the experimental hydration of melt inclusions in olivine at high H 2 O pressure. Earth and Planetary Science Letters 425, 1–11. https://doi.org/10.1016/j.epsl.2015.05.043
Molina, José F., Cambeses, A., Moreno, J.A., Morales, I., Lázaro, C., Montero, P., Bea, F., 2021. A Cautionary Note on Amphibole Geobarometry, in: The 2nd International Electronic Conference on Mineral Science. Presented at the IECMS 2021, MDPI, p. 17. https://doi.org/10.3390/iecms2021-09346
Molina, José Francisco, Cambeses, A., Moreno, J.A., Morales, I., Montero, P., Bea, F., 2021. A reassessment of the amphibole-plagioclase NaSi-CaAl exchange thermometer with applications to igneous and high-grade metamorphic rocks. American Mineralogist 106, 782–800. https://doi.org/10.2138/am-2021-7400

Molina, J.F., Moreno, J.A., Castro, A., Rodríguez, C., Fershtater, G.B., 2015. Calcic amphibole thermobarometry in metamorphic and igneous rocks: New calibrations based on plagioclase/amphibole Al-Si partitioning and amphibole/liquid Mg partitioning. Lithos 232, 286–305. https://doi.org/10.1016/j.lithos.2015.06.027

Mollo, S., Putirka, K., Misiti, V., Soligo, M., Scarlato, P., 2013. A new test for equilibrium based on clinopyroxene–melt pairs: Clues on the solidification temperatures of Etnean alkaline melts at post-eruptive conditions. Chemical Geology 352, 92–100. https://doi.org/10.1016/j.chemgeo.2013.05.026

Moore, G., Carmichael, I.S.E., 1998. The hydrous phase equilibria (to 3 kbar) of an andesite and basaltic andesite from western Mexico: constraints on water content and conditions of phenocryst growth. Contributions to Mineralogy and Petrology 130, 304–319. https://doi.org/10.1007/s004100050367

Moore, L.R., Gazel, E., Bodnar, R.J., 2021. The volatile budget of Hawaiian magmatism: Constraints from melt inclusions from Haleakala volcano, Hawaii. Journal of Volcanology and Geothermal Research 410, 107144. https://doi.org/10.1016/j.jvolgeores.2020.107144

Moore, L.R., Gazel, E., Tuohy, R., Lloyd, A.S., Esposito, R., Steele-MacInnis, M., Hauri, E.H., Wallace, P.J., Plank, T., Bodnar, R.J., 2015. Bubbles matter: An assessment of the contribution of vapor bubbles to melt inclusion volatile budgets. American Mineralogist 100, 806–823. https://doi.org/10.2138/am-2015-5036

Moore, L.R., Mironov, N., Portnyagin, M., Gazel, E., Bodnar, R.J., 2018. Volatile contents of primitive bubble-bearing melt inclusions from Klyuchevskoy volcano, Kamchatka: Comparison of volatile contents determined by mass-balance versus experimental homogenization. Journal of Volcanology and Geothermal Research 358, 124–131. https://doi.org/10.1016/j.jvolgeores.2018.03.007

Müntener, O., Kelemen, P.B., Grove, T.L., 2001. The role of H2O during crystallization of primitive arc magmas under uppermost mantle conditions and genesis of igneous pyroxenites: an experimental study. Contrib Mineral Petrol 141, 643–658. https://doi.org/10.1007/s004100100266

Mutch, E.J.F., Blundy, J.D., Tattitch, B.C., Cooper, F.J., Brooker, R.A., 2016. An experimental study of amphibole stability in low-pressure granitic magmas and a revised Al-in-hornblende geobarometer. Contrib Mineral Petrol 171, 85. https://doi.org/10.1007/s00410-016-1298-9

Mutch, E.J.F., Maclennan, J., Holland, T.J.B., Buisman, I., 2019a. Millennial storage of near-Moho magma. Science 365, 260–264. https://doi.org/10.1126/science.aax4092

Mutch, E.J.F., Maclennan, J., Madden-Nadeau, A.L., 2022. The dichotomous nature of Mg partitioning between plagioclase and melt: Implications for diffusion chronometry. Geochimica et Cosmochimica Acta 339, 173–189. https://doi.org/10.1016/j.gca.2022.10.035

Mutch, E.J.F., Maclennan, J., Shorttle, O., Edmonds, M., Rudge, J.F., 2019b. Rapid transcrustal magma movement under Iceland. Nat. Geosci. 12, 569–574. https://doi.org/10.1038/s41561-019-0376-9

Nakatani, T., Kudo, T., Suzuki, T., 2022. Experimental Constraints on Magma Storage Conditions of Two Caldera-Forming Eruptions at Towada Volcano, Japan. JGR Solid Earth 127. https://doi.org/10.1029/2021JB023665

Nandedkar, R.H., Ulmer, P., Müntener, O., 2014. Fractional crystallization of primitive, hydrous arc magmas: an experimental study at 0.7 GPa. Contrib Mineral Petrol 167, 1015. https://doi.org/10.1007/s00410-014-1015-5

Neave, D.A., Bali, E., Guðfinnsson, G.H., Halldórsson, S.A., Kahl, M., Schmidt, A.-S., Holtz, F., 2019. Clinopyroxene–Liquid Equilibria and Geothermobarometry in Natural and Experimental Tholeiites: the 2014–2015 Holuhraun Eruption, Iceland. Journal of Petrology 60, 1653–1680. https://doi.org/10.1093/petrology/egz042

Neave, D.A., Hartley, M.E., Maclennan, J., Edmonds, M., Thordarson, T., 2017. Volatile and light lithophile elements in high-anorthite plagioclase-hosted melt inclusions from Iceland. Geochimica et Cosmochimica Acta 205, 100–118. https://doi.org/10.1016/j.gca.2017.02.009

Neave, D.A., Putirka, K.D., 2017. A new clinopyroxene-liquid barometer, and implications for magma storage pressures under Icelandic rift zones. American Mineralogist 102, 777–794. https://doi.org/10.2138/am-2017-5968

Newcombe, M.E., Fabbrizio, A., Zhang, Y., Ma, C., Le Voyer, M., Guan, Y., Eiler, J.M., Saal, A.E., Stolper, E.M., 2014. Chemical zonation in olivine-hosted melt inclusions. Contrib Mineral Petrol 168, 1030. https://doi.org/10.1007/s00410-014-1030-6

Newville, M., Stensitzki, T., Allen, D.B., Rawlik, M., Ingargiola, A., Nelson, A., 2016. LMFIT: Non-linear least-square minimization and curve-fitting for Python. Astrophysics Source Code Library ascl-1606.

Nimis, P., 1995. A clinopyroxene geobarometer for basaltic systems based on crystal-structure modeling. Contrib Mineral Petrol 121, 115–125. https://doi.org/10.1007/s004100050093

Onuma, K., Tohara, T., 1983. Effect of chromium on phase relations in the join forsterite-anorthite-diopside in air at 1 atm. Contributions to Mineralogy and Petrology 84, 174–181.
Pamukcu, A.S., Gualda, G.A.R., Ghiorso, M.S., Miller, C.F., McCracken, R.G., 2015. Phase-equilibrium geobarometers for silicic rocks based on rhyolite-MELTS—Part 3: Application to the Peach Spring Tuff (Arizona–California–Nevada, USA). Contrib Mineral Petrol 169, 33. https://doi.org/10.1007/s00410-015-1122-y
Pamukçu, A.S., Gualda, G.A.R., Gravley, D.M., 2021. Rhyolite-MELTS and the storage and extraction of large-volume crystal-poor rhyolitic melts at the Taupō Volcanic Center: a reply to Wilson et al. (2021). Contrib Mineral Petrol 176, 82. https://doi.org/10.1007/s00410-021-01840-2
Pamukçu, A.S., Wright, K.A., Gualda, G.A.R., Gravley, D., 2020. Magma residence and eruption at the Taupo Volcanic Center (Taupo Volcanic Zone, New Zealand): insights from rhyolite-MELTS geobarometry, diffusion chronometry, and crystal textures. Contrib Mineral Petrol 175, 48. https://doi.org/10.1007/s00410-020-01684-2
Papale, P., Moretti, R., Barbato, D., 2006. The compositional dependence of the saturation surface of H2O+CO2 fluids in silicate melts. Chemical Geology 229, 78–95. https://doi.org/10.1016/j.chemgeo.2006.01.013
Parat, F., Streck, M., Holtz, F., Almeev, R.R., 2014. Experimental study into the petrogenesis of crystal-rich basaltic to andesitic magmas at Arenal volcano. Contributions to Mineralogy and Petrology.
Paszke, A., Gross, S., Massa, F., Lerer, A., Bradbury, J., Chanan, G., Killeen, T., Lin, Z., Gimelshein, N., Antiga, L., 2019. Pytorch: An imperative style, high-performance deep learning library. Advances in neural information processing systems 32.
Peccerillo, A., 2003. Relationships between Mafic and Peralkaline Silicic Magmatism in Continental Rift Settings: a Petrological, Geochemical and Isotopic Study of the Gedemsa Volcano, Central Ethiopian Rift. Journal of Petrology 44, 2003–2032. https://doi.org/10.1093/petrology/egg068
Pecher, A., 1981. Experimental decrepitation and re-equilibration of fluid inclusions in synthetic quartz. Tectonophysics 78, 567–583. https://doi.org/10.1016/0040-1951(81)90029-9
Perinelli, C., Mollo, S., Gaeta, M., De Cristofaro, S.P., Palladino, D.M., Armienti, P., Scarlato, P., Putirka, K.D., 2016. An improved clinopyroxene-based hygrometer for Etnean magmas and implications for eruption triggering mechanisms. American Mineralogist 101, 2774–2777. https://doi.org/10.2138/am-2016-5916
Petrelli, M., Caricchi, L., Perugini, D., 2020. Machine Learning Thermo-Barometry: Application to Clinopyroxene-Bearing Magmas. J. Geophys. Res. Solid Earth 125. https://doi.org/10.1029/2020JB020130
Pineda, C., Hammer, J., First, E., Morata, D., 2021. Storage conditions of a caldera-forming volcanic eruption: Insights from the Pudahuel rhyolitic ignimbrite in central Chile (32° 10'S). Lithos 400–401, 106382. https://doi.org/10.1016/j.lithos.2021.106382
Plank, T., Kelley, K.A., Zimmer, M.M., Hauri, E.H., Wallace, P.J., 2013. Why do mafic arc magmas contain ~4wt% water on average? Earth and Planetary Science Letters 364, 168–179. https://doi.org/10.1016/j.epsl.2012.11.044
Powell, R., Holland, T., Worley, B., 1998. Calculating phase diagrams involving solid solutions via non-linear equations, with examples using THERMOCALC. Journal of metamorphic Geology 16, 577–588.
Prissel, T.C., Parman, S.W., Head, J.W., 2016. Formation of the lunar highlands Mg-suite as told by spinel. American Mineralogist 101, 1624–1635. https://doi.org/10.2138/am-2016-5581
Pritchard, M.E., Mather, T.A., McNutt, S.R., Delgado, F.J., Reath, K., 2019. Thoughts on the criteria to determine the origin of volcanic unrest as magmatic or non-magmatic. Phil. Trans. R. Soc. A 377, 20180008. https://doi.org/10.1098/rsta.2018.0008
Profeta, L., Ducea, M.N., Chapman, J.B., Paterson, S.R., Gonzales, S.M.H., Kirsch, M., Petrescu, L., DeCelles, P.G., 2016. Quantifying crustal thickness over time in magmatic arcs. Sci Rep 5, 17786. https://doi.org/10.1038/srep17786
Pu, X., Lange, R.A., Moore, G., 2017. A comparison of olivine-melt thermometers based on D_{Mg} and D_{Ni} : The effects of melt composition, temperature, and pressure with applications to MORBs and hydrous arc basalts. American Mineralogist 102, 750–765. https://doi.org/10.2138/am-2017-5879
Pu, X., Moore, G.M., Lange, R.A., Touran, J.P., Gagnon, J.E., 2021. Experimental evaluation of a new H2O-independent thermometer based on olivine-melt Ni partitioning at crustal pressure. American Mineralogist 106, 235–250. https://doi.org/10.2138/am-2020-7014

Putirka, K., 2017. Geothermometry and geobarometry. Encyclopedia of Geochemistry: A Comprehensive Reference Source on the Chemistry of the Earth, edited by: White, WM, Springer International Publishing, Cham, Switzerland 597–614.
Putirka, K., 2016. Amphibole thermometers and barometers for igneous systems and some implications for eruption mechanisms of felsic magmas at arc volcanoes. American Mineralogist 101, 841–858. https://doi.org/10.2138/am-2016-5506
Putirka, K., 1999. Clinopyroxene + liquid equilibria to 100 kbar and 2450 K. Contributions to Mineralogy and Petrology 135, 151–163. https://doi.org/10.1007/s004100050503
Putirka, K., Johnson, M., Kinzler, R., Longhi, J., Walker, D., 1996. Thermobarometry of mafic igneous rocks based on clinopyroxene-liquid equilibria, 0-30 kbar. Contributions to Mineralogy and Petrology 123, 92–108. https://doi.org/10.1007/s004100050145
Putirka, K.D., 2008. Thermometers and Barometers for Volcanic Systems. Reviews in Mineralogy and Geochemistry 69, 61–120. https://doi.org/10.2138/rmg.2008.69.3
Putirka, K.D., 2005. Igneous thermometers and barometers based on plagioclase + liquid equilibria: Tests of some existing models and new calibrations. American Mineralogist 90, 336–346. https://doi.org/10.2138/am.2005.1449
Putirka, K.D., Mikaelian, H., Ryerson, F., Shaw, H., 2003. New clinopyroxene-liquid thermobarometers for mafic, evolved, and volatile-bearing lava compositions, with applications to lavas from Tibet and the Snake River Plain, Idaho. American Mineralogist 88, 1542–1554. https://doi.org/10.2138/am-2003-1017
Qin, Z., Lu, F., Anderson, A., 1992. Diffusive reequilibration of melt and fluid inclusions. American Mineralogist 77(506), 565–576.
Quinn, E., 2014. Experimental Determination of Pre-Eruptive Storage Conditions And Continuous Decompression of Rhyodacite Magma Erupted from Chaos Crags, Lassen Volcanic Center, California. MSci thesis, Hombold State University.
Rader, E.L., Larsen, J.F., 2013. Experimental phase relations of a low MgO Aleutian basaltic andesite at XH2O = 0.7–1. Contrib Mineral Petrol 166, 1593–1611. https://doi.org/10.1007/s00410-013-0944-8
Ranero, C.R., Torne, M., Banda, E., 1995. Gravity and multichannel seismic reflection constraints on the lithospheric structure of the Canary Swell. Mar Geophys Res 17, 519–534. https://doi.org/10.1007/BF01204342
Rasmussen, D.J., Kyle, P.R., Wallace, P.J., Sims, K.W.W., Gaetani, G.A., Phillips, E.H., 2017. Understanding Degassing and Transport of CO2-rich Alkalic Magmas at Ross Island, Antarctica using Olivine-Hosted Melt Inclusions. Journal of Petrology. https://doi.org/10.1093/petrology/egx036
Rasmussen, D.J., Plank, T.A., Roman, D.C., Zimmer, M.M., 2022. Magmatic water content controls the pre-eruptive depth of arc magmas. Science 375, 1169–1172. https://doi.org/10.1126/science.abm5174
Rasmussen, D.J., Plank, T.A., Wallace, P.J., Newcombe, M.E., Lowenstern, J.B., 2020. Vapor-bubble growth in olivine-hosted melt inclusions. American Mineralogist 105, 1898–1919. https://doi.org/10.2138/am-2020-7377
Reubi, O., Blundy, J., 2009. A dearth of intermediate melts at subduction zone volcanoes and the petrogenesis of arc andesites. Nature 461, 1269–1273. https://doi.org/10.1038/nature08510
Ridolfi, F., 2021. Amp-TB2: An Updated Model for Calcic Amphibole Thermobarometry. Minerals 11, 324. https://doi.org/10.3390/min11030324
Ridolfi, F., Renzulli, A., 2012. Calcic amphiboles in calc-alkaline and alkaline magmas: thermobarometric and chemometric empirical equations valid up to 1,130°C and 2.2 GPa. Contrib Mineral Petrol 163, 877–895. https://doi.org/10.1007/s00410-011-0704-6
Ridolfi, F., Renzulli, A., Puerini, M., 2010. Stability and chemical equilibrium of amphibole in calc-alkaline magmas: an overview, new thermobarometric formulations and application to subduction-related volcanoes. Contrib Mineral Petrol 160, 45–66. https://doi.org/10.1007/s00410-009-0465-7
Riel, N., Kaus, B.J.P., Green, E.C.R., Berlie, N., 2022. MAGEMin, an Efficient Gibbs Energy Minimizer: Application to Igneous Systems. Geochem Geophys Geosyst 23. https://doi.org/10.1029/2022GC010427
Riker, J.M., 2005. The 1859 eruption of Mauna Loa Volcano, Hawai'i. Controls on the development of long lava channels. University of Oregon PhD thesis.
Robidoux, P., Frezzotti, M.L., Hauri, E.H., Aiuppa, A., 2018. Shrinkage Bubbles: The C–O–H–S Magmatic Fluid System at San Cristóbal Volcano. Journal of Petrology 59, 2093–2122. https://doi.org/10.1093/petrology/egy092
Roedder, E., 1984. Fluid Inclusions, Reviews in Mineralogy. Mineralogical Society of America.

Ronga, F., Lustrino, M., Marzoli, A., Melluso, L., 2010. Petrogenesis of a basalt-comendite-pantellerite rock suite: the Boseti Volcanic Complex (Main Ethiopian Rift). Miner Petrol 98, 227–243. https://doi.org/10.1007/s00710-009-0064-3

Rose-Koga, E.F., Bouvier, A.-S., Gaetani, G.A., Wallace, P.J., Allison, C.M., Andrys, J.A., Angeles de la Torre, C.A., Barth, A., Bodnar, R.J., Bracco Gartner, A.J.J., Butters, D., Castillejo, A., Chilson-Parks, B., Choudhary, B.R., Cluzel, N., Cole, M., Cottrell, E., Daly, A., Danyushevsky, L.V., DeVitre, C.L., Drignon, M.J., France, L., Gaborieau, M., Garcia, M.O., Gatti, E., Genske, F.S., Hartley, M.E., Hughes, E.C., Iveson, A.A., Johnson, E.R., Jones, M., Kagoshima, T., Katzir, Y., Kawaguchi, M., Kawamoto, T., Kelley, K.A., Koornneef, J.M., Kurz, M.D., Laubier, M., Layne, G.D., Lerner, A., Lin, K.-Y., Liu, P.-P., Lorenzo-Merino, A., Luciani, N., Magalhães, N., Marschall, H.R., Michael, P.J., Monteleone, B.D., Moore, L.R., Moussallam, Y., Muth, M., Myers, M.L., Narváez, D.F., Navon, O., Newcombe, M.E., Nichols, A.R.L., Nielsen, R.L., Pamukcu, A., Plank, T., Rasmussen, D.J., Roberge, J., Schiavi, F., Schwartz, D., Shimizu, K., Shimizu, K., Shimizu, N., Thomas, J.B., Thompson, G.T., Tucker, J.M., Ustunisik, G., Waelkens, C., Zhang, Y., Zhou, T., 2021. Silicate melt inclusions in the new millennium: A review of recommended practices for preparation, analysis, and data presentation. Chemical Geology 570, 120145. https://doi.org/10.1016/j.chemgeo.2021.120145

Rosso, K.M., Bodnar, R.J., 1995. Microthermometric and Raman spectroscopic detection limits of C02 in fluid inclusions and the Raman spectroscopic characterization of C02. Geochimica et Cosmochimica Acta 59, 3961–3975. https://doi.org/10.1016/0016-7037(95)94441-H

Ruscitto, D.M., Wallace, P.J., Johnson, E.R., Kent, A.J.R., Bindeman, I.N., 2010. Volatile contents of mafic magmas from cinder cones in the Central Oregon High Cascades: Implications for magma formation and mantle conditions in a hot arc. Earth and Planetary Science Letters 298, 153–161. https://doi.org/10.1016/j.epsl.2010.07.037

Ruscitto, D.M., Wallace, P.J., Kent, A.J.R., 2011. Revisiting the compositions and volatile contents of olivine-hosted melt inclusions from the Mount Shasta region: implications for the formation of high-Mg andesites. Contrib Mineral Petrol 162, 109–132. https://doi.org/10.1007/s00410-010-0587-y

Ruth, D.C.S., Costa, F., 2021. A petrological and conceptual model of Mayon volcano (Philippines) as an example of an open-vent volcano. Bull Volcanol 83, 62. https://doi.org/10.1007/s00445-021-01486-9

Rutherford, M.J., 2003. Magmatic Conditions and Magma Ascent as Indicated by Hornblende Phase Equilibria and Reactions in the 1995-2002 Soufriere Hills Magma. Journal of Petrology 44, 1433–1453. https://doi.org/10.1093/petrology/44.8.1433

Rutherford, M.J., Devine, J.D., 1988. The May 18, 1980, eruption of Mount St. Helens: 3. Stability and chemistry of amphibole in the magma chamber. J. Geophys. Res. 93, 11949. https://doi.org/10.1029/JB093iB10p11949

Rutherford, M.J., Sigurdsson, H., Carey, S., Davis, A., 1985. The May 18, 1980, eruption of Mount St. Helens: 1. Melt composition and experimental phase equilibria. J. Geophys. Res. 90, 2929. https://doi.org/10.1029/JB090iB04p02929

Sack, R.O., Ghiorso, M.S., 1994. Thermodynamics of multicomponent pyroxenes: I. Formulation of a general model. Contr. Mineral. and Petrol. 116, 277–286. https://doi.org/10.1007/BF00306497

Sack, R.O., Ghiorso, M.S., 1991. An internally consistent model for the thermodynamic properties of Fe?Mg-titanomagnetite-aluminate spinels. Contr. Mineral. and Petrol. 106, 474–505. https://doi.org/10.1007/BF00321989

Sack, R.O., Ghiorso, M.S., 1989. Importance of considerations of mixing properties in establishing an internally consistent thermodynamic database: thermochemistry of minerals in the system Mg2SiO4-Fe2SiO4-SiO2. Contr. Mineral. and Petrol. 102, 41–68. https://doi.org/10.1007/BF01160190

Sanfilippo, A., MacLeod, C.J., Tribuzio, R., Lissenberg, C.J., Zanetti, A., 2020. Early-Stage Melt-Rock Reaction in a Cooling Crystal Mush Beneath a Slow-Spreading Mid-Ocean Ridge (IODP Hole U1473A, Atlantis Bank, Southwest Indian Ridge). Front. Earth Sci. 8, 579138. https://doi.org/10.3389/feart.2020.579138

Sas, M., DeBari, S., Clynne, M., Rusk, B., 2017. Using mineral geochemistry to decipher slab, mantle, and crustal input in the generation of high-Mg andesites and basaltic andesites from the northern Cascade Arc. msam. https://doi.org/10.2138/am-2017-5756

Scaillet, B., Macdonald, R., 2001. Phase Relations of Peralkaline Silicic Magmas and Petrogenetic Implications. Journal of Petrology 42, 825–845. https://doi.org/10.1093/petrology/42.4.825

Schiavi, F., Bolfan-Casanova, N., Buso, R., Laumonier, M., Laporte, D., Medjoubi, K., Venugopal, S., Gómez-Ulla, A., Cluzel, N., Hardiagon, M., 2020. Quantifying magmatic volatiles by Raman microtomography of glass inclusion-hosted bubbles. Geochem. Persp. Let. 16, 17–24. https://doi.org/10.7185/geochemlet.2038

Schmidt, M.W., 1992. Amphibole composition in tonalite as a function of pressure: an experimental calibration of the Al-in-hornblende barometer. Contr. Mineral. and Petrol. 110, 304–310. https://doi.org/10.1007/BF00310745

Scruggs, M.A., Putirka, K.D., 2018. Eruption triggering by partial crystallization of mafic enclaves at Chaos Crags, Lassen Volcanic Center, California. American Mineralogist 103, 1575–1590. https://doi.org/10.2138/am-2018-6058

Shamloo, H.I., Till, C.B., 2019. Decadal transition from quiescence to supereruption: petrologic investigation of the Lava Creek Tuff, Yellowstone Caldera, WY. Contrib Mineral Petrol 174, 32. https://doi.org/10.1007/s00410-019-1570-x

Shedden, K., 2008. Gene expression–based survival prediction in lung adenocarcinoma: a multi-site, blinded validation study. Nat Med 14, 822–827. https://doi.org/10.1038/nm.1790

Sheehan, F., Barclay, J., 2016. Staged storage and magma convection at Ambrym volcano, Vanuatu. Journal of Volcanology and Geothermal Research 322, 144–157. https://doi.org/10.1016/j.jvolgeores.2016.02.024

Shi, P., 1993. Low-Pressure Phase Relationships in the System Na2O--CaO--FeO--MgO--Al2O3--SiO2 at 1100 C, with Implications for the Differentiation of Basaltic Magmas. Journal of Petrology 34, 743–762. https://doi.org/10.1093/petrology/34.4.743

Shi, P., 1992. Basalt evolution at low pressure: implications from an experimental study in the system CaO-FeO-MgO-Al2O3-SiO2. Contr. Mineral. and Petrol. 110, 139–153. https://doi.org/10.1007/BF00310735

Shi, S., Barth, A., Plank, T., Towbin, W., Flores, O., Arias, C., 2021. Magma stalling weakens eruption. Presented at the AGU Fall Meeting Abstracts, pp. V25E-09.

Shinohara, H., 2013. Volatile flux from subduction zone volcanoes: Insights from a detailed evaluation of the fluxes from volcanoes in Japan. Journal of Volcanology and Geothermal Research 268, 46–63. https://doi.org/10.1016/j.jvolgeores.2013.10.007

Shishkina, T.A., Botcharnikov, R.E., Holtz, F., Almeev, R.R., Jazwa, A.M., Jakubiak, A.A., 2014. Compositional and pressure effects on the solubility of H2O and CO2 in mafic melts. Chemical Geology 388, 112–129. https://doi.org/10.1016/j.chemgeo.2014.09.001

Sides, Edmonds, M., Maclennan, J., Houghton, B.F., Swanson, D.A., Steele-MacInnis, M.J., 2014a. Magma mixing and high fountaining during the 1959 Kīlauea Iki eruption, Hawai'i. Earth and Planetary Science Letters 400, 102–112. https://doi.org/10.1016/j.epsl.2014.05.024

Sides, Edmonds, M., Maclennan, J., Swanson, D.A., Houghton, B.F., 2014b. Eruption style at Kīlauea Volcano in Hawai'i linked to primary melt composition. Nature Geoscience 7, 464–469. https://doi.org/10.1038/ngeo2140

Siegburg, M., Klügel, A., Rocholl, A., Bach, W., 2018. Magma plumbing and hybrid magma formation at an active back-arc basin volcano: North Su, eastern Manus basin. Journal of Volcanology and Geothermal Research 362, 1–16. https://doi.org/10.1016/j.jvolgeores.2018.07.001

Sisson, T.W., Grove, T.L., 1993. Temperatures and H2O contents of low-MgO high-alumina basalts. Contr. Mineral. and Petrol. 113, 167–184. https://doi.org/10.1007/BF00283226

Sisson, T.W., Ratajeski, K., Hankins, W.B., Glazner, A.F., 2005. Voluminous granitic magmas from common basaltic sources. Contrib Mineral Petrol 148, 635–661. https://doi.org/10.1007/s00410-004-0632-9

Skirius, C., Peterson, J., Anderson Jr., A.T., 1990. Homogenizing rhyolitic glass inclusions from the Bishop Tuff. American Mineralogist 75, 1381–1398.

Solaro, C., Martel, C., Champallier, R., Boudon, G., Balcone-Boissard, H., Pichavant, M., 2019. Petrological and experimental constraints on magma storage for large pumiceous eruptions in Dominica island (Lesser Antilles). Bull Volcanol 81, 55. https://doi.org/10.1007/s00445-019-1313-x

Sorby, H.C., 1858. On the Microscopical, Structure of Crystals, indicating the Origin of Minerals and Rocks. QJGS 14, 453–500. https://doi.org/10.1144/GSL.JGS.1858.014.01-02.44

Span, R., Wagner, W., 1996. A New Equation of State for Carbon Dioxide Covering the Fluid Region from the Triple-Point Temperature to 1100 K at Pressures up to 800 MPa. Journal of Physical and Chemical Reference Data 25, 1509–1596. https://doi.org/10.1063/1.555991

Spencer, K.J., Lindsley, D.H., 1981. A solution model for coexisting iron–titanium oxides. American mineralogist 66, 1189–1201.

Steele-Macinnis, M., Esposito, R., Bodnar, R.J., 2011. Thermodynamic Model for the Effect of Post-entrapment Crystallization on the H2O-CO2 Systematics of Vapor-saturated, Silicate Melt Inclusions. Journal of Petrology 52, 2461–2482. https://doi.org/10.1093/petrology/egr052

Sterner, S.M., Pitzer, K.S., 1994. An equation of state for carbon dioxide valid from zero to extreme pressures. Contr. Mineral. and Petrol. 117, 362–374. https://doi.org/10.1007/BF00307271
Stock, M.J., Bagnardi, M., Neave, D.A., Maclennan, J., Bernard, B., Buisman, I., Gleeson, M.L.M., Geist, D., 2018. Integrated Petrological and Geophysical Constraints on Magma System Architecture in the Western Galápagos Archipelago: Insights From Wolf Volcano. Geochem. Geophys. Geosyst. 19, 4722–4743. https://doi.org/10.1029/2018GC007936
Sugawara, T., 2001. Ferric iron partitioning between plagioclase and silicate liquid: thermodynamics and petrological applications. Contrib Mineral Petrol 141, 659–686. https://doi.org/10.1007/s004100100267
Sun, C., Liang, Y., 2012. Distribution of REE between clinopyroxene and basaltic melt along a mantle adiabat: effects of major element composition, water, and temperature. Contrib Mineral Petrol 163, 807–823. https://doi.org/10.1007/s00410-011-0700-x
Sun, C., Lissenberg, C.J., 2018. Formation of fast-spreading lower oceanic crust as revealed by a new Mg–REE coupled geospeedometer. Earth and Planetary Science Letters 487, 165–178. https://doi.org/10.1016/j.epsl.2018.01.032
Tamblyn, R., Hand, M., Morrissey, L., Zack, T., Phillips, G., Och, D., 2020. Resubduction of lawsonite eclogite within a serpentinite-filled subduction channel. Contrib Mineral Petrol 175, 74. https://doi.org/10.1007/s00410-020-01712-1
Taracsák, Z., Hartley, M.E., Burgess, R., Edmonds, M., Iddon, F., Longpré, M.-A., 2019. High fluxes of deep volatiles from ocean island volcanoes: Insights from El Hierro, Canary Islands. Geochimica et Cosmochimica Acta 258, 19–36. https://doi.org/10.1016/j.gca.2019.05.020
Taura, H., Yurimoto, H., Kurita, K., Sueno, S., 1998. Pressure dependence on partition coefficients for trace elements between olivine and the coexisting melts. Physics and Chemistry of Minerals 25, 469–484. https://doi.org/10.1007/s002690050138
Teplow, W., Marsh, B., Hulen, 2009. Dacite Melt at the Puna Geothermal Venture Wellfield, Big Island of Hawaii. GRC Transactions 33.
Thermoengine Code Contributors, 2022. ThermoEngine: Software for Model Building and Computational Thermodynamics Supporting Applications in the Earth Sciences. https://doi.org/10.5281/ZENODO.6527840
Thomas, J.B., Bruce Watson, E., 2012. Application of the Ti-in-quartz thermobarometer to rutile-free systems. Reply to: a comment on: 'TitaniQ under pressure: the effect of pressure and temperature on the solubility of Ti in quartz' by Thomas et al. Contrib Mineral Petrol 164, 369–374. https://doi.org/10.1007/s00410-012-0761-5
Thomas, J.B., Bruce Watson, E., Spear, F.S., Shemella, P.T., Nayak, S.K., Lanzirotti, A., 2010. TitaniQ under pressure: the effect of pressure and temperature on the solubility of Ti in quartz. Contrib Mineral Petrol 160, 743–759. https://doi.org/10.1007/s00410-010-0505-3
Thomas, W.M., Ernst', W.G., 1990. The aluminum content of hornblende in calc-alkaline granitic rocks: A mineralogic barometer calibrated experimentally to 12 kbars 6.
Tommasini, S., Bindi, L., Savia, L., Mangler, M.F., Orlando, A., Petrone, C.M., 2022. Critical assessment of pressure estimates in volcanic plumbing systems: The case study of Popocatépetl volcano, Mexico. Lithos 408–409, 106540. https://doi.org/10.1016/j.lithos.2021.106540
Towbin, W.H., Plank, T., Klein, E., Hauri, E., 2023. Measuring H2O concentrations in olivine by secondary ion mass spectrometry: Challenges and paths forward. American Mineralogist: Journal of Earth and Planetary Materials 108, 928–940. https://doi.org/10.2138/am-2022-8247
Trela, J., Gazel, E., Sobolev, A.V., Moore, L., Bizimis, M., Jicha, B., Batanova, V.G., 2017. The hottest lavas of the Phanerozoic and the survival of deep Archaean reservoirs. Nature Geosci 10, 451–456. https://doi.org/10.1038/ngeo2954
Tucker, J.M., Hauri, E.H., Pietruszka, A.J., Garcia, M.O., Marske, J.P., Trusdell, F.A., 2019. A high carbon content of the Hawaiian mantle from olivine-hosted melt inclusions. Geochimica et Cosmochimica Acta 254, 156–172. https://doi.org/10.1016/j.gca.2019.04.001
Tuohy, R.M., Wallace, P.J., Loewen, M.W., Swanson, D.A., Kent, A.J.R., 2016. Magma transport and olivine crystallization depths in Kīlauea's east rift zone inferred from experimentally rehomogenized melt inclusions. Geochimica et Cosmochimica Acta 185, 232–250. https://doi.org/10.1016/j.gca.2016.04.020
Ubide, T., Caulfield, J., Brandt, C., Bussweiler, Y., Mollo, S., Di Stefano, F., Nazzari, M., Scarlato, P., 2019a. Deep Magma Storage Revealed by Multi-Method Elemental Mapping of Clinopyroxene Megacrysts at Stromboli Volcano. Front. Earth Sci. 7, 239. https://doi.org/10.3389/feart.2019.00239

Ubide, T., Larrea, P., Becerril, L., Galé, C., 2022. Volcanic plumbing filters on ocean-island basalt geochemistry. Geology 50, 26–31. https://doi.org/10.1130/G49224.1

Ubide, T., Mollo, S., Zhao, J., Nazzari, M., Scarlato, P., 2019b. Sector-zoned clinopyroxene as a recorder of magma history, eruption triggers, and ascent rates. Geochimica et Cosmochimica Acta 251, 265–283. https://doi.org/10.1016/j.gca.2019.02.021

Van Den Kerkhof, A.M., 1990. Isochoric phase diagrams in the systems CO2□CH4 and CO2□N2: Application to fluid inclusions. Geochimica et Cosmochimica Acta 54, 621–629. https://doi.org/10.1016/0016-7037(90)90358-R

van Gerve, T., Neave, D.A., Wieser, P., Lamadrid, H.M., Hulsbosch, N. and Namur, O., 2023, July. Crystallisation driven deep volatile degassing in ocean island volcanoes: Integrating 3D imaging with chemical microanalysis of olivine-hosted melt inclusions from Pico (Azores). In *Goldschmidt 2023 Conference*. GOLDSCHMIDT.

Venezky, D.Y., Rutherford, M.J., 1999. Petrology and Fe–Ti oxide reequilibration of the 1991 Mount Unzen mixed magma. Journal of Volcanology and Geothermal Research 89, 213–230. https://doi.org/10.1016/S0377-0273(98)00133-4

Venugopal, S., Schiavi, F., Moune, S., Bolfan-Casanova, N., Druitt, T., Williams-Jones, G., 2020. Melt inclusion vapour bubbles: the hidden reservoir for major and volatile elements. Sci Rep 10, 9034. https://doi.org/10.1038/s41598-020-65226-3

Villiger, S., 2004. The Liquid Line of Descent of Anhydrous, Mantle-Derived, Tholeiitic Liquids by Fractional and Equilibrium Crystallization--an Experimental Study at 1{middle dot}0 GPa. Journal of Petrology 45, 2369–2388. https://doi.org/10.1093/petrology/egh042

Villiger, S., Müntener, O., Ulmer, P., 2007. Crystallization pressures of mid-ocean ridge basalts derived from major element variations of glasses from equilibrium and fractional crystallization experiments. J. Geophys. Res. 112, B01202. https://doi.org/10.1029/2006JB004342

Vogt, J.H.L., 1931. On the Terms Eutectic, Cotectic, Peritectic, Anchi-Eutectic, Anchi-Cotectic, etc., and their Importance in Petrogenesis. The Journal of Geology 39, 401–431. https://doi.org/10.1086/623862

Voigt, A., Cassidy, M., Castro, J.M., Pyle, D.M., Mather, T.A., Helo, C., Abdurrachman, M., Kurniawan, I.A., 2022. Experimental Investigation of Trachydacite Magma Storage Prior to the 1257 Eruption of Mt Samalas. Journal of Petrology 63, egac066. https://doi.org/10.1093/petrology/egac066

Voigt, M., Coogan, L.A., von der Handt, A., 2017. Experimental investigation of the stability of clinopyroxene in mid-ocean ridge basalts: The role of Cr and Ca/Al. Lithos 274–275, 240–253. https://doi.org/10.1016/j.lithos.2017.01.003

Wade, J.A., Plank, T., Hauri, E.H., Kelley, K.A., Roggensack, K., Zimmer, M., 2008. Prediction of magmatic water contents via measurement of H2O in clinopyroxene phenocrysts. Geol 36, 799. https://doi.org/10.1130/G24964A.1

Walker, B.A., Klemetti, E.W., Grunder, A.L., Dilles, J.H., Tepley, F.J., Giles, D., 2013. Crystal reaming during the assembly, maturation, and waning of an eleven-million-year crustal magma cycle: thermobarometry of the Aucanquilcha Volcanic Cluster. Contrib Mineral Petrol 165, 663–682. https://doi.org/10.1007/s00410-012-0829-2

Wallace, P.J., 2005. Volatiles in subduction zone magmas: concentrations and fluxes based on melt inclusion and volcanic gas data. Journal of Volcanology and Geothermal Research 140, 217–240. https://doi.org/10.1016/j.jvolgeores.2004.07.023

Wallace, P.J., Anderson, A.T., Davis, A.M., 1999. Gradients in H_2O, CO_2, and exsolved gas in a large-volume silicic magma system: Interpreting the record preserved in melt inclusions from the Bishop Tuff. J. Geophys. Res. 104, 20097–20122. https://doi.org/10.1029/1999JB900207

Wallace, P.J., Kamenetsky, V.S., Cervantes, P., 2015. Melt inclusion CO2 contents, pressures of olivine crystallization, and the problem of shrinkage bubbles. American Mineralogist 100, 787–794. https://doi.org/10.2138/am-2015-5029

Wallace, P.J., Plank, T., Bodnar, R.J., Gaetani, G.A., Shea, T., 2021. Olivine-Hosted Melt Inclusions: A Microscopic Perspective on a Complex Magmatic World. Annual Review of Earth and Planetary Sciences.

Walowski, K.J., Wallace, P.J., Cashman, K.V., Marks, J.K., Clynne, M.A., Ruprecht, P., 2019. Understanding melt evolution and eruption dynamics of the 1666 C.E. eruption of Cinder Cone, Lassen Volcanic National Park, California: Insights from olivine-hosted melt inclusions. Journal of Volcanology and Geothermal Research 387, 106665. https://doi.org/10.1016/j.jvolgeores.2019.106665

Walowski, K.J., Wallace, P.J., Clynne, M.A., Rasmussen, D.J., Weis, D., 2016. Slab melting and magma formation beneath the southern Cascade arc. Earth and Planetary Science Letters 446, 100–112. https://doi.org/10.1016/j.epsl.2016.03.044

Wan, Z., Coogan, L.A., Canil, D., 2008. Experimental calibration of aluminum partitioning between olivine and spinel as a geothermometer. American Mineralogist 93, 1142–1147. https://doi.org/10.2138/am.2008.2758

Wanamaker, B.J., Evans, B., 1989. Mechanical re-equilibration of fluid inclusions in San Carlos olivine by power-law creep. Contr. Mineral. and Petrol. 102, 102–111. https://doi.org/10.1007/BF01160194

Wanamaker, B.J., Wong, T.-F., Evans, B., 1990. Decrepitation and crack healing of fluid inclusions in San Carlos olivine. Journal of Geophysical Research 95, 15623. https://doi.org/10.1029/JB095iB10p15623

Wang, W., Caumon, M.-C., Tarantola, A., Pironon, J., Lu, W., Huang, Y., 2019. Raman spectroscopic densimeter for pure CO2 and CO2-H2O-NaCl fluid systems over a wide P-T range up to 360 °C and 50 MPa. Chemical Geology 528, 119281. https://doi.org/10.1016/j.chemgeo.2019.119281

Wang, X., Chou, I.-M., Hu, W., Burruss, R.C., Sun, Q., Song, Y., 2011. Raman spectroscopic measurements of CO2 density: Experimental calibration with high-pressure optical cell (HPOC) and fused silica capillary capsule (FSCC) with application to fluid inclusion observations. Geochimica et Cosmochimica Acta 75, 4080–4093. https://doi.org/10.1016/j.gca.2011.04.028

Wang, X., Hou, T., Wang, M., Zhang, C., Zhang, Z., Pan, R., Marxer, F., Zhang, H., 2021. A new clinopyroxene thermobarometer for mafic to intermediate magmatic systems. Eur. J. Mineral. 33, 621–637. https://doi.org/10.5194/ejm-33-621-2021

Wark, D.A., Watson, E.B., 2006. TitaniQ: a titanium-in-quartz geothermometer. Contrib Mineral Petrol 152, 743–754. https://doi.org/10.1007/s00410-006-0132-1

Waters, L.E., Lange, R.A., 2015. An updated calibration of the plagioclase-liquid hygrometer-thermometer applicable to basalts through rhyolites. American Mineralogist 100, 2172–2184. https://doi.org/10.2138/am-2015-5232

Weber, G., Blundy, J., 2023. A machine learning-based thermometer, barometer and hygrometer for magmatic liquids (preprint). Physical Sciences and Mathematics. https://doi.org/10.31223/X5NW9P

Weber, G., Castro, J.M., 2017. Phase petrology reveals shallow magma storage prior to large explosive silicic eruptions at Hekla volcano, Iceland. Earth and Planetary Science Letters 466, 168–180. https://doi.org/10.1016/j.epsl.2017.03.015

White, R.S., McKenzie, D., O'Nions, R.K., 1992. Oceanic crustal thickness from seismic measurements and rare earth element inversions. J. Geophys. Res. 97, 19683. https://doi.org/10.1029/92JB01749

Wieser, P., in prep. Thermobar: An open source... in prep.

Wieser, P., DeVitre, C., 2023. DiadFit: An Open-SourcePython3 Tool for Peak fitting of Raman Data from silicate melts and CO2 fluids (preprint). Earth Sciences. https://doi.org/10.31223/X5CQ1F

Wieser, P., Kent, A., Till, C., Abers, G., 2023a. Geophysical and Geochemical Constraints on Magma Storage Depths along the Cascade Arc: Knowns and Unknowns (preprint). Earth Sciences. https://doi.org/10.31223/X5KX00

Wieser, P., Till, C., Kent, A., Gleeson, M., 2023b. Comment on 'The magmatic architecture and evolution of the Chang'e-5 lunar basalts' Penny E. Wieser1, Christy Till2, Adam Kent3, Matthew Gleeson1 (preprint). Earth Sciences. https://doi.org/10.31223/X5MM3B

Wieser, P. E., Edmonds, M., Gansecki, C., Maclennan, J., Jenner, F.E., Kunz, B., Antoshechkina, P., Trusdell, F., Lee, R.L., Eimf, 2022a. Explosive Activity on Kīlauea's Lower East Rift Zone Fueled by a Volatile-Rich, Dacitic Melt. Geochem Geophys Geosyst 23. https://doi.org/10.1029/2021GC010046

Wieser, P.E., Edmonds, M., Maclennan, J., Jenner, F.E., Kunz, B.E., 2019. Crystal scavenging from mush piles recorded by melt inclusions. Nat Commun 10, 5797. https://doi.org/10.1038/s41467-019-13518-2

Wieser, P. E., Iacovino, K., Matthews, S., Moore, G., Allison, C.M., 2022b. VESIcal: 2. A Critical Approach to Volatile Solubility Modeling Using an Open-Source Python3 Engine. Earth and Space Science 9. https://doi.org/10.1029/2021EA001932

Wieser, P.E., Jenner, F., Edmonds, M., Maclennan, J., Kunz, B.E., 2020. Chalcophile elements track the fate of sulfur at Kīlauea Volcano, Hawai'i. Geochimica et Cosmochimica Acta S0016703720303239. https://doi.org/10.1016/j.gca.2020.05.018

Wieser, P.E., Kent, A., Till, C., Donovan, J., Neave, D., Blatter, D., Mike Krawczynski, M., 2023b. Barometers behaving badly: Assessing the influence of analytical and experimental uncertainty on clinopyroxene thermobarometry calculations at crustal conditions (preprint). Earth Sciences. https://doi.org/10.31223/X5JT0N

Wieser, P.E., Kent, A.J., Till, C., 2023a. Barometers behaving badly II: A critical evaluation of Cpx-only and Cpx-Liq thermobarometry in variably-hydrous arc magmas. EarthArxiv. https://doi.org/10.31223/X59655
Wieser, P.E., Lamadrid, H., Maclennan, J., Edmonds, M., Matthews, S., Iacovino, K., Jenner, F.E., Gansecki, C., Trusdell, F., Lee, R.L., Ilyinskaya, E., 2021. Reconstructing Magma Storage Depths for the 2018 Kīlauean Eruption From Melt Inclusion CO_2 Contents: The Importance of Vapor Bubbles. Geochem Geophys Geosyst 22. https://doi.org/10.1029/2020GC009364
Wieser, P.E., Petrelli, M., Lubbers, J., Wieser, E., Ozaydin, S., Kent, A., Till, C., 2022b. Thermobar: An open-source Python3 tool for thermobarometry and hygrometry. Volcanica 5, 349–384. https://doi.org/10.30909/vol.05.02.349384
Wilke, S., Holtz, F., Li, X., Neave, D.A., Almeev, R.R., 2019. Rhyolite-MELTS vs DERP – Reply to Comment by Gualda et al. on 'The Effect of Anorthite Content and Water on Quartz–Feldspar Cotectic Compositions in the Rhyolitic System and Implications for Geobarometry' by Wilke et al. (2017), Journal of Petrology, 58, No. 4, 789–818. Journal of Petrology 60, 865–870. https://doi.org/10.1093/petrology/egz002
Wilke, S., Holtz, F., Neave, D.A., Almeev, R., 2017. The Effect of Anorthite Content and Water on Quartz–Feldspar Cotectic Compositions in the Rhyolitic System and Implications for Geobarometry. Journal of Petrology 58, 789–818. https://doi.org/10.1093/petrology/egx034
Wilkinson, M.D., Dumontier, M., Aalbersberg, Ij.J., Appleton, G., Axton, M., Baak, A., Blomberg, N., Boiten, J.-W., da Silva Santos, L.B., Bourne, P.E., Bouwman, J., Brookes, A.J., Clark, T., Crosas, M., Dillo, I., Dumon, O., Edmunds, S., Evelo, C.T., Finkers, R., Gonzalez-Beltran, A., Gray, A.J.G., Groth, P., Goble, C., Grethe, J.S., Heringa, J., 't Hoen, P.A.C., Hooft, R., Kuhn, T., Kok, R., Kok, J., Lusher, S.J., Martone, M.E., Mons, A., Packer, A.L., Persson, B., Rocca-Serra, P., Roos, M., van Schaik, R., Sansone, S.-A., Schultes, E., Sengstag, T., Slater, T., Strawn, G., Swertz, M.A., Thompson, M., van der Lei, J., van Mulligen, E., Velterop, J., Waagmeester, A., Wittenburg, P., Wolstencroft, K., Zhao, J., Mons, B., 2016. The FAIR Guiding Principles for scientific data management and stewardship. Sci Data 3, 160018. https://doi.org/10.1038/sdata.2016.18
Wilson, C.J.N., Barker, S.J., Charlier, B.L.A., Myers, M.L., Hansen, K.F., 2021. A comment on: magma residence and eruption at the Taupō Volcanic Center (Taupō Volcanic Zone, New Zealand)—insights from rhyolite-MELTS geobarometry, diffusion chronometry, and crystal textures, by AS Pamukçu et al., Contrib Mineral Petrol 175:48 (2020). Contrib Mineral Petrol 176, 79. https://doi.org/10.1007/s00410-021-01839-9
Wilson, C.J.N., Seward, T.M., Allan, A.S.R., Charlier, B.L.A., Bello, L., 2012. A comment on: 'TitaniQ under pressure: the effect of pressure and temperature on the solubility of Ti in quartz', by Jay B. Thomas, E. Bruce Watson, Frank S. Spear, Philip T. Shemella, Saroj K. Nayak and Antonio Lanzirotti. Contrib Mineral Petrol 164, 359–368. https://doi.org/10.1007/s00410-012-0757-1
Winpenny, B., Maclennan, J., 2011. A Partial Record of Mixing of Mantle Melts Preserved in Icelandic Phenocrysts. Journal of Petrology 52, 1791–1812. https://doi.org/10.1093/petrology/egr031
Wong, K., Ferguson, D., Matthews, S., Morgan, D., Tadesse, A.Z., Sinetebeb, Y., Yirgu, G., 2022. Exploring rift geodynamics in Ethiopia through olivine-spinel Al-exchange thermometry and rare-earth element distributions. Earth and Planetary Science Letters 597, 117820. https://doi.org/10.1016/j.epsl.2022.117820
Wong, K., Ferguson, D., Wieser, P., Morgan, D., Edmonds, M., Tadesse, A.Z., Yirgu, G., Harvey, J., Hammond, S., 2023. Focused Mid-Crustal Magma Intrusion During Continental Break-Up in Ethiopia. Geophysical Research Letters 50, e2023GL103257. https://doi.org/10.1029/2023GL103257
Wood, B.J., 1974. The solubility of alumina in orthopyroxene coexisting with garnet. Contr. Mineral. and Petrol. 46, 1–15. https://doi.org/10.1007/BF00377989
Wood, B.J., Blundy, J., 1997. predictive model for rare earth element partitioning between clinopyroxene and anhydrous silicate melt. Contributions to Mineralogy and Petrology.
Wright, H.M., Bacon, C.R., Vazquez, J.A., Sisson, T.W., 2012. Sixty thousand years of magmatic volatile history before the caldera-forming eruption of Mount Mazama, Crater Lake, Oregon. Contrib Mineral Petrol 164, 1027–1052. https://doi.org/10.1007/s00410-012-0787-8
Yamamoto, J., Kagi, H., 2006. Extended Micro-Raman Densimeter for CO_2 Applicable to Mantle-originated Fluid Inclusions. Chem. Lett. 35, 610–611. https://doi.org/10.1246/cl.2006.610
Yang, H.-J., Kinzler, R.J., Grove, T.L., 1996. Experiments and models of anhydrous, basaltic olivine-plagioclase-augite saturated melts from 0.001 to 10 kbar. Contributions to Mineralogy and Petrology 124, 1–18. https://doi.org/10.1007/s004100050169

Yuan, X., Mayanovic, R.A., 2017. An Empirical Study on Raman Peak Fitting and Its Application to Raman Quantitative Research. Appl Spectrosc 71, 2325–2338. https://doi.org/10.1177/0003702817721527

Zanon, V., Frezzotti, M.L., 2013. Magma storage and ascent conditions beneath Pico and Faial islands (Azores archipelago): A study on fluid inclusions: MAGMA STORAGE BENEATH PICO AND FAIAL. Geochem. Geophys. Geosyst. 14, 3494–3514. https://doi.org/10.1002/ggge.20221

Zellmer, G.F., Sakamoto, N., Iizuka, Y., Miyoshi, M., Tamura, Y., Hsieh, H.-H., Yurimoto, H., 2014. Crystal uptake into aphyric arc melts: insights from two-pyroxene pseudo-decompression paths, plagioclase hygrometry, and measurement of hydrogen in olivines from mafic volcanics of SW Japan. SP 385, 161–184. https://doi.org/10.1144/SP385.3

Zhang, J., Humphreys, M.C.S., Cooper, G.F., Davidson, J.P., Macpherson, C.G., 2017. Magma mush chemistry at subduction zones, revealed by new melt major element inversion from calcic amphiboles. American Mineralogist 102, 1353–1367. https://doi.org/10.2138/am-2017-5928

Zhang, Y., Namur, O., 2022. A re-evaluation of the Al-in-Olivine geothermometer. Presented at the Goldcshmidt 2022 - https://conf.goldschmidt.info/goldschmidt/2022/meetingapp.cgi/Paper/11383.

Zhang, Y., Xu, Z., Zhu, M., Wang, H., 2007. Silicate melt properties and volcanic eruptions: SILICATE MELT PROPERTIES. Rev. Geophys. 45. https://doi.org/10.1029/2006RG000216

Zhukova, I., O'Neill, H., Campbell, I.H., 2017. A subsidiary fast-diffusing substitution mechanism of Al in forsterite investigated using diffusion experiments under controlled thermodynamic conditions. Contrib Mineral Petrol 172, 53. https://doi.org/10.1007/s00410-017-1365-x

Ziberna, L., Green, E.C.R., Blundy, J.D., 2017. Multiple-reaction geobarometry for olivine-bearing igneous rocks. American Mineralogist 102, 2349–2366. https://doi.org/10.2138/am-2017-6154

Ziberna, L., 2021. Geothermobarometry of mafic and ultramafic xenoliths: examples from Hualalai and Mauna Kea volcanoes, Hawaii. *Crustal Magmatic System Evolution: Anatomy, Architecture, and Physico-Chemical Processes*, pp.1-18.

Supporting Information: P-T-X conditions of magmas

Penny E. Wieser[1], Matthew L.M. Gleeson[1], Simon Matthews[2], Charlotte DeVitre[1], Esteban Gazel[3]

1. Earth and Planetary Sciences, UC Berkeley

2. Earth Science Department, University of Cambridge

3. Department of Earth and Atmospheric Sciences, Cornell University, Ithaca, NY 14850, USA

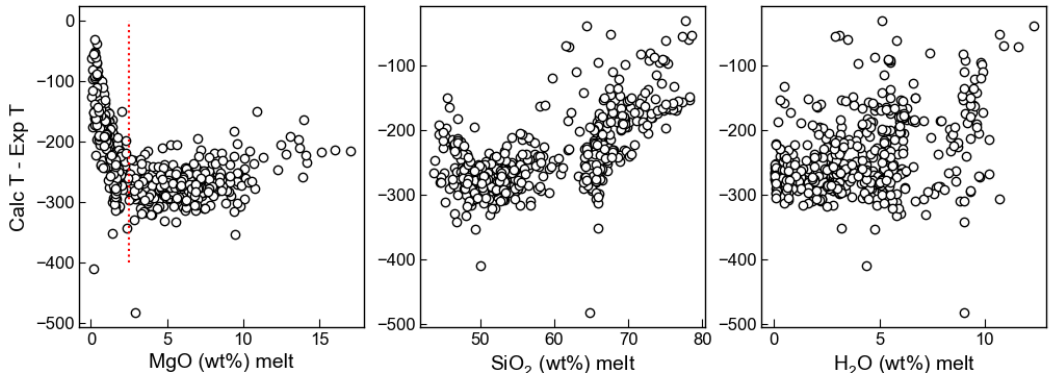

Supporting Fig. 1– Offset between calculated tempreature using Shi et al. (2021) and experimental temperature shows a strong relationship with MgO content.

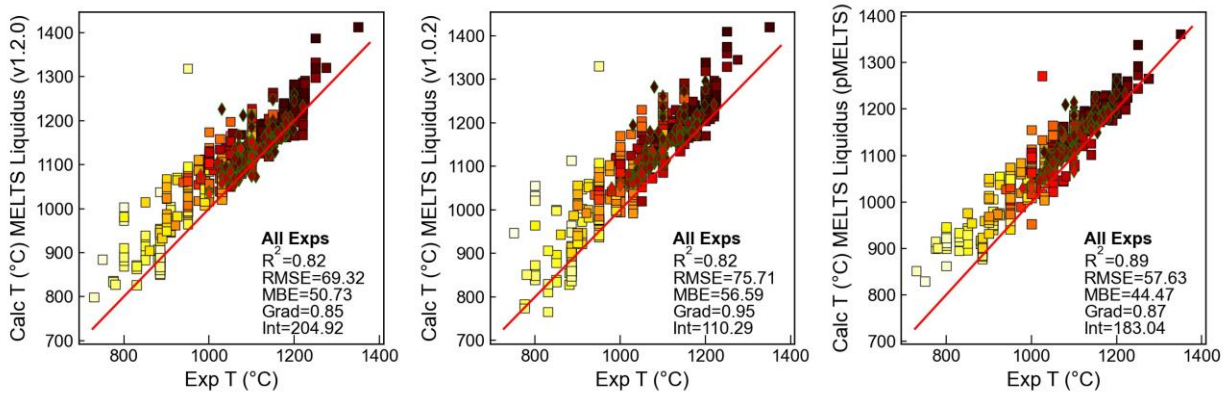

Supporting Fig. 2 – Liquidus calculations performed with different versions of MELTS for comparison with the main text.

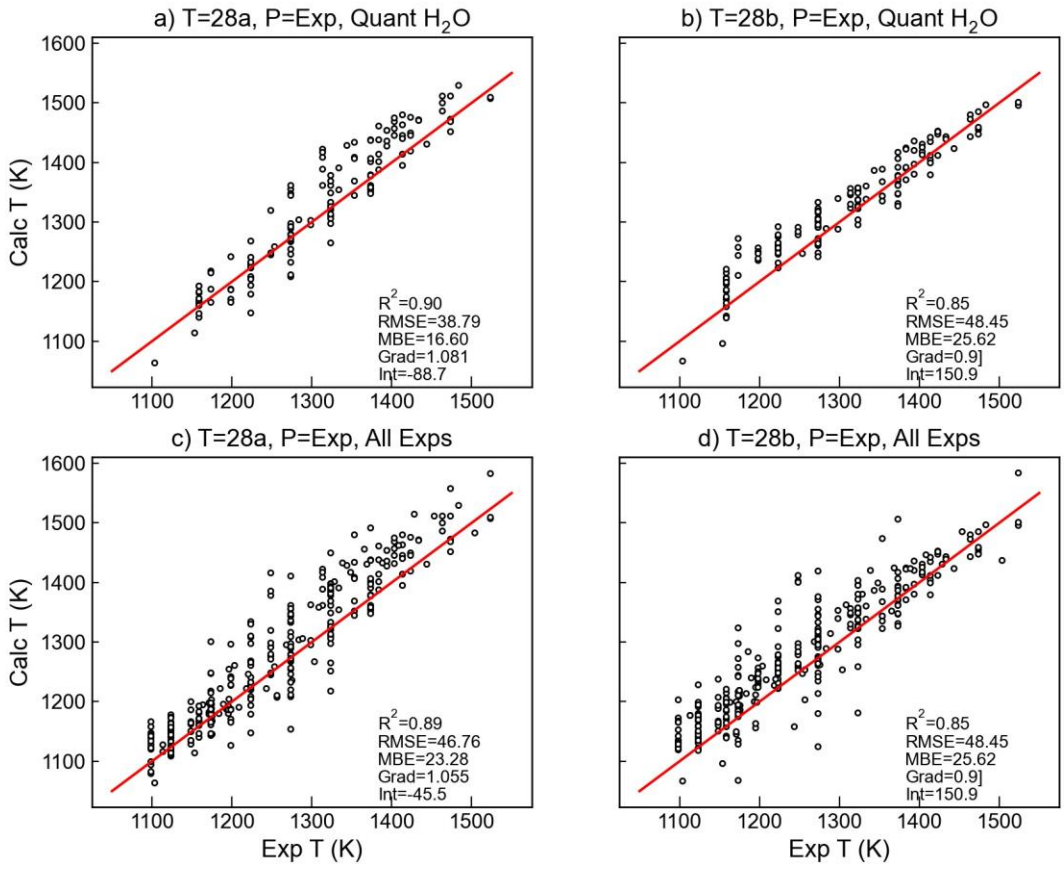

Supporting Fig. 3– Comparison of different Opx-Liq thermometers. a-b) uses only experiments where H_2O was measured using a quantitative method, while c-d shows all experiments.

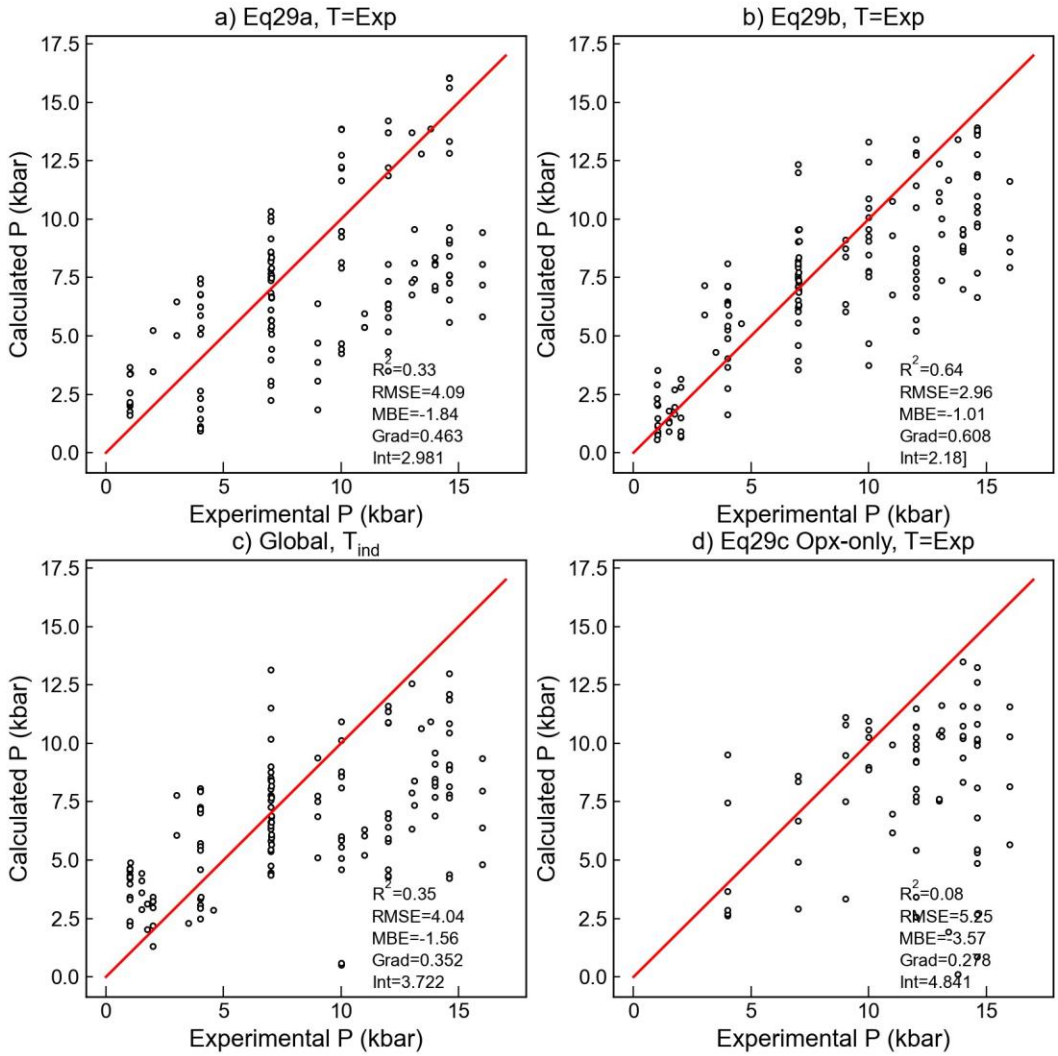

Supporting Fig. 4: Comparison of 4 different Opx-Liq and Opx-only barometers using experimental temperatures and H_2O contents. Eq29b provides the best match.

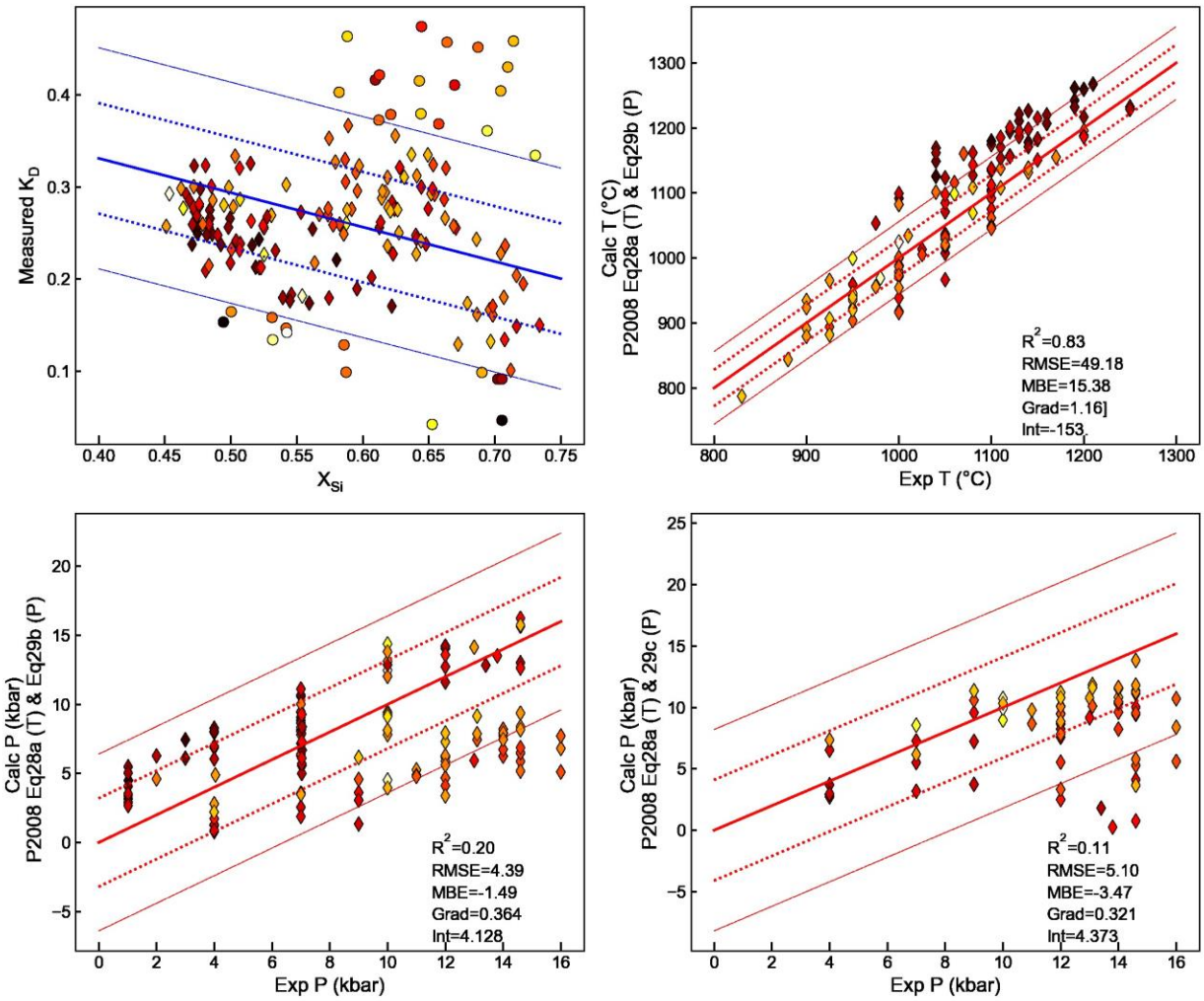

Supporting Fig. 5 – As for Fig. 9 in the main text, but only using experiments where H_2O was reported using a quantitative method.

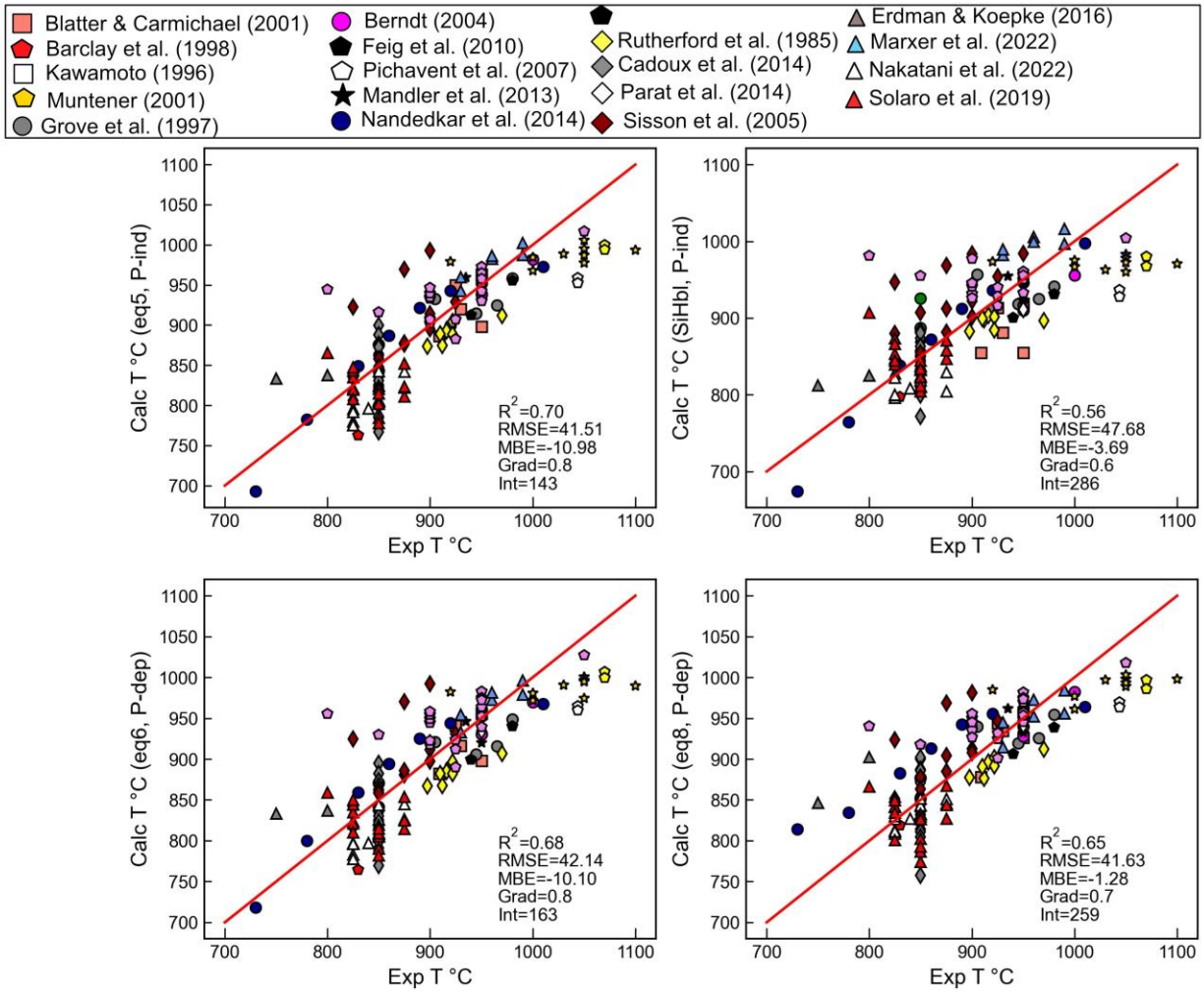

Supporting Fig. 6 – Assessment of Amp-only thermometers from Putirka (2016) on data not used during equation calibration.

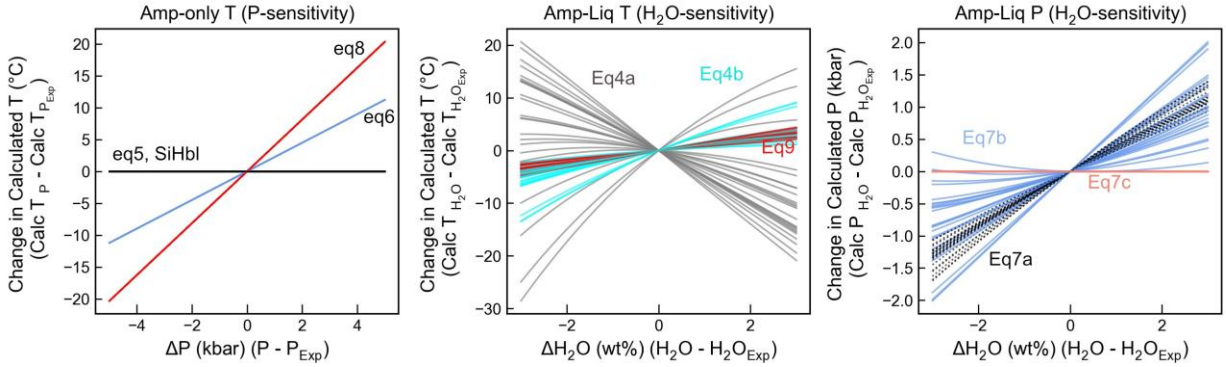

Supporting Fig. 7 – Sensitivity testing of Putirka (2016) Amp expressions to unknowns in each equation.

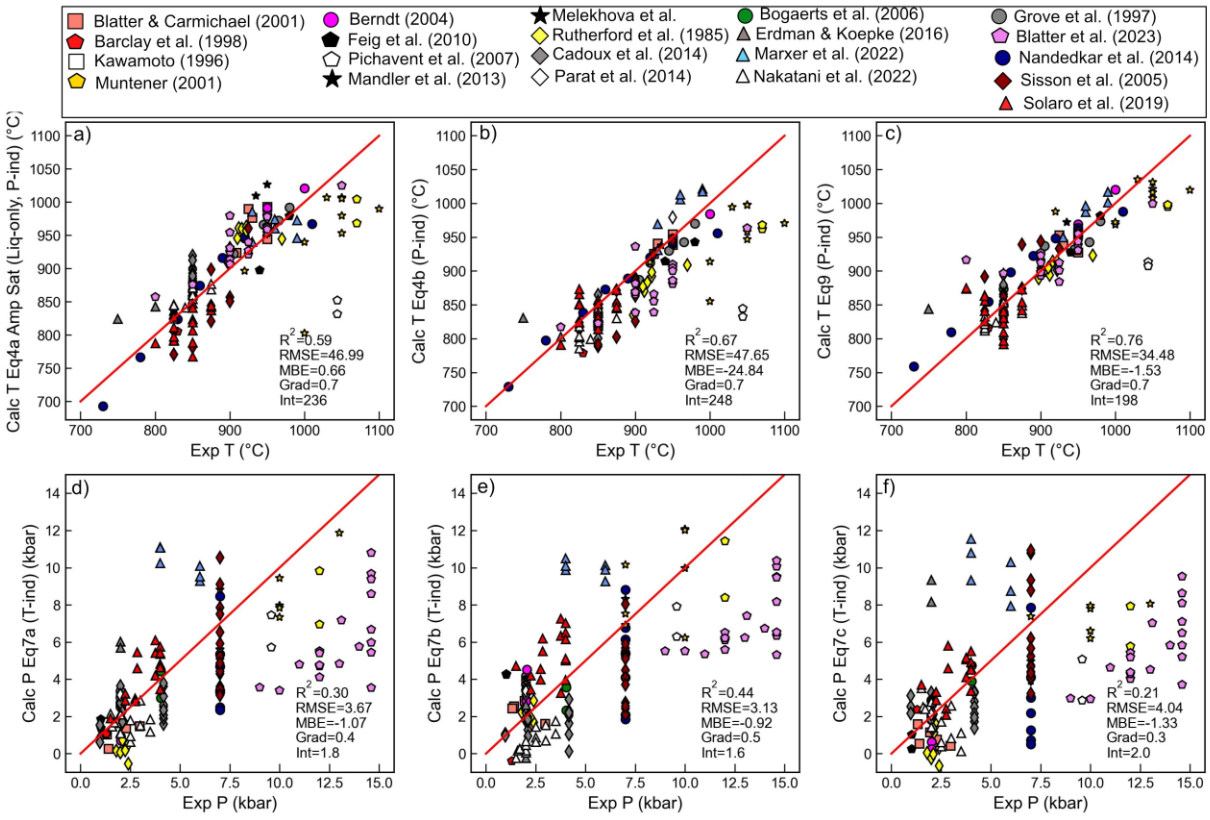

Supporting Fig. 8 – Assessment of Amp-Liq thermometers and barometers from Putirka (2016) on data not used during equation calibration.

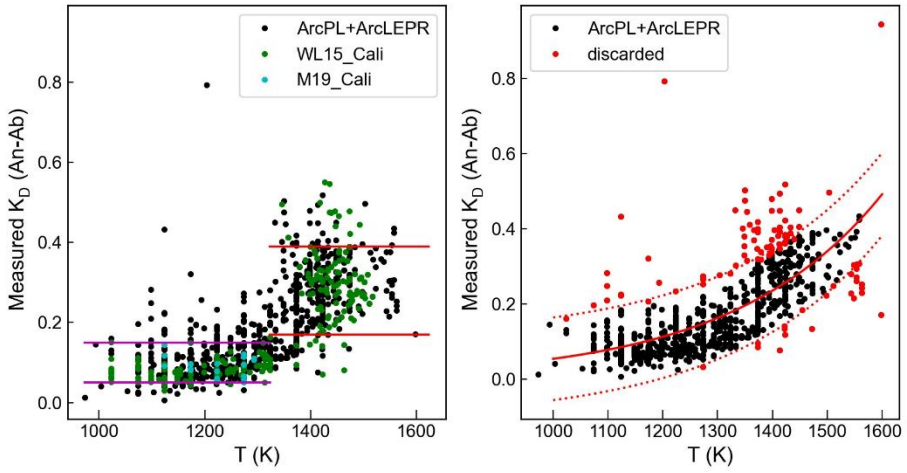

Supporting Fig. 9 – Assessing Plag-Liquid equilibrium tests using our new dataset. WL15 – Waters and Lange (2015) calibration dataset. M19-Masotta et al. (2019) calibration dataset. Lower plots are the same as Fig 16 in the main text, but without application of any equilibrium filters.

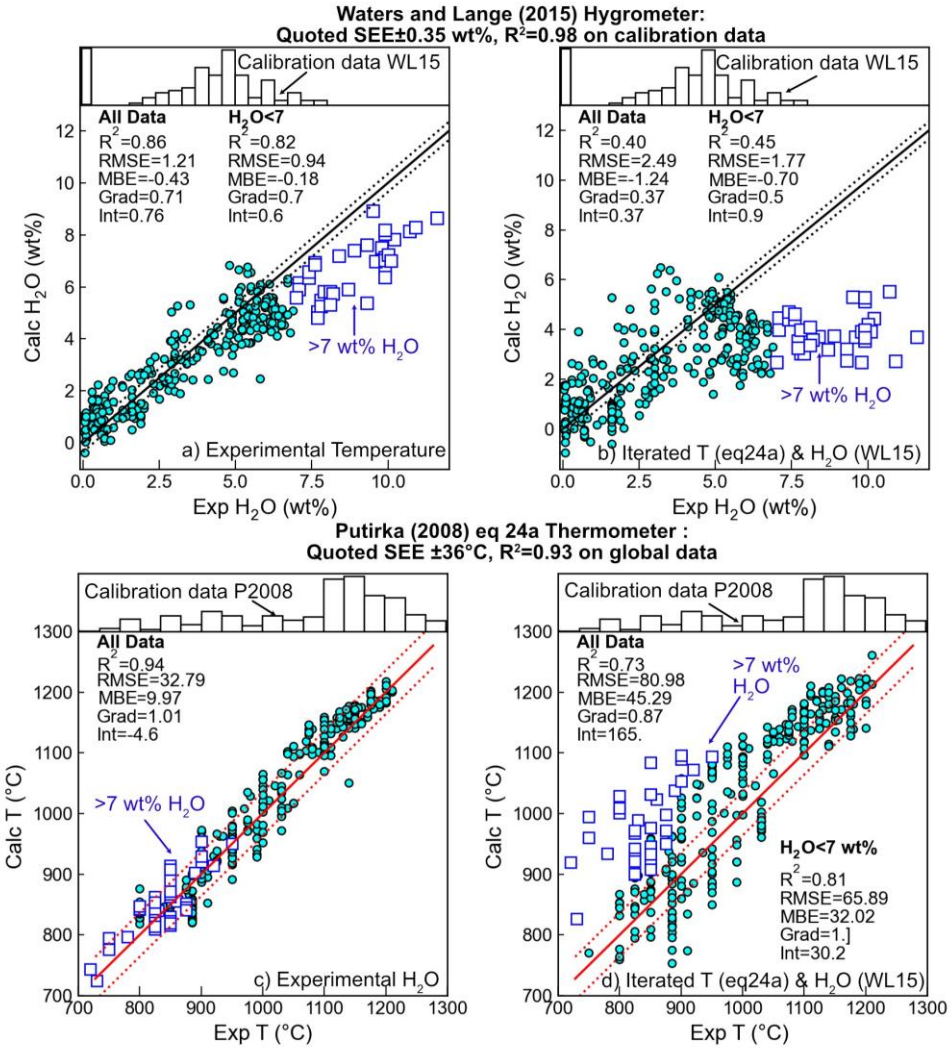

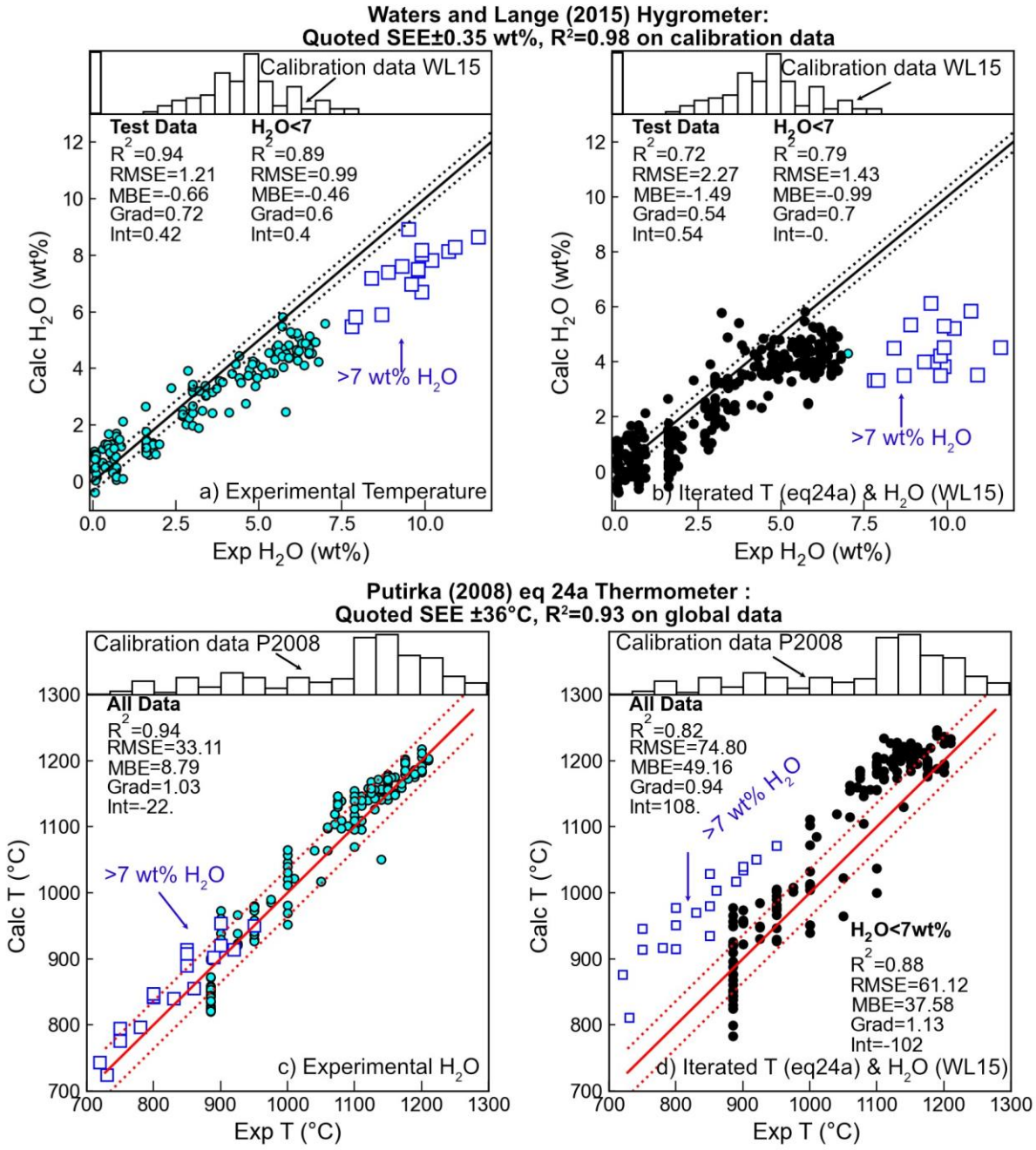

Supporting Fig. 10 – As for Fig. 16 in the text, but only using experiments where H_2O was measured using Raman, FTIR or SIMS.

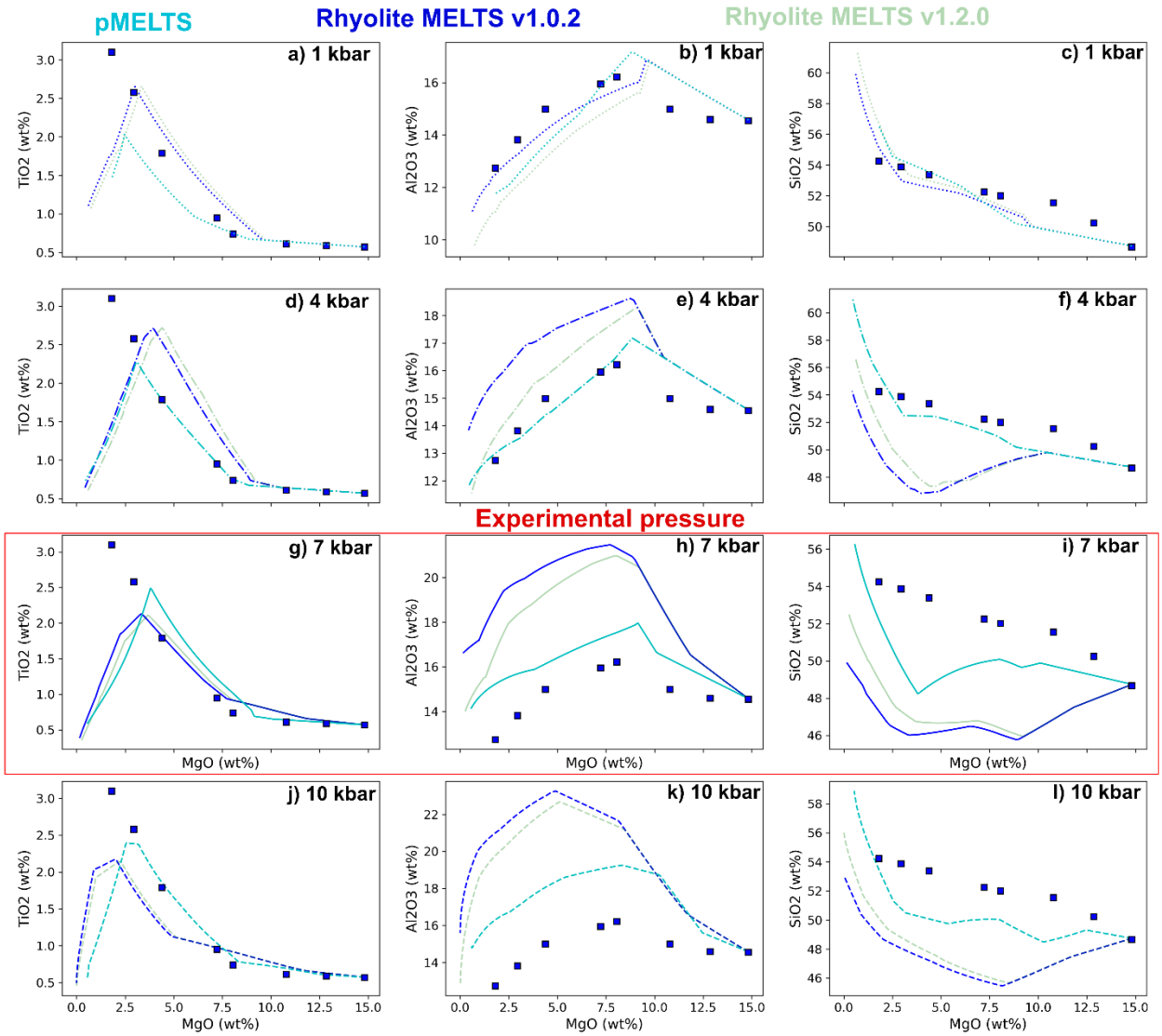

Supporting Fig 11 – As for main text, but showing different MELTS models against the experimental data of Villiger et al. (2007).

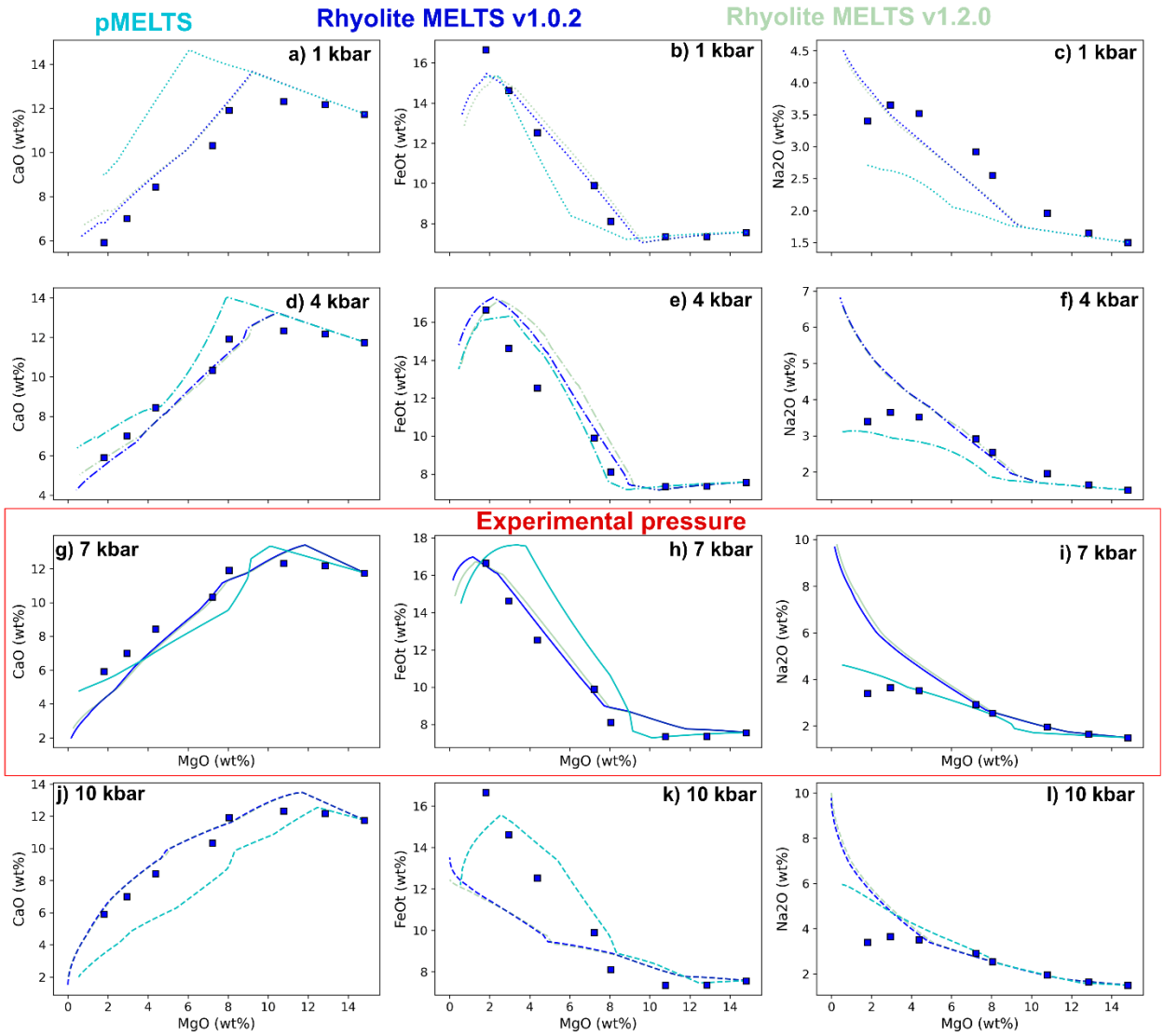

Supporting Fig 12 – As for Fig. 11, but for different major elements

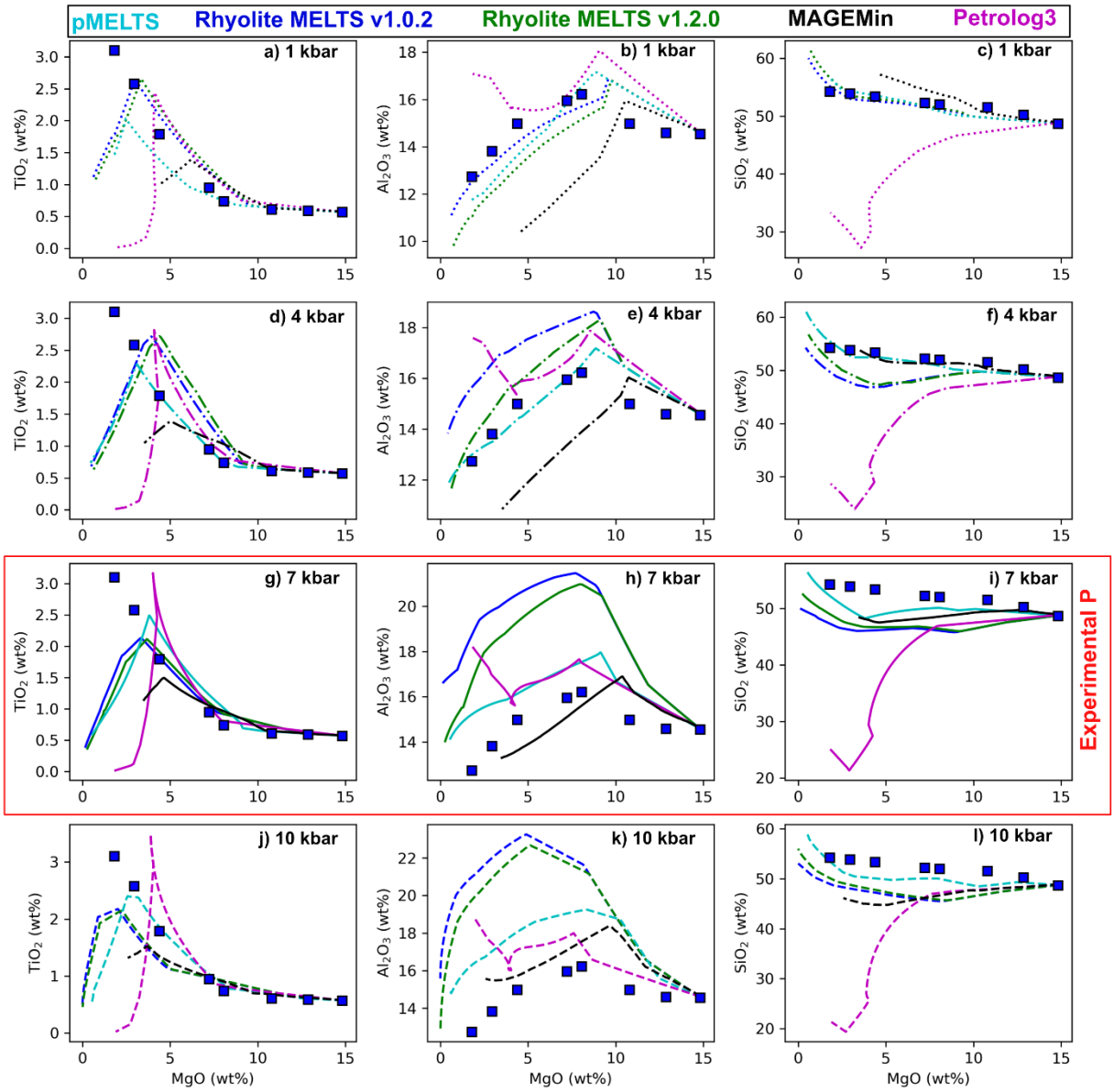

Supporting Fig. 13 – Models at 4 pressures for the Villiger et al. (2007) experiments, showing MageMin and Petrolog3